



**University Library**

Author/Filing Title ..... RANGA DINESH, K

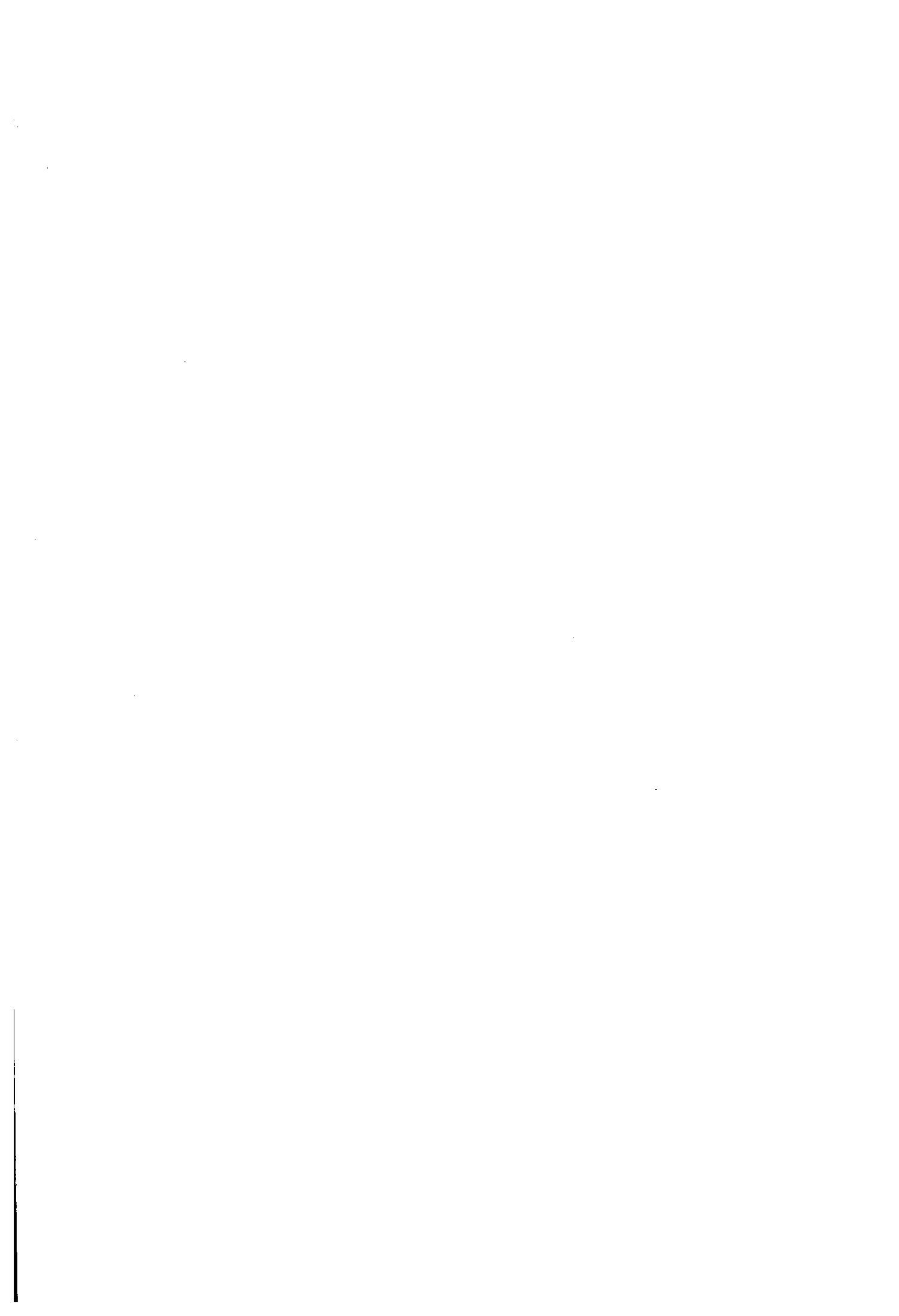
.....  
Class Mark ..... T

Please note that fines are charged on ALL  
overdue items.

<b>FOR REFERENCE ONLY</b>		
---------------------------	--	--

0403474302





# Large Eddy Simulation of Turbulent Swirling Flames

K.K.J.Ranga Dinesh

A Doctoral Thesis

Submitted in partial fulfilment of the requirements for the award  
of **Doctor of Philosophy** of the Loughborough University

January 2007

© by K.K.J.Ranga Dinesh 2007

 <b>Northampton University</b> Kingston Library
Date: <i>July 08</i>
Class: <i>T</i>
Acc No. <i>0403476302</i>

## Abstract

Large eddy simulation (LES) is attractive as it provides a reasonable compromise between accuracy and cost, and is rapidly evolving as a practical approach for many engineering applications. This thesis is concerned with the application of large eddy simulation to unconfined swirl in turbulent non-premixed flames and isothermal flows. The LES methodology has been applied for the prediction of turbulent swirling reacting and non-reacting flows based on laboratory scale swirl burner known as the Sydney swirl burner, which has been a target flame of the workshop series of turbulent non-premixed flames (TNF). For that purpose a LES code was developed that can run wide range of applications. An algorithm was developed for LES of variable density reacting flow calculations. Particular attention was given to primitive conservation (mass, momentum and scalar) and kinetic energy of the flow and mixing field. The algorithm uses the primitive variables, which are staggered in both space and time. A steady laminar flamelet model which includes the detailed chemical kinetics and multi component mass diffusion, has been implemented in the LES code. An artificial inlet boundary condition method was implemented to generate instantaneous turbulent velocity fields that are imposed on the inflow boundary of the Cartesian grid. To improve the applicability of the code, various approaches were developed to improve stability and efficiency. LES calculations for isothermal turbulent swirling jets were successful in predicting experimentally measured mean velocities, their rms fluctuations and Reynolds shear stresses. The phenomenon of vortex breakdown (VB) and recirculation flow structures at different swirl and Reynolds numbers were successfully reproduced by the present large eddy simulations indicating that LES is capable of predicting VB phenomena which occurs only at certain conditions. For swirling flames, the LES predictions were able to capture the unsteady flow field, flame dynamics and showed good agreement with experimental measurements. The LES predictions for the mean temperature and major species were also successful.

## Acknowledgements

I am grateful to my supervisors Dr. W.Malalasekera and Dr. S.S.Ibrahim for their supervision, guidance, invaluable suggestions and limitless patience have been instrumental in enabling me to develop my ideas and research goals.

I am also indebted to Dr. M.P.Kirkpatrick for his steadfast support, and encouragement, with whom I worked closely during the code development of this entire work. I would also like to express my gratitude to late Dr. J.M.J.J.Peiris for generating my initial interest in CFD through his excellent teaching, and his guidance in my early explorations of the field. I am also grateful to O.Stein, M.Ravikanti and A.Odedra for many helpful discussions throughout this work. Finally I express my deep gratitude to my parents and two sisters for their constant encouragement and understanding through all these years of my life.

# Contents

<b>1</b>	<b>Introduction</b>	<b>1</b>
1.1	General introduction . . . . .	1
1.2	Motivation of the present investigation . . . . .	2
1.3	Background and objectives of the present investigation . . . . .	8
1.4	Outline of the thesis . . . . .	12
<b>2</b>	<b>Literature Review On Swirling Flows</b>	<b>14</b>
2.1	Introduction . . . . .	14
2.2	Generation of swirl . . . . .	16
2.3	Flame stabilization by bluff body or swirl . . . . .	18
2.4	Physical background . . . . .	21
2.5	Characteristic of swirling flows . . . . .	24
2.6	Vortex breakdown . . . . .	25
2.6.1	Characteristic of vortex breakdown . . . . .	26
2.6.2	Types of vortex breakdown . . . . .	27
2.6.3	Experimental description of vortex breakdown . . . . .	28
2.6.4	Numerical computation of vortex breakdown . . . . .	33
2.6.5	Theoretical studies of vortex breakdown . . . . .	35
2.7	The Sydney swirl burner . . . . .	36
2.7.1	Burner configuration . . . . .	36

2.7.2	Non-reacting swirling flows . . . . .	38
2.7.3	Reacting swirling flames . . . . .	39
<b>3</b>	<b>Mathematical Description of Turbulent Reactive Flows</b>	<b>42</b>
3.1	Introduction . . . . .	42
3.2	Governing conservation equations . . . . .	42
3.2.1	Conservation of Mass . . . . .	43
3.2.2	Conservation of momentum . . . . .	43
3.2.3	General transport equation . . . . .	45
3.2.4	The equation of state . . . . .	48
3.3	Turbulence and turbulence modelling . . . . .	48
3.3.1	Turbulence properties . . . . .	49
3.3.2	Resolution of turbulent scales . . . . .	50
3.3.3	Modelling methods . . . . .	53
3.3.4	Direct numerical simulation . . . . .	55
3.3.5	Large eddy simulation . . . . .	55
3.3.6	Reynolds averaged Navier-Stokes equations . . . . .	56
<b>4</b>	<b>Large eddy simulation</b>	<b>58</b>
4.1	Introduction . . . . .	58
4.2	Spatial filtering . . . . .	61
4.3	Filtered governing equations . . . . .	62
4.3.1	Transport equation of mass . . . . .	62
4.3.2	Transport equation of momentum . . . . .	63
4.3.3	Transport equation of mixture fraction . . . . .	64
4.4	Modelling the subgrid stresses . . . . .	64
4.4.1	Residual stress decomposition . . . . .	65
4.4.2	Eddy viscosity models . . . . .	67

4.4.3	The Smagorinsky model . . . . .	68
4.4.4	Dynamic procedure of the Smagorinsky model . . . . .	70
4.5	Modelling the mixture fraction fluxes . . . . .	73
<b>5</b>	<b>Combustion modelling in LES</b>	<b>75</b>
5.1	Introduction . . . . .	75
5.2	The role of mixture fraction in reactive flow . . . . .	80
5.3	Simple chemical reaction model . . . . .	81
5.4	Probability density function approach . . . . .	81
5.5	Beta probability density function . . . . .	83
5.6	Laminar flamelet model . . . . .	86
5.6.1	Generating flamelet libraries in the mixture fraction space	87
5.6.2	Statistics of the non-equilibrium parameter . . . . .	89
<b>6</b>	<b>Numerical Approach</b>	<b>92</b>
6.1	Introduction . . . . .	92
6.2	Finite volume method . . . . .	92
6.3	Discretization of transport equations . . . . .	94
6.3.1	Unsteady term . . . . .	95
6.3.2	Discretization of convective fluxes . . . . .	96
6.3.3	Discretizing diffusive fluxes . . . . .	100
6.3.4	Source terms . . . . .	101
6.3.5	Complete equation . . . . .	102
6.4	Advancing in time . . . . .	103
6.4.1	Time integration of scalar equation . . . . .	103
6.4.2	Time integration of momentum equations . . . . .	105
6.4.3	Pressure correction equation . . . . .	107
6.4.4	Iteration procedure for the variable density calculation . .	109

6.4.5	Solutions of algebraic equations . . . . .	111
6.5	Initial and boundary conditions . . . . .	112
6.5.1	Inflow boundary conditions . . . . .	113
6.5.2	Outflow boundary conditions . . . . .	114
6.5.3	Solid boundary conditions . . . . .	115
<b>7</b>	<b>LES of Isothermal Swirling Flows: Results and Discussion</b>	<b>117</b>
7.1	Introduction . . . . .	117
7.2	Experimental observations . . . . .	118
7.3	Numerical description . . . . .	119
7.4	Grid resolutions and boundary conditions . . . . .	121
7.5	Statistics . . . . .	123
7.6	Flow structures of the non-swirl case . . . . .	124
7.7	Flow structures of the medium-swirl case . . . . .	133
7.8	Flow structures of the high-swirl case . . . . .	145
7.9	Vortex breakdown and recirculation . . . . .	157
7.10	Swirl number variation . . . . .	169
<b>8</b>	<b>LES of Swirling Flames: Results and Discussion</b>	<b>170</b>
8.1	Introduction . . . . .	170
8.2	Experimental observations . . . . .	171
8.3	Numerical description . . . . .	172
8.4	Grid resolutions and boundary conditions . . . . .	173
8.5	Statistics . . . . .	173
8.6	SMH1 flame . . . . .	175
8.7	SMH2 flame . . . . .	196
<b>9</b>	<b>Conclusions and Future Directions</b>	<b>213</b>
9.1	Conclusions . . . . .	213

## CONTENTS

---

9.2 Present contribution . . . . .	217
9.3 Future directions . . . . .	219
<b>References</b>	<b>235</b>

# List of Tables

2.1	Flow conditions investigated and controlled parameters for non-reacting swirling flows. . . . .	40
2.2	Flow conditions investigated and controlled parameters for reacting swirling flames. . . . .	40
3.1	Comparisons between RANS, LES and DNS approaches for numerical simulation of turbulent flows. . . . .	54
7.1	Grid resolution and typical run time (s) for non-reacting test cases	124
8.1	Grid resolution and typical run time (s) for reacting swirling flames	175

# List of Figures

2.1	Flame stabilization by bluff body or swirl . . . . .	20
2.2	Left hand side: the spreading of non-swirling jet, right hand side: the spreading of swirling jets, $S$ represent the swirl number and $F_c$ represent the centrifugal force. . . . .	23
2.3	Appearance of centrifugal instabilities, $F_{CA}$ and $F_{CB}$ are two cen- trifugal forces acting on the points $A$ and $B$ . . . . .	23
2.4	Double helix: a dye filament introduced on the vortex axis is decel- erated and expands into a slightly curved triangular sheet occurs at low Reynolds numbers. . . . .	29
2.5	Spiral: characterised by a rapid deceleration of a dye filament marking the swirl axis, which cause stagnation and by abrupt kink followed by a corkscrew-shaped motion. . . . .	29
2.6	Bubble: Dual ring, the flow is decelerated along the centreline and a stagnation point is formed. But the interior is dominated by a bubble shaped recirculation zones. . . . .	30
2.7	Bubble: Single ring, the flow is decelerated along the centreline and a stagnation point is formed. Interior is again dominated by bubble shaped recirculation zones. . . . .	30

---

## LIST OF FIGURES

2.8	Bubble: Annular, the flow is decelerated along the centreline and a stagnation point is formed. If the axial velocity at the centreline is high the bubble can resulted the annular structure. . . . .	31
2.9	Schematic of Sydney swirl burner . . . . .	41
6.1	Staggered grid and node placement in two dimensions. Circles are scalar nodes, horizontal arrows are nodes of the $u$ velocity component and vertical arrows the nodes of the $v$ velocity component. Examples of a $u, v$ and scalar cells are highlighted. . . . .	93
6.2	A finite volume cell and its neighbors in three dimensions. . . . .	96
6.3	A finite volume cell and its neighbors in the $xy$ -plane . . . . .	97
7.1	Computational domain. . . . .	120
7.2	Radial profiles of mean axial velocity in the N21S00, lines represent LES results and symbols represent experimental measurements. . . . .	122
7.3	Streamlines generated from the mean velocity fields of the non-swirl case obtained from LES calculation. . . . .	125
7.4	Radial profiles of mean axial velocity in the N21S00, lines represent LES results and symbols represent experimental measurements. . . . .	127
7.5	Radial profiles of mean radial velocity in the N21S00, lines represent LES results and symbols represent experimental measurements. . . . .	128
7.6	Radial profiles of RMS fluctuations of axial velocity in the N21S00, lines represent LES results and symbols represent experimental measurements. . . . .	130
7.7	Radial profiles of RMS fluctuations of radial velocity in the N21S00, lines represent LES results and symbols represent experimental measurements. . . . .	131

**LIST OF FIGURES**

---

7.8 Radial profiles of Reynolds shear stress in the N21S00, lines represent LES results and symbols represent experimental measurements. 132

7.9 Streamlines generated from the mean velocity field of the medium-swirl case obtained from LES calculation. . . . . 136

7.10 Radial profiles of mean axial velocity in the N29S054, lines represent LES results and symbols represent experimental measurements. 137

7.11 Radial profiles of mean radial velocity in the N29S054, lines represent LES results and symbols represent experimental measurements. 138

7.12 Radial profiles of mean swirling velocity in the N29S054, lines represent LES results and symbols represent experimental measurements. . . . . 139

7.13 Radial profiles of RMS fluctuations of axial velocity in the N29S054, lines represent LES results and symbols represent experimental measurements. . . . . 140

7.14 Radial profiles of RMS fluctuations of radial velocity in the N29S054, lines represent LES results and symbols represent experimental measurements. . . . . 141

7.15 Radial profiles of RMS fluctuations of swirling velocity in the N29S054, lines represent LES results and symbols represent experimental measurements. . . . . 142

7.16 Radial profiles of Reynolds shear stress in the N29S054, lines represent LES results and symbols represent experimental measurements. 143

7.17 Radial profiles of Reynolds shear stress in the N29S054, lines represent LES results and symbols represent experimental measurements. 144

7.18 Streamlines generated from the mean velocity field of the high-swirl case obtained from LES calculation. . . . . 146

## LIST OF FIGURES

---

7.19	Radial profiles of mean axial velocity in the N16S159, lines represent LES results and symbols represent experimental measurements.	149
7.20	Radial profiles of mean radial velocity in the N16S159, lines represent LES results and symbols represent experimental measurements.	150
7.21	Radial profiles of mean swirling velocity in the N16S159, lines represent LES results and symbols represent experimental measurements. . . . .	151
7.22	Radial profiles of RMS fluctuations of axial velocity in the N16S159, lines represent LES results and symbols represent experimental measurements. . . . .	152
7.23	Radial profiles of RMS fluctuations of radial velocity in the N16S159, lines represent LES results and symbols represent experimental measurements. . . . .	153
7.24	Radial profiles of RMS fluctuations of swirling velocity in the N16S159, lines represent LES results and symbols represent experimental measurements. . . . .	154
7.25	Radial profiles of Reynolds shear stress in the N16S159, lines represent LES results and symbols represent experimental measurements.	155
7.26	Radial profiles of Reynolds shear stress in the N16S159, lines represent LES results and symbols represent experimental measurements.	156
7.27	Instantaneous streamlines of the medium-swirl case on XY plane at $z=70\text{mm}$ at $t=30\text{ms}$ . . . . .	158
7.28	velocity vector field of the medium-swirl case on XY plane at $z=70\text{mm}$ at $t=30\text{ms}$ . . . . .	159
7.29	Instantaneous streamlines of the medium-swirl case on XZ plane at $t=30\text{ms}$ . . . . .	160
7.30	Contour plot for mean axial velocity for medium swirl-case. . . . .	163

**LIST OF FIGURES**

---

7.31 Contour plot for mean swirling velocity for medium swirl-case. . . 163

7.32 Centreline mean axial velocity for the medium-swirl case, lines represent LES results and symbols represent experimental measurements. . . . . 164

7.33 Turbulent kinetic energy for the medium-swirl case, lines represent LES results and symbols represent experimental measurements. . 165

7.34 Recirculation and vortex breakdown, contour plot of the mean axial velocity for medium swirl case and dash line indicate the negative mean axial velocity. . . . . 166

7.35 Bluff body stabilized recirculation zone, contour plot of the mean axial velocity for medium swirl case and dash line indicate the negative mean axial velocity. . . . . 167

7.36 Vortex breakdown (VB) bubble, contour plot of the mean axial velocity for medium swirl case and dash line indicate the negative mean axial velocity. . . . . 168

7.37 Distribution of the swirl number and mean axial velocity along the central axis (left side: N29S054, right side: N16S159. . . . . 169

8.1 Radial profiles of mean axial velocity in the SMH1 flame, solid lines represent grid 1 results, dashed lines represent grid 2 results and symbols represent experimental measurements. . . . . 174

8.2 Laminar flamelet profiles, scatter plots of temperature, and mass fraction verses mixture fraction at  $x/D = 0.8$  for flame SMH1. Solid line represent strain rate of  $500s^{-1}$  and dashed line represent strain rate of  $300s^{-1}$  respectively. . . . . 177

8.3 Snapshot of the filtered mixture fraction of flame SMH1. . . . . 178

8.4 Snapshot of the filtered temperature(K) of flame SMH1. . . . . 179

## LIST OF FIGURES

---

8.5	Contour plot of mean axial velocity and mean velocity vector field of flame SMH1. . . . .	184
8.6	Radial profiles of mean axial velocity in the SMH1 flame, lines represent LES results and symbols represent experimental measurements. . . . .	185
8.7	Radial profiles of mean swirling velocity in the SMH1 flame, lines represent LES results and symbols represent experimental measurements. . . . .	186
8.8	Radial profiles of RMS axial velocity in the SMH1 flame, lines represent LES results and symbols represent experimental measurements. . . . .	187
8.9	Radial profiles of RMS swirling velocity in the SMH1 flame, lines represent LES results and symbols represent experimental measurements. . . . .	188
8.10	Contour plot of mean temperature, $T(K)$ of flame SMH1. . . . .	189
8.11	Radial profiles of mean mixture fraction in the SMH1 flame, lines represent LES results and symbols represent experimental measurements. . . . .	190
8.12	Radial profiles of mixture fraction variance in the SMH1 flame, lines represent LES results and symbols represent experimental measurements. . . . .	191
8.13	Radial profiles of mean temperature in the SMH1 flame, lines represent LES results and symbols represent experimental measurements. . . . .	192
8.14	Radial profiles of mass fraction of H <sub>2</sub> O in the SMH1 flame, lines represent LES results and symbols represent experimental measurements. . . . .	193

## LIST OF FIGURES

---

8.15 Radial profiles of mass fraction of CO <sub>2</sub> in the SMH1 flame, lines represent LES results and symbols represent experimental measurements. . . . .	194
8.16 Radial profiles of mass fraction of CO in the SMH1 flame, lines represent LES results and symbols represent experimental measurements. . . . .	195
8.17 Contour plot of mean axial velocity and mean velocity vector field of flame SMH2. . . . .	199
8.18 Radial profiles of mean axial velocity in the SMH1 flame, lines represent LES results and symbols represent experimental measurements. . . . .	200
8.19 Radial profiles of mean radial velocity in the SMH2 flame, lines represent LES results and symbols represent experimental measurements. . . . .	201
8.20 Radial profiles of mean swirling velocity in the SMH2 flame, lines represent LES results and symbols represent experimental measurements. . . . .	202
8.21 Radial profiles of RMS axial velocity in the SMH2 flame, lines represent LES results and symbols represent experimental measurements. . . . .	203
8.22 Radial profiles of RMS radial velocity in the SMH2 flame, lines represent LES results and symbols represent experimental measurements. . . . .	204
8.23 Radial profiles of RMS swirling velocity in the SMH2 flame, lines represent LES results and symbols represent experimental measurements. . . . .	205
8.24 Contour plot of mean temperature of flame SMH2. . . . .	206

## LIST OF FIGURES

---

8.25	Radial profiles of mean mixture fraction in the SMH2 flame, lines represent LES results and symbols represent experimental measurements. . . . .	207
8.26	Radial profiles of mixture fraction variance in the SMH2 flame, lines represent LES results and symbols represent experimental measurements. . . . .	208
8.27	Radial profiles of mean temperature in the SMH2 flame, lines represent LES results and symbols represent experimental measurements. . . . .	209
8.28	Radial profiles of mass fraction of H2O in the SMH2 flame, lines represent LES results and symbols represent experimental measurements. . . . .	210
8.29	Radial profiles of mass fraction of CO2 in the SMH2 flame, lines represent LES results and symbols represent experimental measurements. . . . .	211
8.30	Radial profiles of mass fraction of CO in the SMH2 flame, lines represent LES results and symbols represent experimental measurements. . . . .	212

# Nomenclature

## Roman Symbols

$A$	surface of the control volume
$C(x, t)$	dynamic model parameter
$C_s$	Smagorinsky constant
$C_{ij}$	cross stress term
$D$	diameter of the bluff body (50mm)
$f$	mixture fraction
$f_i$	external forces acting on the flow field
$F_{conv}$	convective flux across the cell face
$F_{diff}$	diffusive flux across the cell face
$G$	grid filter function
$H$	discrete convection operator
$h$	enthalpy
$J_{\alpha,i}$	diffusion flux vector for species $\alpha$
$K$	turbulent kinetic energy
$l_i$	integral length scale
$l$	subgrid length scale
$L$	discrete diffusion operator
$L_{ij}$	Leonard stress
$N_t$	number of samples
$N_x$	number of grid points along x direction
$N_y$	number of grid points along y direction
$N_z$	number of grid points along z direction

## NOMENCLATURE

---

$P$	pressure
$\bar{P}_\phi(\phi; x, t)$	unweighted subgrid pdf
$q_{sgs}$	velocity scale
$R$	radius of the bluff body (25mm)
Re	Reynolds number
$R_{ij}$	Reynolds stress
$r_i$	grid expansion ratio
$r$	radial distance from centreline
$S$	swirl number
$S_{ij}$	strain rate tensor
$S_\phi$	source term
$t$	time
$T$	temperature in degrees Kelvin
$T_{ij}$	subtest scale stress
$U_j$	fuel jet velocity
$U_s$	axial velocity of the primary annulus
$U_e$	coflow velocity
$u_i$	velocity components in Cartesian coordinates
$W_s$	tangential velocity of the primary annulus
$x_i$	Cartesian coordinate direction
$Y_\alpha$	mass fraction of species $\alpha$
$Z_\beta$	mass fraction of element $\beta$

## NOMENCLATURE

---

### Greek Symbols

$\alpha_{ij}$	subgrid model kernel for the dynamic procedure
$\beta_{ij}$	subgrid model kernel for the dynamic procedure
$\Gamma$	molecular diffusivity
$\Gamma(a)$	Gamma function
$\delta_{ij}$	Kronecker delta
$\delta(f)$	Dirac delta function
$\Delta$	grid filter width
$\hat{\Delta}$	test filter width
$\Delta t$	numerical time step
$\Delta x$	spatial mesh spacing
$\varepsilon$	turbulent kinetic energy dissipation rate
$\eta$	Kolmogorov length scale
$\theta(\varphi; x, t)$	fine grained pdf
$\nu$	kinematic viscosity
$\nu_t$	turbulent viscosity
$\rho$	fluid density
$\sigma_{ij}$	viscous stress tensor
$\tau_{ij}$	subgrid scale stress tensor
$\phi$	general scalar
$\chi$	scalar dissipation rate

# Chapter 1

## Introduction

### 1.1 General introduction

Combustion is one of the most important processes in engineering which depend upon interrelated processes of fluid mechanics, heat and mass transfer, chemical kinetics, thermodynamics and turbulence. A significant part of the energy (80%) comes from combustion of liquids (gasoline or hydrocarbon fuels), solids (coal and woods), and gases (natural gas). There are wide range of applications of combustion in the areas of aero engines, gas turbine combustors, boilers, furnaces, internal combustion engines, power station combustors and many other combustion equipment. It is well known that combustion will remain a predominant source of power for many generations. Combustion not only generates heat, which can be converted into power, but also produces pollutants such as oxides of nitrogen ( $NO_x$ ), soot and unburnt hydrocarbons ( $HC$ ). In addition unavoidable  $CO_2$  emissions leads to occur the global warming. Therefore the study of combustion has advanced substantially by improving the efficiency of combustion processes in experimental, theoretical and computational areas while increasing the fuel economy. Well developed diagnostic techniques allow researchers to discover

## 1.2 Motivation of the present investigation

---

detailed phenomena associated with combustion processes. At the same time, increased computational power helps to simulate detailed reaction mechanisms and transport processes. Comprehensive computer simulations can be conducted in many complex physiochemical processes including multidimensional time dependent combustion problems with intricate details.

In most of the situations, combustion takes place within a turbulent rather than a laminar flow field. This is because turbulence increases the mixing processes and thereby enhances combustion. Additionally combustion releases heat and thereby generates flow instability by buoyancy and gas expansion, which then enhances the transition to turbulence. Turbulence itself is quite challenging and probably the most significant unresolved problem in classical physics. The success of turbulence models in solving engineering problems has encouraged similar approaches for turbulent combustion, which consequently led to the formulation of turbulent combustion models. As combustion processes are difficult to handle using analytical techniques the numerical simulation of turbulent combustion has developed to be a valuable tool for the development of combustion processes, which involve strong coupling between chemistry, transport and fluid dynamics.

## 1.2 Motivation of the present investigation

Computational fluid dynamics (CFD) is being used with increasing regularity in the design and development of problems involving academic and industrial fields. The advantage of the CFD approach is that the complex physical interactions which occur in a problem can be modelled simultaneously, and hence, their relative influence on the total behavior understood. CFD calculations may not exist for the complete underlying physics, which involves assumptions in the mathematical process and leads to occur possible inaccuracy. With, care, however,

## 1.2 Motivation of the present investigation

---

these approximations can be minimized to a level where the accuracy of CFD technique is perfectly satisfactory for design purposes. In the study of turbulent flows, the ultimate objective is to obtain a tractable quantitative theory or model that can be used to calculate quantities of interest and practical relevance. The numerical simulations of turbulent flows has been mainly pursued by three different approaches known as Reynolds Averaged Navier-Stokes (RANS), large eddy simulation (LES) and direct numerical simulation (DNS). Most commercial codes are based on Reynolds average Navier-Stokes (RANS) formulation and compute only the time averaged flow field. The RANS based solvers usually need low computational costs and codes are optimized to cooperate with commercial CAD softwares and are able to handle complex geometries. So far, the main issue in connection with RANS has been the development of statistical turbulence models in the context of linear and non-linear eddy viscosity models, and second moment closures, Pope (2000). The primary aim of RANS turbulence modelling is to create a simpler framework for simulating flows of engineering interest. However, this is far from being the case, especially when complex models such as non-linear eddy viscosity models are employed. For example, in the design of practical engineering applications such as industrial gas turbines characterized by complex flow patterns often require rapid mixing and modelling of such flows typically cannot be achieved using Reynolds average Navier-Stokes equations.

Direct numerical simulation (DNS) try to resolve the all turbulent length scales down to the Kolmogorov length in space and time. In this approach DNS grids must ensure that the mesh is fine enough to resolve the smallest scales (Kolmogorov scales). Highly accurate numerical methods have been developed to solve the Navier-Stokes equations, and the numerical accuracy of DNS is generally of high standard. However, the fundamental limitation of DNS is determined by the Reynolds number and it is well known that the main drawback of DNS

## 1.2 Motivation of the present investigation

---

is of course its very large computational cost which increases rapidly with the Reynolds number. The DNS calculation is only possible for low or moderate Reynolds number flows and it is highly impossible for practical engineering applications such as DNS of industrial gas turbine combustors even for the next decade. As a way between these two extremes, large Eddy Simulation (LES) is the best possible way to handle the transient nature of turbulence, while offering an affordable computational economy. The objective of large eddy simulation is to explicitly compute the largest structure of the flow field (typically structures larger than the computational mesh size) whereas the effects of the small unresolved scales and their effects on the large scales are modelled. Since the small scales contain only a tiny portion of total energy, are more isotropic than the large scales, are thus thought to be more universal and homogeneous, their models can be simpler and relatively easier to model. Over the last few years large eddy simulation (LES) has undergone considerable progress simulating the unsteady behavior of more engineering-oriented configurations from relatively simple flows to complex reacting flames and proved its possibilities to increase the quality of prediction, Piomelli (1999), Poinso and Veynante (2001). Especially in the context of geometrically complex flows and in the presence of aerodynamic instabilities as typical features of the flow, LES become very attractive compared to classical statistical modelling. The present computational power and memory has made LES applicable to variety of incompressible and compressible flows, including heat transfer, stratification, passive scalars and chemical reactions. Deardorff (1970) was the first to published large eddy simulation results based on a three dimensional turbulent channel flow. Since then the underlying theory has been advanced, new models have been developed and tested, more efficient numerical schemes have been implemented.

LES technique is attractive for a number of reasons for calculating the flows

## 1.2 Motivation of the present investigation

---

in combustion systems: the unsteady nature of the calculation and ability to capture the multiple length and time scales should allow the calculation of structures which are poorly predicted by many Reynolds averaged techniques. Large structures in turbulent flows depend on the system geometry whereas small structures are generally assumed to have more universal features and models are good enough to describe these small structures. That allows the calculations to predict the combustion instabilities which occurs due to a coupling between heat release, hydrodynamic flow field and acoustic waves. LES also allows a detailed description of turbulence/chemistry interactions, Poinso and Veynante (2001). LES does not however, overcome, the closure problem associated with reaction since combustion is a molecular process that occurs at the smallest scales. The main challenge in modelling combustion using LES comes from the fact that the reaction occurs at a layer which can not be resolved by a typical filter width used in LES. Thus, the chemical reaction and its interaction with the flow field must be modelled, completely. The required theoretical background for combustion modelling through LES is still under development, and its full predictive strength has not yet been reached. In the way to develop this potential ability, it is more important to consider the properties of numerical algorithms, such as accuracy of scalar mixing process, dissipation rate and energy conservation in LES of chemically reactive flows.

LES provides acceptable solution to study coupled combustion, transport and multiphase processes that is unattainable using DNS technique with a degree of fidelity and more accurate than conventional computational fluid dynamics methods based on RANS calculation. Significant model development and validation is required, however, to achieve an acceptable level of confidence in the accuracy prediction from various submodels. As the modelling becomes more sophisticated, the theory that LES accurately captures the relevant dynamical processes must be

## 1.2 Motivation of the present investigation

---

validated for the hierarchy of cases to qualify the accuracy with which submodels can represent the actual physical phenomena of interest, Piomelli (1999). Given the simulation modelling development and validation requirements, the focus can be divided into two distinct areas. First the introduction of contemporary aspects related to modelling and validation based on fundamental issues related to systematic model validation, with emphasis placed on algorithmic requirements, validation requirements and accurate boundary conditions implementation. Second focus on more practical applications, related to the complexity of the flow and combustion dynamics, and provide a hierarchy of case studies investigated by numerous authors, aimed at the progressive prediction of the key phenomena observed in practical devices, Piomelli (1999), Pitsch (2006), Poinso and Veynante (2001). Although LES is more computationally expensive than RANS, it offers two significant advantages. First, the large scale motion of the turbulence that contains most of the turbulent kinetic energy and controls the dynamics of the turbulence is resolved, and hence computed directly. Second the knowledge of the large scale dynamics can be used to calculate the model coefficients dynamically so called dynamic models, which are independent of the filter size, Germano *et al.* (1991).

Molecular mixing of scalar quantities and chemical reactions in turbulent flows, occurs essentially at the smallest turbulent scales and it is characterised and quantified by the dissipation rate of the scalar variance, which plays a central role in combustion modelling. In LES as for RANS, the filtered chemical source term has to be modelled. Hence the two previously mentioned advantages for LES apparently do not apply to the chemical source term. However, LES still provides substantial advantages for modelling turbulent combustion that the scalar mixing process and dissipation rates are predicted with considerably improved accuracy compared to RANS, especially in complex flows. For example, Raman

## 1.2 Motivation of the present investigation

---

and Pitsch (2005) carried out simulation of bluff body stabilized flames, where a simple steady state diffusion flamelet model in the context of LES with a recursive filter refinement method led to excellent results. Such accuracy has not been achieved with RANS simulations of the same configurations, Kim and Huh (2002).

Consequently, combustion models that have been proposed and applied in LES are mostly similar to RANS models. Although the basic ideas and fundamental concept of RANS models can still be used for LES, additional changes required have to be addressed. Recently the application of LES to turbulence combustion has extensively applied to variety of combustion problems of technical interest including real combustion devices. For example Pitsch (2006) has reviewed recent progress of LES combustion and Poinso and Veynante (2001) have shown various LES calculations on practical combustion devices. A state of the art LES calculation of a section of a modern Pratt and Whitney gas turbine combustor has been performed by Mahesh *et al.* (2005). Collectively, these applications present a wide variety of turbulence and turbulence-chemistry interaction modelling approaches currently being used in practical LES combustor studies. The importance of identifying adequate tools to effectively analyse the general LES database is also addressed in this context, Pitsch (2006). Establishing such tools is crucial to provide enhanced understanding of the fundamental driving mechanisms and phenomena involved. Finally it can be concluded that the unsteady three dimensional nature of the LES approach promises possibilities of the usage of LES as a design tool. Furthermore the knowledge of the unsteady flow field facilitates the modelling of the combustion process. As a design tool, LES can examine two main phenomena, the time evolving mixing behavior and the time evolving combustion. The current investigation examine these two phenomena by applying LES to turbulent swirling flames, which have a range of applications

### 1.3 Background and objectives of the present investigation

in combustion equipment for power generation and transportation.

## **1.3 Background and objectives of the present investigation**

Swirl is commonly used in many engineering applications of combustion to control essential characteristics of high intensity turbulent flows and to stabilise flames. Introduction of swirl has the capability to generate strong recirculation zones, which helps to improve the whole mechanism of the mixing process. Swirl can reduce the flame length by producing higher rates of entrainment and fast mixing particularly in the shear layer region, which improve flame stability, reduce emissions and as a result the burner can be minimized and has an extended life, Syred and Beer (1974). In swirling jets and flames sufficient strength of swirl will produce a maximum pressure gradient in the direction of the flow, which in turn produces a reversal of the flow or vortex breakdown. Depending on the degree of swirl, furnace and burner geometry, different recirculation patterns and vortex breakdown regimes can be achieved and these can be controlled by adjusting the degree of swirl to promote better mixing, flame stabilisation and minimise pollutant formation, Sloan *et al.* (1986).

In the literature different flow configurations have been experimentally investigated to study the formation of recirculation zones and the vortex breakdown process. Theoretical studies have been carried out to analyse the instabilities and onset of vortex breakdown for reacting and non-reacting swirling flows and it has been reported that the influence of swirl depends on different flow parameters such as inflow velocity profiles, Reynolds number, level of swirl and geometrical configuration. A number of good reviews and a body of literature exist on these

### 1.3 Background and objectives of the present investigation

---

topics ranging from vortex breakdown to instabilities of swirling flows. For example Sarpkaya (1971), Syred and Beer (1974), Escudier (1988), Lucca-Negro and O'Doherty (2001). Numerical modelling has also been used as a tool to understand the fundamental flow physics of laminar and turbulent swirling flows. The numerical prediction of turbulent swirling flows is a challenging subject due to anisotropic turbulence structure in recirculation zones. An extensive review of the modelling work on swirling flows has been reported by Sloan *et al.* (1986), which describe the difficulties and complexities associated with CFD approaches to swirling flow calculations.

The majority of current methods to model turbulent swirling flames and practical combustion systems are based on Reynolds averaged Navier-Stokes (RANS) equations accompanying different turbulence models. The review by Sloan *et al.* (1986) summaries many RANS type swirling flow calculations concludes that the performance is generally discouraged in the vicinity of recirculation zones. The review also describes various advanced turbulence models such as Reynolds stress model and algebraic Reynolds stress model options which appear to show some improvements and note that swirling flows are three-dimensional phenomena therefore steady-state axi-symmetric transport equations are incapable of reproducing complex swirl flows. Weber (1986) has assessed three turbulence models  $k - \epsilon$  model, Reynolds stress model (RSM) and algebraic Reynolds stress models (ASM) to simulate confined swirling flows. It was observed that neither the generation of turbulence nor the distribution of tangential momentum was correctly predicted by the  $k - \epsilon$  model. In contrast the Reynolds stress model and algebraic Reynolds stress model performance were better and produced reasonable agreement with experimental data for certain confined swirl cases but for certain other cases none of the turbulence models was able to predict the correct reverse flow when compared with measured data. In general RANS models are

### 1.3 Background and objectives of the present investigation

primarily suitable to calculate stationary flows with non-gradient transport and it is difficult to capture the unsteady nature of the large-scale flow structures typically found in turbulent swirling flows. Spall and Gatski (1987), Breuer and Hanel (1993), Krause (1990) have used a three-dimensional unsteady RANS approach to compute behavior of swirling flows. However those studies confirmed that to achieve any degree of success in RANS type computations have to be transient and three-dimensional.

Large eddy simulation (LES) in contrast is a powerful and effective tool for handling large-scale turbulent motions as the method is based on time resolved three-dimensional unsteady large-scale turbulent motions. In LES only the small scale eddies which have more universal behavior and contain less turbulent kinetic energy are modelled. With adequate spatial and temporal resolution the method is capable of capturing large-scale dynamic behavior in flows. Large eddy simulation technique as a tool for the simulation of swirling flow fields in both reacting and a non-reacting cases has emerged only in the 1990s and hence a relatively new field. LES has been applied to variety of swirling applications including combustion such as aircraft engine combustion by DiMare *et al.* (2004), Kim *et al.* (1999), dynamics of swirling premixed and spray flames by Sankaran and Menon (2002) and combustion instabilities by Wall and Moin (2005). As mentioned before the application of LES to real combustion devices including highly transient swirling motion has gained increased popularity due to its potential ability to capture detailed flow and mixing fields and the availability of computing power to perform large calculations.

One of the main advantages of LES applications is in swirl flows LES can capture oscillatory motions such as precessing vortex core (PVC) seen in experiments. Pierce and Moin (2004) for example showed promising agreement between LES

### 1.3 Background and objectives of the present investigation

and experimental data for a low swirl number case and Wang and Bai (2005) have showed successful comparison between LES predictions and experimental measurements operating under different conditions in confined turbulent swirling flows. More recently several LES simulations have also been carried out for laboratory scale bluff body stabilized flames, Raman and Pitsch (2005), Kempf *et al.* (2006), which are not as complex as swirling flows but contain similar recirculation zones near bluff body. The predicted results show very good agreement with experimental data. This bluff body flame series was major step toward more realistic laboratory scale flames, but still lack of swirl, which is probably the most common mechanism to improve the mixing and flame stabilization in technical applications.

The objective of this research is to conduct the large eddy simulation (LES) based methodology for the modelling of turbulent swirling flames based on laboratory scale swirl burner. The configuration considered is an unconfined, swirling flow configuration known as the Sydney swirl burner, which is an extension of the above mentioned bluff body burner to swirling flames, experimentally investigated by Al-Abdeli and Masri (2003a), Al-Abdeli and Masri (2003b), Masri *et al.* (2004). The Sydney burner is a target swirl burner of the workshop series of turbulent non-premixed flames, TNF (2006). This flame series allows the examination of the effect of various parameters such as fuel composition, flow rates and swirl number. The LES for the Sydney swirling flame series is major steps toward more realistic laboratory applications in turbulent combustion and the entire flame series provide detailed experimental data suitable for validation of LES. For that purpose, the LES code was developed that can be run on a single workstation computer to simulate a wide range of applications.

## 1.4 Outline of the thesis

The Thesis is organized as follows:

- **Chapter 1** provides an introduction section and the objective of this thesis to develop LES methodology capable of performing LES of Sydney swirling flame series.
- **Chapter 2** describes the physics of swirling flows followed by the phenomenon of vortex breakdown (VB) under experimental, numerical and theoretical consideration and experimental details about the Sydney swirl burner targeted in this work.
- **Chapter 3** provides fundamental aspects of theory presented in this work. The first part present the governing equations and corresponding conservation laws while the second part describes the important physics behind the concept of turbulence.
- **Chapter 4** introduces the basic concept of large eddy simulation (LES). Partitioning is generally achieved by application of a spatial filter which leads to a filtered form of the equations. The non-commutativity of the filtering operation with respect to multiplication leads to extra terms which are interpreted as subgrid scale stresses. Furthermore the chapter presents the filtered forms of the governing equations and the theory behind the subgrid scale models.
- **Chapter 5** provides an overview of the combustion modelling in LES and then discuss the combustion model used in this work. Details of the laminar flamelet model and the use of probability density function (PDF) of the scalars are also discussed.

- **Chapter 6** presents the numerical implementations of previously mentioned mathematical formulations. The first part presents a description of the spatial discretization schemes. The spatial discretization uses a finite volume method on a staggered Cartesian grid. The second order central difference approximation uses as a basic scheme for all spatial derivative terms. In terms of stability a number of higher order upwind schemes are also used for the advection terms. The second part presents a discussion of a number of schemes used for the time integration of the equations. The Crank-Nicolson scheme and second and third order hybrid Adams schemes are discussed. The full set of equations is advanced using a fractional step method. For reacting flows involving large rapid changes in density, both the velocity and density fields must be corrected simultaneously to ensure conservation of mass. Since density depends on mixture fraction (flamelet model) an iterative method is required and this is discussed.
- **Chapter 7** presents LES results of isothermal test cases for different swirl numbers starting from zero to higher swirl numbers. The results are compared with experimental data and discussed.
- **Chapter 8** presents the LES results for selected Sydney swirling flames known as SMH1 and SMH2. The results are compared with experimental data and discussed.
- **Chapter 9** summarises the conclusions of this research and the future recommendations.

## Chapter 2

# Literature Review On Swirling Flows

### 2.1 Introduction

Powerful geophysical flows such as tornados, dust devils or water spouts are dominated by swirl and can be seen in natural situations. Swirl flows are present in turbo-machinery, propulsion systems and chemical reactors; they are also used as a basic tool for process engineering. Around the tips of wings, strong swirl flows occur which are vital for creating lift. In burners and combustors by creating regions of reverse flow where the reaction occurs, the reactants are kept inside the combustor for an enhanced time, allowing for better mixing and more complete reaction. This helps to stabilize the flame and to control the emission of pollutants. An improved understanding of swirl flows and their interaction with flames help to devise strategies to enhance the performance and safety of a given combustor, to reduce its size, weight and cost, and to minimise the emission of pollutants.

In high intensity combustion systems, swirl can improve the flame stability by forming toroidal recirculation zones, which reduce the combustion length by producing higher rates of entrainment of the ambient fluid and fast mixing in strongly swirling zones. It is a result of an impartation of a tangential velocity component by use of a swirl generator positioned upstream of the reacting chamber. At sufficient degree of swirl can cause an adverse pressure gradient, which creates flow reversal and recirculation zones. It can reduce the flame length by producing the rates of entrainment of the ambient fluid and fast mixing close to the exit nozzle and on the boundaries of the recirculation zones. The lower velocities on the edge of the recirculation zone also assist in the stabilization process by helping to prevent flame lift off. The additional presence of swirl develops the strong coupling between axial and swirl velocity, which also produces vortex breakdown phenomena.

An introduction into the basic physics of swirling flows was given by Gupta *et al.* (1984), while more advanced aspects on vortex breakdown have been reviewed by Hall (1972), Leibovich (1978) and Escudier (1987). The high swirl strength can produce the large adverse pressure gradient in the direction of the flow, which cause to form the vortex breakdown. In combustion systems it can cause high rate of heat release as product of combustion and reignite in fuel air streams. Especially the swirl distribution produces a central recirculation zone link with the vortex breakdown, which provide a stable compact flame with controlling pollutant emissions, e.g. Weber (1986). The swirl flows are subject to a various structural changes involving very large disturbances when a swirl velocity components is varied. These flow patterns depend on several key parameters such as Reynolds number, swirl number, inlet conditions, geometry, e.g. Lucca-Negro and O'Doherty (2001).

In these applications there is the necessity of understanding the interactions of the competing dynamical mechanism that arise in swirling jets and their evolution. For example, the occurrence of vortex breakdown and the structure of the breakdown region have to be investigated in great detail. The objective of this chapter is to discuss the fundamental theories of swirling flows and its physical description in terms of experimental observations, numerical simulations and theoretical studies. The next section describes an overview of the generation of swirl, swirl and bluff body stabilized recirculation zones followed by a more complete description of the phenomenon of the vortex breakdown.

## 2.2 Generation of swirl

In literature, various experimental techniques have been used to generate swirl by using multiple experimental configurations. The generation of swirl in a flowing medium is simply achieved by the impartation of tangential or azimuthal velocity components to the medium. Some of these methods can be summarized as:

- Injected tangential streams via lateral ports into an axial pipe flow (Tangirala and Driscoll (1988) (1988) , Chen (1995)).
- Feeding a flow through multiple guide vanes (Sheen and Chen (1996)).
- Multi-port, fixed concentric pipes mounted in an axial through flow (Farokhi *et al.* (1988)).

Several structural or geometrical perturbations may exist for each mode of swirl generation with their accompanying disparities in efficiencies and resultant velocity profiles. Since the velocity profile exiting from the swirler determines in part, the downstream aerodynamics, it is important to examine the shape of such profiles.

The tangential velocity profile is generally discussed in terms of forced vortex flow (rigid body rotation) and free vortex flow (potential vortex). Forced vortex flow is categorised as a subset of rotational flow. Free vortex flow which describes the approximate motion in tornados and whirlpools, is classified as an example of irrotational flow. Tangential velocity profiles issuing from swirl generators generally assume a combination of the forced and free vortex distributions, Sloan *et al.* (1986). The mean tangential velocity in the flow field must go to zero at the axis of symmetry and hence solid body rotation necessarily exists in the center line region. Since the tangential velocity must go to zero either within the enveloping stagnant fluid or at the reaction chamber wall, a free vortex is characteristic of the outer jet skirt. The two vortex distributions, patched together with the resultant profile denoted as the combined, Rankine vortex. In practice the Rankine vortex distribution is less than idealised, but the term forced and free vortex still serve as rough guides for the apparent behavior of the vortex. The location of the tangential velocity maximum and its interaction with the axial velocity profile constitute critical element in the downstream aerodynamics development.

The central forced vortex region exhibits flowfield and turbulence characteristics which appear to be significantly different from those displayed by the surrounding irrotational vortex flowfield. Because of its unusual and interesting behavior, this central region is often defined as an inner, viscous or vortex core. Specially the vortex core is described as being shear or strain free, but not vorticity free. The core is generally limited to that region of flow which is substantially rigid body rotation.

### 2.3 Flame stabilization by bluff body or swirl

This section provides details about two common ways for flame stabilization: by bluff bodies or by swirl. A method of using a blunt object (bluff body) is one of the typical ways of flame stabilization. A recirculating eddy system is formed that can act as a continuous source of ignition for an inverted flame, a flame that originates behind the bluff body and spreads obliquely across the flow. The recirculating eddy system receives heat from the flame, carries it back upstream, and ignites the flow of explosive mixture with which it comes in contact.

Flow around a bluff body immersed in an airstream is characterized by the formation, behind the bluff body, of a region of recirculating flow (see Figure 2.1). Usually the maximum width of the recirculation zone exceeds that of the body by an amount that depends primarily on the shape of the bluff body. The determination of the mass flow rates within the recirculation zone is particularly important to determine the effectiveness of the zone for flame stabilization. The determination of the mass flow rate in the recirculation zone can measure the relative strength of the vortex motion. A vortex or an eddy is generally driven by the main stream, such that there is no net mass flow across the boundaries. The boundary of the eddy is thus determined by radial points at which the forward mass flow equals the reverse flow at that axial station and coincides with the zero streamlines. When the recirculation eddy is not attached to a solid surface the two boundaries coincide at the forward and rear stagnation points. The two zones can be distinguished by the terms reverse flow zone, which is bounded by the zero velocity and the recirculation eddy, which is bounded by the zero mass flow line. The center or 'eye' of the eddy lies on the reverse flow boundary and for the case of a bluff body, is the point where the static pressure is at minima. A detailed description can be found from Gupta *et al.* (1984). The bluff body

### 2.3 Flame stabilization by bluff body or swirl

---

system provides a boundary layer flow, where a combustion wave may propagate in close proximity to a region of continuously recirculating flow, which acts to provide the boundary layer with a supply of heat and chemically active species. This aerodynamic interaction permits a flame to be stabilized over wide range of flow velocities and mixture ratios.

Flame stabilization by swirl is based on the observation, when the angular to linear momentum ratio exceeds a critical value, a toroidal vortex type recirculation zone (see Figure 2.1) is set up in the central region of the jet close to the nozzle. This toroidal vortex system plays an important role in flame stabilization since it constitutes a well mixed zone of hot combustion products and acts as a storage of heat and chemically active species. Heat and mass are then transported effectively from combustion products to fresh combustible mixture by the high intensity turbulence that prevails in the vortex region. The recirculation zone in swirling jets exhibits similarities with those produced with bluff bodies, but there are also some important differences between these two systems. In contrast to bluff body wakes, the blockage in swirling jets is entirely aerodynamic. In swirling jets, there are some important factors that influence the dimensions of the recirculation zone: degree of the swirl imparted to the flow, blockage ratio of the flame holder in the stream and flame holder. In swirl flames the recirculation bubble plays an important role in flame stabilization by providing a continuous heat source of recirculated combustion products. Flame lengths and the distance from the burner at which the flame is stabilized are shortened significantly by swirl. The following sections will discuss more details of swirl and its physical description in terms of swirl induced recirculation and vortex breakdown.

### 2.3 Flame stabilization by bluff body or swirl

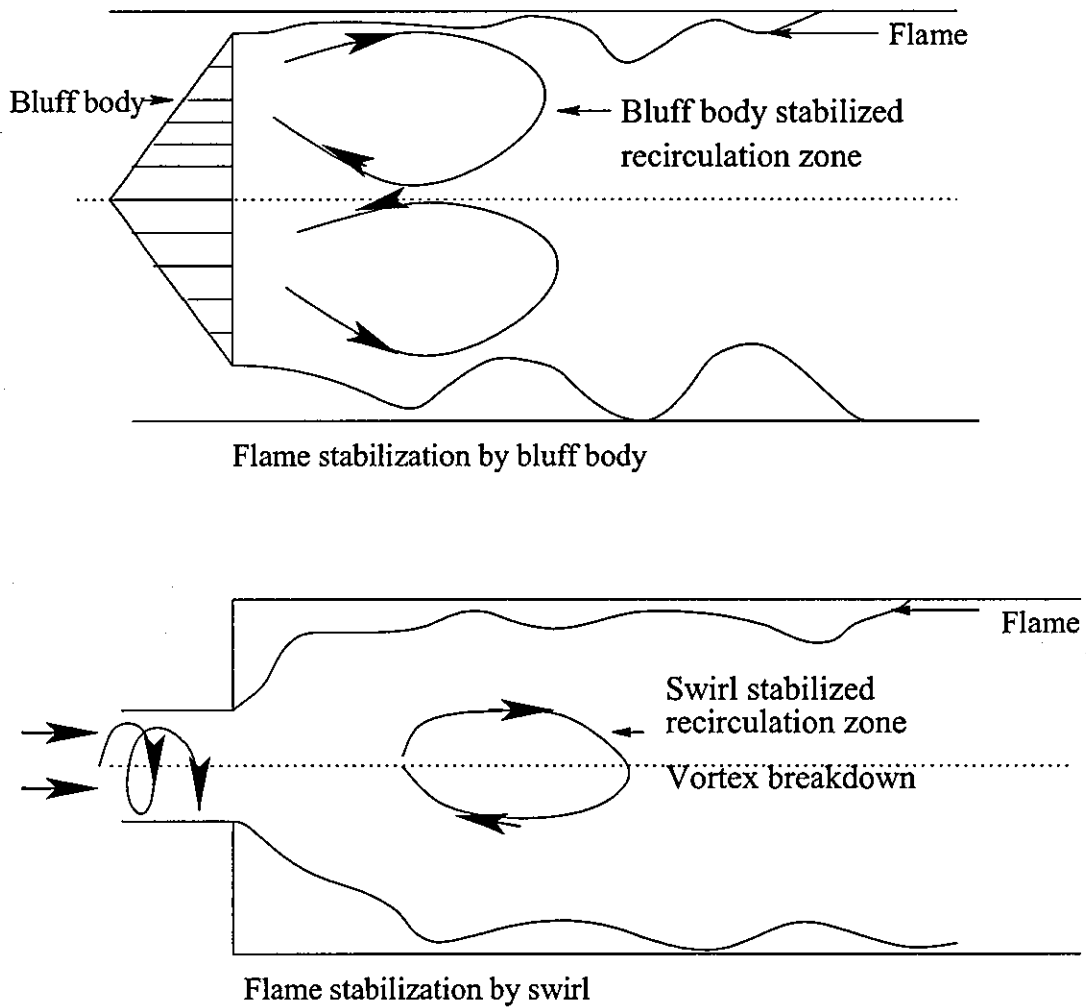


Figure 2.1: Flame stabilization by bluff body or swirl

## 2.4 Physical background

The physical mechanism of swirling flows is extremely challengeable and quite complex to fully understand theoretically, numerically and experimentally due to its complex transient behavior, Chanaud (1965). The objective of this section is to discuss details about the important physical characteristics of swirling jets. It has been observed, that even at low amount of swirl the spreading rate of jet is higher than that of the non-swirling counterpart. For example, Naughton *et al.* (1997) have observed that adding swirl to a jet can increase the entrainment up to 60%. Two main cases can be considered to analyse the spreading rate of swirling jets (see Figure 2.2). In non-swirling case the mechanism of jet spread is dominated by coherent structure and turbulent mixing at the interface of the jet and the ambient fluid, Farokhi *et al.* (1988). When swirl is added to the jet (see the jet on the right in Figure 2.2), extra components appear from the centrifugal forces which are acting in the sense of increasing the spreading rate of the jet. In this context, the centrifugal force generated by swirling motion forces the center fluid to move outward, and it results in a decrease of the axial velocity in the inner part near the axis and an increase in the outer part, Wang and Bai (2005). High spreading rate is an important property of swirling flows. Additionally, the sudden expansion at the backward-facing step wall introduces another axial velocity deceleration to the already low speed flow at the axis center of combustor. These two effects lead to the formation of internal recirculation zones.

Before the late 1980's, the major focus of most of the experiments was to measure the time mean flow field and turbulent stresses, and expose some of the interesting characteristics of swirling jets, such as the displacement of the location of the maximum axial velocity from the axis, documenting the existence of a strong

reverse flow near the center line of the jet, the change in the magnitude of the velocity components with increase of the swirl velocity, and the high spreading rate of such jets. Only recently researchers have begun to pay attention to the dominant role played by underlying vortical flow structures and their dynamical evolution, Panda and McLaughlin (1994) and Billant and Chomaz (1998).

Panda and McLaughlin (1994) have observed that the addition of swirl to the jet substantially increased the levels of turbulence, which cause to occur the instabilities of the swirling jets. In the investigation of swirling jet, Nejad (1989) concluded that the turbulent triple product and Reynolds stresses values are 25 times higher than the non-swirling flow. Naughton *et al.* (1997) found two main factors in swirling jets, which can increase the level of turbulence up to certain stage. First is the existence of the centrifugal instabilities appears when the angular momentum decreases with increasing radius. This produces higher centrifugal forces close to the axis (see Figure 2.3) and forms a secondary vortical motion leading to enhanced turbulence. The second factor is the additional shear stresses coming from the swirl velocity and that increases the level of turbulence.

The increased turbulence levels and entrainment of the surrounding fluid always increases the mixing rate. Naughton *et al.* (1997) suggested that the particle traversing a longer distance in the presence of swirl can contribute to the enhanced mixing, even if the swirl effect is small. However, it is important to note that, the additional effect of the increase of turbulence levels may weaken the coherent structure of the swirling motion and streamlines should lose their continuity close to the nozzle compared to non-swirling jets, Panda and McLaughlin (1994).

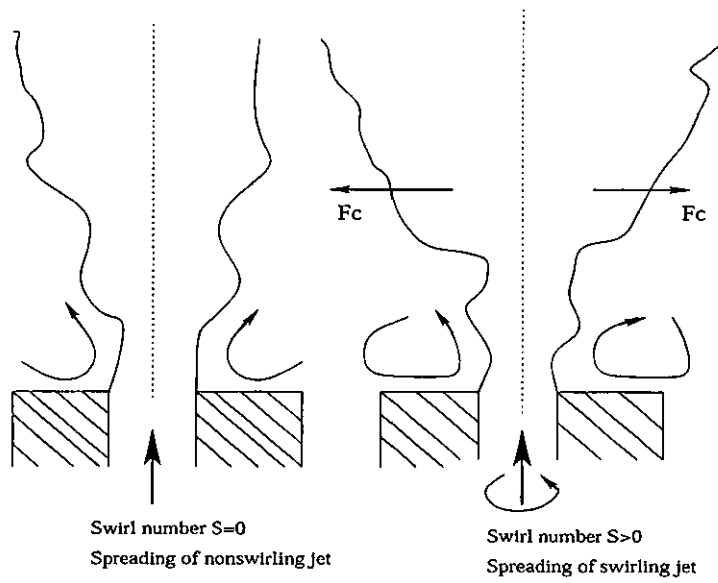


Figure 2.2: Left hand side: the spreading of non-swirling jet, right hand side: the spreading of swirling jets,  $S$  represent the swirl number and  $F_c$  represent the centrifugal force.

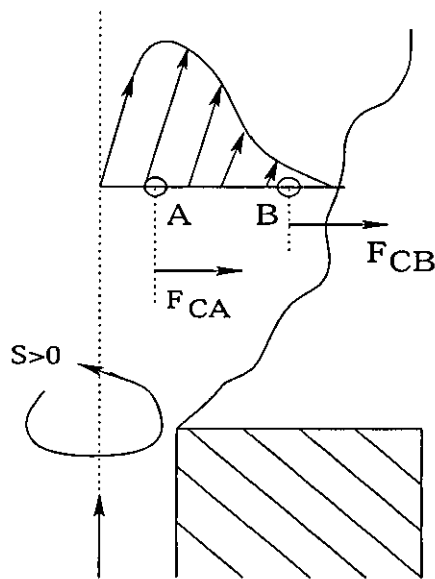


Figure 2.3: Appearance of centrifugal instabilities,  $F_{CA}$  and  $F_{CB}$  are two centrifugal forces acting on the points A and B.

## 2.5 Characteristic of swirling flows

Chigier and Beer (1964) formulated most commonly used non-dimensional expression for the characterization of swirling flows known as the swirl number. It has been found that the characteristics of a swirling jet such as pressure in a swirl generator, exit profiles, minimum pressure, maximum negative velocity and the length of the internal vortex are largely determined by the swirl number. The swirl number is expressed as  $(G_\phi/G_x r_s)$  by Chigier and Beer (1964). In this ratio,  $G_\phi$  is the axial flux of angular momentum ( $kg.m^2.s^{-2}$ ),  $G_x$  the axial flux of linear momentum ( $kg.m.s^{-2}$ ) and  $r_s$  ( $m$ ) the outer radius of the swirling annulus.  $r_s$  was used as the characteristic length scale, to obtain a non-dimensional form for the momentum ratio.

Both  $G_\phi$  and  $G_x$  were found to be conserved along the axis of the swirling jet and could be evaluated from

$$G_\phi = 2\pi\rho \int_0^\infty \langle u \rangle \langle w \rangle r^2 dr \quad (2.1)$$

$$G_x = 2\pi\rho \int_0^\infty \langle u \rangle^2 r dr + 2\pi \int_0^\infty P r dr \quad (2.2)$$

Where  $\rho$  is the density of air ( $kg.m^{-3}$ ),  $\langle u \rangle$  and  $\langle w \rangle$  are the axial and tangential velocity components ( $m.s^{-1}$ ) respectively,  $r$  ( $m$ ) is radial distance from the axis and  $P$  ( $kg.m^{-1}.s^{-2}$ ) is the static pressure at  $r$ . Being an integral quantity, it has been demonstrated by several researchers that the swirl number is not enough to characterize the flow field. Farokhi *et al.* (1989) observed, that jet with the same swirl number but different tangential velocity profile evolves differently. Farokhi *et al.* (1989) noted that small increments in the radial inlet velocity profile had a strong influence on the flow field, even if the amplitude of the radial

velocity was much smaller than the other components. It was suggested that the appearance of breakdown is more strongly related to the ratio of the momentums than the ratio of the velocity components. To reflect this Chigier and Beer (1964) introduced the modified swirl number, defined as a more representative swirl number

$$S = \frac{\int_{r_1}^{r_2} r^2 \rho \langle u \rangle \langle w \rangle dr}{r_2 \int_{r_1}^{r_2} r \rho \langle u \rangle^2 dr} \quad (2.3)$$

Moreover, the above modified swirl number has been found to be linearly proportional to the ratio of volumetric mean tangential  $\langle w \rangle$  to axial  $\langle u \rangle$  velocities at the exit plane of a swirl generator, Sheen and Chen (1996). This ratio of velocities has also been used to measure swirl intensity by Escudier (1987).

## 2.6 Vortex breakdown

Vortex breakdown (VB) is a phenomenon that occurs in swirl flows if the level of swirl surpasses a critical level. If the swirl is strong enough, centrifugal forces will reduce the pressure on the swirl-axis far enough to create significant adverse pressure gradients in the axial direction. The flow is hence decelerated and eventually reversed, creating a semi-stable recirculation zone. Vortex breakdown usually occurs downstream of the nozzle, where it can create a strongly fluctuating recirculation zone if the swirl was strong enough. Chanaud (1965), Syred and Beer (1972) and Escudier (1988) have all observed that the flow encountered with VB is asymmetric and variable in time. To date, there are no general criteria to predict the occurrence or the type of VB that must be expected in a given flow situation, although a swirl number of 0.6 is typically accepted as a critical value for the onset of breakdown in single swirling jets. However, swirl flows must be considered to be highly sensitive and other parameters can affect breakdown as well. Below the phenomenon of vortex breakdown is discussed under three

sections, experimental, numerical and theoretical explanation.

### 2.6.1 Characteristic of vortex breakdown

The vortex breakdown happens when the swirl level reaches a certain limit. Harvey (1962) carried out experiments on swirling flows within a tube and concluded that vortex breakdown is an intermediate stage between weakly swirling flows and rapidly swirling flows and hence resulting flow reversal indicates the critical phenomena. Chanaud (1965) described the occurrence and position of vortex breakdown as a function of Reynolds number and the swirl level. However Billant and Chomaz (1998) concluded that occurrence of vortex breakdown is independent of the Reynolds number and nozzle diameter and it exists when the swirl level reaches a well defined threshold. Phenomenologically, at low swirl level  $S < 0.6$  the radial pressure gradient at any axial position is not high enough to raise the axial pressure gradient and hence the axial recirculation or vortex breakdown does not occur. Under low swirl conditions, there is no coupling between axial and swirling velocity components. Within a general criteria, the acceptable condition for the occurrence of vortex breakdown in a single jet is the swirl number greater than 0.6, Gupta *et al.* (1984).

The vortex core has different sizes and conditions, which depend on various flow conditions. In devices using guide vanes, the viscous core of the vortex forms as a result of the separation of the boundary layer on the center of the swirl generator, Harvey (1962). Several authors have figured out that the simplest form of the vortex breakdown takes the form of an axisymmetric bubble of recirculating fluid, Harvey (1962), Sarpkaya (1971). It was found that the vortex breakdown is not only asymmetric, but also highly time dependent, Chanaud (1965), Escudier (1988), Syred and Beer (1972). This is the result of the forced vortex region of the

flow becoming unstable and starting to precess about the axis of symmetry thus forming the phenomenon precessing vortex core (PVC). Syred and Beer (1972) found that the PVC lies on the boundary of the reverse flow zone between the zero velocity and zero streamline. Anacleto *et al.* (1996) found that the parameters describing PVC, like the precessing frequency and core circulation, depend on the generation of vortex in isothermal conditions and the parameters are independent of combustion. These periodical motions can be important in combustion applications as this motion is eventually used to improve the mixing and control the mixing rate between fuel and oxidant stream in order to achieve flame geometries and heat release rates appropriate to the particular problem.

### 2.6.2 Types of vortex breakdown

As discussed earlier, the vortex breakdown occurs as a result of the formation of an internal stagnation point on a vortex axis, followed by a recirculation region of limited axial extent. Sarpkaya (1971) carried out a parametric investigation of the VB phenomenon by measuring the relationship between Reynolds number, the position of breakdown and the strength of the swirl in the flow and identified two distinct modes of vortex breakdown, axisymmetric or bubble breakdown and spiral breakdown. It is characterized by a rapid deceleration of the dye filament marking the swirl axis and occurs stagnation characterized by a stagnation point on the swirl axis followed by a sudden expansion of the centreline dye filament to form the recirculating bubble. Sarpkaya (1971) described another form of vortex breakdown called double helix breakdown in which at low Reynolds numbers a dye filament introduced on the vortex axis decelerated and expanded into a slightly curved triangular sheet in the experiment based on the swirling flows in a diverging cylindrical tube. Billant and Chomaz (1998) observed another breakdown form called conical vortex breakdown, which is similar to bubble type

but after the expansion the jet will have the shape of an open conical sheet and breaks down into turbulent structures. Faler and Leibovich (1977) found seven forms of vortex breakdown from their visualization using a liquid dye tracer that included five forms already discussed earlier. Furthermore Faler and Leibovich (1977) observed and confirmed that these VB occurs at different transition flow states as swirl number increased at fixed Reynolds number or Reynolds number is increased at fixed swirl number. Increasing the axial velocity or swirl velocity from above two operations have same effect on the form of VB and its stagnation position, since both operations increase peak swirl, axial vorticity, axial velocity overshoot in the upstream vortex core, Leibovich (1978). Leibovich (1978) described the existence of other forms of VB as well. However, those were different variants or combinations of the states observed by Sarpkaya (1971). Following figures show different types of vortex breakdown patterns.

- Double helix type breakdown (see Figure 2.4)
- Spiral type breakdown (see Figure 2.5)
- Bubble type breakdown ( see Figures 2.6, 2.7, 2.8 )

### 2.6.3 Experimental description of vortex breakdown

Previous sections provided a sketch of the phenomenon of vortex breakdown. Peckham and Atkinson (1957) were the first researchers who conducted initial investigation into the vortex breakdown by performing experiments on a highly swept delta wing. Since then the phenomenon of 'vortex breakdown' or 'vortex core burst' has been widely investigated and growing rapidly among the community. Much of the necessary theories, explanations and visualizations have been developed up to certain stage in simple as well as complicated manner, but still

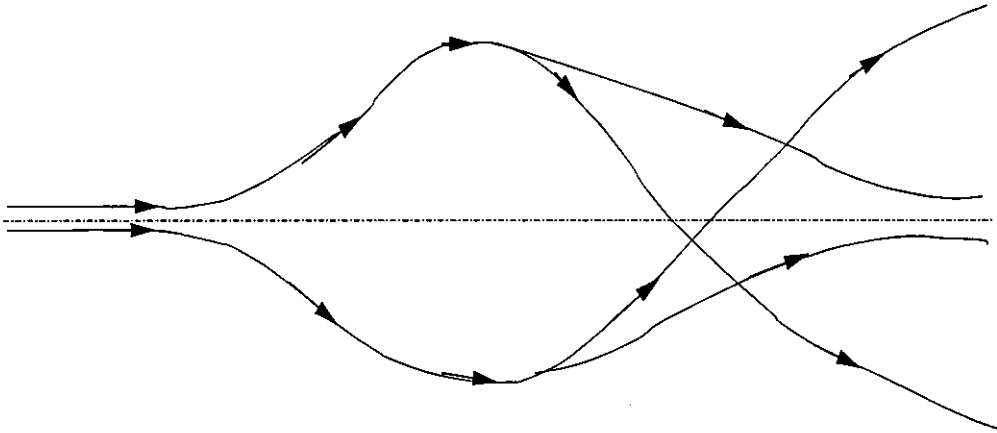


Figure 2.4: Double helix: a dye filament introduced on the vortex axis is decelerated and expands into a slightly curved triangular sheet occurs at low Reynolds numbers.

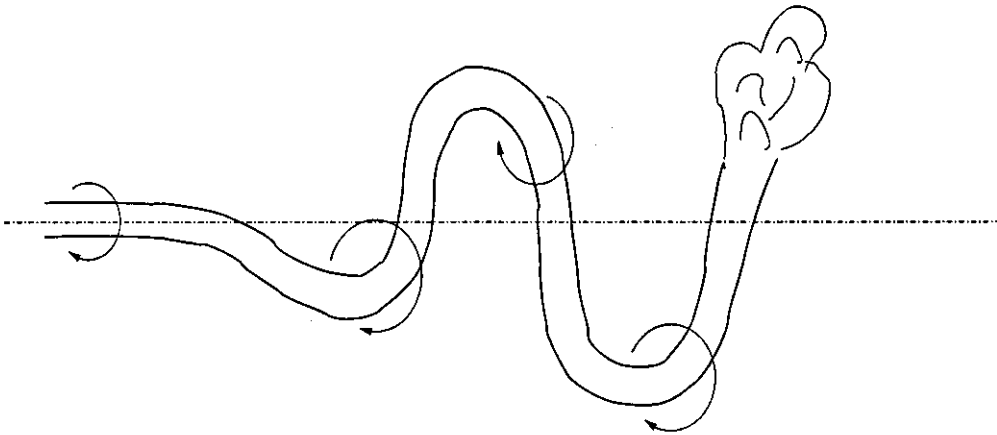


Figure 2.5: Spiral: characterised by a rapid deceleration of a dye filament marking the swirl axis, which cause stagnation and by abrupt kink followed by a corkscrew-shaped motion.

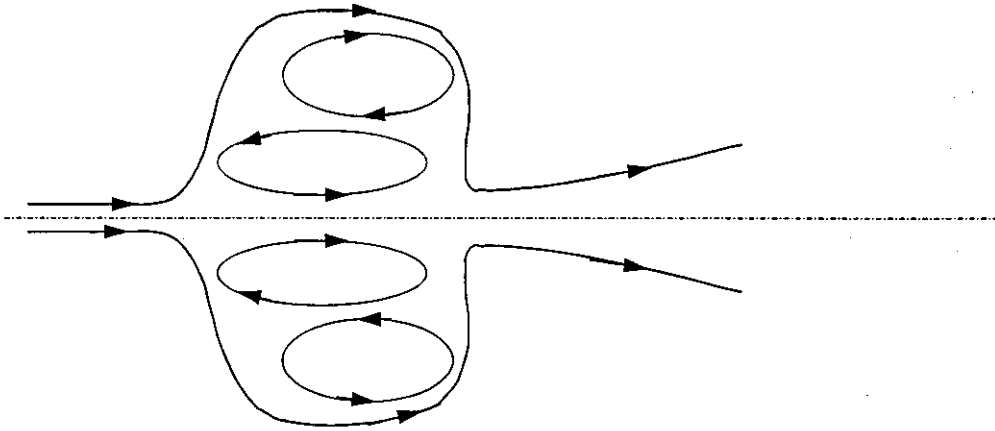


Figure 2.6: Bubble: Dual ring, the flow is decelerated along the centreline and a stagnation point is formed. But the interior is dominated by a bubble shaped recirculation zones.

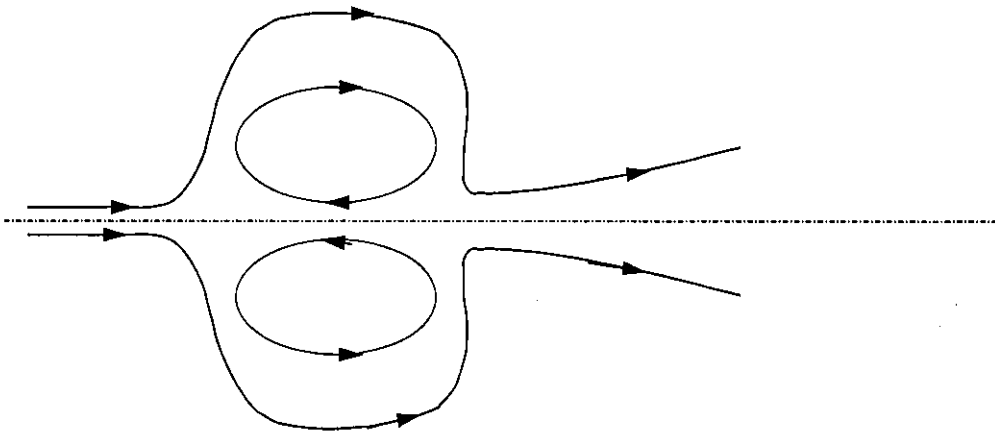


Figure 2.7: Bubble: Single ring, the flow is decelerated along the centreline and a stagnation point is formed. Interior is again dominated by bubble shaped recirculation zones.

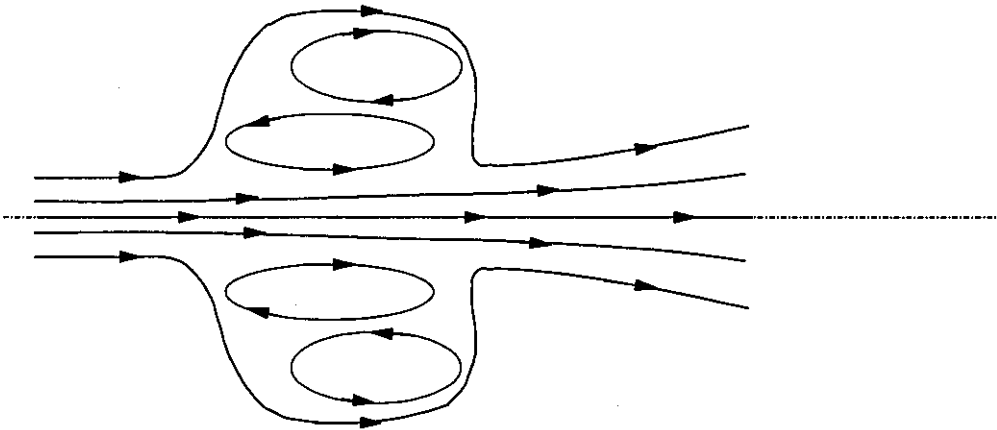


Figure 2.8: Bubble: Annular, the flow is decelerated along the centreline and a stagnation point is formed. If the axial velocity at the centreline is high the bubble can result in the annular structure.

many unresolved problems such as predictions of vortex breakdown and their flow physics have to be addressed in greater detail. There are some common difficulties encountered in experimental observations in terms of vortex breakdown such as the sensitivity of the external perturbations in the flow field, random motion of the vortex breakdown around the mean position, see Lucca-Negro and O'Doherty (2001).

The first investigations of vortex breakdown tried to identify the basic patterns of breakdown and to find a criteria which determine the appearance of VB. Harvey (1962) simplified the problem by doing experiments on swirling flows inside a tube, and found a sudden transition to breakdown. They considered vortex breakdown as the intermediate state between weakly swirling flows without flow reversal and rapidly swirling flows with strong, columnar flow reversal. More quantitative results were provided by Chanaud (1965), who studied the breakdown position in swirling jets as a function of the Reynolds number and of swirl levels. Sarpkaya (1971) altered Harvey's experiment by using a slightly diverging

conical tube. The group also provided charts on the vortex breakdown position depending on the Reynolds number and the level of swirl. These charts show that with increasing Reynolds number, the vortex core size decreases, as the vortex breakdown moves further upstream; and the length of the internal recirculation zone increases with growing strength of swirl. A very interesting finding of Sarpkaya and coworkers was the possibility of more than one vortex breakdown in the divergent pipe-flow if the swirl was strong enough. Finally, this paper by Sarpkaya has introduced the distinction of the three major vortex breakdown modes of double helix, spiral and axisymmetric bubble breakdown. Leibovich (1978) extended this classification to further types of vortex breakdown, although many of these modes resulted from variations and combinations of Sarpkaya's classical modes.

Buckley *et al.* (1983) did further investigations on the parameters that cause vortex breakdown by applying different methods to generate the tangential velocity profiles. Buckley *et al.* (1983) found that different inlet velocity profiles at identical axial flux and swirl numbers greatly affected the flow field. Buckley's work was extended by Farokhi *et al.* (1988), who confirmed that the behavior of swirling flows depends strongly on the distribution of the axial and circumferential velocity, that strongly vary with different swirl generation methods. Naughton *et al.* (1997) examined compressibility effects on the swirl induced growth of a jet, and found no significant influence, supporting the validity of the low-mach assumption even in such sensible flows. Billant and Chomaz (1998) added a fourth type (axisymmetric conical) of vortex breakdown to the three modes identified by Sarpkaya (1971), 27 years after their original work. Finally, Shtern and Hussain (1999) divided the flow field into four well distinguished regions, jet formation, where the axial velocity is still increasing, developed jet, where the axial velocity decreases along the centreline, recirculation zone which is located behind the stagnation

point and features negative axial flow velocities, which then tend towards the free stream velocity with in the vortex wake, which is fluid-mechanically similar to the wake of a solid bluff-body. Lucca-Negro and O'Doherty (2001) confirmed the that spiral breakdown tends to occur at lower swirl than the axisymmetric bubble or conical breakdown, and showed that the mean vortex breakdown positions were reproducible, even though the breakdown point moves in a highly transient way.

### 2.6.4 Numerical computation of vortex breakdown

Numerical computation of swirling flows is important in order to gain deep understanding of the flow physics of their three dimensional structure, which assists in confirming the available experimental evidence in great detail. Numerical simulation is attractive in that it provides additional details concerning the structure of swirling flow field such as formation of vortex breakdown and recirculation. The modelling of swirling flow field is a challenging task due to the strong coupling between the momentum equations, especially when the influence of the swirling velocity components is large. The inlet boundary conditions is an important issue, which requires accurate definition to obtain a satisfactory solution for the numerical simulation, Escudier (1988).

In earlier stages, the numerical simulations based on full Navier-Stokes equations have been restricted to axisymmetric, steady, laminar and incompressible investigations. Kopecky and Torrance (1973) and Grabowski and Berger (1976) have conducted initial numerical simulations for vortex breakdown under the set of steady axisymmetric solutions. Shi (1985) carried out an unsteady axisymmetric simulation and predicted axisymmetric breakdown with periodic flow behavior. Hafez *et al.* (1987) simulated laminar axisymmetric swirling flow field and pre-

dicted multiple breakdowns as experimentally observed by Harvey (1962) and Sarpkaya (1971).

The first unsteady three dimensional simulations have been carried out by Spall and Gatski (1987). More recently, several authors have applied conventional Reynolds average Navier-Stokes (RANS) to simulate turbulent swirling flows, e.g. Xia *et al.* (1998). Weber *et al.* (1990) tested three turbulence models in their computations,  $k - \epsilon$ , Reynolds stress model (RSM) and an algebraic Reynolds stress model (ARSM). However, as suggested by Nejad (1989),  $k - \epsilon$  based models require further modifications to predict swirling flows accurately. The  $k - \epsilon$  model cannot capture the recirculation, anisotropy and strong streamline curvature and it certainly needs further modifications to obtain improved predictions. Repp *et al.* (2002) performed flow field simulation in swirling flow and showed that important flow features can be predicted using Reynolds stress model, but the central recirculation zone is overestimated.

It is essential to use more sophisticated computational techniques, which can handle the anisotropy and transient motion of turbulent swirling flows. Large eddy simulation (LES) is one of the promising techniques, which can handle the highly dynamic anisotropic behavior of turbulent swirling flows. This method has been successfully used by several researchers to predict swirling flow field from simple non-reacting swirling jets to complex swirl stabilized combustion systems. For example, Wang and Bai (2005) have showed successful LES predictions for the non-reacting swirling flow fields in a confined geometry under different flow conditions. LES has been applied to variety of swirling applications including combustion such as aircraft engine combustion, DiMare *et al.* (2004), Kim *et al.* (1999), dynamics of premixed swirling and spray flames, Sankaran and Menon (2002), and combustion instabilities, Wall and Moin (2005). Pierce and Moin

(2004) showed encouraging LES results for the gas turbine combustor and Mahesh *et al.* (2005) also carried out a LES calculation for a section of modern Pratt and Whitney gas turbine combustor. However, one of the major difficulties encountered in LES is setting appropriate boundary conditions. The numerical generation of swirl at inlet is quite challenging due to the complexity of the physical swirl generation. Several methods can be used to generate the inlet boundary conditions such as experimental profiles, algebraic equations introduced by Buckley *et al.* (1983) and body force technique used by Pierce and Moin (2004). The outlet boundary conditions also create difficulties in numerical simulations. In numerical simulations, the zero gradient outflow condition and the convective outflow condition have been used for swirl flow simulations. However, if there is no recirculation region that extends far downstream to the outlet, the influence of the outlet condition can be limited to a region close to the outlet.

### 2.6.5 Theoretical studies of vortex breakdown

Theoretical studies of vortex breakdown have been carried out in parallel with the experimental and numerical studies. In simple theoretical investigations, vortex breakdown have been discussed under three main categories such as concept of critical state with wave phenomena, flow stagnation and hydrodynamic instability.

The theoretical descriptions on vortex breakdown under the wave propagation characteristics were independently derived by Squire (1962), and Benjamin (1962). Lambourne and Bryer (1961) also carried out theoretical studies on an inviscid model vortex. Randall and Leibovich (1973) have presented a model called a trapped wave model of vortex breakdown at the critical state. Bilanin and Widnall (1973) also carried out theoretical investigation using the trapped wave theory

on vortex breakdown and derived similar conclusions as Randall and Leibovich (1973). Krisbus and Leibovich (1994) have extended the wave solution for fully nonlinear and weakly nonlinear cases.

Numerous authors have carried out further theoretical investigations on vortex stability, this include Rayleigh (1916) , Ludweig (1964), Jones (1964). The first hydrodynamic instability theory on vortex breakdown was derived by Jones (1964). Ludweig (1964) derived another criteria assuming that the formation of stagnation point appearing in the vortex core is more sensitive to spiral disturbances than axisymmetric disturbances. Leibovich and Ma (1983) derived more general criterion for instability than the criteria derived by Ludweig (1964). Lessen *et al.* (1974) analysed a linear inviscid stability from different form of disturbances and calculated the swirl strength needed to stabilize the jets and wake against asymmetric disturbances on a vortex. However most investigations conclude that the vortex flows are more stable to axisymmetric situation than asymmetric disturbances.

## 2.7 The Sydney swirl burner

### 2.7.1 Burner configuration

Shown in Figure 2.9 is a sketch of the Sydney swirl burner configuration that forms the basis of this LES investigation. The burner design is relatively simple and has well defined uniform boundary conditions. It has a central fuel jet of diameter 3.8 *mm* surrounded by a ceramic face bluff body of 50 *mm* diameter. Surrounding the bluff-body is a 60 *mm* diameter primary annulus machined down to 0.2 *mm* thickness at the exit plane. The center of the fuel jet is taken as the geometric centreline of the flow, where  $r = 0$  and  $x = 0$ . ( $r$  is the radial distance

## 2.7 The Sydney swirl burner

---

and  $x$  is the axial distance). Swirl is introduced aerodynamically into the primary air stream by using three tangential (air) swirl ports (7 mm diameter) that are inclined at 15 degrees upwards off the horizontal plane and located circumferentially at 120 degrees to each other (see Figure 2.9). These swirl ports are at a distance of 300 mm upstream of the burner exit. Two diametrically opposed ports, located on the periphery of the burner but ahead of the tangential inlets, supply the axial air to the swirl stream. Before entering the swirl annulus to exit at the burner face the swirl flow stream passes through a tapered neck section that is 185 mm long and ends 140 mm from the burner exit plane. Primary purpose of this section is to promote uniformity of boundary conditions at the exit plane by combining axial and tangential streams to form a uniform swirl flow stream. The burner is housed in a secondary axial (co-flow) wind tunnel with a square exit cross section and 130 mm sides. Compositional measurements, performed at Sandia National Laboratories, used an alternative wind tunnel which also had a square (exit) section but 305 mm sides, Masri *et al.* (2004).

In this burner the geometric swirl number  $S_g$  is used for the quantitative representation of the swirl strength and is defined as the ratio of (bulk) tangential to axial primary air velocities  $W_s/U_s$ , measured through laser Doppler velocimetry (LDV), above the annulus. The actual swirl number  $S$  is linearly proportional to  $S_g$  which can vary by changing the magnitude of the tangential and axial air flow rates, Al-Abdeli and Masri (2003b). The Reynolds number of the swirling annulus is defined in terms of bulk axial velocity and outer radius of the annulus.

The Sydney swirl burner configuration allows for the manipulation of four parameters. These are the bulk jet velocity of central fuel jet velocity,  $U_j$  ( $m.s^{-1}$ ), the bulk axial and tangential velocities of the primary annulus (air) stream,

$U_s$  ( $m.s^{-1}$ ) and  $W_s$  ( $m.s^{-1}$ ) respectively, and the mean co-flow velocity of the secondary (air) stream in the wind tunnel,  $U_e$  ( $m.s^{-1}$ ). For all the swirl flames investigated,  $U_e$  were maintained at  $U_e = 20m/s$ . All central jet velocities,  $U_j$ , quoted are bulk values based on the diameter of the central jet (3.6 mm). The Reynolds number through the central jet,  $Re_j = (U_j \times d_j/\nu)$ , is based on the diameter of the central jet and the bulk jet velocity  $U_j$ . Depending on the case the Reynolds number for the central jet is calculated with viscosities for the relevant gases at approximately 293 k (air or fuel mixture).

### 2.7.2 Non-reacting swirling flows

In this experimental series a number of non-reacting isothermal swirl flow cases have been investigated. They cover a wide range of swirl numbers with sufficiently high Reynolds numbers and therefore suitable as model problems for the validation of computations. At sufficiently high swirl numbers these flows exhibit interesting features. Recirculation and flow field regimes of isothermal swirling flows in this series have been discussed in detail by Al-Abdeli and Masri (2003a). They found several important issues for a wide range of swirl numbers and annular velocities. For example, the formation of the typical upstream recirculation zone introduced by the sudden expansion at the bluff body wall, which is almost same as the Sydney bluff body burner investigated by Dally *et al.* (1998), and the occurrence of the downstream recirculation region known as the vortex breakdown are interesting flow features in these isothermal swirl cases. Al-Abdeli and Masri (2004) also carried out investigations into the precession and recirculation in these turbulent isothermal flows. Their study describe how precession frequency depends on the swirl number as well as the Reynolds number of both central jet and the swirling annulus. The main conclusion of their studies was that the addition of swirl leads to more complex flow patterns, which may in-

clude the central recirculation zone (in more downstream axial locations), flow instabilities and precession. In the present study, before attempting to model reacting swirl flames of this series, application of the current LES capabilities to capture important flow structures of non-reacting swirling flows have been considered to understand the capabilities and limitations of LES in the absence of turbulence/chemistry interactions. Table 2.1 shows the operating parameters of the non-reacting swirling jets that have been chosen for investigation.

### 2.7.3 Reacting swirling flames

The present LES work uses the Sydney swirl flame series described in Al-Abdeli and Masri (2003b) and Masri *et al.* (2004) as our reacting flow test cases. Detailed measurements have been conducted to establish the flow field, temperature, species distribution and stability characteristics of three different types of swirling flames known as SM, SMH and SMA flames. Compressed natural gas (CNG) was used as the fuel for the SM flames. The SMA flames used fuel mixtures of CNG/Air (1:2 by volume) and the SMH flame used CNG/H<sub>2</sub> (1:1 by volume). CNG used in these experiments contained more than 90% methane by volume, the remaining components being carbon dioxide, propane and ethane. Depending on the fuel and operating parameters used, the above flames showed different physical and compositional features. In the experiments flow field measurements have been conducted using LDV while single-point Raman-LIF and Reyleigh techniques has been used to conduct the compositional and temperature measurements. Key flow features and stability characteristics of these flames has been described in detail by Al-Abdeli and Masri (2003b) and Masri *et al.* (2004).

In physical appearance all flames were blue in colour and free from soot and

## 2.7 The Sydney swirl burner

Flow case	$U_s(m/s)$	$W_s(m/s)$	$U_j(m/s)$	$U_e(m/s)$	$S_g$	$Re_s$
N16S159	16.3	25.9	66	20	1.59	32400
N16S058	16.3	11.1	66	20	0.68	34200
N16S034	16.3	5.5	66	20	0.34	32400
N29S054	29.7	16	66	20	0.54	59000
N21S000	21.1	0	61	20	0	41900

Table 2.1: Flow conditions investigated and controlled parameters for non-reacting swirling flows.

Flames	$U_s(m/s)$	$W_s(m/s)$	$U_j(m/s)$	$U_e(m/s)$	$S_g$	$Re_s$
SM1	38.2	19.1	32.7	20	0.5	75900
SM2	38.2	19.1	88.4	20	0.5	75900
SMH1	42.8	13.8	140.8	20	0.32	85000
SMH2	29.7	16	140.8	20	0.54	12000
SMH3	29.7	16	226	20	0.54	12000
SMA1	32.9	19.1	66.3	20	0.5	75900
SMA2	16.3	25.9	66.3	20	1.59	32400
SMA3	16.3	25.9	132.6	20	1.59	32400

Table 2.2: Flow conditions investigated and controlled parameters for reacting swirling flames.

hence suited for Raman and Rayleigh diagnostics. CH<sub>4</sub>/H<sub>2</sub> flames were longer than those of pure CH<sub>4</sub> and CH<sub>4</sub>/air flames. All CH<sub>4</sub>/H<sub>2</sub> flames showed a necking region just downstream of the bluff body as a result of the bluff body stabilized recirculation zone before spreading out except for some of the SMA flames, which operated at higher swirl numbers. Certain flames showed considerable amount of local extinction, re-ignitions and operated close to blow-off limits. Some flames also showed acoustic instabilities causing rumbling noise and high temperature fluctuations. These flames are free from instabilities and suitable for model validation. Table 2.2 shows the operating parameters of the Sydney swirling flames.

2.7 The Sydney swirl burner

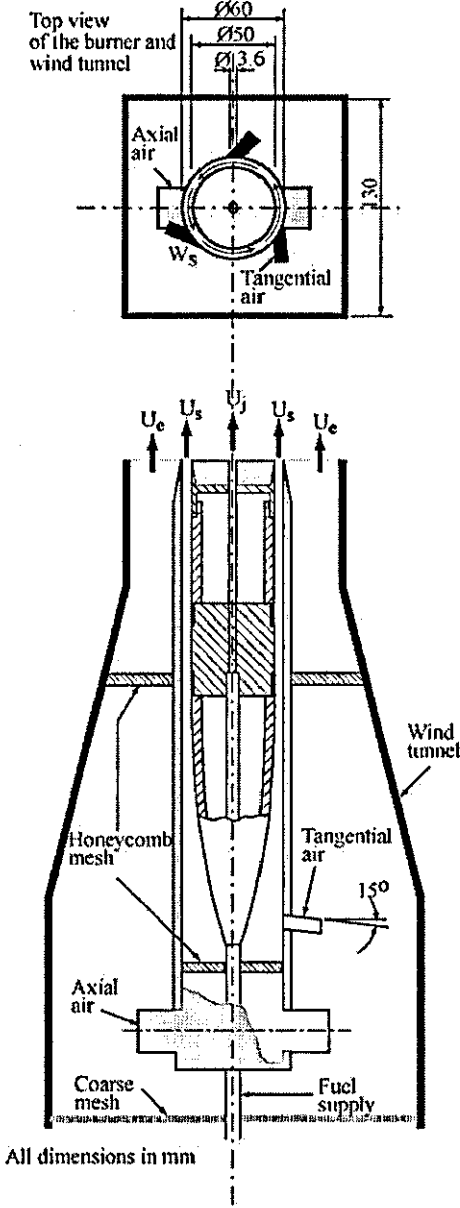


Figure 2.9: Schematic of Sydney swirl burner

## Chapter 3

# Mathematical Description of Turbulent Reactive Flows

### 3.1 Introduction

This chapter provides the governing equations of a reacting mixture of fluids and an overview of the physics of turbulence. The first part presents the physics of fluid flows governed by the transport equations and corresponding conservation laws. The second part describes the concept of turbulence and current modelling strategies based on turbulence modelling.

### 3.2 Governing conservation equations

In chemically reacting flows, the flow field and mixing are described by a set of coupled partial differential equations known as conservation of mass, momentum, energy, transport of chemical species and an equation of state. The number of equations depends on the nature of the problem. The derivations of the equations can be found in text books related to fluid dynamics , e.g Tennekes and Lumley

## 3.2 Governing conservation equations

---

(1972). In this section the governing equations for the reacting flow are presented in incompressible form. The assumption of incompressibility is valid for all liquids and for gas flows where the fluid velocity is low with respect to the speed of sound. However, when fluid velocity reaches to speed of sound, the conservation equations have to be in compressible form. In reacting flows the density is a variable and depends on species distribution and local temperature.

### 3.2.1 Conservation of Mass

The governing flow equation which results from the application of physical principle that mass is conserved, is called the continuity equation. Several different starting points are in used to derive these equations for example by considering continuum flow through an infinitesimal control volume.

The conservation equation for mass in Cartesian coordinate system is written as

$$\frac{\partial \rho}{\partial t} + \frac{\partial(\rho u_j)}{\partial x_j} = 0 \quad (3.1)$$

The continuity equation transports the mass by the velocity components  $u_j$  in  $x_j$  direction ( $j \in \{1, 2, 3\}$ ) and describes the change of density  $\rho$  in time  $t$ . This equation is valid for both incompressible and compressible fluids.

### 3.2.2 Conservation of momentum

The momentum equation is derived from another fundamental physical principle known as Newton's second law in that, the rate of change of momentum of a fluid particle is proportional to the resultant force acting on the fluid particle in the same direction. Hence momentum is conserved. The transport of momentum is

### 3.2 Governing conservation equations

---

written as

$$\frac{\partial \rho u_i}{\partial t} + \frac{\partial(\rho u_i u_j)}{\partial x_j} = -\frac{\partial P}{\partial x_i} + \frac{\partial \sigma_{ij}}{\partial x_j} + f_i \quad (3.2)$$

Where  $x_i$  is any of the three coordinate direction and  $t$  is the time. The hydrodynamic variables  $u_i$  is the velocity components,  $P$  is the pressure and  $\rho$  is the density which in reacting flow varies due to heat released by chemical reaction and chemical composition of the fluid.  $f_i$  represents any other forces such as gravitational and coriolis forces which may be acting on the field.

We consider the incompressible flow of Newtonian fluid and it is assumed that stress  $\sigma_{ij}$  is proportional to the rate of strain. Hence

$$\sigma_{ij} \propto \text{rate of strain}$$

$$\Rightarrow \sigma_{ij} = \rho\nu(\text{rate of strain})$$

$$\sigma_{ij} = \rho\nu\left(\frac{\partial u_i}{\partial x_j} + \frac{\partial u_j}{\partial x_i} - \frac{2}{3}\delta_{ij}\frac{\partial u_k}{\partial x_k}\right) \quad (3.3)$$

Where  $\delta_{ij}$  is the kronecker delta and  $\nu$  is the kinematic viscosity.

Inserting equation (3.3) into (3.2) for  $\sigma_{ij}$ , the conservation equation for momentum convert into the well known Navier-Stokes equations and written as

$$\frac{\partial \rho u_i}{\partial t} + \frac{\partial(\rho u_i u_j)}{\partial x_j} = -\frac{\partial P}{\partial x_i} + \frac{\partial}{\partial x_j}\left[\rho\nu\left(\frac{\partial u_i}{\partial x_j} + \frac{\partial u_j}{\partial x_i} - \frac{2}{3}\delta_{ij}\frac{\partial u_k}{\partial x_k}\right)\right] + f_i \quad (3.4)$$

The strain rate  $S_{ij}$  can be defined as

$$S_{ij} = \frac{1}{2}\left(\frac{\partial u_i}{\partial x_j} + \frac{\partial u_j}{\partial x_i}\right)$$

## 3.2 Governing conservation equations

---

Hence the equation (3.4) can also be written as

$$\frac{\partial \rho u_i}{\partial t} + \frac{\partial(\rho u_i u_j)}{\partial x_j} = -\frac{\partial P}{\partial x_i} + \frac{\partial}{\partial x_j} \left( 2\rho\nu[S_{ij} - \frac{1}{3}\delta_{ij}S_{kk}] \right) + f_i \quad (3.5)$$

and it is known as Navier-Stokes equation for the momentum. The hydrodynamic variables in the above equations are general functions of space and time. It is well known that no analytical solution exists for the Navier-Stokes equation system under general conditions and is still a well open problem in mathematical analysis. For incompressible flow of a Newtonian fluid, the Navier-Stokes equations (3.4), with the continuity equation (3.1) fully describe the fluid flow.

### 3.2.3 General transport equation

The most convenient form of general transport equation for a scalar variable  $\phi$  can be written as follows

$$\frac{\partial \phi}{\partial t} + \frac{\partial(u_j \phi)}{\partial x_j} = \frac{\partial}{\partial x_j} \left( \Gamma \frac{\partial \phi}{\partial x_j} \right) + S_\phi \quad (3.6)$$

The four terms in the above equation represent the transient term, the convection term, the diffusion term and the source term.

To simulate combustion, transport equations for the mixing of fuel, oxidizer and combustion products must be included. The transport equations must be solved for each individual species to determine the chemical composition of the fluid mixture. The transport equation for species  $\alpha$  can be written as:

$$\frac{\partial \rho Y_\alpha}{\partial t} + \frac{\partial(\rho u_j Y_\alpha)}{\partial x_j} = -\frac{\partial J_{\alpha,i}}{\partial x_j} + \dot{\omega}_\alpha \quad (3.7)$$

Where  $Y_\alpha$  is the mass fraction of species  $\alpha$ . The diffusion flux of  $Y_\alpha$  in the  $x_i$  direction  $J_{\alpha,i}$  will contain contributions arising from concentration gradients,

### 3.2 Governing conservation equations

---

pressure gradients, external forces. In turbulent reacting flows the Reynolds number is usually high and hence the turbulent transport is much higher than the molecular transport, Jones (1994). Hence, it can retain the diffusion component of  $J_{\alpha,i}$  and represented by Fick's Law:

$$J_{\alpha,i} = -\Gamma \frac{\partial Y_\alpha}{\partial x_i} \quad (3.8)$$

Where  $\Gamma$  is the kinematic diffusion coefficient for species  $\alpha$ . Inserting (3.8) to (3.7), the transport equation for the species  $\alpha$  can be written as

$$\frac{\partial \rho Y_\alpha}{\partial t} + \frac{\partial (\rho u_j Y_\alpha)}{\partial x_j} = \frac{\partial}{\partial x_j} \left( \Gamma \frac{\partial Y_\alpha}{\partial x_j} \right) + \dot{\omega}_\alpha \quad (3.9)$$

The source term  $\dot{\omega}_\alpha$  is the rate of production and destruction of  $Y_\alpha$  by chemical reactions. In the simulation of turbulent reacting flows the existence of the source term  $\dot{\omega}_\alpha$  produces much complexity for the problem, which leads to finding another direction to avoid this situation through the concept of conserved scalar formulation.

The element mass fractions  $Z_\beta$  can form a set of conserved variables and hence we can define the element mass fractions by using mass fractions of each species  $Y_\alpha$  such that

$$Z_\beta = \sum_{\alpha} \psi_{\beta\alpha} Y_\alpha \quad (3.10)$$

Where  $\sum_{\alpha}$  is the summation over species,  $\psi_{\beta\alpha}$  is the number of grams of element  $\beta$  in a species  $\alpha$ . The element mass fraction  $Z_\beta$  is conserved and therefore the source term corresponding to their transport equation is zero,

$$\Rightarrow \sum_{\alpha} \psi_{\beta\alpha} \dot{\omega}_\alpha = 0 \quad (3.11)$$

### 3.2 Governing conservation equations

---

Hence the transport equation for element mass fraction  $Z_\beta$  can be written as

$$\frac{\partial \rho Z_\beta}{\partial t} + \frac{\partial(\rho u_j Z_\beta)}{\partial x_j} = \frac{\partial}{\partial x_j} \left( \sum_\alpha \psi_{\beta\alpha} \Gamma \frac{\partial Y_\alpha}{\partial x_j} \right) \quad (3.12)$$

For the single diffusion coefficient the equation can be rewritten as

$$\frac{\partial \rho Z_\beta}{\partial t} + \frac{\partial(\rho u_j Z_\beta)}{\partial x_j} = \frac{\partial}{\partial x_j} \left( \Gamma \frac{\partial Z_\beta}{\partial x_j} \right) \quad (3.13)$$

In which  $Z_\beta$  is transported by convection and diffusion alone. To define the conserved scalar mixture fraction the transport equations for conserved element mass fractions  $Z_A$  and  $Z_B$  of elements  $A$  and  $B$  can be written as

$$\frac{\partial \rho Z_A}{\partial t} + \frac{\partial(\rho u_j Z_A)}{\partial x_j} = \frac{\partial}{\partial x_j} \left( \Gamma \frac{\partial Z_A}{\partial x_j} \right) \quad (3.14)$$

$$\frac{\partial \rho Z_B}{\partial t} + \frac{\partial(\rho u_j Z_B)}{\partial x_j} = \frac{\partial}{\partial x_j} \left( \Gamma \frac{\partial Z_B}{\partial x_j} \right) \quad (3.15)$$

We also assume that all mass exchange coefficients, which appear in the diffusion term are identical and the summation of the all element mass fractions equal to one. Therefore  $Z_B$  can replace from  $Z_A$  such that  $Z_B = (1 - Z_A)$ . Now the mixture fraction for the reaction can be introduced as the mass fraction of one of the species. Hence the transport equation for the mixture fraction  $f$  can be written as

$$\frac{\partial \rho f}{\partial t} + \frac{\partial(\rho u_j f)}{\partial x_j} = \frac{\partial}{\partial x_j} \left( \Gamma \frac{\partial f}{\partial x_j} \right) \quad (3.16)$$

However in a chemically reacting system the reactions depend on the temperature, which can be determined through the transport equation of enthalpy  $h$ . If we avoid the radiation effect, the transport equation for enthalpy  $h$ , which conserves

### 3.3 Turbulence and turbulence modelling

---

$\rho h$  in an incompressible flow can be written as,

$$\frac{\partial \rho h}{\partial t} + \frac{\partial(\rho u_j h)}{\partial x_j} = \frac{\partial}{\partial x_j} \left( \Gamma \frac{\partial h}{\partial x_j} \right) \quad (3.17)$$

#### 3.2.4 The equation of state

The equation of state used for the gases is the ideal gas equation involving pressure, temperature and density such that

$$PV = nRT \quad (3.18)$$

$$P = \frac{\rho R_u T}{M} \quad (3.19)$$

$R_u$  is the universal gas constant,  $M$  is the molecular weight of the gas and  $T$  is the temperature.

### 3.3 Turbulence and turbulence modelling

Turbulence is a phenomena that occurs frequently in nature, and has been a challenging topic of study for several centuries. Turbulence is characterized by multitude of scales in time and space and associated mixing and diffusion of momentum, heat etc. that are orders of magnitude stronger than in laminar flows. Most flows occurring in technical applications as well as other situations, such as geophysical flows and even in astrophysics are turbulent. In physical three dimensional turbulence the dynamics of the eddies is also characterized by an energy cascade from large to small eddies and finally, through the action of viscosity into heat. This energy cascade phenomena is clearly coupled with the action of vortex stretching and thereby not present in strictly two dimensional turbulence.

### 3.3 Turbulence and turbulence modelling

---

Turbulence motion have been analyzed in great detail, however, because of its complexity, turbulence is still not completely understood and remain a challenge to make accurate quantitative predictions without relying on empirical data.

#### 3.3.1 Turbulence properties

In eighteen century Osborne Reynolds carried out scientific research towards turbulence. In his experiment, he has observed the occurrence of turbulence in a pipe flow when a non-dimensional parameter exceeds a critical value. This parameter is known as Reynolds number and define as,

$$Re = \frac{UL}{\nu} \quad (3.20)$$

Where  $U$  is the velocity scale and,  $L$  is the characteristic length scale and  $\nu$  is the kinematic viscosity of the fluid. If the Reynolds number of the flow is large enough, the major characteristics of flow are controlled by the molecular properties of the fluid in which the turbulence occurs. In turbulent flow, the non-linearity of the equations of motion leads to certain unique characteristics in each individual flow pattern, that are associated with its initial and boundary conditions. These important characteristics can be describe as follows:

- The random nature of turbulence: Turbulence is a random phenomena. The flow field has unavoidable perturbations in both space and time and statistical theory has been used to identify these motions.
- Turbulence is always three dimensional in spatial character.
- Wide range of length scales: Visualisations of turbulent flows reveal turbulent eddies containing a wide range of length scales.

### 3.3 Turbulence and turbulence modelling

---

- Three dimensional vorticity fluctuations: Turbulence is rotational and is characterized by high levels of fluctuating vorticity.
- High Reynolds numbers: Turbulence occurs when the convective forces dominate the diffusive forces, expressed by critical Reynolds number.
- Diffusivity: The diffusivity causes rapid mixing and increased rates of mass, momentum and heat transfer.
- Dissipation: Turbulent flows are always dissipative.
- Turbulence is a property of the flow. It is not a property of the fluid.

The turbulent flow field is usually dominated by eddies. The largest turbulent eddies are determined by the geometry of the flow. During vortex stretching, the large eddies are effectively inviscid and their angular momentum is conserved. This can increase the rotation rate and decrease the radius of their cross sections. Thus the process creates motions at smaller transverse length scales as well as smaller time scales. The stretching work done by the mean flow on the large eddies supplies the energy which maintains the turbulence. However, these large eddies will break up due to vortex stretching into smaller and smaller eddies. As the size of the eddies decrease the influence of viscous forces becomes more and more important.

#### 3.3.2 Resolution of turbulent scales

Turbulent fluctuations are associated with different scales ranging from the largest, the integral length scale  $l_t$ , to the smallest ones, known as the Kolmogorov length scale  $\eta_k$ . The integral scale is usually close to the characteristic size of the flow. For example, in a ducted flow, the integral scale is of the order of the duct size.

### 3.3 Turbulence and turbulence modelling

---

A Reynolds number  $Re(r)$  is introduced for each turbulent scale as

$$Re(r) = \frac{u'(r)r}{\nu} \quad (3.21)$$

where  $u'$  is the characteristic velocity of the motion of size  $r$  and  $\nu$  is the flow kinematic viscosity. When  $r$  corresponds to the integral scale  $l_t$ , the corresponding Reynolds number is the integral Reynolds number

$$Re_t = Re(l_t) = \frac{u' l_t}{\nu} \quad (3.22)$$

Since the Reynolds number represents the ratio of inertia to viscous forces, the largest scales in a turbulent flow are mainly controlled by inertia and not affected by viscous dissipation.

For homogeneous isotropic turbulence the energy of the large scales flows to the smaller scales through the Kolmogorov cascade, Tennekes and Lumley (1972). The energy flux from one scale to another (due to non-linear terms  $u_i u_j$ ) is constant along scales and given by the dissipation  $\epsilon$  of the kinetic energy  $k$ . This dissipation  $\epsilon$  is estimated as the ratio of the kinetic energy,  $u'^2(r)$  divided by the time scale  $r/u'(r)$

$$\epsilon = \frac{u'^2(r)}{r/u'(r)} = \frac{u'(r)^3}{r} \quad (3.23)$$

Along the cascade, the Reynolds number  $Re(r)$  goes down from  $Re_t$  to values close to unity, where inertia and viscous forces balance. This limit determines the smallest scale found in the turbulent flow, the Kolmogorov scale  $\eta_k$ , controlled by viscosity and by the dissipation rate  $\epsilon$  of the turbulent kinetic energy  $k$ , Tennekes and Lumley (1972),

$$\eta_k = \left(\frac{\nu^3}{\epsilon}\right)^{1/4} \quad (3.24)$$

### 3.3 Turbulence and turbulence modelling

---

corresponding to a unity Reynolds number

$$Re_k = Re(\eta_k) = \frac{u' \eta_k}{\nu} = \frac{\epsilon^{1/3} \eta_k^{1/3}}{\nu} = 1 \quad (3.25)$$

The ratio of the integral length scale  $l_t$ , to the Kolmogorov length scale  $\eta_k$ , comparing the largest and smallest turbulence eddies, is expressed as

$$\frac{l_t}{\eta_k} = \frac{u'^3/\epsilon}{(\nu^3/\epsilon)^{1/4}} = Re_t^{3/4} \quad (3.26)$$

In numerical calculations turbulent scales are correctly resolved when the largest and smallest eddies are captured by the grid. This leads to a standard condition derived as follows. Consider a computational domain with a typical size  $L$ . The grid comprises  $N$  points in each dimension leading to a typical cell size  $\Delta x = L/N$ . The turbulent flow may be characterized by the large scale velocity fluctuations  $u'$  and integral length scale  $l_t$ . The size of the domain should be at least of order of one integral scale ( $L = N\Delta x \geq l_t$ ). The smallest scale of turbulent eddies  $\eta_k$  is estimated from the Kolmogorov cascade argument such that  $\eta_k \approx l_t/(Re_t)^{3/4}$ . This scale is resolved by the computation if it is larger than the grid size such that  $\eta_k > \Delta x$ . Combining all these expressions leads to

$$\frac{l_t}{\eta_k} < N \quad (3.27)$$

corresponding to  $N > Re_t^{3/4}$  or equivalently  $Re_t < N^{4/3}$ . These inequalities determine the number of grid points  $N$  required in each direction for a given Reynolds number  $Re_t$  or the limiting values of the Reynolds number for a selected number of grid points in each direction.

### 3.3.3 Modelling methods

With the complexity associated with complex flow systems, numerical modelling is often used to assist designers of complex systems such as industrial gas turbines and aero engines. In the past, design engineers have relied heavily upon low order empirical and, to a lesser extent, physical models for performance, emission, and stability predictions. Due to the lack of sufficient computational power, modelers were forced to make sometimes sweeping assumptions and simplifications about the highly coupled (non-linear) and complex combustion processes. The turbulent nature of the flow inside most practical applications makes modelling even more difficult.

Computational fluid dynamics (CFD) tools have been developed in which the governing flow field equations of motions are solved on a discretized computational mesh. In the past and even at present, multi dimensional modelling of complex systems employing CFD has been largely limited to steady state analysis. However most practical processes occurring in engineering applications are naturally dynamic or unsteady (e.g. pressure oscillations) and this makes steady state previous CFD predictions less representative. In turbulent flows, kinetic energy is transferred from larger to smaller scales until it finally reaches a scale at which molecular viscosity dominates (and where kinetic energy is converted to thermal energy). This so-called energy cascade from large to small scales is a fundamental nature of turbulence (the smallest scale is known as the Kolmogorov micro scale ( $\eta$ )). The dynamics of turbulent flow at the different length scales are quite different. Large scale fluctuations are caused by large eddies often referred to coherent structures. These eddies, which contain most of the kinetic energy are controlled by the geometry of the system and are generally anisotropic while small scales, which receive their energy from the large scales and isotropic and

### 3.3 Turbulence and turbulence modelling

Approach	Advantages	Drawbacks
RANS	-coarse numerical grid -geometrical simplification -reduced numerical costs	-only mean flow field -models required
LES	-unsteady features -reduced modelling impact	-models required -3D simulations required -computational cost is high
DNS	-no models needed for turbulence -tool to study models	-high computational cost -limited to academic problems

Table 3.1: Comparisons between RANS, LES and DNS approaches for numerical simulation of turbulent flows.

more universal. It is therefore important that the dynamics of the large scale turbulent motion is resolved to capture the unsteady dynamics.

Although DNS of practical devices is not possible and restricted to very low  $Re$  ( $Re < 3000$ ) number flows, a relatively newer modelling technique known as Large Eddy Simulation (LES) is becoming feasible. In LES turbulent fluctuations smaller than the local grid volume (known as subgrid scales (SGS)) are modelled while all larger scales are fully resolved in space and time. Since the large eddy dynamics are fully resolved, a realistic representation of part of the turbulent field is possible. It should be noted that the accuracy of LES is dependent not only on the resolution of the large eddies but also on the fidelity of the SGS models used to characterize the effect of the unresolved scales on the resolved scale motion. Unlike steady state modelling methods, LES is capable of capturing unsteady phenomena such as vortex breakdown in complex swirling flow field and combustion instabilities in combustion systems and has therefore earned much attention as a next generation design tool. Table 3.1 shows major advantages and drawbacks between main three modelling approaches.

#### 3.3.4 Direct numerical simulation

Analytical solutions for flows encountered in turbulent complex flows simply do not exist. Increasingly, researchers are turning to numerical techniques to obtain discrete solutions of the governing equations both to answer the questions of engineering importance and also to gain insight into the fundamental physics of turbulence. The latter is achieved by using numerical methods of high accuracy on fine grids which resolve the wide range of scales present in the turbulent flows. This approach is referred to as Direct numerical simulation (DNS). Direct numerical simulation uses no averaging, but resolves all the length and time scales of the turbulent flow field and somewhat beyond the Kolmogorov scales. In this way, there is no modelling needed at all. In DNS, the required number of grid points for three dimensional simulation is based on:

$$N_{nodes} \sim \left(\frac{l}{\eta}\right)^3 \sim Re^{\frac{3}{4}} \quad (3.28)$$

The required number of time steps being proportional to  $Re^{\frac{3}{4}}$ , which implies that the total computational effort needed for DNS is proportional to  $Re^3$ . Therefore DNS is only possible for the application of low Reynolds number cases such as  $Re < 10^4$ . Despite the high computational cost, DNS requires the use of higher order accurate numerical schemes to reduce the dissipative effect of the numerical schemes.

#### 3.3.5 Large eddy simulation

In past three decades researches have seen the emergence of different approach to the simulation of turbulent flows based on the idea of separation of scales. In turbulent flow, the large scale flow structures which depend strongly on the nature of the flow are responsible for most of the transport of mass and momentum.

### 3.3 Turbulence and turbulence modelling

---

Since the small eddies containing less turbulent kinetic energy, have more universal behavior and more isotropic (based on Kolmogorov hypothesis), it is more amenable to modelling than the large eddies. This theoretical consideration leads to find an approach whereby scales which cannot be represented on the numerical grid are removed from the description of the turbulence in the simulation, leaving only the large, energy containing eddies which are calculated directly. However, the effect of unresolved scales (small scales) on large scales have to be considered and are modelled in a simple way. The method is referred to as large eddy simulation (LES). LES technique needs more computational resources than conventional RANS approach and much less expensive than DNS and therefore LES represents an approach where computational effort can be scaled to match accuracy requirements.

#### 3.3.6 Reynolds averaged Navier-Stokes equations

Averaging the flow equations either in time or in statistically homogeneous directions of the flow or over an ensemble of equivalent flows has become the standard means by which turbulent engineering flows are treated. The procedure results in the Reynolds-average Navier Stokes (RANS) equations so named in honor of Osborne Reynolds who first derived them in 1895. When averaging of this type is applied to the Navier-Stokes equations additional terms arise due to the non-linearity of the convective terms. These additional terms are second order moments involving the fluctuations of the velocity components about their mean values have the properties of the stress and also called Reynolds stresses. In order to obtain the numerical solution to these equations the closure problem caused by the Reynolds stress must be overcome. In turbulence modelling an eddy viscosity type model is used to represent the Reynolds stresses where the eddy viscosity is calculated from representative local length and velocity scales

### **3.3 Turbulence and turbulence modelling**

---

which can be obtained from modelled transport equations. These models contain a large number of parameters and require calibration. The aim of developing a universal Reynolds average turbulence model, which gives reliable predictions in complex flows where stream line curvature intermittency or counter gradient diffusion may be present is therefore very difficult task to achieve.

# Chapter 4

## Large eddy simulation

### 4.1 Introduction

Large eddy simulation (LES) has emerged as a next generation modelling technique to simulate the turbulent flows based on the idea of separation of scales. During the last three decades, this technique has matured considerably while developing underline theories, new models and more efficient numerical schemes, Piomelli (1999). The first LES calculation on turbulent channel flow has been carried out by Deardorff (1970). Since then LES has been applied to variety of flow problems from simple turbulent channel flow to complex aircraft gas turbine combustor with available computational power and memory.

The turbulent flow is usually dominated by large scale structures (large eddies), which depend strongly on the boundaries and nature of the flow and responsible for most of the transport of mass, momentum, and in flows involving mixtures of gases, species concentrations. At the same time, the small scales (small eddies) formed by the interaction of the large scales whose main function is to dissipate fluctuations of transported quantities, affect the mean characteristics of the flow only slightly. These small scales are more universal in nature and therefore more

amenable to modelling than the large scales. This strong observation leads to find an approach, whereby scales which cannot be represented on the numerical grid are removed from the description of the turbulent in the simulation, leaving only the large, energy containing eddies whose evaluation is calculated directly. This approach is referred to as large eddy simulation (LES). The direct numerical simulation (DNS) is the most straightforward approach to the solution of turbulence. As discussed earlier (section 3.3.4), the time dependent DNS solution of the governing equations completely free of modelling assumptions and, which can only involve the numerical discretization errors. DNS has been very useful tool for the study of turbulent flow physics of simplified test cases, but impossible to apply for complex practical engineering application even in next decade. On the other end, Reynolds average Navier-Stokes (RANS), which model all the scales is extensively used in engineering applications to predict the flow in fairly complex configurations ,Weber (1986). Large eddy simulation (LES) is a technique intermediate between the DNS and RANS. In LES the contribution of large, energy carrying structures to momentum and energy transfer is computed exactly, and only the effect of the small scales of turbulence is modelled. Since the small scales have more universal, homogeneous behavior and less affected by the boundary conditions than the large scales, the finding appropriate models is relatively simple on the small scale modelling. LES is similar to DNS in that it provides instantaneous three dimensional solution and still this technique requires fairly fine meshes.

Pioneering works on LES have been done by Smagorinsky (1963), Lilly (1967), Deardorff (1970), Schumann (1975) and several others. Since then, several advances have been made through the LES calculations in modelling the unresolved processes (small scales), accurate numerical methods on structured and unstructured grids, comprehensive validation of LES predictions with DNS and experi-

mental data, extension of LES technique to different phenomena such as turbulent combustion and acoustics etc. have been undertaken. More comprehensive review of LES and its applications can be found in Sagaut (2002), Pope (2000), Piomelli (1999).

As mentioned earlier, LES explicitly computes the large energy carrying structure and models the effect of the small scales on large scales. In this chapter, the filtered governing equations formally obtained by applying a spatial filter to the governing equations will be presented. The method of applying a spatial filter was first adopted by Lilly (1967) and then generalized by Leonard (1974). However, introducing filter leads to additional unknowns to the governing equations, which have the properties of stresses and provide a means by which turbulent kinetic energy can be drained from the large scales. Therefore the subgrid models enter into the system by the way of modelling additional unknowns in the filtered governing equations by using the hypothesis: the action of the subgrid scales on the resolved scales (large scales) is essentially an energetic action, so that the balance of the energy transfers alone between the two scale ranges is sufficient to describe the action of the subgrid scales. In energy conserving codes, the only way for the turbulence kinetic energy to leave the resolved modes is by the dissipation provided by the subgrid scale model. Thus the most important feature of a subgrid scale model is to provide adequate dissipation from resolved scales to unresolved subgrid scale. There are several modelling approaches in the literature for the subgrid scale stresses and, the most common one being the Smagorinsky model, Smagorinsky (1963), which will be discussed in section 4.4. In the following sections, the filtering procedure, filtered governing equations and methods for their closure will be presented.

## 4.2 Spatial filtering

Spatial filtering of Leonard (1974) is the most common approach to conceptually and in some models operationally, decompose the velocity field into large (resolved) and small (subgrid) scales. In LES the small, unresolvable scales of motion are removed by applying the spatial filter to the governing equations. The application of the spatial filter  $G$  to the function  $\mathbf{f} = f(x, y, z, t)$  is defined as

$$\bar{f}(x, y, z, t) = \int_{-\infty}^{\infty} \int_{-\infty}^{\infty} \int_{-\infty}^{\infty} G(x - x', y - y', z - z') f(x, y, z, t) dx dy dz \quad (4.1)$$

The filter function determines the size and structure of the small scales. The sharp Fourier cutoff filter, the Gaussian filter and the tophat (box filter) are the most commonly used filters for spatial scale separation. A typical tophat filter (rectangular filter) of the widths three  $\Delta_i$  can be defined as:

$$G(x_i - x'_i) = \begin{cases} \prod_{j=1}^3 \frac{1}{\Delta_j} & \text{if } |x'_i| \leq \frac{\Delta_i}{2} \\ 0 & \text{otherwise} \end{cases} \quad (4.2)$$

The difference between the filtered field (resolved field)  $\bar{\mathbf{f}}$  and the original field  $\mathbf{f}$  is described as small unresolved scale  $\mathbf{f}'$ :

$$\mathbf{f} - \bar{\mathbf{f}} = \mathbf{f}' \Leftrightarrow \mathbf{f} = \bar{\mathbf{f}} + \mathbf{f}' \quad (4.3)$$

The most commonly used approach is to use the implicit filtering where  $\Delta$  is the characteristic width of the filter. In present work the tophat filter is employed as it naturally fits into a finite volume discretization, because the process of rewriting the continuous equations in discrete form using a finite volume formulation is

### 4.3 Filtered governing equations

---

equivalent to applying a box filter of width to the equations.

$$\Delta = (\Delta x \Delta y \Delta z)^{\frac{1}{3}} \quad (4.4)$$

Where  $\Delta x, \Delta y, \Delta z$  refer to width of finite volume in the three coordinate directions. In turbulent reacting flows large density variations can occur which must be properly accounted for. In LES, fluctuations in the resolved scale density field are calculated explicitly. Also subgrid scale fluctuations for the density must be treated in some manner. Jones (1994) argues in the context of time or ensemble averaging of the governing transport equations that the most straightforward approach to account density fluctuations is through the use of density weighted or Favre averages, Favre (1969). Where  $\tilde{f}$  can be defined as

$$\tilde{f} = \frac{\overline{\rho f}}{\bar{\rho}} \quad (4.5)$$

## 4.3 Filtered governing equations

The spatial filtering operator is applied to the governing equations, thereby producing filtered governing equations. The filtering operator removes the small scales (below than the filter width) that cannot be resolved by the numerical method and appear through a subgrid scale (SGS) model.

### 4.3.1 Transport equation of mass

The Favre filtered equation for conservation of mass in incompressible form is written as

$$\frac{\partial \bar{\rho}}{\partial t} + \frac{\partial (\bar{\rho} \tilde{u}_j)}{\partial x_j} = 0 \quad (4.6)$$

### 4.3.2 Transport equation of momentum

Applying the Favre filter to the Navier-Stokes equations gives

$$\frac{\partial \overline{\rho \tilde{u}_i}}{\partial t} + \frac{\partial (\overline{\rho \tilde{u}_i \tilde{u}_j})}{\partial x_j} = -\frac{\partial \overline{P}}{\partial x_i} + \frac{\partial}{\partial x_j} \left[ \overline{\rho} \left( \nu \frac{\partial \tilde{u}_j}{\partial x_i} + \nu \frac{\partial \tilde{u}_i}{\partial x_j} \right) - \frac{2}{3} \overline{\rho} \nu \frac{\partial \tilde{u}_k}{\partial x_k} \delta_{ij} \right] + \overline{\rho} g_i \quad (4.7)$$

The diffusion term can be rewritten through an approximation

$$\nu \frac{\partial \tilde{u}_j}{\partial x_i} = \tilde{\nu} \frac{\partial \tilde{u}_j}{\partial x_i} \quad (4.8)$$

The filtered momentum equation includes unknown terms. Because of the non-linearity of the convective terms in filtered Navier-Stokes equations, the Favre filtering introduces an unknown term  $\overline{\tilde{u}_i \tilde{u}_j}$  leaving the equations unclosed. This non-linear correlation  $\overline{\tilde{u}_i \tilde{u}_j}$  can be decomposed into resolved part  $\tilde{u}_i \tilde{u}_j$  and a residual stress  $\tau_{ij}^{SGS}$ .

$$\overline{\tilde{u}_i \tilde{u}_j} = \tilde{u}_i \tilde{u}_j + \tau_{ij}^{SGS} \quad (4.9)$$

The residual stress  $\tau_{ij}^{SGS}$  also known as sub-grid stress represents the shear stress of the small scale (unresolved) turbulent motion.

Hence the filtered momentum equation can be re-written as

$$\frac{\partial \overline{\rho \tilde{u}_i}}{\partial t} + \frac{\partial (\overline{\rho \tilde{u}_i \tilde{u}_j})}{\partial x_j} = -\frac{\partial \overline{P}}{\partial x_i} + \frac{\partial}{\partial x_j} \left[ \overline{\rho} \tilde{\nu} \left( \frac{\partial \tilde{u}_j}{\partial x_i} + \frac{\partial \tilde{u}_i}{\partial x_j} \right) - \frac{2}{3} \overline{\rho} \tilde{\nu} \frac{\partial \tilde{u}_k}{\partial x_k} \delta_{ij} - \overline{\rho} \tau_{ij}^{SGS} \right] + \overline{\rho} g_i \quad (4.10)$$

The additional sub-grid stress  $\tau_{ij}$  term has to be modelled in order to represent the sub-grid contribution on resolved velocity field.

### 4.3.3 Transport equation of mixture fraction

The filtered transport equation for mixture fraction is formulated by applying the Favre filter

$$\frac{\partial \bar{\rho} \tilde{f}}{\partial t} + \frac{\partial (\bar{\rho} \tilde{f} u_j)}{\partial x_j} = \frac{\partial}{\partial x_j} \left( \tilde{\Gamma} \frac{\partial \tilde{f}}{\partial x_j} \right) \quad (4.11)$$

Here, the convection term  $\bar{\rho} \tilde{f} u_j$  includes the non-linear relation and has to be decompose into resolved part  $\tilde{f} \tilde{u}_j$  and the subgrid part  $F_j^{SGS}$ , which contribute the small unresolved flux of turbulent motion:

$$\tilde{f} u_j = \tilde{f} \tilde{u}_j + F_j^{SGS} \quad (4.12)$$

Inserting (4.12) into (4.11) the favre filtered transport equation for the mixture fraction is obtained:

$$\frac{\partial \bar{\rho} \tilde{f}}{\partial t} + \frac{\partial (\bar{\rho} \tilde{f} \tilde{u}_j)}{\partial x_j} = \frac{\partial}{\partial x_j} \left( \tilde{\Gamma} \frac{\partial \tilde{f}}{\partial x_j} + \bar{\rho} F_j^{SGS} \right) \quad (4.13)$$

These filtered governing equations subjected to the implicit grid filter for mass (4.6), momentum (4.10) and mixture fraction (4.13), form a set of coupled partial differential equations which can be numerically solved. The instantaneous subgrid fluctuations  $\tau_{ij}^{SGS}$  and  $F_j^{SGS}$  are modelled through the known resolved field and added to close the equations.

## 4.4 Modelling the subgrid stresses

The filtered momentum equations govern the evolution of the resolved scale motion. Therefore the subgrid scale contribution on the momentum equation  $\tau_{ij}^{SGS}$  is not solved on the filtered governing equations. Hence that must be modelled as a function of known resolved values.

#### 4.4.1 Residual stress decomposition

It is possible to expand the subgrid stress by substituting into (4.9) a decomposition of the velocity field of the form

$$u_i = \tilde{u}_i + u'_i \quad (4.14)$$

Where  $u'_i$  is the subgrid scale velocity. The subgrid stresses can be decomposed into three parts, Leonard (1974):

$$\tau_{ij}^{SGS} = \widetilde{u_i u_j} - \tilde{u}_i \tilde{u}_j = L_{ij} + C_{ij} + R_{ij} \quad (4.15)$$

Where

$$L_{ij} = \widetilde{\tilde{u}_i \tilde{u}_j} - \tilde{u}_i \tilde{u}_j \quad (4.16)$$

$$C_{ij} = \widetilde{\tilde{u}_i u'_j} + \widetilde{\tilde{u}_j u'_i} \quad (4.17)$$

and

$$R_{ij} = \widetilde{u'_i u'_j} \quad (4.18)$$

$L_{ij}$  is called the Leonard stress,  $C_{ij}$  is called the cross stress and  $R_{ij}$  is the subgrid scale Reynolds stress. The Leonard stress represents interactions between resolved scales that result in subgrid scale contributions. The cross terms represent interactions between resolved and unresolved scales, whereas the subgrid scale Reynolds stress represent interaction between small unresolved scales.

The representation of turbulent stresses through the use of simplified linear models based on the eddy viscosity approach is well known among the turbulence modelers. The classical model of this group introduced by Smagorinsky (1963) is, from an historical point of view, the progenitor of all subgrid scale stress

models. The introduction of dynamic modelling concept Germano *et al.* (1991) has spurred significant progress in the subgrid scale modelling in non-equilibrium flows(see section 4.5.4). In dynamic model the coefficient(s) of the model are determined as the calculation progresses, based on the energy content of the smallest resolved scales rather than input a priori as standard Smagorinsky model. A detailed discussion of this method is given in the following section.

While eddy viscosity models may be able to represent the global dissipative, effects of the small scales in a satisfactory way, they cannot reproduce the stresses (and the energy exchange) accurately on the local levels, and in particularly the correlation that exists between large scale, energy producing events and energy transfer to and from the small scales, Piomelli and Chasnov (1996). Scale similarity and mixed models try to reproduce this correlation more accurately. They are based on the assumption that the most active subgrid scales are those closer to the cutoff wave number and that the scales with which they interact most are those right above the cutoff. Scale similarity and mixed models have been revisited in the concept of dynamic modelling ideas, Horiuti (1997).

Two point closure for LES involve the use of statistical theories of turbulence to derive subgrid scale models for the equations in Fourier space. Kraichnan (1976) carried out the spectral eddy viscosity model, which computed the energy transfer from resolved to the unresolved scales given a cutoff wave number using a two point closure model for isotropic turbulence. Chollet and Lesieur (1981) proposed a modification to the structure function model. These approaches use the energy spectrum calculated using test field model (TFM) Kraichnan (1976) to compute a spectral eddy viscosity whose effect is equivalent to including the energy spectrum up to the cut-off frequency. This spectral dynamic model resulted in improved results in transitional flows in the near-wall region of turbulent flows

or in regions of intermittent flows.

In parallel with the development of models based on the Smagorinsky model, a number of alternative approaches have been proposed. Schumann (1975) carried out LES of channel and annulus using a model in which the subgrid scale stresses are divided into an isotropic and anisotropic components. In this model the velocity scale is calculated by solving the transport equation for the turbulent kinetic energy  $k$ . Horiuti and Yoshizawa (1985) tested a similar one equation model for turbulent channel flow. This model has been used effectively by Menon *et al.* (1996) on the computation of interscale energy transfer in isotropic turbulence.

### 4.4.2 Eddy viscosity models

Most subgrid scale models in present use are eddy viscosity models that parameterise the SGS stress in terms of an eddy viscosity by assuming that the anisotropic part of the SGS stress tensor  $\tau_{ij}$  is proportional to the large scale rate tensor  $S_{ij}$ :

$$\tau_{ij}^{SGS} - \frac{2}{3}\delta_{ij}\tau_{kk}^{SGS} = -\nu_t\left(\frac{\partial\tilde{u}_j}{\partial x_i} + \frac{\partial\tilde{u}_i}{\partial x_j}\right) \quad (4.19)$$

Classically, the eddy viscosity  $\nu_t$  is calculated algebraically to avoid solving additional equations that could increase the cost of an already expensive calculation. Additionally, since small scales have more universal, homogeneous behavior than the large scales, one can conclude that simple algebraic models can describe the accurate physics of turbulence. Finally, since the SGS stresses only account for a fraction of total stresses, modelling errors should not affect the overall accuracy of the results as in the standard turbulence modelling approach.

In eddy viscosity approach the SGS stress term  $\tau_{ij}$  should be modelled by adding a turbulent viscosity  $\nu_t$  to the molecular viscosity  $\nu$ , resulting in an effective viscosity  $\nu_{ef} = \nu + \nu_t$ .

With the substitution of effective viscosity  $\nu_{ef}$ , the filtered Navier-Stokes equation can be rewritten to yield,

$$\frac{\partial \bar{\rho} \tilde{u}_i}{\partial t} + \frac{\partial (\bar{\rho} \tilde{u}_i \tilde{u}_j)}{\partial x_j} = -\frac{\partial \bar{P}}{\partial x_i} + \frac{\partial}{\partial x_j} [\bar{\rho} \nu_{ef} (\frac{\partial \tilde{u}_j}{\partial x_i} + \frac{\partial \tilde{u}_i}{\partial x_j}) - \frac{2}{3} \bar{\rho} \nu_{ef} \frac{\partial \tilde{u}_k}{\partial x_k} \delta_{ij}] - \frac{1}{3} \frac{\partial}{\partial x_i} \bar{\rho} \tau_{kk} + \bar{\rho} g_i \quad (4.20)$$

For incompressible flows, the isotropic part of the SGS stress tensor  $\tau_{kk}$  is absorbed into the pressure:

$$\bar{p} = \bar{P} - \frac{1}{3} \bar{\rho} \tau_{kk} \quad (4.21)$$

Substituting this relation into eq.(4.20) the filtered momentum equations become

$$\frac{\partial \bar{\rho} \tilde{u}_i}{\partial t} + \frac{\partial (\bar{\rho} \tilde{u}_i \tilde{u}_j)}{\partial x_j} = -\frac{\partial \bar{p}}{\partial x_i} + \frac{\partial}{\partial x_j} [\bar{\rho} \nu_{ef} (\frac{\partial \tilde{u}_j}{\partial x_i} + \frac{\partial \tilde{u}_i}{\partial x_j}) - \frac{2}{3} \bar{\rho} \nu_{ef} \frac{\partial \tilde{u}_k}{\partial x_k} \delta_{ij}] + \bar{\rho} g_i \quad (4.22)$$

#### 4.4.3 The Smagorinsky model

To solve the momentum equation, the effective viscosity  $\nu_{ef}$  has to be known. To calculate the effective viscosity, the model is needed to calculate the eddy viscosity  $\nu_t$ . As mentioned earlier, this work uses the well known Smagorinsky eddy viscosity model, Smagorinsky (1963).

The Smagorinsky model is based on the equilibrium hypothesis, according to which small scales of motion have shorter time scales than the large energy carrying eddies; thus it can be hypothesised that they adjust more rapidly than the large scales to perturbations, and recover equilibrium nearly instantaneously. The equilibrium assumption implies inertial range dynamics: energy is generated at the large scale level, and transmitted to smaller and smaller scales, where the viscous dissipation takes place. Very little testing of the applicability of this assumption to the small scales of turbulence is available. It is well known that in

most flows of interest, the large scales are not in equilibrium, Smith and Yakhot (1993). However, Bardina *et al.* (1985) suggested that the small scales may tend to equilibrium faster than the large ones, and thus satisfy the equilibrium assumption better than the large scales, or that, as long as the correct non-equilibrium response of the small scales is captured, the overall development of a turbulent flow may be predicted accurately. In more complex flows, it is not known whether the small scale would still be represented adequately by equilibrium based models as extra strains, backscatter, intermittency and other phenomena play a role.

The equilibrium hypothesis based Smagorinsky model can be described as follows:

The eddy viscosity is by dimensional analysis, the product of length scale  $l$ , and the velocity scale,  $q_{sgs}$ . Since the most active of the unresolved scales are those closest to the cutoff, the natural length scale in LES modelling is the filter width, which is the size of the smallest structure in the flow, and is proportional to the grid size, Piomelli and Chasnov (1996)

$$\nu_t \sim l q_{sgs} \quad (4.23)$$

Under the equilibrium assumption the viscous dissipation become

$$-\tau_{ij} \frac{1}{2} \left( \frac{\partial \tilde{u}_j}{\partial x_i} + \frac{\partial \tilde{u}_i}{\partial x_j} \right) = \epsilon \quad (4.24)$$

From this one can obtain

$$q_{sgs} \sim l \left| \frac{1}{2} \left( \frac{\partial \tilde{u}_j}{\partial x_i} + \frac{\partial \tilde{u}_i}{\partial x_j} \right) \right| \quad (4.25)$$

Letting  $l \sim \Delta$ , the eddy viscosity can be written

$$\nu_t = (C_s \Delta)^2 \left| \frac{1}{2} \left( \frac{\partial \tilde{u}_j}{\partial x_i} + \frac{\partial \tilde{u}_i}{\partial x_j} \right) \right| \quad (4.26)$$

or

$$\nu_t = (C_s \Delta)^2 |\tilde{S}| \quad (4.27)$$

Where

$$\tilde{S}_{ij} = \frac{1}{2} \left( \frac{\partial \tilde{u}_j}{\partial x_i} + \frac{\partial \tilde{u}_i}{\partial x_j} \right) \quad (4.28)$$

with  $|\tilde{S}| = \sqrt{2\tilde{S}_{ij}\tilde{S}_{ij}}$ . This classical model has a number of significant problems. Firstly the model coefficient is not a constant, but is flow dependent, with different values typically in the range  $C_s = 0.05 - 0.25$  used by various authors. Lilly (1967) suggested that the  $C_s \sim 0.17$  for homogeneous isotropic turbulence with a filter cutoff in the inertial subrange based on equilibrium argument. Piomelli and Chasnov (1996) found  $C_s = 0.065$  to be the optimal for a turbulent channel flow. Other types of flows such as transitional and shear flows require a different value of  $C_s$  again. However, Piomelli and Chasnov (1996) showed that some flows, such as transitional flows contain large regions in which energy flows in the reverse direction, namely from the subgrid scales to the resolved scales. This process (known as backscatter) cannot be represented in the classical Smagorinsky model. To overcome this problem Germano *et al.* (1991) introduced a very smart calculation procedure known as dynamic procedure, that will be discussed in the next section.

#### 4.4.4 Dynamic procedure of the Smagorinsky model

Germano *et al.* (1991) presented a procedure to dynamically calculate the Smagorinsky model coefficient using local instantaneous flow conditions. In this method,

## 4.4 Modelling the subgrid stresses

---

the model coefficients are computed dynamically as the calculation progresses (rather than imposed a priori) based on the energy content of the smallest resolved scale. The procedure involves the application of two filters. In addition to the grid filter, which defines the resolved and subgrid scales, a test filter (denoted by a caret) is used, whose width  $\widehat{\Delta}$  is larger than the grid filter width  $\Delta$ .

By analogy with the grid scale filtering, the test filter defines the new set of stresses leading to a test level subgrid stress tensor known as the subtest scale stresses:

$$T_{ij} = \widehat{\tau}_{ij} = \widehat{\widetilde{u}_i \widetilde{u}_j} - \widetilde{\widehat{u}_i \widehat{u}_j} \quad (4.29)$$

The resolved turbulent stresses or Leonard stresses,

$$L_{ij} = \widetilde{\widehat{u}_i \widehat{u}_j} - \widehat{\widetilde{u}_i \widetilde{u}_j} \quad (4.30)$$

which represent the contribution of the smallest resolved scales to the Reynolds stresses, can be computed from the resolved velocity and they are related to the SGS stresses,  $\tau_{ij}$  by the identity, Germano *et al.* (1991)

$$L_{ij} = T_{ij} - \widehat{\tau}_{ij} \quad (4.31)$$

The subgrid and subtest scale stresses are then parameterized by eddy viscosity approach

$$\tau_{ij} - \frac{\delta_{ij}}{3} \tau_{kk} = -2C\Delta^2 |\widetilde{S}| \widetilde{S}_{ij} = -2C\beta_{ij} \quad (4.32)$$

$$T_{ij} - \frac{\delta_{ij}}{3} T_{kk} = -2C\widehat{\Delta}^2 |\widehat{S}| \widehat{S}_{ij} = -2C\alpha_{ij} \quad (4.33)$$

Substituting (4.32) and (4.33) into (4.31) yields

$$L_{ij}^a = L_{ij} - \frac{\delta_{ij}}{3} L_{kk} = -2C\alpha_{ij} + 2C\widehat{\beta}_{ij} \quad (4.34)$$

This is set of five independent equations. To obtain a single coefficient from the five independent equations, Lilly (1992) proposed to minimize the sum of the squares of the residual,

$$E_{ij} = L_{ij}^a + 2C\alpha_{ij} - 2C\widehat{\beta}_{ij} \quad (4.35)$$

by contracting both sides of (4.35) with  $\alpha_{ij} - \widehat{\beta}_{ij}$  to yield:

$$C(x, t) = -\frac{1}{2} \frac{L_{ij}^a (\alpha_{ij} - \widehat{\beta}_{ij})}{(\alpha_{mn} - \widehat{\beta}_{mn})(\alpha_{mn} - \widehat{\beta}_{mn})} \quad (4.36)$$

The Smagorinsky coefficient  $C_s$  can be computed as  $C_s = \sqrt{C}$ . This procedure yields a coefficient that is function of space and time, and whose value is determined by the energy content of the smallest resolved scales, rather than a priori as in the standard Smagorinsky (1963) model. An interesting feature of this Germano *et al.* (1991) model is that, it can calculate negative values for the model coefficient, which is inconsistent with the Smagorinsky model. The negative Smagorinsky coefficient leads to negative eddy viscosity  $\nu_t$ , which then results in negative effective viscosity  $\nu_{ef}$ . This destabilizes the numerical schemes and results in counter gradient species diffusion if a gradient flux approach is used for species transport. Various methods have been developed to avoid negative peaks in the Germano *et al.* (1991) procedure such as spatial averaging along the homogeneous direction, time averaging the local value (Eulerian), time averaging along streamline (Lagrangian), filtering in space. More details can be found in Kempf (2003).

## 4.5 Modelling the mixture fraction fluxes

---

This work uses an alternative less expensive method known as localized dynamic procedure of Piomelli and Liu (1995), which involves finding an approximate solution to the integral equation by using the value of  $C$  at the previous time step to give a first approximation  $C^*$ . Equation (4.69) is recast in the form

$$L_{ij}^a = L_{ij} - \frac{\delta_{ij}}{3} L_{kk} = -2C\alpha_{ij} + 2C^*\widehat{\beta}_{ij} \quad (4.37)$$

Where  $C^*$  is an estimate of the dynamic constant  $C$ , which is assumed to be known. Writing the new formulation of the residual  $E_{ij}$ , the dynamic constant is now evaluated as

$$C = -\frac{\alpha_{ij}(L_{ij}^a - 2C^*\widehat{\beta}_{ij})}{2\alpha_{ij}\alpha_{ij}} \quad (4.38)$$

Piomelli and Liu (1995) propose to evaluate the estimate  $C^*$  by a time extrapolation:

$$C^* = C^{n-1} + \Delta t \left. \frac{\partial C}{\partial t} \right|^{(n-1)} + \dots \quad (4.39)$$

Where the  $(n-1)$  is related to the value of the variable at the  $(n-1)th$  time step, and  $\Delta t$  is the value of the time step. In practice Piomelli and Liu (1995) consider first and second order extrapolation schemes. the resulting dynamic procedure is fully local, and does not induce large extra computational effort. However, this procedure still requires clipping to yield a well behaved algorithm.

## 4.5 Modelling the mixture fraction fluxes

To close the filtered mixture fraction equation (4.13), the unknown term  $F_j^{SGS}$  has to be modelled. Once again the turbulence is incorporated into mixing like additional diffusion and  $F_j^{SGS}$  is modelled by using eddy diffusivity approach, which is similar to eddy viscosity approach. To model the term  $F_j^{SGS}$ , turbulent

## 4.5 Modelling the mixture fraction fluxes

---

diffusivity  $\Gamma_t$  is used along with the gradient of the filtered mixture fraction  $\frac{\partial f}{\partial x_j}$ :

$$F_j^{SGS} = \Gamma_t \frac{\partial f}{\partial x_j} \quad (4.40)$$

This can insert into the filtered mixture fraction equation and the right hand side can be rewritten as follows,

$$\frac{\partial}{\partial x_j} (\bar{\rho} (\tilde{\Gamma} + \Gamma_t) \frac{\partial \tilde{f}}{\partial x_j}) \quad (4.41)$$

Here the diffusion coefficients  $\tilde{\Gamma}$  and  $\Gamma_t$  can be written in terms of the laminar viscosity  $\tilde{\nu}$  and the dynamic viscosity  $\nu_t$  and are only scaled by the Schmidt number  $\sigma$ . The Schmidt number defines the ratio of momentum transport due to viscosity to mixture fraction transport due to diffusion:

$$\sigma = \frac{\nu}{\Gamma} \approx \frac{\tilde{\nu}}{\tilde{\Gamma}} \quad (4.42)$$

and

$$\sigma_t = \frac{\nu_t}{\Gamma_t} \quad (4.43)$$

Substituting into (4.13), the filtered equation for the mixture fraction becomes

$$\frac{\partial \bar{\rho} \tilde{f}}{\partial t} + \frac{\partial (\bar{\rho} \tilde{u}_j \tilde{f})}{\partial x_j} = \frac{\partial}{\partial x_j} \left( \bar{\rho} \left( \frac{\tilde{\nu}}{\sigma} + \frac{\nu_t}{\sigma_t} \right) \frac{\partial \tilde{f}}{\partial x_j} \right) \quad (4.44)$$

# Chapter 5

## Combustion modelling in LES

### 5.1 Introduction

Combustion is one of the important phenomena in energy production which depends upon interrelated processes of fluid mechanics, heat and mass transfer, thermodynamics, chemical kinetics and turbulence. The combustion is involved in wide range of applications including power production, rocket propulsion, fire prevention and safety and other combustion equipment. During the last four decades, theoretical explanations and experimental investigations have been extensively used in the field of combustion. With rapid development of computational power, modelling of combustion processes has emerged as a technical tool from 1980's. Since then various CFD modelling techniques have been used for combustion modelling. However, combustion phenomenon is a complex chemical process and therefore requires a great deal of attention and experience.

Combustion could be categorized mainly into three sections such as premixed, non-premixed and partially premixed. Further, classification can be made depending on type of fuel, whether liquid fuel, gaseous fuel or solid fuel. The present work deal with non-premixed combustion using gaseous fuel. The com-

bustion with gaseous fuel avoid of complexities involved with spray modelling such as atomization of fuel, droplet dispersion, evaporation and the interaction with turbulence. Hence in gaseous combustion, a more accurate assessment of predictions capability of combustion model is made possible.

In non-premixed combustion the fuel and air enter in separate streams and mixed at a molecular level. Turbulence itself is probably the most complex phenomenon in non-reacting fluid mechanics and adds another complexity to non-premixed combustion, thereby forming the most complex two way turbulence-chemistry interaction called turbulent non-premixed combustion. Turbulent non-premixed flames are relatively easier to design compared with premixed flames, because of the perfect reactant mixing procedure. These flames are mainly governed by turbulent mixing, because chemistry is faster than turbulent times. Their diffusivity speed strongly depends on turbulent motions and overall reaction rate is often limited by the molecular diffusion towards the flame front. The turbulent non-premixed flame stabilization processing where the incoming reactants are continuously mixed and ignited by the hot gases is an important issue in high power combustion chambers where is routinely employed. The usual flame stabilization methods employed in burners are dependent on inlet speed of the reactants. More details can be found in Poinso and Veynante (2001).

The three main numerical approaches used in turbulence combustion modelling are Reynolds average Navier-Stokes (RANS), Large eddy simulation (LES) and Direct numerical simulation (DNS). DNS of real combustion devices is not possible at present, and hence much attention has been directed to Large eddy simulation of turbulent combustion. Unlike steady state modelling methods, LES is capable of capturing unsteady combustion phenomena such as combustion instabilities and has therefore, gained much attention as a next generation design tool.

It has several advantages over classical RANS technique and resolves the large scales of the flow domain, which usually dominate most part of the turbulent kinetic energy. LES modelling of turbulent combustion offers dramatic savings over DNS, but still needs expensive simulations to study the complex systems compared to RANS. The major issue of LES modelling of turbulent combustion is the fact that reactive phenomena occur in the scales that fall well below the resolution limit of the LES filter width (smallest scale) and it has to be completely modelled similar to RANS.

The conserved scalar mixture fraction formulation of Bilger (1988), based sub-grid scale models can be described as preliminary non-premixed combustion models in LES. In this approach, all thermodynamic variables are obtainable from the knowledge of that conserved scalar mixture fraction. Several authors have applied LES applications of conserved scalar models based on equilibrium chemistry with a presumed shape beta pdf formulation called Large Eddy Probability Density Function (LEPDF) for mixture fraction, e.g. Cook and Riley (1994) and infinitely fast chemistry used by Pierce and Moin (1998).

The use of flamelet models, especially in LES is more often due to its improvement over the fast chemistry assumptions. The flamelet model for non-premixed combustion was originally developed by Peters (1983). The model is derived by using the basic assumption, that the chemical time scales are very small in the thin layer around the stoichiometric mixture on a scale less than the Kolmogorov scales. Cook and Riley (1998), DeBruyn *et al.* (1998) have implemented steady laminar flamelet model as a subfilter combustion model for LES and found reasonably accurate comparison with DNS data and experimental measurements. Recently Raman and Pitsch (2005), Kempf *et al.* (2006) have successfully predicted bluff body stabilized flames in LES with steady flamelet model. However steady

flamelet assumption cannot describe chemically reacting system with slower time scales such as combustion and pollutant formation in diesel engines, e.g. Pitsch (2006). The unsteady flamelet equations have to be used in such cases. Pitsch and Steiner (2000) applied Lagrangian flamelet model (LFM) as a subgrid combustion model for LES to simulate the piloted non-premixed flame experimentally investigated by Barlow and Frank (1998) and obtained an encouraging results. However, this model did not perform well in complex transitional flows. In this case, the Eulerian Particle Flamelet model (EPFM) have been used by Pitsch (2002), which is derived from Eulerian form of the flamelet equations and have to be implemented in LES solver as a subfilter combustion model.

The Conditional Moment Closure (CMC) independently proposed by Klimenko (1990) and Bilger (1993) defines transport equations for the conditional means of scalars conditioned on mixture fraction. Kim and Pitsch (2005) applied CMC model for LES. Bilger *et al.* (2005) and Kim and Pitsch (2005) presented several important issues based on CMC especially in LES. Bushe and Steiner (1999) were the first to implement the conditional source term estimation model (CME), which is derived from CMC. Pope (1990) applied the transported joint scalar/velocity PDF methods to LES by using filtered density function (FDF) to turbulent combustion. In this case the molecular mixing happens in subgrid scales, therefore the mixing models for LES is same as those developed for RANS. However, the computational cost is expensive for FDF methods in LES and virtually impossible without having special treatment for the chemical source terms, Pitsch (2006).

Pierce and Moin (2004) introduced the flamelet/progress variable approach for LES in non-premixed combustion. In this approach a transport equation is solved for the filtered reaction progress variable and the source term is closed using flamelet library and joint filtered probability density function of mixture fraction

and reaction progress variable. Pierce and Moin (2004) applied this technique to model a non-premixed dump combustor and obtained good improvements including the prediction of local extinction and reignition.

The applications of LES to real combustion devices has increased due to its potential ability in capturing the flow field and mixing. Some of these applications contain complex geometries and have used either structured or curvilinear grids. Several authors have attempted simulations of real combustion devices in both premixed and non-premixed with LES. Kim *et al.* (1999) applied LES to model the GE lean premixed combustion chamber using flamelet approach and DiMare *et al.* (2004) also carried out LES of model can type gas turbine combustor. The LES simulation of the section of a Pratt and Whitney gas turbine combustor has been carried out by Mahesh *et al.* (2005).

LES technique is thus transforming from an advanced academic tool into a practical engineering application in complex flows. Recent LES applications carried out by Raman and Pitsch (2005) and Kempf *et al.* (2006) for the Sydney bluff-body flame series experimentally studied by Dally *et al.* (1998) were major steps towards practically relevant laboratory test cases. Recently more emphasis has been placed on applications of LES to swirling flames. For example, at the recent TNF workshop (2006) some predictions were presented and detailed discussions were taken place for swirling flames based on the laboratory scale Sydney swirl burner.

Next section provides a theoretical background on turbulent non-premixed combustion models used in the present investigation. In conserved scalar models of non-premixed combustion using the mixture fraction approach significantly reduces the reacting flow problem into a tractable form. In this approach the instantaneous thermochemical state of the mixture can be determined by a single

## 5.2 The role of mixture fraction in reactive flow

---

conserved scalar called mixture fraction. The conserved scalar approach and its formulations have been extensively discussed by Williams (1985), Warnatz *et al.* (1996). The conserved mixture fraction approach based on the assumptions of equal diffusivity, unity lewis number and adiabatic combustion. The thermochemical scalar variables such as temperature and mass fraction of species are obtained using the relationship between the mixture fraction and the scalar variables. Following sections give detailed description of the conserved scalar models for turbulent non-premixed combustion.

## 5.2 The role of mixture fraction in reactive flow

In the present work the conserved scalar formulation used for the mixture fraction is that proposed by Bilger (1988), based on the notion that species are consumed or produced during chemical reactions, but chemical elements are conserved during reactions. Mass fraction  $Z$  of chemical elements (e.g. C, H, O) can be obtained from the mass fractions  $Y$  of species containing these elements:

$$Z_j = \sum_{i=1}^N \frac{a_{ij}W_j}{MW_i} Y_i \quad (5.1)$$

Where  $MW_i$  is the molecular weight of species  $i$ ,  $W_j$  is the atomic weight of element  $j$ ,  $a_{ij}$  is the number of atoms of element  $j$  in a molecular of species  $i$ . The summation is carried out over all  $N$  molecular species. Using these element mass fractions, Bilger's formula for the mass fraction for the case of fuel stream that contains only fuel and an oxidizer stream that contains only element O is as follows:

$$f = \frac{2Z_C/W_C + Z_H/2W_H - 2(Z_O - Z_{O,ox})/W_O}{2Z_{C,fu}/W_C + Z_{H,fu}/2W_H + 2Z_{O,ox}/W_O} \quad (5.2)$$

Here  $f_u$  and  $ox$  refer to fuel and oxidant stream.

### 5.3 Simple chemical reaction model

The simple chemical reaction model is the simplest reaction scheme, which uses a single step reaction at an infinitely fast rate. The model has made from the simplifications: single step reaction between fuel and oxident, one reactant which is locally in excess causes all the other reactants to be consumed stiochiometrically to form reaction products. These assumptions fix algebraic relationships between the mixture fraction and all other dependent variables such as mass fractions and temperature. In this model the fluctuations of dependent thermochemical variables such as temperature and mas fraction of species are taken into account by incorporating a probability density function (PDF) to calculate the mean quantities. In the PDF method (which originate from turbulence modelling) the average value of a thermochemical scalar variable is obtained by weighting the instantaneous value with a probability density function for mixture fraction  $f$ . For LES calculation, it is important to note that the instantaneous mixture fraction  $f$ , which is used to calculate the thermochemical variables is not filtered mixture fraction  $\tilde{f}$ , which results from mixture fraction transport equation. In LES, the filtered values of the thermochemical variables can be calculated through the probability density function approach.

### 5.4 Probability density function approach

The standard statistical approach has been used to calculate the filtered quantities using what is known as the probability density function (PDF) for the fluctuating scalar (mixture fraction), Jones (1994). Lets assume a single scalar  $\phi$ , which is

## 5.4 Probability density function approach

---

bounded between 0 and 1. This can be used to introduce a 'fine-grained' pdf  $\theta(\psi; \mathbf{x}, t)$  such as

$$\theta(\psi; \mathbf{x}, t) = \delta(\psi - \phi[\mathbf{x}, t]) \quad (5.3)$$

Where  $\delta(y)$  is the Dirac delta function. The values of  $\psi$  represents the random scalar field whose probability density function is sought and represents the range of values  $\phi$  may adopt. For a random variable  $\phi$  the unweighted probability density function is defined as

$$\bar{P}_\phi(\psi; \mathbf{x}, t) = \int_{\Omega} \delta(\psi - \phi[\mathbf{x}, t]) G(\mathbf{x} - \mathbf{x}') d^3 \mathbf{x}' \quad (5.4)$$

and it can relate to density weighted PDF through

$$\tilde{P}_\phi(\psi; \mathbf{x}, t) = \frac{\rho(\psi) \bar{P}_\phi(\psi; \mathbf{x}, t)}{\bar{\rho}(\mathbf{x}, t)} \quad (5.5)$$

Where  $\bar{\rho}$  is the filtered density. If  $G$  is positive definite then properties of a probability density functions are

$$\bar{P}_\phi \geq 0; \quad 0 \leq \psi \leq 1 \quad (5.6)$$

and

$$\bar{P}_\phi = 0; \quad \psi < 0, \psi > 1 \quad (5.7)$$

In LES combustion calculations, the Favre filtered values for any scalar  $\phi$  can be calculated by using the density weighted probability density function  $\tilde{P}_\phi$  for the mixture fraction at every location,

$$\tilde{\phi}(x, t) = \int_0^1 \phi(f)(\psi) \tilde{P}_f(\psi; \mathbf{x}, t) d\psi \quad (5.8)$$

For example

$$\tilde{Y}_\alpha(x, t) = \int_0^1 Y_\alpha(f)(\psi) \tilde{P}_f(\psi; \mathbf{x}, t) d\psi \quad (5.9)$$

Where  $Y_\alpha(f)$  is known from the fast chemistry assumption or any other combustion model used, which is known from the relation with mixture fraction. To perform the integration, the probability density function has to be known. Various forms for the PDF have been suggested, such as the double delta function and clipped Gaussian. However, the beta probability function is well established and used for the present work. More details can be found in Pope (1990), Bilger (1976).

## 5.5 Beta probability density function

The Beta( $\beta$ ) PDF is define as

$$\tilde{P}_f(\psi; \mathbf{x}, t) = \frac{\psi^{\beta_1-1}(1-\psi)^{\beta_2-1}}{\int_0^1 \psi^{\beta_1-1}(1-\psi)^{\beta_2-1} d\psi} \quad (5.10)$$

Where

$$\beta_1 = \tilde{f} \left[ \frac{\tilde{f}(1-\tilde{f})}{\tilde{f}''^2} - 1 \right] \quad (5.11)$$

and

$$\beta_2 = \frac{(1-\tilde{f})}{\tilde{f}} \beta_1 \quad (5.12)$$

Where  $\tilde{f}$  and  $\tilde{f}''^2$  are the filtered mixture fraction and the subgrid variance. The parameters  $\beta_1$  and  $\beta_2$  are both positive and the shape of the beta function is dependent on their values. To generate the beta probability density function, the filtered mixture fraction  $\tilde{f}$  and subgrid variance  $\tilde{f}''^2$  have to be known. The filtered mixture fraction is obtained from its transport equation. The subgrid variance can be obtained in different ways. In RANS based combustion simula-

## 5.5 Beta probability density function

---

tions, a transport equation for conserved scalar variance is solved, Jones (1994). However in LES, the use of simple model for  $\widetilde{f''^2}$  rather than solving a transport equation has been established which has given successful predictions, Cook and Riley (1994), Branley and Jones (2001), Pierce and Moin (1998), Kempf (2003). Cook and Riley (1994) by comparing with DNS data suggested the scale similarity model

$$\widetilde{f''^2} = C_1(\widehat{\widetilde{f^2}} - \widetilde{\widehat{f}}^2) \quad (5.13)$$

where hat indicates the test filtering operator in dynamic procedure. With  $C_1 = 1$ , reasonable predictions have been obtained. In this work, the model equation based on local equilibrium argument, Branley and Jones (2001) is used and it can be written as

$$\widetilde{f''^2} = C_2 \Delta^2 \left( \frac{\partial \widetilde{f}}{\partial x_j} \frac{\partial \widetilde{f}}{\partial x_j} \right) \quad (5.14)$$

$\Delta$  is the local grid spacing given by

$$\Delta = (\Delta x \Delta y \Delta z)^{\frac{1}{3}} \quad (5.15)$$

Where  $\Delta x, \Delta y, \Delta z$  are the grid size for the  $x, y$  and  $z$  directions in the cartesian coordinate system. The value of 0.1 for the parameter  $C_2$  has proved successful. More details can be found in Branley (1999).

Using the equation (5.10), the favre filtered value of any variable  $\phi$  can be written as

$$\widetilde{\phi} = \int_0^1 \phi(f) \widetilde{P}(f) df = \int_0^1 \frac{f^{\beta_1-1} (1-f)^{\beta_2-1}}{\int_0^1 f^{\beta_1-1} (1-f)^{\beta_2-1} df} \phi(f) df \quad (5.16)$$

## 5.5 Beta probability density function

---

Defining the Gamma function,  $\Gamma(a)$  for  $a > 0$  as

$$\Gamma(a) = \int_0^{\infty} e^{-f} f^{a-1} df \quad (5.17)$$

It can be shown that

$$\int_0^1 f^{\beta_1-1} (1-f)^{\beta_2-1} df = \frac{\Gamma(\beta_1)\Gamma(\beta_2)}{\Gamma(\beta_1 + \beta_2)} \quad (5.18)$$

and the equation (5.16) rewritten as

$$\tilde{\phi} = \int_0^1 \phi(f) \tilde{P}(f) df = \frac{\Gamma(\beta_1 + \beta_2)}{\Gamma(\beta_1)\Gamma(\beta_2)} \int_0^1 f^{\beta_1-1} (1-f)^{\beta_2-1} df \quad (5.19)$$

Numerical integration has been done by using Romberg method with mid point approximation, Press *et al.* (1996). However, when  $\beta_1$  and  $\beta_2$  are less than 1.0, the integration becomes singular at two end points 0 and 1. To avoid this difficulty an analytical method suggested by Chen *et al.* (1996) has been used. Thus the integration is approximated by

$$\tilde{\phi} = \int_0^1 \phi(f) \tilde{P}(f) df \cong \frac{\eta^{\beta_1}}{\beta_1} \phi(0) + \int_{\eta}^{1-\eta} f^{\beta_1-1} (1-f)^{\beta_2-1} + \frac{\eta^{\beta_2}}{\beta_2} \phi(1) \quad (5.20)$$

Where  $\eta$  is a very small number. Another numerical difficulty can arise if two parameters  $\beta_1$  and  $\beta_2$  have very high values (for example, it can take several hundred thousands in the iteration process). To avoid this problem, a delta function is used when either  $\beta_1$  and  $\beta_2$  are sufficiently large (above 500). In that case  $\tilde{P}(f)$  is approximated by a delta function  $\tilde{P}(f) = \delta(f - \tilde{f})$  and the Favre filtered value of variable  $\phi$  is given by

$$\tilde{\phi} = \int_0^1 \phi(f) \tilde{P}(f) df = \int_0^1 \phi(f) \delta(f - \tilde{f}) df = \phi(\tilde{f}) \quad (5.21)$$

Since the integration gives the Favre filtered scalars and filtered density is obtained from

$$\bar{\rho} = \left[ \int_0^1 \frac{\tilde{P}(f)}{\rho(f)} df \right]^{-1} \quad (5.22)$$

Since the probability density function is a prescribed one (beta function), hence its called presumed pdf approach. There are some other ways such as transported PDF methods extensively used by Pope (1990). However, in LES these approaches are computationally expensive as suggested by Pitsch (2006).

## 5.6 Laminar flamelet model

The laminar flamelet model views the turbulent flame as consisting of an ensemble of laminar locally one dimensional structures within a turbulent flow fields. The complete theoretical details about laminar flamelet model can be found in Peters (1984), Peters (2000). In turbulent flames, major heat release and moving laminar sheets of reaction occur in narrower regions about stoichiometric surfaces, which can be described as wrinkled. These are called flamelets and are considered to be embedded within the turbulent flame. The approach is based on the notion that, if the chemical time scales are much shorter than the characteristic turbulence time scales, reaction takes place in locally thin one dimensional structures. In turbulent non-premixed combustion, the high temperature thin reaction zone is occurring on the stoichiometric mixture fraction surface, and advected and diffused with the mixture fraction field, Bray and Peters (1994). In non-premixed flames, the flame fronts have no intrinsic flow field dependent length scale and the flame thickness is completely dominated by mixture fraction. Bray and Peters (1994) have demonstrated the effect of two parameters known as Damkohler number and mixture fraction fluctuations around the flame front, which introduce

phase diagram for the non-premixed flame regimes. The separated flamelets exist when the turbulent fluctuations of mixture fraction are higher than the flame thickness in the mixture fraction space. The flame regime is observed when the value of the Damkohler number is greater than 1.0 and fluctuation of the mixture fraction along the flame front is greater than flame thickness in mixture fraction space.

The laminar flamelet model is a non-equilibrium model and scalar dissipation rate characterizes the shift from equilibrium model, Bray and Peters (1994). The scalar dissipation rate is used to represent the non-equilibrium effect caused by both convection and diffusion. In the flamelet approach, one dimensional calculation procedure is applied and thus it can incorporate detailed chemical kinetics. Under the one dimensional framework, the laminar diffusion flamelets represent the thermochemical state of the non-premixed flame. The use of one dimensional counterflow diffusion flame is the most standard way to generate the flamelet library. There are mainly two methods of producing laminar flamelet libraries. The first method is to solve the governing equation for counterflow diffusion flames such as the Tsuji burner configuration and the second method it to transform the governing equations of opposed flow diffusion flame into a different coordinate system (mixture fraction space) and solve them to generate laminar flamelet libraries. In the present study, the second method is used.

### 5.6.1 Generating flamelet libraries in the mixture fraction space

The flamelet equations can derived by using coordinate transformation on the mixture fraction space. These equations are derived for temperature and species mass fractions of a one dimensional counter flow diffusion flame. The flamelets

equations in the mixture fraction space are, Bray and Peters (1994), Peters (1984)

$$\rho \frac{\partial Y_\alpha}{\partial t} - \rho \frac{\chi}{2} \frac{\partial^2 Y_\alpha}{\partial f^2} - \omega_\alpha = 0 \quad (5.23)$$

$$\rho \frac{\partial T}{\partial t} - \rho \frac{\chi}{2} \frac{\partial^2 T}{\partial f^2} - \frac{1}{c_p} \frac{\partial p}{\partial t} + \sum_{\alpha=1}^N h_\alpha \omega_\alpha = 0 \quad (5.24)$$

Where  $\chi$  is the scalar dissipation rate and has to be introduced as an input. As suggested by Bray and Peters (1994), Peters (1984), this formulation is independent of the flow field and the effects of the convection and diffusion normal to the stoichiometric mixture fraction surface appear through the corresponding scalar dissipation rate. However, the formulation is derived by neglecting the higher order terms involving convection and curvature along the stoichiometric mixture fraction surface and also based on the assumption of unity Lewis number. A more advanced formulation which does not rely on assumptions mentioned above has also been presented by Pitsch and Peters (1998). The new formulation uses a conserved scalar which can handle non-unity Lewis numbers and does not rely on two stream formulations. However, this formulation is not utilised in the present study.

The laminar flamelet profiles in the mixture fraction space can be generated by solving the above set of governing equations for species concentrations and temperature with a prescribed scalar dissipation rate. The flamelet library includes a set of data for temperature, species concentrations and density in mixture fraction space for different scalar dissipation rates. In this work, a well established computer program known as the Flame-Master code Pitsch (1998) is used to generate the flamelet libraries. The scalar dissipation rate and the strain rate are the two parameters which directly represent the flow dependent effects in the laminar flamelet calculations. The scalar dissipation rate can be expressed from strain

rate  $a_s$  and the mixture fraction  $f$  such that

$$\chi_{st} = \frac{a_s}{\pi} \exp \left\{ -2 \left[ \operatorname{erfc}^{-1}(2f_{st}) \right]^2 \right\} \quad (5.25)$$

Here  $\chi_{st}$  is the stoichiometric scalar dissipation rate and  $\operatorname{erfc}^{-1}$  is the inverse of the complementary error function.

### 5.6.2 Statistics of the non-equilibrium parameter

In laminar flamelet model, the mixture fraction and the non-equilibrium parameter scalar dissipation rate are the two key parameters, which determine the thermochemical composition of the turbulent flame. In flamelet approach the joint probability density function (PDF)  $P(f, \chi)$  of mixture fraction  $f$  and scalar dissipation rate  $\chi$  is used to determine the filtered values of temperature, density and species mass fractions. Thus the filtered value of the scalar variable is given by

$$\tilde{\phi} = \int_0^\infty \int_0^1 \phi(f, \chi) \tilde{P}(f, \chi) df d\chi \quad (5.26)$$

According to the flamelet model formulations, it is assumed that the mixture fraction and the scalar dissipation rate are statistically independent. Thus the joint PDF can be decomposed into two parts such that

$$\tilde{\phi} = \int_0^\infty \int_0^1 \phi(f, \chi) \tilde{P}(f) \tilde{P}(\chi) df d\chi \quad (5.27)$$

As mentioned in the previous section, the beta function is used as pdf for mixture fraction. Effelsberg and Peters (1988) suggested that the log-normal function fits well for the pdf of the scalar dissipation rate. The two independent pdf's can be

written as

$$\tilde{P}(f) = \frac{\Gamma(\beta_1 + \beta_2)}{\Gamma(\beta_1)\Gamma(\beta_2)} f^{\beta_1-1} (1-f)^{\beta_2-1} \quad (5.28)$$

$$\tilde{P}(\chi) = \frac{1}{\chi\sigma\sqrt{2\pi}} \exp\left(-\frac{1}{2\sigma^2}(\ln\chi - \mu)^2\right) \quad (5.29)$$

Where the parameters  $\mu$  and  $\sigma$  are related to the first and second moment of  $\chi$  by

$$\tilde{\chi} = \exp\left(\mu + \frac{1}{2}\sigma^2\right) \quad (5.30)$$

$$\widetilde{\chi''^2} = \tilde{\chi}^2(\exp\sigma^2 - 1) \quad (5.31)$$

Here the filtered scalar dissipation rate still remains an unknown quantity and has to be modelled. Cook and Riley (1998) suggested that filtered scalar dissipation rate can be derived from effective viscosity (molecular and turbulent viscosity), Schmidt number and filtered mixture fraction gradient. The model equation can be written as

$$\tilde{\chi} = 2\left(\frac{\nu}{\sigma} + \frac{\nu_t}{\sigma_t}\right) \left(\frac{\partial \tilde{f}}{\partial x_j} \frac{\partial \tilde{f}}{\partial x_j}\right) \quad (5.32)$$

More details can be found in Pierce and Moin (1998), Kempf (2003).

To calculate the filtered variables it is required to evaluate the two independent integrations of the beta PDF and log-normal PDF. The log-normal integration can be done by using the approximation of Lentini (1994). However, in this study only a single flamelet is used and hence the integration corresponding to scalar dissipation rate is not essential (for a single flamelet the entire integration corre-

sponding to scalar dissipation rate is equal to 1.0).

In LES the entire integration is tabulated prior to the simulation called look up table , Pierce (2001), Kempf (2003) so that the chemical state can be determined from a look up table. The present work relies on integration during CFD calculation rather than using preintegrated lookup table for a single flamelet calculation. However, such a table will be useful in reducing computational cost for multiple flamelet calculations.

# Chapter 6

## Numerical Approach

### 6.1 Introduction

This chapter presents the numerical approaches used in the LES code. The following sections will discuss the spatial discretization schemes, procedures used to integrate the fluid flow equations in time and boundary conditions. The spatial and time discretization schemes in the present LES code PUFFIN were originally developed by Kirkpatrick (2002), Kirkpatrick *et al.* (2003). Finally, a summary of the LES algorithm will be presented detailing the sequential flow of the code.

### 6.2 Finite volume method

In the finite volume method, the entire region is divided into discrete cells or finite volumes. In each of these volumes, the governing equations are integrated, which leads to a set of simultaneous algebraic equations, whose solution is an approximation to the solution of the continuous equations at a set of discrete points or nodes. There is one node in each cell and the solution found for each node is considered representative of the solution within the cell. The numerical

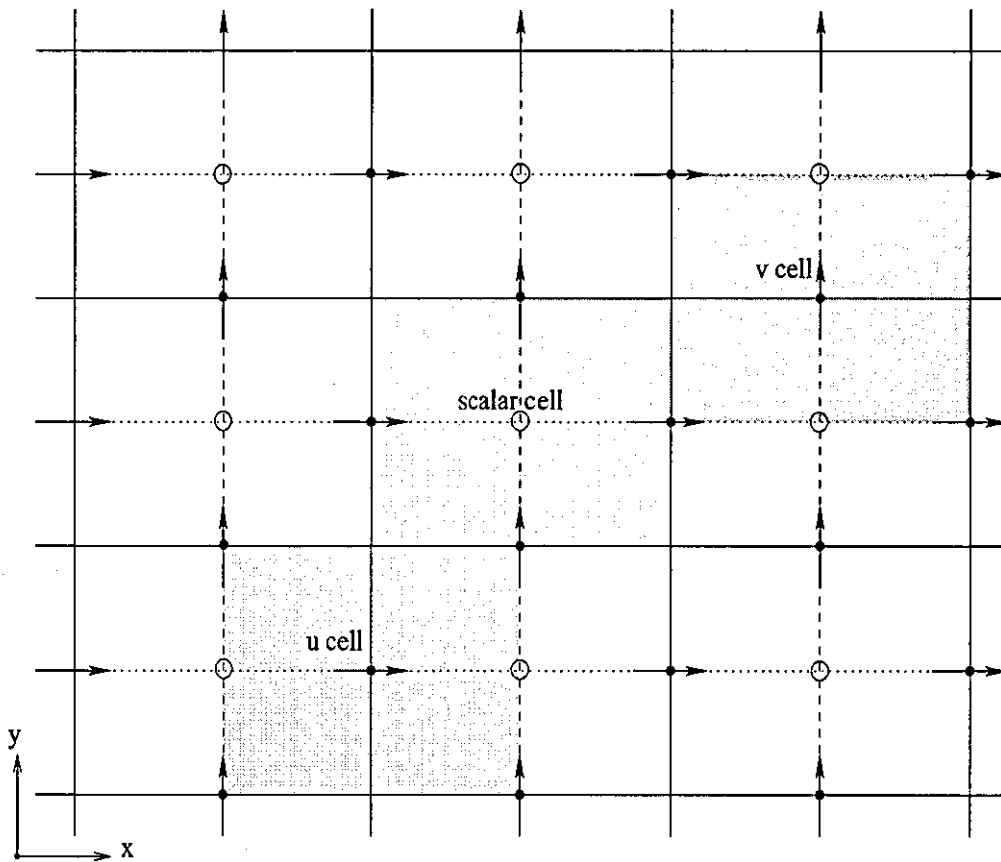


Figure 6.1: Staggered grid and node placement in two dimensions. Circles are scalar nodes, horizontal arrows are nodes of the  $u$  velocity component and vertical arrows the nodes of the  $v$  velocity component. Examples of a  $u$ ,  $v$  and scalar cells are highlighted.

### 6.3 Discretization of transport equations

---

discretization used in this work is based on a staggered Cartesian grid and defines the boundaries of the rectangular finite volumes (see Figure 6.1). Pressure and mixture fraction are calculated at the scalar nodes while the solution for the velocity components is found at the velocity nodes. The formation uses a staggered grid, meaning that velocity cells are staggered with respect to the scalar cells. Velocity nodes are placed at the centroid of the scalar cell faces. The following section describes the spatial discretization schemes for momentum and mixture fraction transport equations.

### 6.3 Discretization of transport equations

The general transport equation for any generic variable  $\phi$  can be written as follows:

$$\frac{\partial(\rho\phi)}{\partial t} + \frac{\partial(\rho u_j \phi)}{\partial x_j} = \frac{\partial}{\partial x_j} \left( \Gamma \frac{\partial \phi}{\partial x_j} \right) + S_\phi \quad (6.1)$$

The equation (6.1) can be rewritten as:

$$\frac{\partial(\rho\phi)}{\partial t} = - \frac{\partial(\rho u_j \phi)}{\partial x_j} + \frac{\partial}{\partial x_j} \left( \Gamma \frac{\partial \phi}{\partial x_j} \right) + S_\phi \quad (6.2)$$

Here  $\Gamma$  is a kinematic diffusion coefficient, and  $S_\phi$  is a source term. The equation (6.2) is integrated over a volume  $V$  of arbitrary shape:

$$\int_V \frac{\partial(\rho\phi)}{\partial t} dV = - \int_V \frac{\partial(\rho u_j \phi)}{\partial x_j} dV + \int_V \frac{\partial}{\partial x_j} \left( \Gamma \frac{\partial \phi}{\partial x_j} \right) dV + \int_V S_\phi dV \quad (6.3)$$

In the resulting equation (6.3), the convection and diffusion terms can be transformed into surface integrals by using Gauss divergence theorem yields the integral form of the equation,

$$\frac{\partial}{\partial t} \int_V (\rho\phi) dV = - \int_S \rho u_j \phi dS_j + \int_S \Gamma \frac{\partial \phi}{\partial x_j} dS_j + \int_V S_\phi dV \quad (6.4)$$

---

### 6.3 Discretization of transport equations

The differential surface area vector  $d\mathbf{S}$  has a magnitude equal to the area of the segment of surface and direction corresponding to the direction of the outward normal to the segment. The equation (6.4) represents unsteady term on (LHS), advection term, diffusion term and the source term. Spatial discretization involves approximating the volume and surface integrals within finite volume of known shapes (cuboid here) to obtain a set of simultaneous linear algebraic equations in  $\phi$ .

Figure 6.2 shows a typical three dimensional cell and its neighbors. In Figure 6.2, the central node  $P$  refers to the cell for which the integrals are to be calculated and surrounded by its northern ( $N$ ), eastern ( $E$ ), southern ( $S$ ), western ( $W$ ), up ( $U$ ) and down ( $D$ ) neighbors. The surfaces separating two cells are denoted as  $A_n, A_e, A_s, A_w, A_u$  and  $A_d$ , the associated fluxes are  $F_n, F_e, F_s, F_w, F_u$  and  $F_d$ . East ( $E$ ), North ( $N$ ) and up ( $U$ ) correspond to positive  $x, y$  and  $z$  directions, respectively ( or  $x_1, x_2$  and  $x_3$  in index notation), and west ( $W$ ), south ( $S$ ) and down ( $D$ ) to the negative  $x, y$  and  $z$  directions. Small letters  $e, n$  etc. refer to the points at the centroid of the respective cell faces.

In the following section,  $nb$  is used as a generic subscript for neighbor cell and  $f$  is a generic subscript for a quantity evaluated at a cell face. To reduce the complexity of the notation, the fluxes are given for a particular face such as the east or north face. All results can be applied in a similar manner to other faces.

#### 6.3.1 Unsteady term

The unsteady term of the general transport equation is advanced using a central difference approximation for the time derivative  $n + \frac{1}{2}$

$$\int_V \frac{\partial(\rho\phi)}{\partial t} dV \approx \frac{(\rho\phi)^{n+1} - (\rho\phi)^n}{\Delta t} \Delta V \quad (6.5)$$

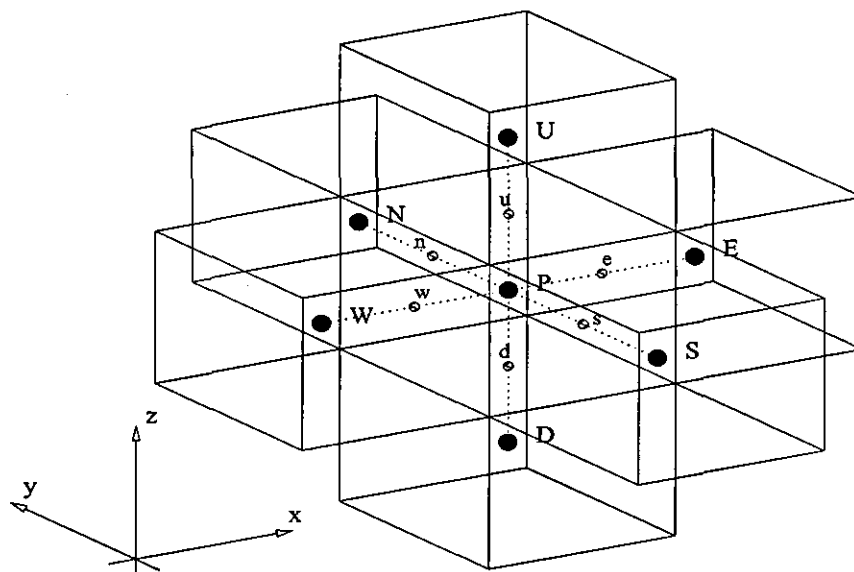


Figure 6.2: A finite volume cell and its neighbors in three dimensions.

Here  $n$  is the time level, which indicates that the values are taken at the start of the current time step, while  $n + 1$  indicates the end of the time step.

### 6.3.2 Discretization of convective fluxes

In turbulent flows, the convective fluxes play an important role and their description is essential for the simulation. This section will present the numerical scheme for the discretization of convection and show that special treatment is necessary to achieve both stability and accuracy.

The convective term is discretized for one control volume:

$$\int_S \rho u_j \phi dS_j = \sum_{n,e,\dots} F_{conv} \quad (6.6)$$

### 6.3 Discretization of transport equations

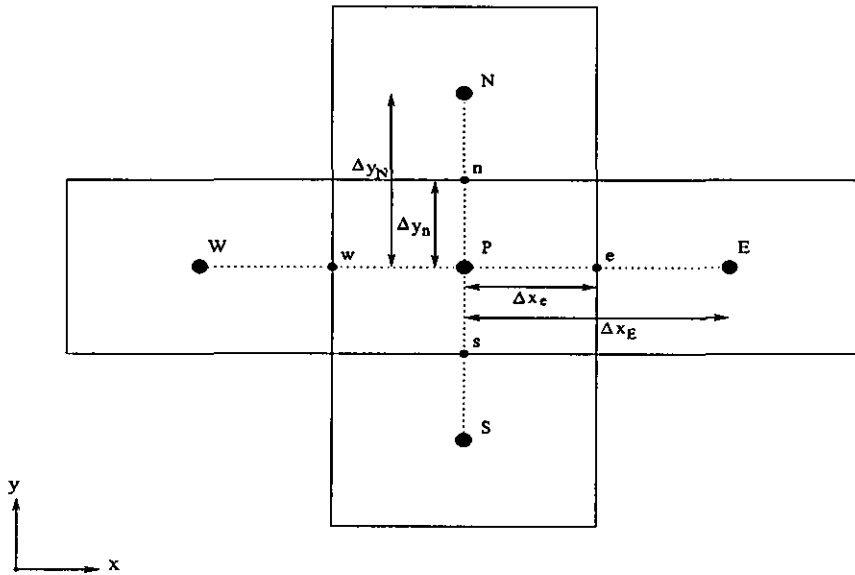


Figure 6.3: A finite volume cell and its neighbors in the xy-plane

The convection flux across the cell face is given by

$$F_{conv} = (\rho u_{normal} \Delta A \phi)_f \quad (6.7)$$

Where  $u_{normal}$  is the velocity component normal to the surface  $A$  and  $\Delta A$  is the area of the face. The convection for the east face can be written as:

$$F_{conv} = (\rho u \Delta A)_e \phi_e \quad (6.8)$$

Interpolation of the neighboring cells is carried out to find the  $\phi_e$  at the centre of the face

$$\phi_e = (1 - \theta) \phi_P + \theta \phi_E \quad (6.9)$$

### 6.3 Discretization of transport equations

---

Here the weighting factor for the interpolation is

$$\theta = \frac{\Delta x_e}{\Delta x_E} \quad (6.10)$$

$\Delta x_e$  and  $\Delta x_E$  are the distances from the node  $P$  to the face of the centroid  $e$  and the east neighbor node  $E$ , as shown in two dimensional view of a cell and its neighbors in figure 6.3.

In the staggered grid it is required to find the convective velocity  $u_e$  at the face and the density  $\rho_e$  at the face depending on whether the variable  $\phi$  is a scalar or velocity component. When  $\phi$  is a scalar, the convective velocity is available, as  $u$  is established at the cell face. However, density must be interpolated using an equation (6.9) such as

$$\rho_e = (1 - \theta)\rho_P + \theta\rho_E \quad (6.11)$$

In contrast, when  $\phi$  is velocity component, linear interpolation is required to find the convective velocity while  $\rho$  is readily available. Finally the resulting formulation for the convection fluxes can be described using a second order central difference scheme:

$$F_{conv} = (\rho u \Delta A)_e [(1 - \theta)\phi_P + \theta\phi_E] \quad (6.12)$$

This linear interpolation based numerical scheme used to calculate the variables at cell faces of the finite volumes is equivalent to a second order central difference scheme in finite difference method. This scheme is second order accurate, computationally efficient, simple to implement and desirable for LES since numerical damping acts as an extra unquantified contribution to the eddy viscosity and contaminates the effects of the subgrid scale model. However this scheme tends to give solutions containing non-physical oscillations or 'wiggles' in areas of the field containing high gradients. The convection terms in the scalar equations are

### 6.3 Discretization of transport equations

---

particularly problematic due to the large gradients which often occur in the scalar fields. Because scalars are often coupled with the velocity field through density, wiggles which result from use of the central difference for the scalar convection terms cause problems with the numerical stability of the overall solution. Hence this scheme is hardly suited for scalar transport, especially when they have to remain bounded. For example, mixture fraction is limited to a range from 0 to 1. From this scheme, wiggles may lead to unphysical results such as predictions of mixture fraction outside the range 0 and 1, which do not yield a chemical state. For this reason, the convection term for the scalar equation is discretized using non-centered schemes, QUICK of Leonard (1979) or SHARP Leonard (1987).

A third order numerical scheme QUICK reduce numerical oscillations by introducing fourth order dissipation. Quadratic interpolation is used to find the value  $\phi$  at the centre of the cell faces. The formula for the the east face can be written as:

$$\phi_e = [(1 - \theta)\phi_P + \theta\phi_E] - \frac{1}{8}CRV \times \Delta x_E^2 \quad (6.13)$$

Here the upwind biased curvature term define as

$$CRV = \frac{\phi_P - 2\phi_E + \phi_{EE}}{\Delta x_E^2}, \quad u < 0 \quad (6.14)$$

$$CRV = \frac{\phi_E - 2\phi_P + \phi_W}{\Delta x_E^2}, \quad u > 0 \quad (6.15)$$

The double subscript such as  $EE$  refers to the cell east of the eastern neighbor. The weighting factor  $\theta$  is calculated from equation (6.10). The first term in equation (6.13) is the value of  $\phi$  at the cell face calculated using linear interpolation. The second term is an upwind biased curvature term which makes the overall interpolation quadratic.

### 6.3 Discretization of transport equations

---

The linear interpolation term accounts for the non-uniform grid through the weighting factor  $\theta$ , while the curvature terms have no grid weighting included. Castro and Jones (1987) have shown that the uniform grid formula for QUICK gives negligible errors for grid expansion ratios ( $r_x = \frac{\Delta x_{i+1}}{\Delta x_i}$ ) between 0.8 and 1.25. Substituting equation (6.13) into equation (6.5) gives the convective flux of  $\phi$  across the east face as

$$F_{conv} = (\rho u \Delta A)_e [(1 - \theta)\phi_P + \theta\phi_E] + S_{QUICK} \quad (6.16)$$

Where  $S_{QUICK} = -\frac{1}{8}CRV \times \Delta x_E^2$ . The source term  $S_{QUICK}$  indicates the curvature of the field. In the code, this terms  $S_{QUICK}$  is included as part of the source term  $S_\phi$ .

However, QUICK scheme does not remove the wiggles completely. In this case another scheme called SHARP, Leonard (1987), which is a modification to QUICK is used. SHARP introduces second order diffusion where local conditions are such that oscillations will not occur, thereby ensuring that the solution remains monotonic. An outline of this scheme can be found in Leonard (1987). Finally the summation of the convective fluxes across all faces can be described as a discrete convection operator,

$$\int_S \rho u_j \phi dS_j \approx \sum (\rho u \Delta A)_f [(1 - \theta_f)\phi_P + \theta_f\phi_{nb} + \sum S_{QUICK}] \quad (6.17)$$

#### 6.3.3 Discretizing diffusive fluxes

The diffusion term is proportional to the gradient of  $\phi$  across a cell face and is given by

$$F_{diff} = [\Gamma \Delta A (\frac{\partial \phi}{\partial \mathbf{n}})]_f \quad (6.18)$$

### 6.3 Discretization of transport equations

---

Where  $\mathbf{n}$  is the direction normal to the face,  $\Gamma$  is the kinematic diffusion coefficient and  $\Delta A$  the area of the face. The flux at the centre of the east cell face is then computed from the values at the two neighboring points and their distance from central difference approximation,

$$F_{diff} = (\Gamma \Delta A)_e \frac{(\phi_E - \phi_P)}{\Delta x_E} \quad (6.19)$$

The diffusion coefficient at the centre of the face  $\Gamma_e$  is calculated by linear interpolations same as density calculation in the convective fluxes. Finally the summation of the diffusive fluxes across all faces can be described as a discrete diffusion operator,

$$\int_S \Gamma \frac{\partial \phi}{\partial x_j} dS_j \approx \sum \frac{(\Gamma \Delta A)_e}{\Delta x_E} (\phi_{nb} - \phi_P) \quad (6.20)$$

It is important to note that the discrete diffusion operator does not suffer from numerical instability as observed in advection operator.

#### 6.3.4 Source terms

Source terms are different in each variables for each transport equations. In momentum equations, the effect of the pressure gradient and the gravitational force act as source terms. In spatial integration, source terms are usually treated in similar manner. They are calculated by evaluating the function representing the source term  $S_\phi$  at the node and multiplying by the volume of the cell such that,

$$\int_V S_\phi dV \approx S_{\phi p} \Delta V \quad (6.21)$$

Gradients are calculated using second order central differences while interpolations use a linear profile similar to that used for the convective and diffusive

### 6.3 Discretization of transport equations

---

fluxes. Generally source term can be described as a combination of an implicit and explicit component,

$$S_{\phi p} \Delta V = S_{imp} \phi_p + S_{exp} \quad (6.22)$$

Here 'implicit' and 'explicit' refers to the manner in which the components of the source term are integrated in time. The implicit component is integrated using an implicit time stepping scheme, while integration of the explicit component uses explicit scheme.

#### 6.3.5 Complete equation

For a general variable  $\phi$  the discretized transport equation can be written as

$$\begin{aligned} \frac{(\rho\phi)^{n+1} - (\rho\phi)^n}{\Delta t} \Delta V = & \left\{ \sum (\rho u \Delta A)_f [(1 - \theta_f) \phi_P + \theta_f \phi_{nb}] \right\}^{(n-2, n-1, n, n+1)} \\ & + \left\{ \sum \frac{(\Gamma \Delta A)_e}{\Delta x_E} (\phi_{nb} - \phi_P) \right\}^{(n-1, n, n+1)} \\ & + \{S_{imp} \phi_p\}^{(n-1, n, n+1)} + \{S_{exp}\}^{(n-2, n-1, n, n+1)} \end{aligned} \quad (6.23)$$

Here the curly brackets  $\{\}$  with superscripts  $(n - 2, n - 1, n, n + 1)$  represent a weighted average of the term evaluated at the listed time intervals, which gives an estimate of the term at the  $(n + \frac{1}{2})$  time level, which will be discussed in next

section. Finally collecting coefficients the equation becomes

$$\begin{aligned}
A_P^{n+1}\phi_P^{n+1} = & \sum_{nb} (A_{nb}^{n+1}\phi_{nb}^{n+1}) + S_{imp}\phi_P^{n+1} + S_{exp}^{n+1} \\
& + \left[ \sum_{nb} (A_{nb}^n\phi_{nb}^n) - A_P^n\phi_P^n + S_{imp}\phi_P^n + S_{exp}^n \right] \\
& + \left[ \sum_{nb} (A_{nb}^{n-1}\phi_{nb}^{n-1}) - A_P^{n-1}\phi_P^{n-1} + S_{imp}\phi_P^{n-1} + S_{exp}^{n-1} \right] \\
& + \left[ \sum_{nb} (A_{nb}^{n-2}\phi_{nb}^{n-2}) - A_P^{n-2}\phi_P^{n-2} + S_{exp}^{n-2} \right]
\end{aligned} \tag{6.24}$$

Where the coefficients corresponding to the node  $A_P$  and its neighbors are formed from the convective and diffusive flux contributions. More details of spatial discretization methods can be found in Kirkpatrick (2002), Kirkpatrick *et al.* (2003).

## 6.4 Advancing in time

This section describes the method in which the partial differential equations are integrated in time. The time integration schemes for the scalar and momentum equations are described, which are then applied to the system of governing equations.

### 6.4.1 Time integration of scalar equation

In the present work the Crank-Nicolson scheme is used for the time integration of scalar equation. The time dependent conservation equation integrated in time

using Crank-Nicolson scheme is written

$$\begin{aligned}
\frac{(\rho\phi)^{n+1} - (\rho\phi)^n}{\Delta t} \Delta V = & -\frac{1}{2} [H^{n+1}(\phi^{n+1}) + H^n(\phi^n)] \\
& + \frac{1}{2} [L^{n+1}(\phi^{n+1}) + L^n(\phi^n)] \\
& + \frac{1}{2} [S_{imp}^{n+1}\phi^{n+1} + S_{imp}^n\phi^n] \\
& + \frac{1}{2} [S_{exp}^{n+1}\phi^{n+1} + S_{exp}^n\phi^n]
\end{aligned} \tag{6.25}$$

Here  $H$  is the discrete convection operator

$$H(\phi) = \sum (\rho u \Delta A)_f [(1 - \theta_f)\phi_P + \theta_f\phi_{nb}] \tag{6.26}$$

$L$  is the discrete diffusion operator

$$L(\phi) = \sum \frac{(\Gamma \Delta A)_e}{\Delta x_E} (\phi_{nb} - \phi_P) \tag{6.27}$$

and  $S_{imp}\phi$  and  $S_{exp}$  the discrete implicit and explicit source terms. It is to be noted that  $S_{imp}$  is a coefficient of  $\phi$  rather than a function of  $\phi$ .

Second order accurate scheme is used to evaluate each term at the  $n$  and  $n+1$  time levels and uses linear interpolation to estimate their value at  $n + \frac{1}{2}$ . At least two iterations of scalar equation per time step are required due to the contributions of terms containing  $\phi^{n+1}$  to the explicit source term which result from the use of the QUICK and SHARP spatial discretization schemes. It is important to note that the number of outer iterations of the entire time advancement scheme per time step is heavily dependent on the density variation thereby needing more number of iterations than expected for larger variation to maintain the stability of the solution. This will be discussed later with the proposed algorithm.

The Crank-Nicolson scheme has to satisfy the following condition to retain non-oscillation behavior:

$$\Delta t \leq \frac{(\Delta x)^2}{\Gamma} \quad (6.28)$$

While this criterion is rather stringent, it results from an error term in the Taylor series expansion which contains the second derivative in space  $\frac{\partial^2 \phi}{\partial x_i^2}$ . However this term is relatively small in most flow problems and the scheme remains stable for considerably large time steps.

### 6.4.2 Time integration of momentum equations

Time integration of the momentum equations use either Crank-Nicolson or the second and third order hybrid Adams schemes. In the hybrid schemes, Adams-Bashforth methods are used for the advection terms and Adams-Moulton methods for the diffusive terms. The momentum equations for velocities are integrated by using Crank-Nicolson scheme is:

$$\begin{aligned} \frac{\rho^{n+1}u^* - \rho^n u^n}{\Delta t} \Delta V = & -\frac{1}{2} [H^{n+1}(u^*) + H^n(u^n)] \\ & + \frac{1}{2} [L^{n+1}(u^*) + L^n(u^n)] \\ & + \frac{1}{2} [S_{imp}^{n+1}u^* + S_{imp}^n u^n] \\ & + \frac{1}{2} [S_{exp}^{n+1}u^* + S_{exp}^n u^n] \\ & - Gp^{n-\frac{1}{2}} \end{aligned} \quad (6.29)$$

The form of this equation is similar to the Crank-Nicolson scheme used for the scalar equation. However an additional term added as a pressure gradient term  $Gp^{n-\frac{1}{2}}$ , which considers  $n-\frac{1}{2}$  time level concerning the pressure correction scheme will be discussed in next section. Here the approximate velocity obtained before

pressure correction step at  $n + 1$  time level is specified with superscript  $u^*$ .

The advection terms in the momentum equations are treated from explicit time advancement scheme as Crank-Nicolson required iterations to retain second order accuracy. In the code, second and third order hybrid schemes are used such that advection terms are treated explicitly using an Adam-Basforth scheme while diffusion term are treated implicitly using Adams-Moulton. The additional terms such as gravitational terms are treated explicitly with Adams-Bashforth.

The second order Adams-Bashforth/ Adams-Moulton scheme for the momentum equations is,

$$\begin{aligned}
 \frac{\rho^{n+1}u^* - \rho^n u^n}{\Delta t} \Delta V = & -\frac{1}{2} [3H^n(u^n) - H^{n-1}(u^{n-1})] \\
 & + \frac{1}{2} [L^{n+1}(u^*) + L^n(u^n)] \\
 & + \frac{1}{2} [S_{imp}^{n+1}u^* + S_{imp}^n u^n] \\
 & + \frac{1}{2} [3S_{exp}^n u^n - S_{exp}^{n-1} u^{n-1}] \\
 & - Gp^{n-\frac{1}{2}}
 \end{aligned} \tag{6.30}$$

and the third order Adams-Basforth/ Adams-Moulton scheme is,

$$\begin{aligned}
 \frac{\rho^{n+1}u^* - \rho^n u^n}{\Delta t} \Delta V = & -\frac{1}{12} [23H^n(u^n) - 16H^{n-1}(u^{n-1}) + 5H^{n-2}(u^{n-2})] \\
 & + \frac{1}{12} [5L^{n+1}(u^*) + 8L^n(u^n) - L^{n-1}(u^{n-1})] \\
 & + \frac{1}{12} [5S_{imp}^{n+1}u^* + 8S_{imp}^n u^n - S_{imp}^{n-1} u^{n-1}] \\
 & + \frac{1}{12} [23S_{exp}^n u^n - 16S_{exp}^{n-1} u^{n-1} + 5S_{exp}^{n-2} u^{n-2}] \\
 & - Gp^{n-\frac{1}{2}}
 \end{aligned} \tag{6.31}$$

From these schemes, the non-linear advection terms and explicit source terms are calculated at previous time steps where all necessary details are known, hence these schemes do not require any iterations as Crank-Nicolson to maintain the accuracy. However, when the density and viscosity vary significantly, iteration of the overall solution procedure is required to include the correct value of density in the unsteady term and viscosity in the diffusion term at the  $n + 1$  time step. The advective transport within one time step has to be limited to at least satisfy the Courant number,  $C = \frac{u_i \Delta t}{\Delta x_i} < 1.0$ . Simply, this criteria requires that, within a time step, information may only travel to the neighboring cell but no further. For advection terms, the maximum time step is proportional to the characteristic convection time  $\frac{\Delta x_i}{u_i}$ , which is usually described in terms of the Courant number. For diffusion term the maximum usable time step is proportional to the characteristic diffusion time  $\frac{\Delta x_i^2}{\nu}$ . However the Adams methods require some treatment for the initial steps where no information about previous time steps is available. Therefore the Crank-Nicolson is used for the initial time steps to enable the calculation of the  $n - 1$  and  $n - 2$  source terms for the Adams schemes.

### 6.4.3 Pressure correction equation

The calculation uses the fractional step method based pressure correction scheme introduced by VanKan (1986) and Bell and Colella (1989). In this scheme, first the momentum equations for three velocity components are integrated to find an approximate solution for the velocity field  $\mathbf{u}^*$ . Mass conservation is then enforced through a pressure correction step in which the approximate velocity field is projected onto a subspace of divergence free velocity fields. The projection is achieved by solving a Poisson equation for the pressure correction  $p'$  in which the

source term is the mass conservation error in each cell,

$$\Delta t \frac{\delta^2 p'}{(\delta x_i)^2} = - \left[ \frac{\rho^{n+1} - \rho^n}{\Delta t} + \frac{\delta(\rho^{n+1} u_i^*)}{\delta x_i} \right] \quad (6.32)$$

The pressure correction is then used to correct the velocity field,

$$u_i^{n+1} = u_i^* - \Delta t \frac{\delta p'}{\delta x_i} \quad (6.33)$$

and the pressure field

$$p^{n+\frac{1}{2}} = p^{n-\frac{1}{2}} + p^* \quad (6.34)$$

The pressure correction equation is discretized in space in a similar manner to the discretization of the transport equations of momentum presented earlier. The integration of equation (6.32) over a finite volume cell and applying the Divergence Theorem gives

$$\Delta t \sum (\Delta A \frac{\delta p'}{\delta x_i})_f = - \left[ \frac{\rho^{n+1} - \rho^n}{\Delta t} \Delta V + \sum (\rho^{n+1} u_i^* \Delta A)_f \right] \quad (6.35)$$

Where summation is performed over each of the faces of area  $\Delta A$ , and  $\Delta V$  is the volume of the cell. Second order central differences are used to calculate the gradients  $\frac{\delta p'}{\delta x_i}$ . It is important to use the same discretization for the pressure gradient in the momentum equation and the pressure correction in the pressure correction equation. This minimizes the projection error and ensures convergence if an iterative scheme is used. More details of time advancement schemes can be found in Kirkpatrick (2002), Kirkpatrick *et al.* (2003).

#### 6.4.4 Iteration procedure for the variable density calculation

In this work, an iterative time advancement scheme for variable density calculation has been implemented. The implemented algorithm is similar to the algorithm proposed by Pierce (2001). For incompressible variable density flow, both the velocity and density fields must be corrected to ensure conservation of mass. Since density depends on mixture fraction (in flamelet calculation), an iterative method is required. The iteration procedure employed in the present study is described below. In the following, the superscript  $n$  refers to solution values that are known from the previous time level, the superscript  $k$  refers to the iteration cycle between the solutions at time step  $n$  and  $n + 1$ , the superscript 0 indicates the initial guess for the first iteration when  $k = 0$ .

**Step 1:** Choose predictors for the values of the variables at the next time level. Simply, this indicate the initial guess for the first iteration when  $k = 0$ .

$$\phi^0 = \phi^n, u_i^0 = u_i^n, \text{ etc.} \quad (6.36)$$

It is important to note that, Pierce (2001) used linear extrapolation for the density predictor in time. However, present work used  $\rho^0 = \rho^n$  as the density predictor.

**Step 2:** First the scalar transport equation is solved, which can obtained the estimate value for the density early in the iteration process. Solving the scalar transport gives predictor for  $\phi^{k+1}$  and current density predictor gives the value  $\hat{\phi}$ ,

$$\hat{\phi} = \frac{(\rho\phi)^{k+1}}{\rho^k} \quad (6.37)$$

**Step 3:** Calculate the density from the flamelet library, using the provisional scalar values:

$$\rho^{k+1} = f(\widehat{\phi}) \quad (6.38)$$

It is to be noted that the mixture fraction coming from step 2 is used to calculate the  $\beta$  PDF integrated density at the  $k + 1$  time step.

**Step 4:** Re-update the scalars based on the new density to preserve primary scalar conservation:

$$\phi^{k+1} = \frac{(\rho\phi)^{k+1}}{\rho^{k+1}} \quad (6.39)$$

**Step 5:** Solve the momentum equations.

**Step 6:** Solve the pressure correction equation

**Step 7:** Correct pressure and velocity field. The continuity equation, based density determined in step 3, is now satisfied exactly. This completes full one cycle of the iterative process. In addition to these steps inside the iteration process, one more calculation is required at the end of the time step and it is defined as step 8.

**Step 8:** Calculate eddy viscosity

Typically 8 – 10 outer iterations of this procedure are required to obtain satisfactory convergence at each time step. The details of numerical solutions parameters such as time step and iterations vary for different flow problems. Time step is varied to ensure that the Courant number  $C = \Delta t u_i / \Delta x_i$  remains approximately constant. In general, the solutions are advanced with a time step corresponding to a Courant number in the range  $C = 0.2 - 0.7$ . However this may change in the context of the individual case studies presented in later chapters.

With this iterative scheme, the CFD-code requires under-relaxation of density in time. With the current method, the density  $\bar{\rho}^{n+1}$  computed from the flamelet library is no longer applied to the CFD-code, but rather its under-relaxed value

$\bar{\rho}_r^{n+1}$  is taken as

$$\bar{\rho}_r^{n+1} = \alpha \bar{\rho}_r^{n+1} + (1 - \alpha) \bar{\rho}_r^n \quad (6.40)$$

Where  $\alpha$  being a real number  $0 < \alpha < 1$ , and the relaxation factor used in this study is 0.25. This is required to establish stability in the initial stages.

### 6.4.5 Solutions of algebraic equations

The system of linear equations obtained from the numerical discretization are solved using a linear equations solver. In this work, the Bi-Conjugate Gradient Stabilized (BiCGStab) solver with a Modified Strongly Implicit (MSI) preconditioner was used to solve the momentum and scalar equations, which is more efficient for the large variations in cell size. The BiCGStab is also used for the pressure correction equation.

Convergence of the solvers is measured using the  $L_2$  norm of the residual ( $L_2$  norm is a vector norm that is commonly encountered in vector algebra and vector operations such as dot product). The residual was set to be less than  $10^{-10}$  for the solution of the momentum and scalar equations, which typically required one or two sweeps of the solver to obtain convergence. At each time step, a number of iterations of the pressure/velocity correction step are generally required to ensure adequate conservation of mass.

Within each iteration the pressure correction equation is solved until either the residual is reduced to 10% of its original value or the BiCGStab solver has performed 7 sweeps. Each sweep of the solver includes 2 sweeps of the preconditioner. The solution is then used to correct the pressure and velocity field and the divergence of the corrected velocity field is calculated. The process is repeated until the  $L_2$  norm of the divergence error is less than a pre-set value. The minimum

attainable divergence error is typically reached after 6 or 8 projections.

## 6.5 Initial and boundary conditions

It is well recognized that besides the mathematical model and the numerical scheme, properly chosen boundary conditions are of great importance for successful LES predictions. From a mathematical point of view the imposition of exact boundary and initial values is a necessary condition for a unique solution of the set of partial differential equations to be solved. For the case of turbulent flows, in contrast to time-evolving turbulence, direct numerical or large eddy simulations of spatially inhomogeneous flows require turbulence boundary conditions. This fact makes the results strongly influenced by the velocity data prescribed at the inflow. Turbulence has to be prescribed at the inflow in order to simulate turbulence.

To solve the governing equations of the physical problem to which a numerical solution is being sought, initial and boundary conditions must be set. In all simulations presented in this work, the flow is impulsively started at  $t = 0$ , when the simulation is switched on. Thus by the time the flow pattern has established and statistical sampling begins, the initial conditions will have been swept entirely from the domain. To initialise a new simulation, the velocity and scalar fields are initially set to zero everywhere. Pressure impulsively starts the flow as inlet conditions are applied, initially producing a potential flow. Turbulence from the inlet gradually fills the domain, eventually forming a fully developed flow field.

When solving isothermal flows, the boundary conditions must be supplied for five dependent variables:  $\rho$ ,  $u_i$  and  $p$ . Additionally when combustion takes place boundary conditions for other scalars such as mixture fraction, subgrid variance (mixture fraction variance), scalar dissipation have to be supplied. Since density

is dependant on the mixture fraction, the boundary condition for density can be specified from mixture fraction. Continuity requires that mass conservation be satisfied over the complete domain at all times, and the boundary conditions for the velocity field must therefore ensure that

$$\int_{\Omega} \frac{\partial \rho}{\partial t} dV + \int_S \rho u_i n_i dS = 0 \quad (6.41)$$

If this is not the case, a solution to the Poisson equation for the pressure increment will not exist Jones (1994).

In this work, either Dirichlet or Neumann boundary are applied for all variables. In Dirichlet condition, the value on the boundary  $\partial\Delta V$  of any scalar variable  $\phi$  of the computational domain  $\Delta V$  is given by:

$$\phi = \phi_{\partial} \quad (6.42)$$

With the Neumann condition, the gradients  $\frac{\partial \phi}{\partial x_j}$  in surface normal direction  $n_j$  are given by  $c_{\partial}$ :

$$\frac{\partial \phi}{\partial x_j} n_j = c_{\partial} \quad (6.43)$$

### 6.5.1 Inflow boundary conditions

Several methods are available to introduce the turbulent inlet boundary conditions such as mean velocity profiles with random fluctuations Branley and Jones (2001), digital filter method Klein *et al.* (2003), immersed boundary method Kempf *et al.* (2005), body force method Pierce and Moin (2004). In this study the instantaneous inflow boundary conditions have been generated by using mean velocity profiles with random fluctuations. The mean velocity distributions were

specified using power law velocity profiles such as

$$\langle U \rangle = C_0 U_j \left( 1 - \frac{|y|}{\delta} \right)^{1/7} \quad (6.44)$$

Where  $U_j$  is the bulk velocity,  $y$  is the radial distance from the jet centreline and  $\delta = 1.01 \times R_j$ , with the fuel jet radius  $R_j$ . The coefficient  $C_0$  is selected as 1.218 to ensure correct mass flow rate at the inlet Masri *et al.* (2000). The fluctuations are generated from a Gaussian distribution such that the inflow has the correct level of turbulent kinetic energy obtained from the experimental measurements, Branley and Jones (2001). The instantaneous inflow velocity  $u_i$  is then computed as

$$u_i(x_i, t) = \langle U_i \rangle + \theta(x_i, t) \langle u_i' \rangle_{rms} \quad (6.45)$$

Where  $\langle U_i \rangle$  is the mean velocity from equation (6.44),  $\langle u_i' \rangle_{rms}$  is the root mean square of turbulent fluctuations obtained from experimental measurements at the inflow and  $\theta(x_i, t)$  is a random number from a Gaussian distribution. The mixture fraction at the inflow is set to unity in the fuel stream and to zero elsewhere.

### 6.5.2 Outflow boundary conditions

The outflow boundary conditions generally use a zero normal gradient condition or a convective outlet boundary condition. The use of a zero gradient condition at an out flow boundary is given by the formula

$$\frac{\partial \phi}{\partial n} = 0 \quad (6.46)$$

where  $\frac{\partial}{\partial n}$  denotes the gradient taken normal to the outflow boundary. There is another form of outlet boundary condition known as a mass conserving convective

outlet boundary condition. The latter is given by the formula

$$\frac{\partial \phi}{\partial t} + U_b \frac{\partial \phi}{\partial n} = 0 \quad (6.47)$$

Where  $U_b$  is the bulk velocity across the boundary.

### 6.5.3 Solid boundary conditions

The natural boundary condition for velocity at solid wall boundaries is to set the normal and tangential velocity components to zero at the wall. These conditions correspond to the impermeability condition and the no-slip condition respectively.

For domain boundaries coinciding with a stationary impermeable wall, the no-slip condition can be applied,

$$u_i(x, t) = 0 \quad (6.48)$$

When simulating a free flows, the size of the computational domain must be restricted to a size that is affordable, yet large enough to ensure the effects of artificially constraining the flow are kept to a minimum. Free slip walls are designed to assist in this area by treating boundaries as frictionless surfaces. The flow adjacent to the boundary is allowed to move in the direction parallel to the boundary by enforcing a zero gradient condition normal to the surface,

$$\frac{\partial u_i}{\partial n} = 0 \quad (6.49)$$

whilst the wall normal component is set to zero,

$$u_i(x, t) = 0 \quad (6.50)$$

## 6.5 Initial and boundary conditions

---

The distinction between the energy containing scales and the viscous scales, considerably important in LES, vanishes as the wall is approached. For turbulent boundary layers in which it is not possible to resolve laminar sublayer, it is necessary to use an approximate boundary condition or wall function in order to apply the correct shear force to the fluid. The implemented wall function is that of Werner and Wengle (1991) which uses a power-law approximation to the log-law.

# Chapter 7

## LES of Isothermal Swirling Flows: Results and Discussion

### 7.1 Introduction

In this chapter, the models and numerical methods described in previous chapters are tested against experimental data based on Sydney swirl burner, Al-Abdeli and Masri (2004), Al-Abdeli and Masri (2003a). The introduction of swirl intrinsically associated with the phenomenon of vortex breakdown (VB) adds another dimension to the complexity of the problem. This necessitates that the comprehensive computation of swirling flows be not only three dimensional but also time dependent. The systematic validation of computation is therefore necessary to have a complete understanding of the complex transient behavior of swirling motion. The simulations attempt to find the fundamental aspects of swirling flow structure through LES, that originate from simple well defined boundary conditions hence forming a suitable model problem for the validation of computations. To achieve this task, three different non-reacting swirling flow fields Al-Abdeli and Masri (2003a) based on Sydney swirl burner have been selected. These flows

exhibit different flow structures due to different swirl and Reynolds numbers.

## 7.2 Experimental observations

This work deals with modelling the three non-reacting test cases known as N21S00, N29S054, N16S159 Al-Abdeli and Masri (2003a) and hence discussion of the important features of the flow field based on experimental measurements is given. The flowfield of the non-swirl case N21S000 ( $S = 0.0$ ) consist of typical bluff body stabilized recirculation zone. In this case, there is no swirl velocity and the flow field is very much similar to bluff body stabilized non-reacting jet conducted by Dally *et al.* (1998).

The case N29S054 which has a swirl number of  $S = 0.54$  is particularly useful for model validation as it exhibits key features of swirling flow motion. In this case a typical upstream recirculation zone above the bluff body is present and it stagnates about 25 mm from the burner exist plane. With the influence of swirl, the central jet is also subjected to a centrifugal like lateral spread with parcels of gas moving outwards to the inner side of the upstream recirculation zone. The other key feature of this flow field is the existence of a second recirculation zone which stagnates along the jet centreline between 50 mm and 110 mm from the burner exit plane. This is the vortex breakdown region. This zone of air takes on the form of a closed bubble. In this region the velocity field also form a non-recirculating collar-like flow structure in further downstream regions and just beyond the end of the first recirculation zone. A vortex break down bubble occurs only when axial momentum (Reynolds number) of the swirling annulus provides the right conditions for the onset of vortex breakdown, Al-Abdeli and Masri (2003a). Numerical capture of such delicate conditions is viewed as a stern test for the LES simulations.

The flow field of case N16S159 ( $S=1.59$ ) has an extended recirculation zone that stagnates about 70 *mm* downstream of the bluff body face. This recirculation zone is much longer than that typically formed with non-swirling bluff body stabilized flow (N21S000). The central jet decays very fast and is almost totally consumed by about  $x = 90$  *mm* where the centreline velocity decreases almost to zero. The high swirl causes the flow to spread radially outwards creating a long stagnation zone. Above the face of the burner on the inner size of the recirculation zone, there exists a strong rotating non-recirculating collar like zone where the tangential velocity attains a peak value of around 13  $m.s^{-1}$  with high rms fluctuations. Finally it is important to note that no vortex breakdown (VB) is observed in this flow case.

### 7.3 Numerical description

The large eddy simulation code PUFFIN originally developed by Kirkpatrick (2002) is used to perform all calculations presented here. The equations are discretised in space by using a finite volume formulation on a non-uniform, staggered, Cartesian grid. A second order central difference approximation is used for all terms in the momentum equations and pressure correction equation. The solutions are advanced in time by using the fractional step method. First the momentum equations are integrated using a third order hybrid Adam-Bashforth/Adam-Moulton scheme to give an approximate solution for the velocity field. Then the mass conservation is enforced through a pressure correction step in which the approximate velocity field is projected onto a subspace of divergence free velocity fields. The pressure correction method of VanKan (1986) and Bell and Colella (1989) was used in the present calculations. The time step is varied to ensure that the Courant number  $C_0 = \Delta t U_i / \Delta x_i$  remains approximately con-

### 7.3 Numerical description

stant. Where  $\Delta x_i$  is the cell width,  $\Delta t$  is the time step and  $u_i$  is the velocity components in the  $x_i$  direction. The solution is advanced with a time stepping corresponding to Courant number  $C_0 < 0.6$ . The equations, discretised as described above, are solved using a linear equation solver. Here a Bi-Conjugate Gradient Stabilized (BiCGStab) solver with a Modified Strongly Implicit (MSI) preconditioner is used. The momentum residual error is typically of the order  $10^{-8}$  per time step and the mass conservation error is of the order of  $10^{-10}$ .

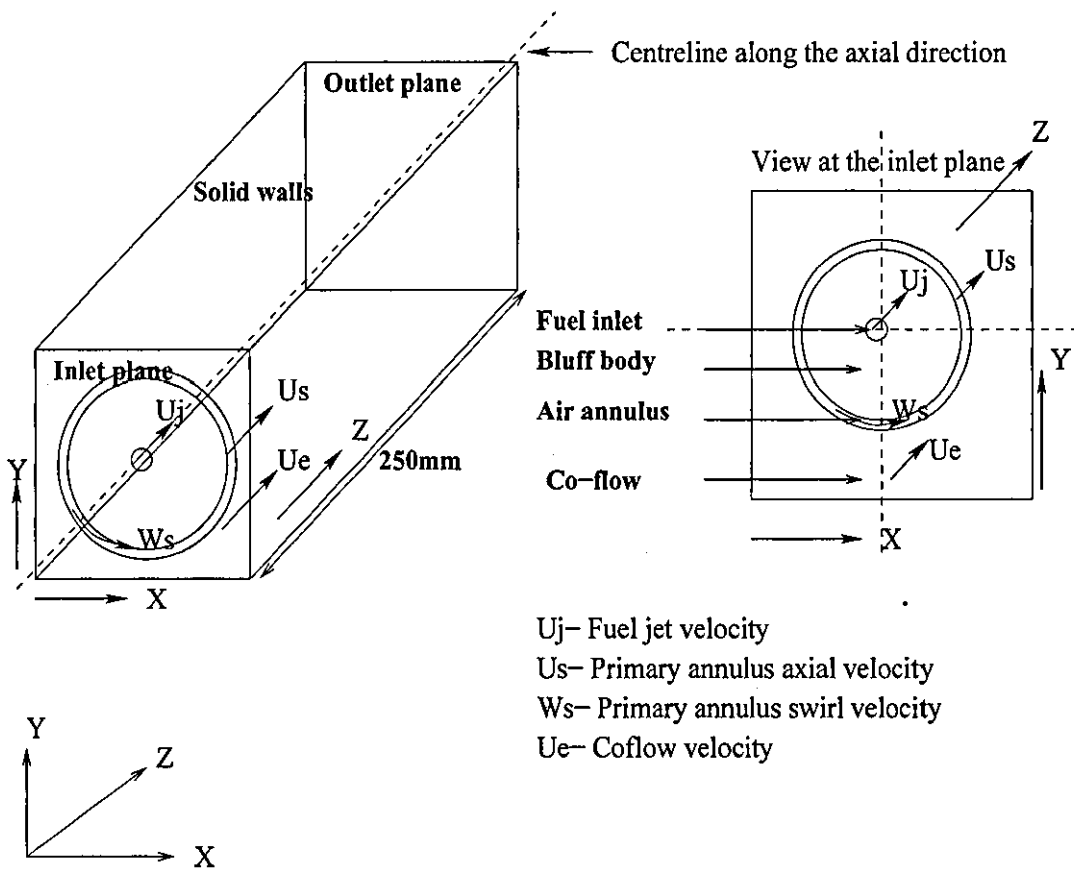


Figure 7.1: Computational domain.

## 7.4 Grid resolutions and boundary conditions

Figure 7.1 shows the computational domain used in the present study. The computational domain has dimensions  $130 \times 130 \times 250mm$  in  $X, Y$  and  $Z$  directions respectively. Two grids were employed to conduct a grid sensitivity analysis of LES. Grid 1 consisted of  $100 \times 100 \times 100$  cells in  $x, y$  and  $z$  directions respectively giving a total of one million grid points. A second grid, Grid 2 that is finer than Grid 1 was used with a total of 1.44 million grid points and consisted of  $120 \times 120 \times 100$  cells in  $x, y$  and  $z$  directions respectively. The axial resolution was kept the same for both grids due to computer resource limitations. For Grid 1, grid lines in  $x$  and  $y$  directions used an expansion ratio of  $\gamma_{xy} = \Delta x(i)/\Delta x(i-1) = 1.08$  and an expansion ratio of  $\gamma_z = 1.07$  was used in the  $z$  direction. The expansion ratio for Grid 2 was  $\gamma_{xy} = 1.06$  in the  $x$  and  $y$  directions and  $\gamma_z = 1.07$  in the  $z$  direction.

The case N16S159, which has the highest swirl number 1.59 was used as the test case for grid sensitivity analysis. It is not possible to define classical grid independence with implicit filtering where filter width directly affected by the grid. However a refined grid can minimize both numerical and modelling errors through better resolution. LES results obtained using the above two grids are compared with experimental measurements. Figure 7.2 shows the mean axial velocity and its rms fluctuations at two different axial locations. Solid lines represent the Grid 1 results (1 million points), dashed lines represent the Grid 2 results (1.44 million grid points), and symbols represent experimental measurements. The comparisons between the experimental measurements and computed mean axial velocity and its rms fluctuations at  $x/D = 0.136, 0.2$  are reasonably good. There is a slight difference between grid 1 and grid 2 predictions in the mean axial velocity plots, especially in the outer shear layer of the bluff body stabilized recirculation

## 7.4 Grid resolutions and boundary conditions

zone. However, it has been found that both grids give same results for mean, rms and Reynolds stresses for the case N16S159 and hence the grid 1 with 1 million grid points has been used for all the LES simulations to reduce the computational cost.

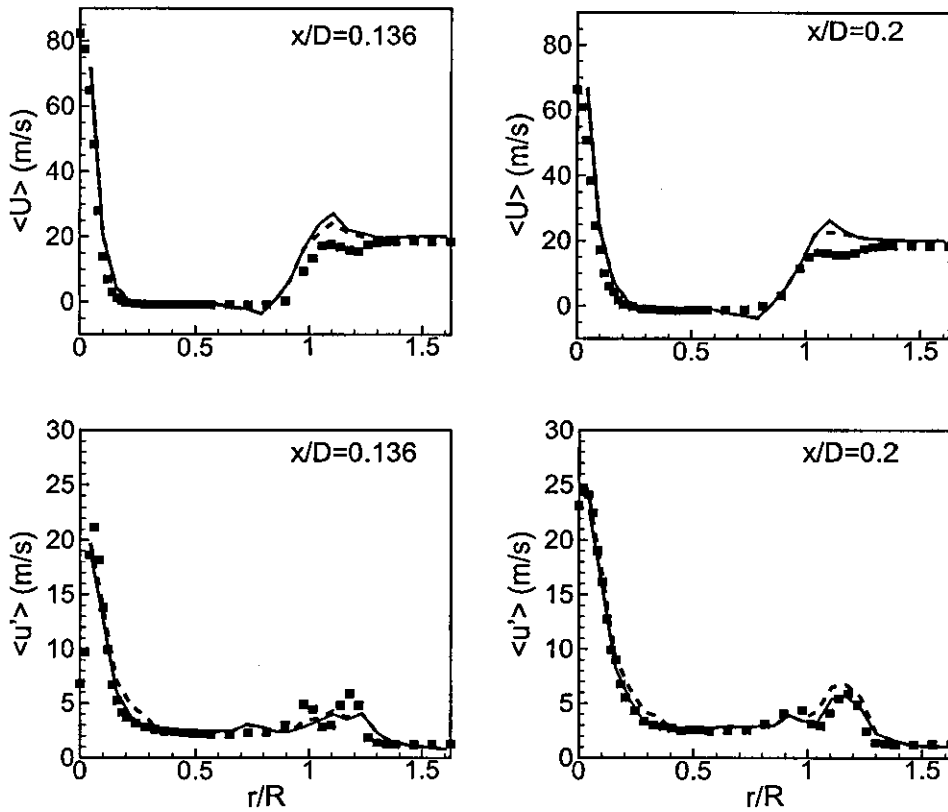


Figure 7.2: Radial profiles of mean axial velocity in the N21S00, lines represent LES results and symbols represent experimental measurements.

## 7.5 Statistics

The time averaged mean velocity components and their mean fluctuating values in the axial, radial and azimuthal directions are obtained by time averaging the transient flow variables obtained from LES results, i.e

$$\langle \bar{\phi} \rangle = \frac{1}{N_t} \sum_{n=1}^{N_t} \bar{\phi}^n, \quad \bar{\phi}_{rms} = \sqrt{\frac{1}{N_t} \sum_{n=1}^{N_t} (\bar{\phi}^n - \langle \bar{\phi} \rangle)^2} \quad (7.1)$$

Where  $N_t$  represents the number of samples. To remove the non-physical artefact of the initialization, the simulation should evolve for a sufficiently long time before gathering any statistical results. This allows the flow field to fully develop and initial transients to exit the computational domain. The samples are only taken after the flow field has fully developed. In this study to obtain statistically stationary results, time averaging of the primitive variables was performed after 12 flow-through-times ( $\tau$ ), which is defined here as the time for a fluid element to propagate through the computational domain, i.e.  $\tau = L/U$ ,  $L$  and  $U$  are axial length of the computational domain and inlet bulk axial velocity respectively. Two non-consecutive sampling periods yielded similar results indicating that the statistics were sufficiently converged.

The calculations were performed on a Pentium 4, personal computer with 4GB RAM and 3GHz processor running under Linux operating system. A typical run takes 10 – 17 days depending on the inlet parameters and the number of flow passes. Table 7.1 summaries grid resolution and typical run times in days for each case considered.

## 7.6 Flow structures of the non-swirl case

Flow case	Grid Type	$N_x$	$N_y$	$N_z$	Time(s)	Cost days
N21S000	Grid 1	100	100	100	0.15	10
N29S054	Grid 1	100	100	100	0.15	12
N16S159	Grid 1	100	100	100	0.2	14
N16S159	Grid 1	120	120	100	0.3	17

Table 7.1: Grid resolution and typical run time (s) for non-reacting test cases

## 7.6 Flow structures of the non-swirl case

The non-swirl case (N21S000) has a complex flow structure in the form of bluff body stabilized recirculation and LES predictions of this case is described below. Figure 7.3 shows the streamlines generated from the mean velocity field in the central  $x - z$  plane of the N21S00 case. The mean streamlines show a two-zone flow/turbulence structure. A typical torroidal shape recirculation zone is formed due to the sudden expansion at the bluff body wall. The central jet velocity dominates the wake and hence there is no stagnation point located along the centreline. The schematic of streamlines of the two counter-rotating vortices associated with the central jet and co-flow can be identified in the plot. The co-flow driven vortex is wider than the central jet affected vortex. Although both central jet and co-flow velocity are operating, the external airflow principally manages the recirculation zone structure. Figure 7.4 shows the detailed measured and computed radial profiles of time averaged mean axial velocity at different positions along the axis. The predicted mean axial velocity at  $x/D = 0.074, 0.2, 0.4$  shows minor under prediction at the centreline as a result of the early break up of the central jet. The two counter rotating vortices observed from the simulation can lead to occurs this behaviour. Despite this small discrepancy, the predictions for the mean axial velocity are in good agreement with experimental measurements. The existence of negative mean axial velocity indicates the flow reversal, which generates the bluff body stabilized recirculation zone. It can be seen that

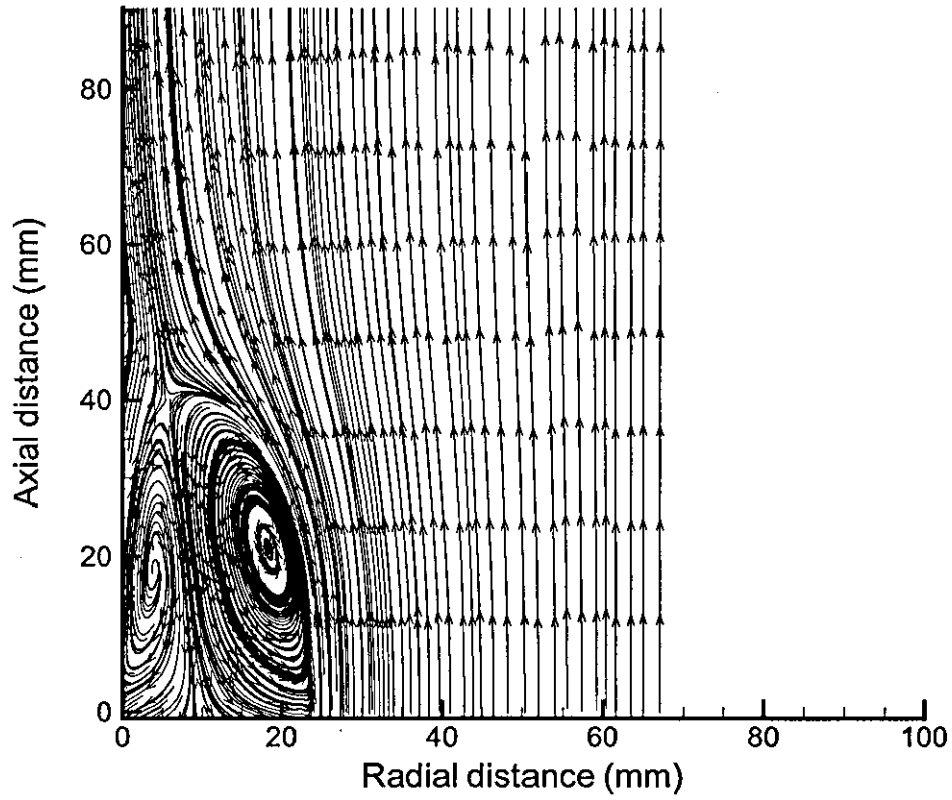


Figure 7.3: Streamlines generated from the mean velocity fields of the non-swirl case obtained from LES calculation.

the length of the bluff body wake is completely captured by the simulation. The recirculation zone mainly created due to the deceleration of the axial velocity by the sudden expansion at the bluff body wall. It can be noted that the recirculation zone extends up to  $x/D = 0.8$  in the axial direction. This can be seen where the mean axial velocity exhibits some negative values at  $x/D = 0.8$  and becomes completely positive at the measurement location  $x/D = 1.4$  and remains positive after that for all downstream axial positions.

Figure 7.5 shows the comparison of mean radial velocity with experimental data. Some notable discrepancies are evident at near burner locations. However, at  $x/D = 0.074$ , correct trend is obtained with a slight over-prediction for the peak value. Some differences between calculated and measured results are observed at  $x/D = 0.2$ , where experimental data show an unusual abrupt reversal of the radial velocity magnitude, which is not captured by the LES model. Data taken in an equivalent bluff body configuration Dally *et al.* (1998) in which similar non-swirling experiments were conducted does not show such a discontinuity in radial velocity. This could be due to experimental difficulties in measuring radial velocities very near the exit of the swirl annulus, Al-Abdeli and Masri (2003a). The predicted profile at this location captures the experimental data up to  $r/R = 1.0$  reasonably well. Further downstream the radial velocity is under predicted between the regions  $r/R = 0.2 - 1.0$  at locations  $x/D = 0.4, 0.6$ . It can be seen that despite the upstream discrepancies, the agreement between predictions and experiments are good at most downstream axial locations. It is worth noting that the magnitude of the radial component is small compared to the axial velocity values hence the discrepancies are relatively small.

## 7.6 Flow structures of the non-swirl case

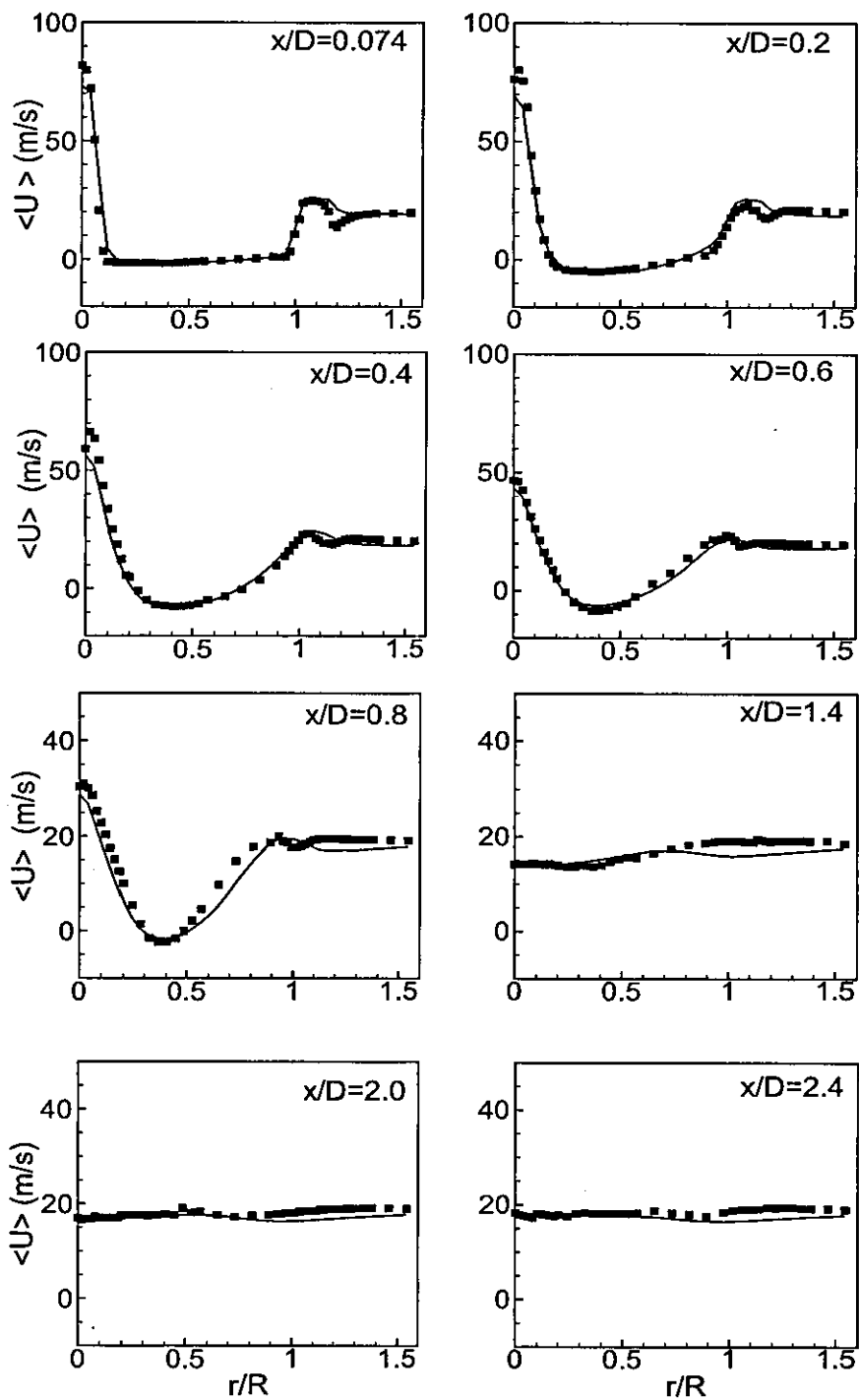


Figure 7.4: Radial profiles of mean axial velocity in the N21S00, lines represent LES results and symbols represent experimental measurements.

7.6 Flow structures of the non-swirl case

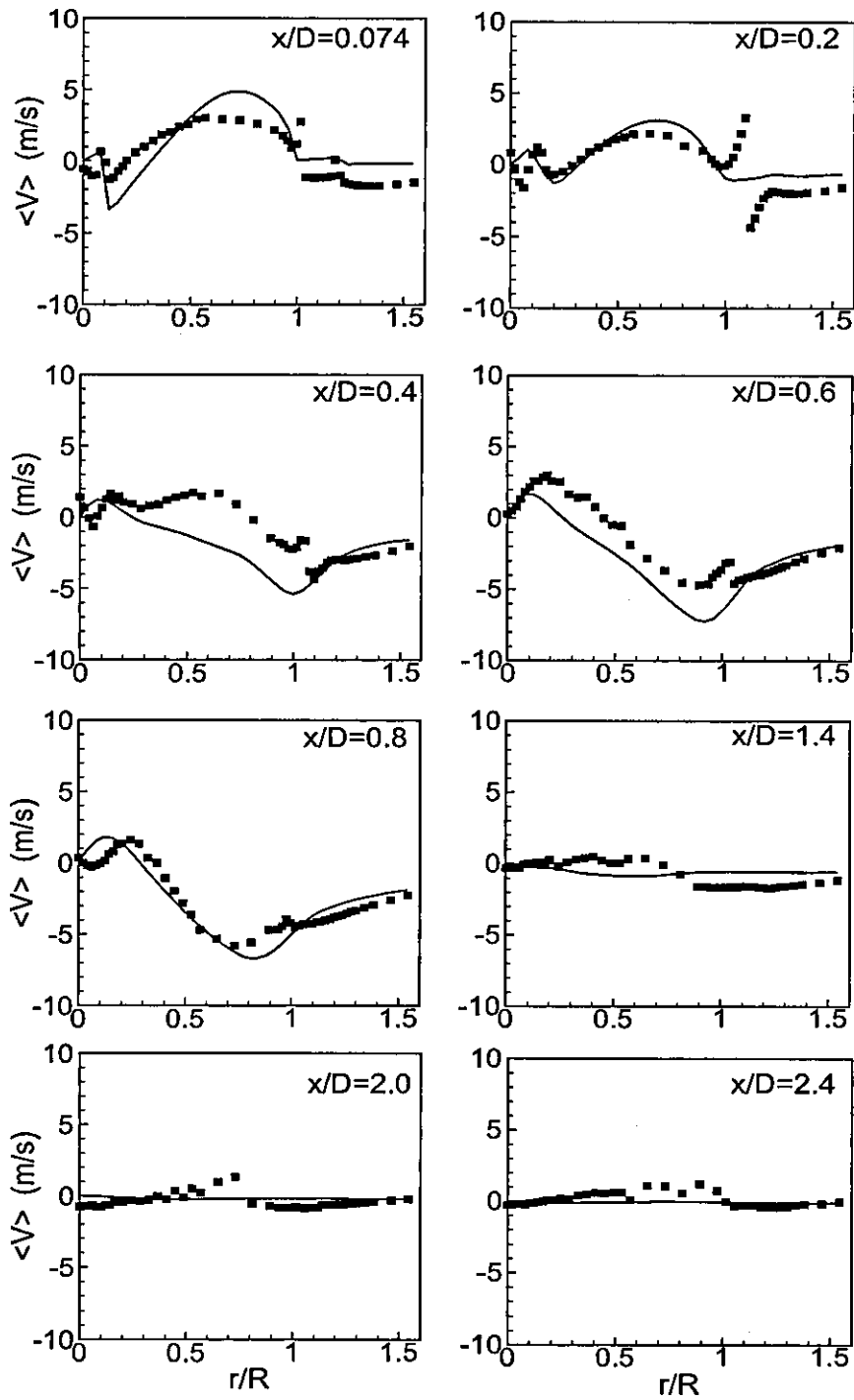


Figure 7.5: Radial profiles of mean radial velocity in the N21S00, lines represent LES results and symbols represent experimental measurements.

## 7.6 Flow structures of the non-swirl case

---

Predicted rms fluctuations of axial and radial velocities are compared in Figures 7.6 and 7.7. In agreement with the observed wake properties, results show high rms values for both axial and radial fluctuations in regions where the central jet is constrained by the recirculating flow. At most upstream locations the comparisons for the axial rms velocity are good (Figure 7.6). Sharp changes and peak values have been correctly predicted and calculations show good agreement up to  $x/D = 0.8$ . Further downstream the predicted profiles of rms axial velocity show slight over-predictions.

Comparison of rms radial velocity shown in Figure 7.7 shows some discrepancies with experimental data. However, rms of radial velocities are slightly over predicted between the region  $r/R = 0.5 - 1.0$  at the first five axial locations. Further downstream, the comparison shows slight over predictions. Given that absolute magnitudes of rms velocities are difficult to calculate, the model's overall ability to predict the peak in rms velocities and their trend appears to be good.

Finally the comparisons for the Reynolds shear stresses are given in Figure 7.8. The LES model found to capture the peaks and the changes of the stresses inside the recirculation region reasonably well. Although some under predictions can be seen in region between  $r/R = 0.0 - 0.7$  at the axial location  $x/D = 1.4, 2.0, 2.5$ . The predictions, however, produced better agreement with the experimental data in the near burner region. In general, the LES model described in this work, has been successful in predicting key flow features of the N21S000 case. The overall agreement for this case between measurements and calculations for mean velocities, rms fluctuations and Reynolds shear stress is seen to be good.

## 7.6 Flow structures of the non-swirl case

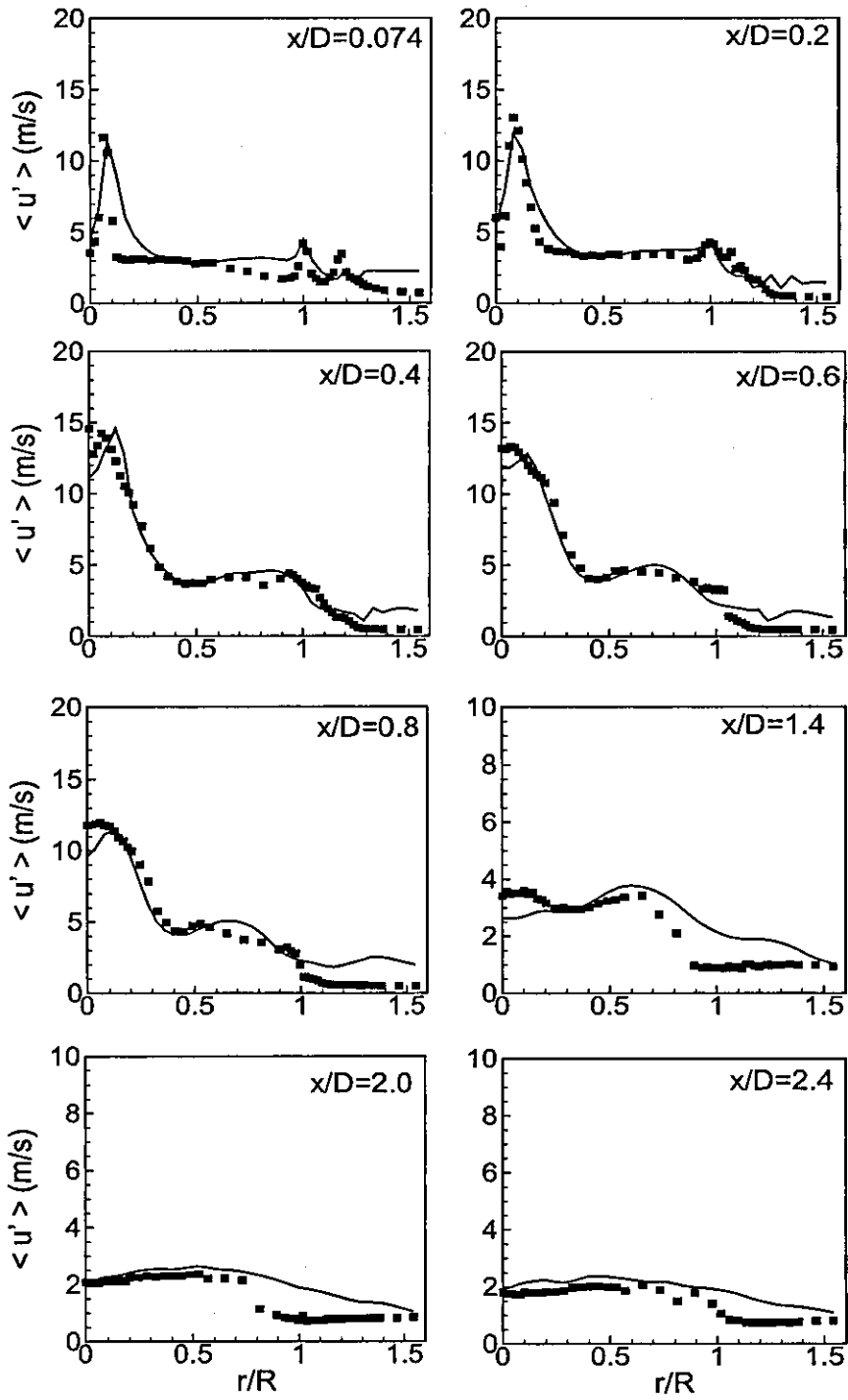


Figure 7.6: Radial profiles of RMS fluctuations of axial velocity in the N21S00, lines represent LES results and symbols represent experimental measurements.

## 7.6 Flow structures of the non-swirl case

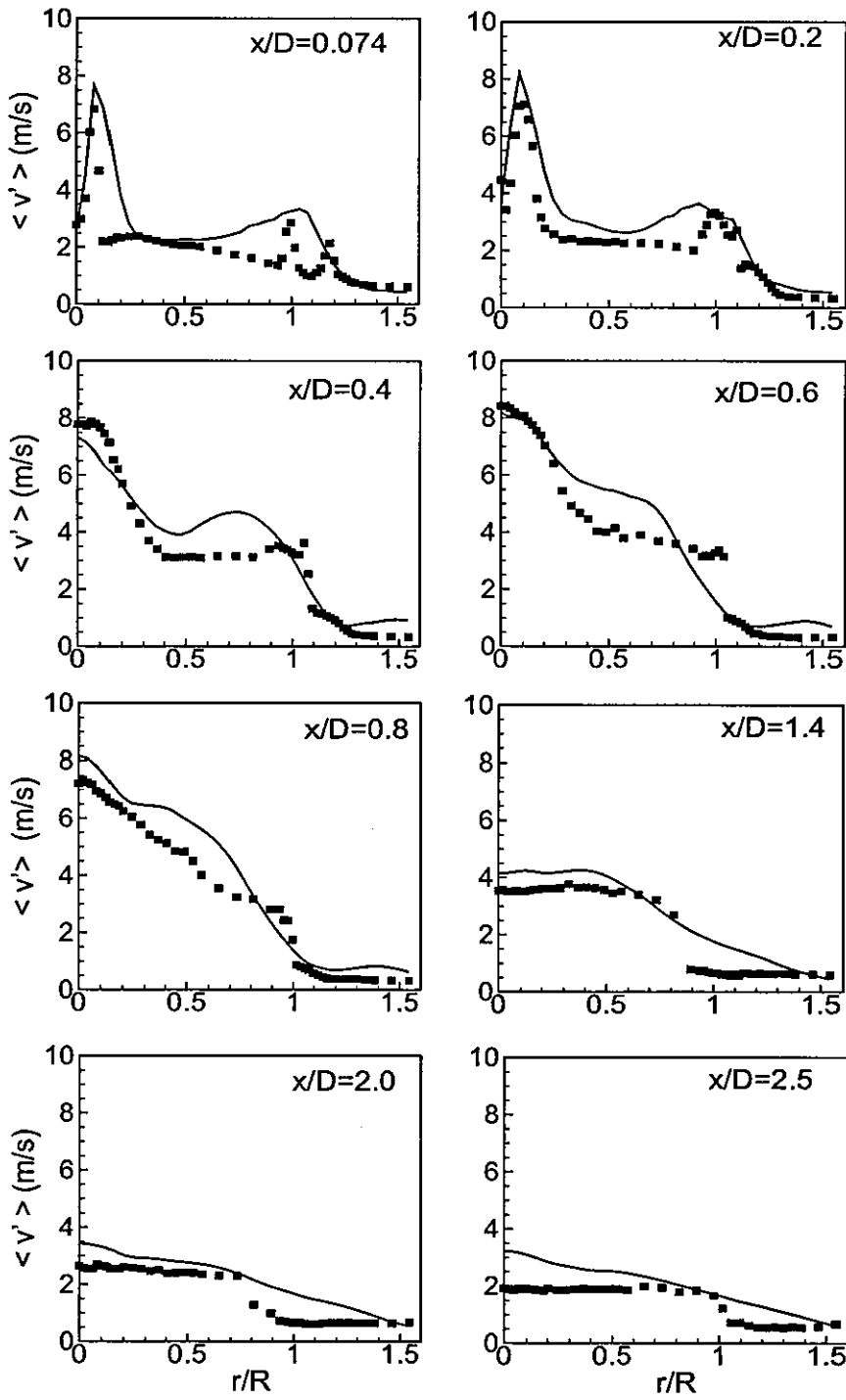


Figure 7.7: Radial profiles of RMS fluctuations of radial velocity in the N21S00, lines represent LES results and symbols represent experimental measurements.

## 7.6 Flow structures of the non-swirl case

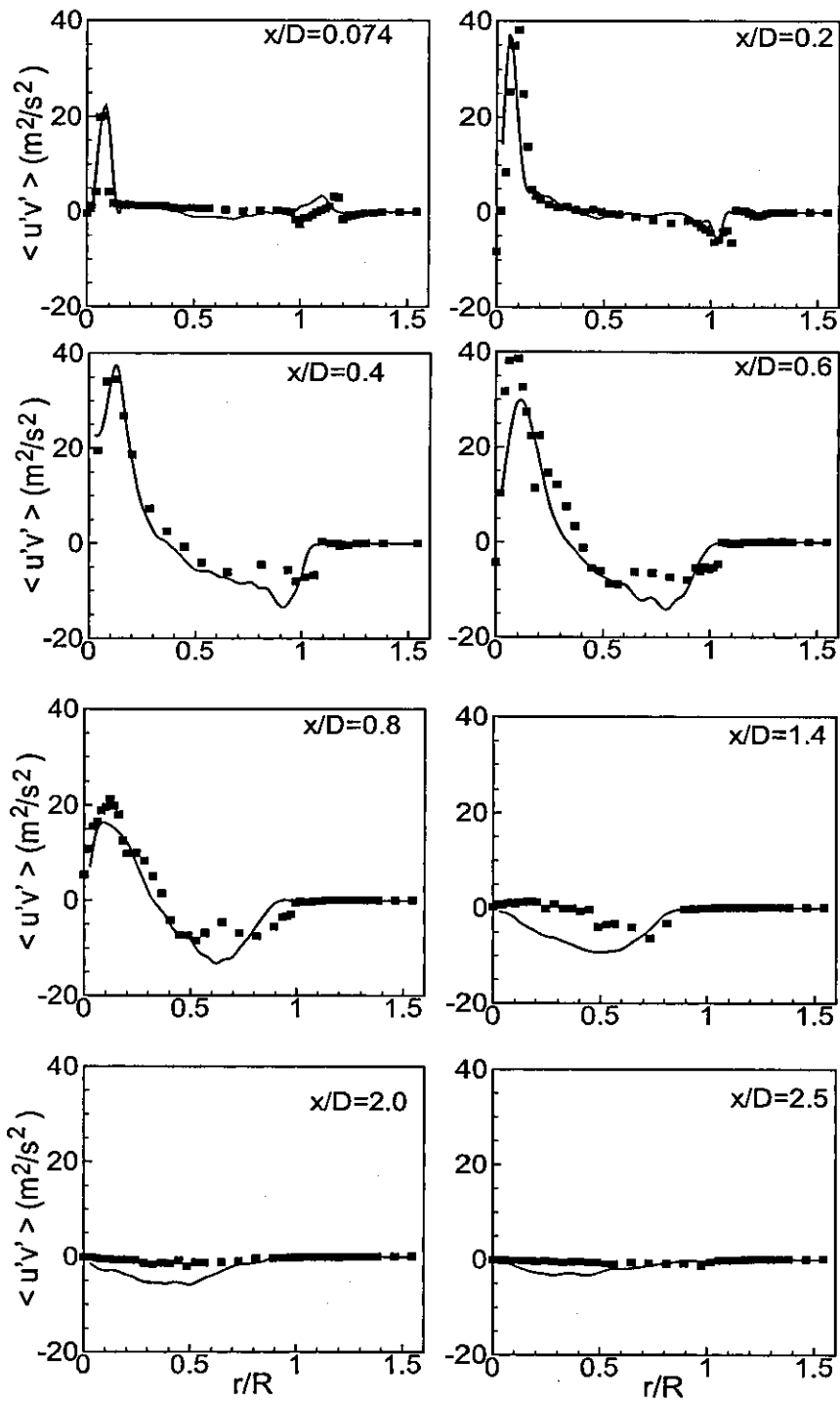


Figure 7.8: Radial profiles of Reynolds shear stress in the N21S00, lines represent LES results and symbols represent experimental measurements.

## 7.7 Flow structures of the medium-swirl case

Here the LES results for the medium swirl case N29S054, which has a swirl number of  $S = 0.54$  are presented. The streamlines generated from the mean velocity field of the medium swirl case are shown in Figure 7.9. Recirculation patterns seen in this case are different to pattern observed in Figure 7.3. The non-swirl flows stabilized on this burner showed only a single recirculation zone. With the addition of swirl, the flowfield can exhibit different flow structure. The addition of swirl forms more complex flow pattern involving the formation of a second recirculation zone, Al-Abdeli and Masri (2003a). This second zone, stabilizes further downstream of the burner face and takes on the shape of a closed, bubble shaped vortex. Such recirculating flow features are attributed to vortex breakdown.

In the upstream recirculation zone, two counter rotating vortices similar to the non-swirl case and one small vortex on the bluff body wall seen in Figure 7.9. However the flow inside the upstream recirculation zone is different to the non-swirl case as it is also affected by the primary annulus axial and swirling velocity. The size of the vortices inside the upstream recirculation zone is relatively smaller than those formed in the non-swirl case. As seen in Figure 7.9, the swirl induced downstream recirculation zone stagnates around the central axis away from the burner surface ( $x = 70 \text{ mm}$ ). This centreline recirculation zone leads to occurrence of the bubble type vortex breakdown. It is interesting to note that LES simulation captures both recirculation zones. The comparison of mean data shown in further figures described below confirm the success of LES simulations in predicting of recirculation and vortex breakdown.

Figure 7.10 shows the measured and computed mean axial velocity at different downstream positions. A positive to negative change in mean axial velocity indicates the development of recirculation regions. The first recirculation zone

## 7.7 Flow structures of the medium-swirl case

---

develops above the bluff body and stagnates at about  $x/D = 0.4$  from the burner exit plane. The computations show that the length of the bluff body wake is slightly underpredicted. As mentioned in introduction, swirl is often used to increase mixing rates and for flame stability. At sufficiently high level of swirl, the Vortex-Breakdown (VB) phenomenon is known to occur. The centreline negative axial velocity occurs at  $x = 70 \text{ mm}$  due to the vortex breakdown (VB). As can be seen in the near field of the inlet (Figure 7.10), the centreline velocity rapidly decays with increased distance downstream. Between  $1.1 < x/D < 2.0$ , the centreline velocity become negative and the flow stagnate.

The mean radial velocities are shown in Figure 7.11. Profiles at upstream locations capture the correct trend and sharp changes and the comparisons with data are reasonably good, especially the peaks at  $x/D = 0.136, 0.2$  have been correctly predicted. LES correctly predict the trend at  $x/D = 0.4$  and  $0.6$  but in the inner-region underpredicts peak values of radial velocity. Further downstream at  $x/D = 1.4, 2.0, 2.5$  radial velocity is overpredicted. However, data shows that at  $x/D = 2.0, 2.5$  the experimental mean radial velocity is about  $-5 \text{ m.s}^{-1}$  at the centreline. This means the flow has been constantly tilted towards one direction and there has been considerable asymmetry. The LES predictions, presented here, have been axi-symmetrically averaged in the calculation of mean values therefore a non zero value for the mean radial velocity is not expected at the centre line. The predictions therefore show zero radial velocity at the centre line at these locations (which is the correct mean). There are some concerns over experimental data for mean radial velocity at some axial positions  $x/D = 1.4, 2.0, 2.5$ .

Comparison of predicted and measured swirl velocity is shown in Figure 7.12. The agreement is generally good. Predictions compares well at locations  $x/D = 0.136, 0.2, 0.4, 1.4$  capturing the sharp changes and peak values. At locations

$x/D = 0.6, 0.8$  the trend is correctly predicted but the peak values are under predicted. Further downstream calculations show slight over predictions with increasing radial distance but overall agreement is reasonably good.

Figures 7.13-7.15 show comparison of measured and computed rms fluctuations of axial, radial and swirling velocities. The centreline rms axial velocity fluctuations are underpredicted at most of the axial locations. Although the predictions are in good agreement with experimental data along the radial direction. The agreement for rms radial velocity and rms swirling velocity are generally encouraging at almost all axial locations. The rms radial velocity slightly overpredicted at the outer shear layer of the upstream recirculation zone at  $x/D = 0.136, 0.2$ . Similar behavior is observed for the rms swirling velocity as well. Magnitudes and distribution of  $\langle u' \rangle$ ,  $\langle v' \rangle$  and  $\langle w' \rangle$  show significant anisotropy of turbulence inside the upstream and downstream recirculation zones and LES computations have been successful in predicting the trends as well as profiles. Figures 7.16-7.17 show Reynolds stresses  $\langle u'v' \rangle$  and  $\langle u'w' \rangle$ . Given the complexity of the flow LES predicted Reynolds stresses show good agreement, particularly the calculations seems to capture the sharp changes in Reynolds stresses reasonably well. While the mean velocities are quite low inside the vortex bubble, the root mean square (rms) fluctuations remain relatively high in comparison. This is especially true along the boundary of the vortex bubble. Wang and Rusak (1997) concluded that the impact of rms velocity fluctuations on the dynamics of the flow field is consistent with experimental studies of unconfined swirling flows. The rms fluctuations on the boundary of the vortex bubble remain relatively high compared to the local mean velocity. For this case, the overall LES predictions are in reasonably good agreement with the experimental data and the vortex breakdown found to be well predicted.

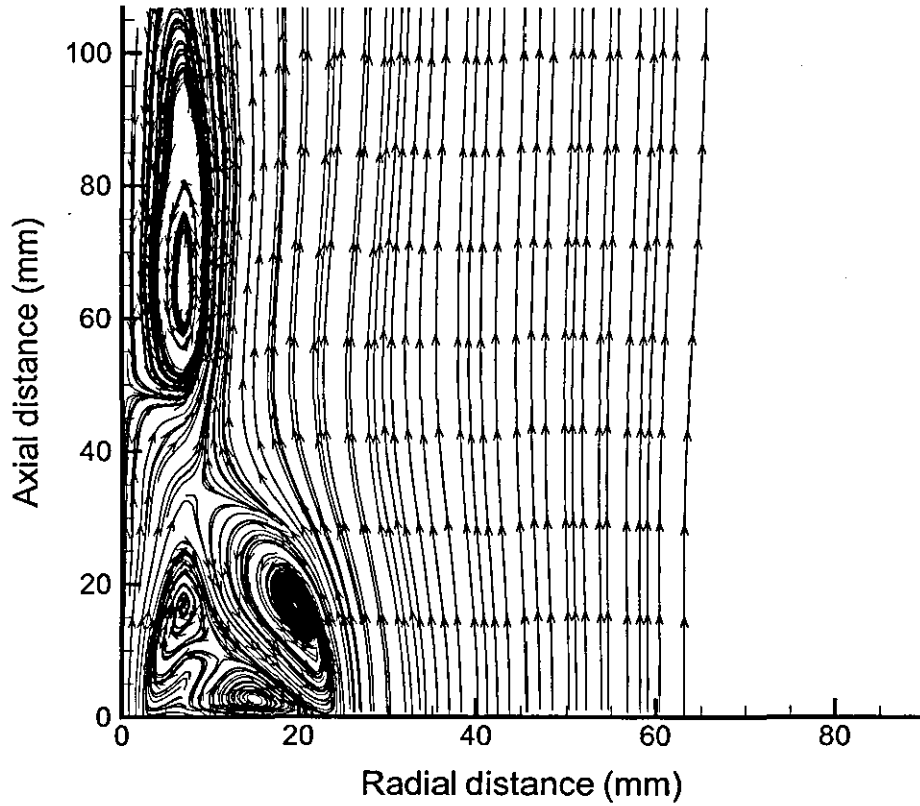


Figure 7.9: Streamlines generated from the mean velocity field of the medium-swirl case obtained from LES calculation.

### 7.7 Flow structures of the medium-swirl case

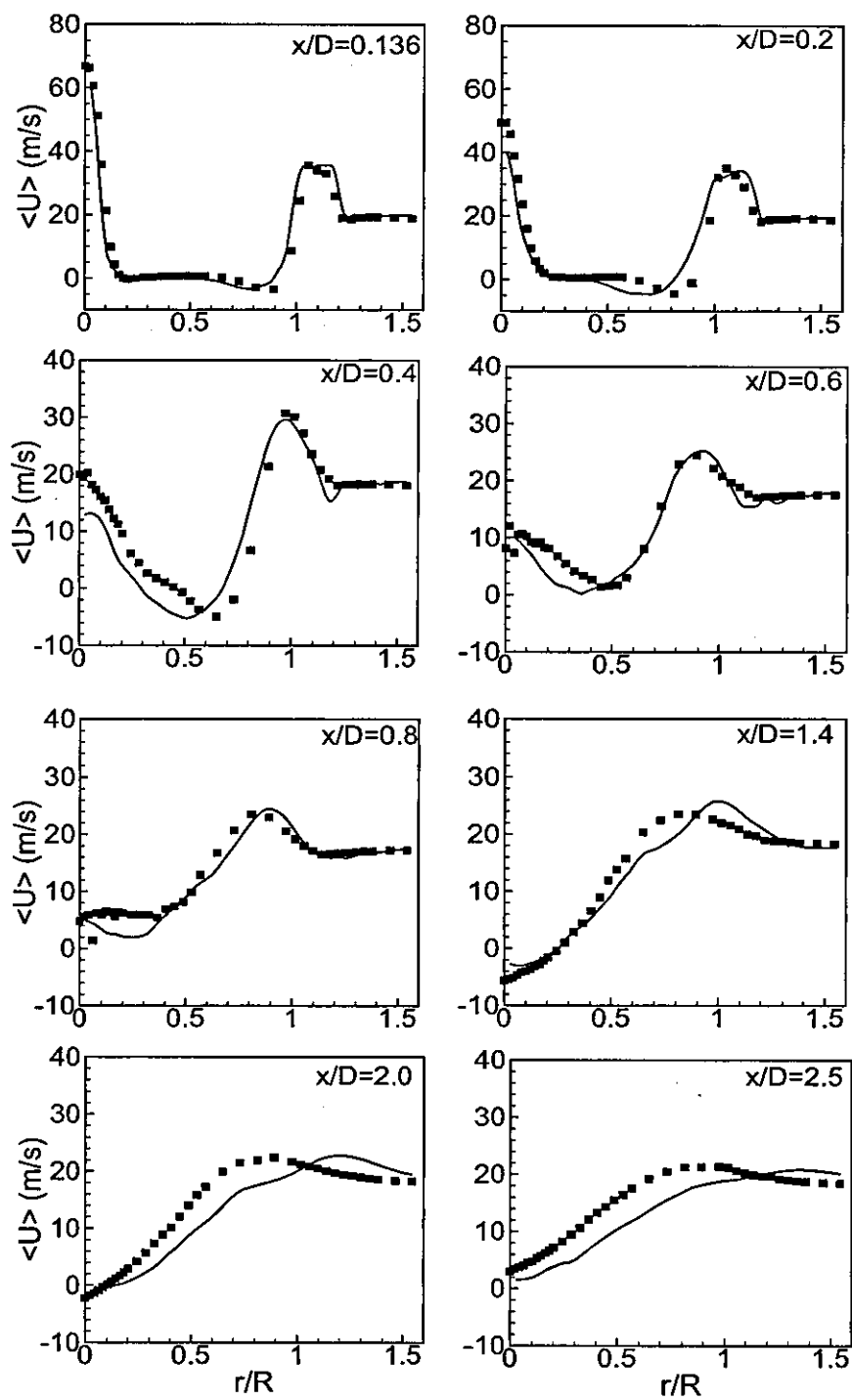


Figure 7.10: Radial profiles of mean axial velocity in the N29S054, lines represent LES results and symbols represent experimental measurements.

### 7.7 Flow structures of the medium-swirl case

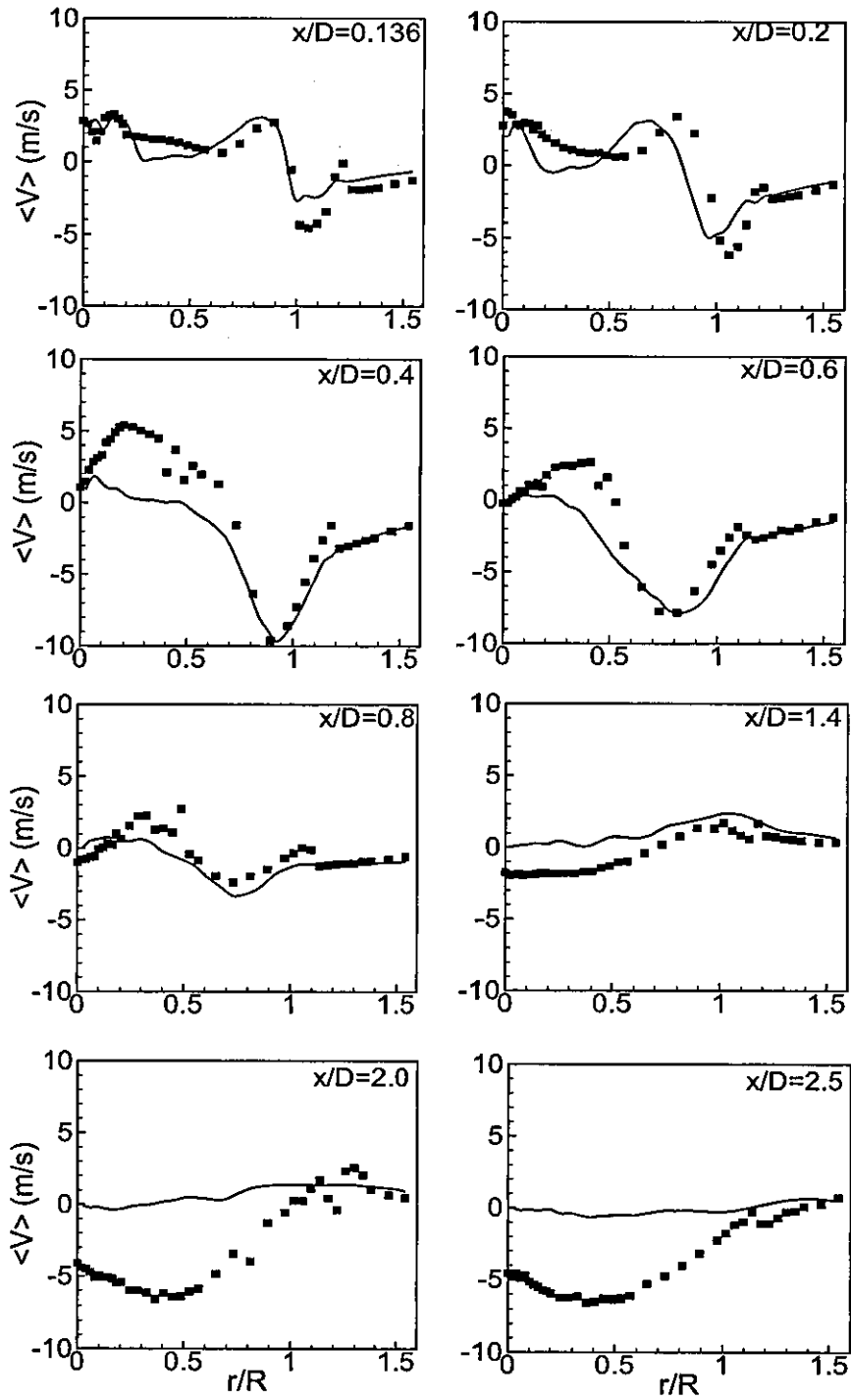


Figure 7.11: Radial profiles of mean radial velocity in the N29S054, lines represent LES results and symbols represent experimental measurements.

7.7 Flow structures of the medium-swirl case

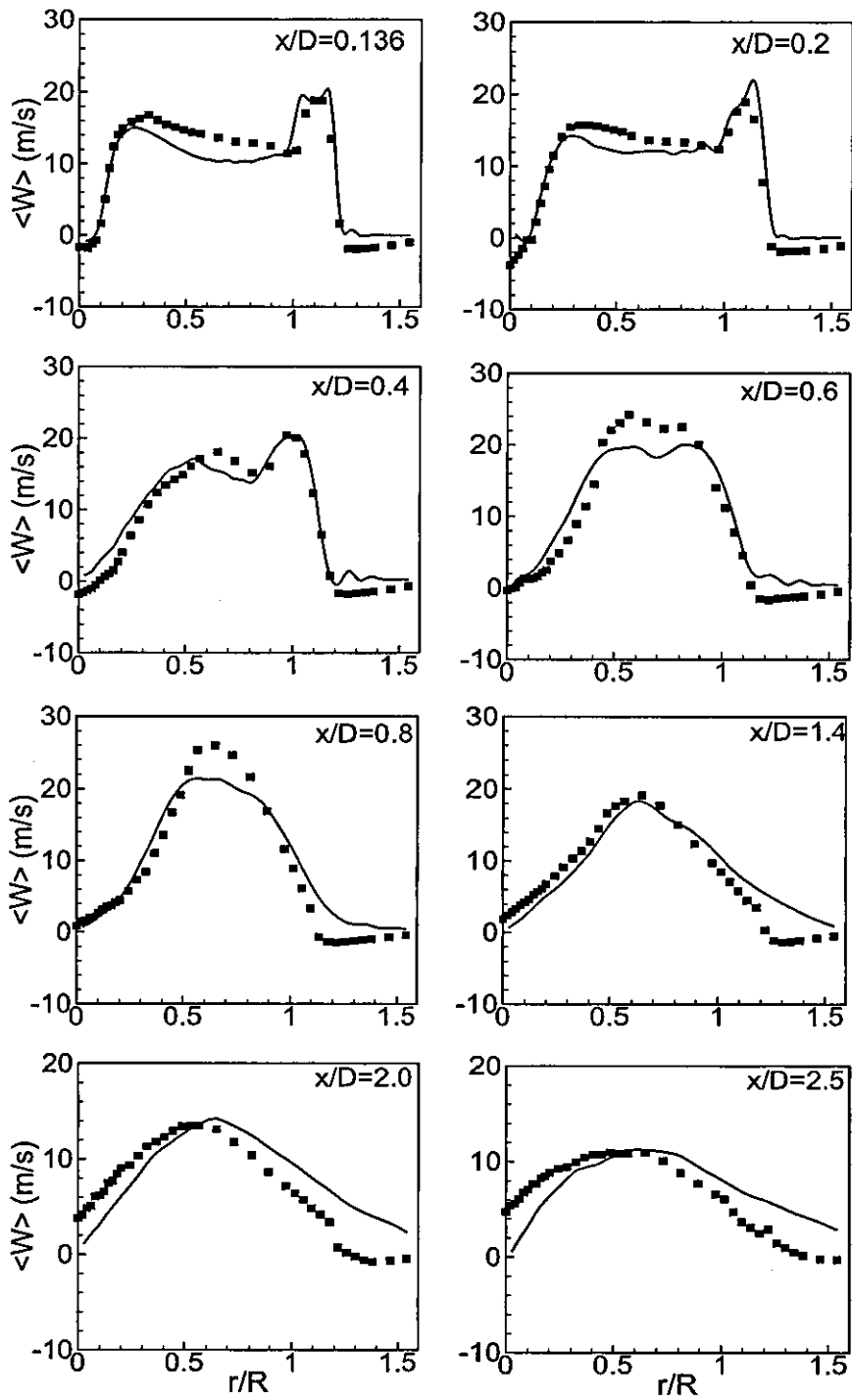


Figure 7.12: Radial profiles of mean swirling velocity in the N29S054, lines represent LES results and symbols represent experimental measurements.

## 7.7 Flow structures of the medium-swirl case

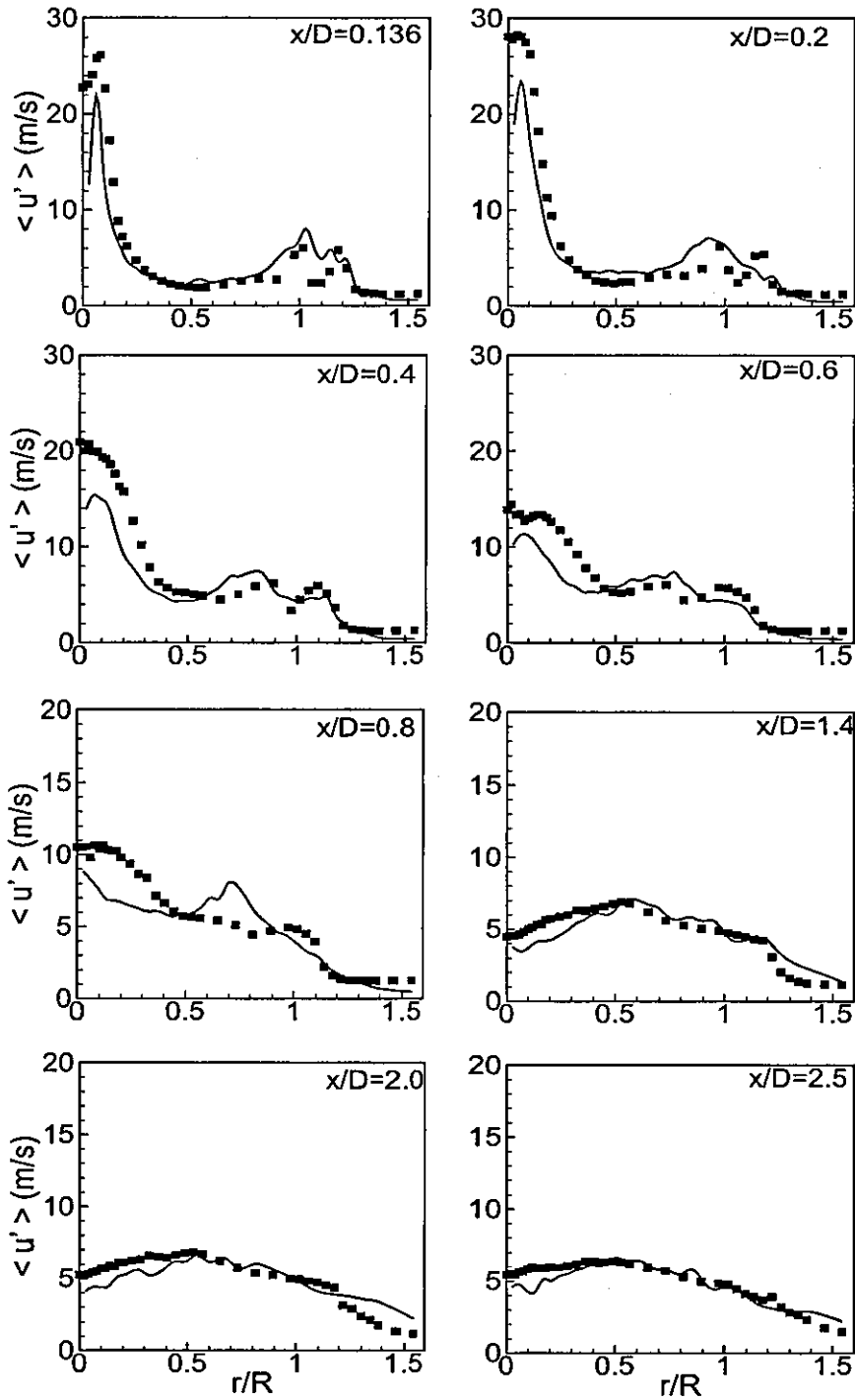


Figure 7.13: Radial profiles of RMS fluctuations of axial velocity in the N29S054, lines represent LES results and symbols represent experimental measurements.

### 7.7 Flow structures of the medium-swirl case

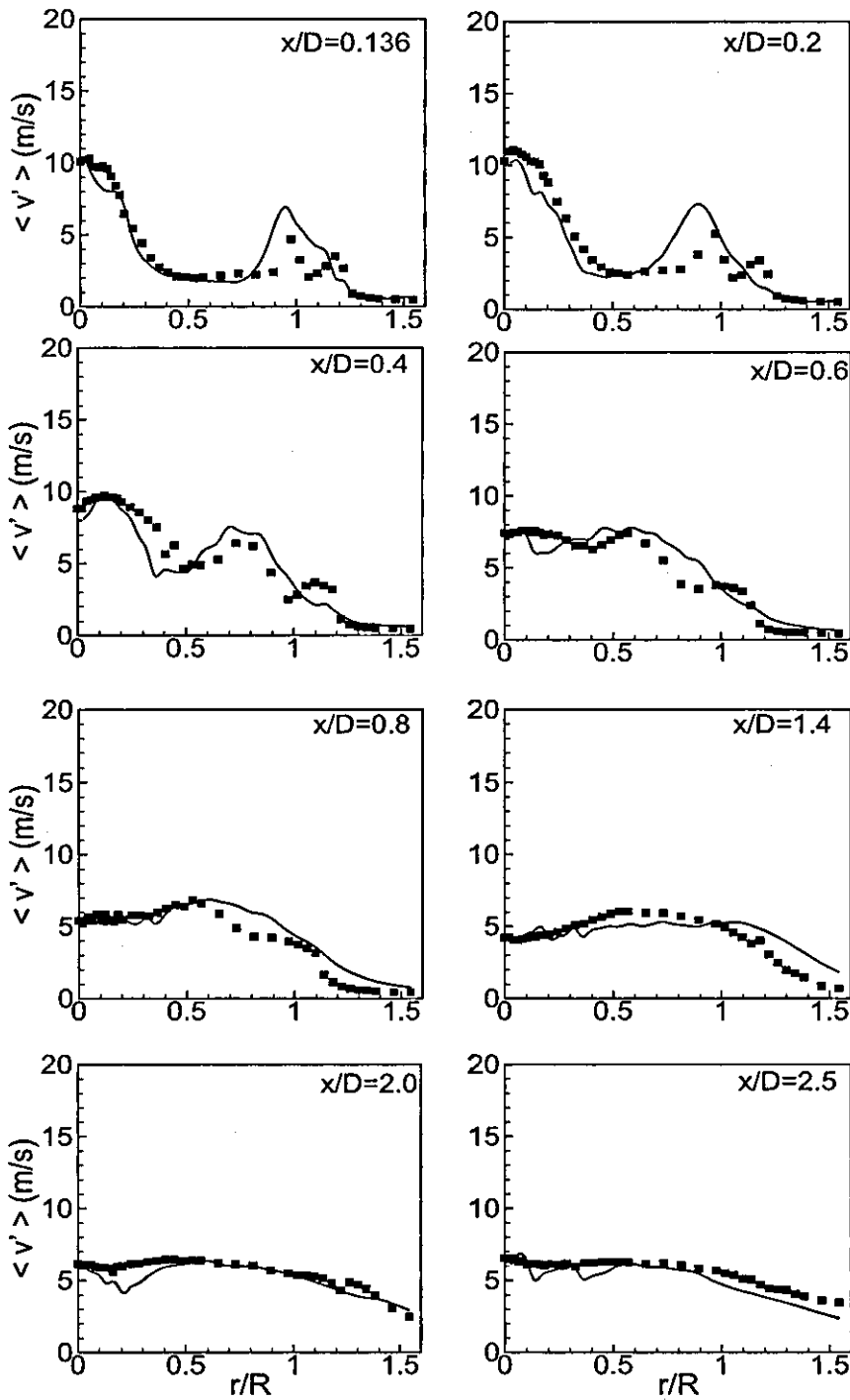


Figure 7.14: Radial profiles of RMS fluctuations of radial velocity in the N29S054, lines represent LES results and symbols represent experimental measurements.

### 7.7 Flow structures of the medium-swirl case

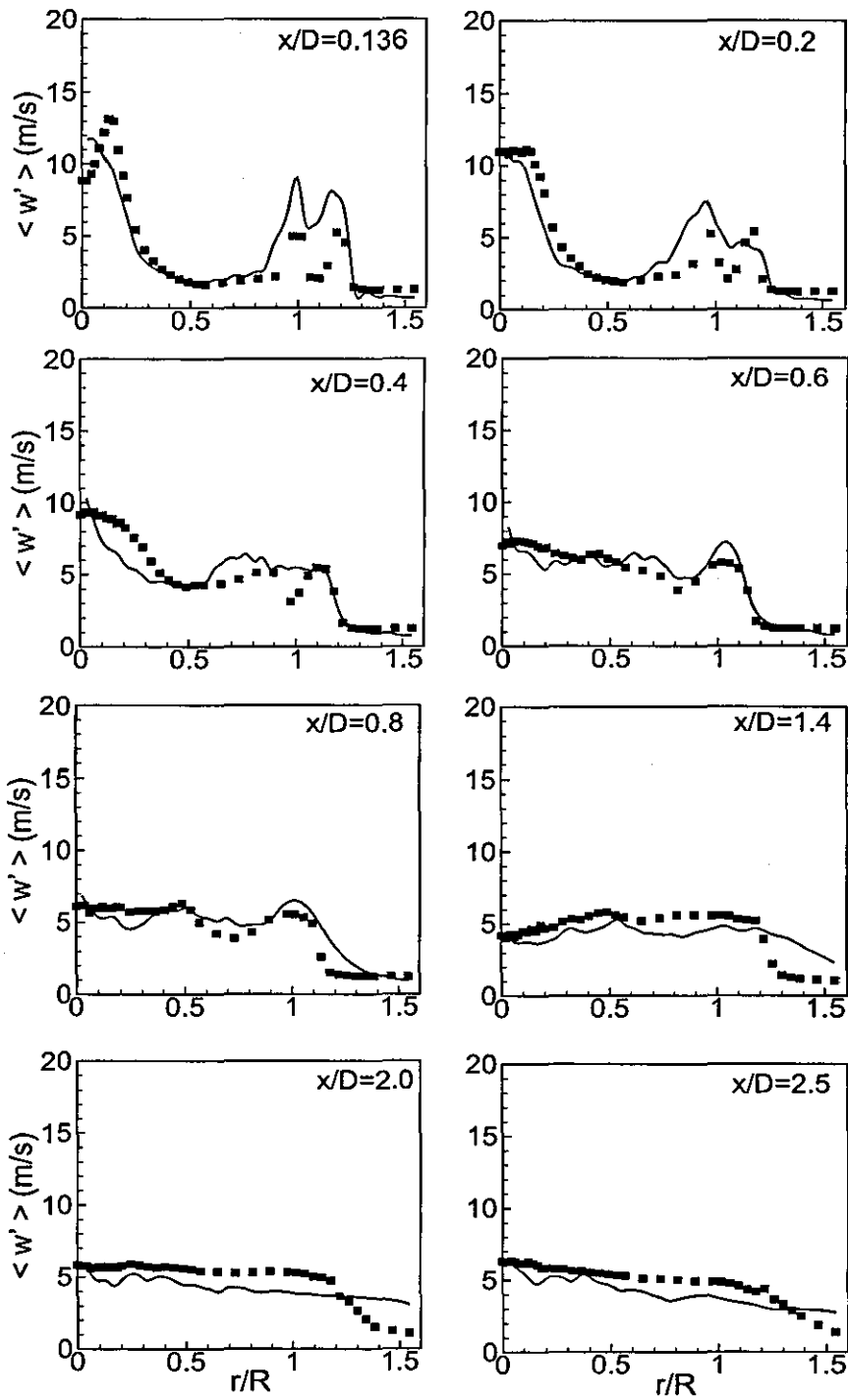


Figure 7.15: Radial profiles of RMS fluctuations of swirling velocity in the N29S054, lines represent LES results and symbols represent experimental measurements.

### 7.7 Flow structures of the medium-swirl case

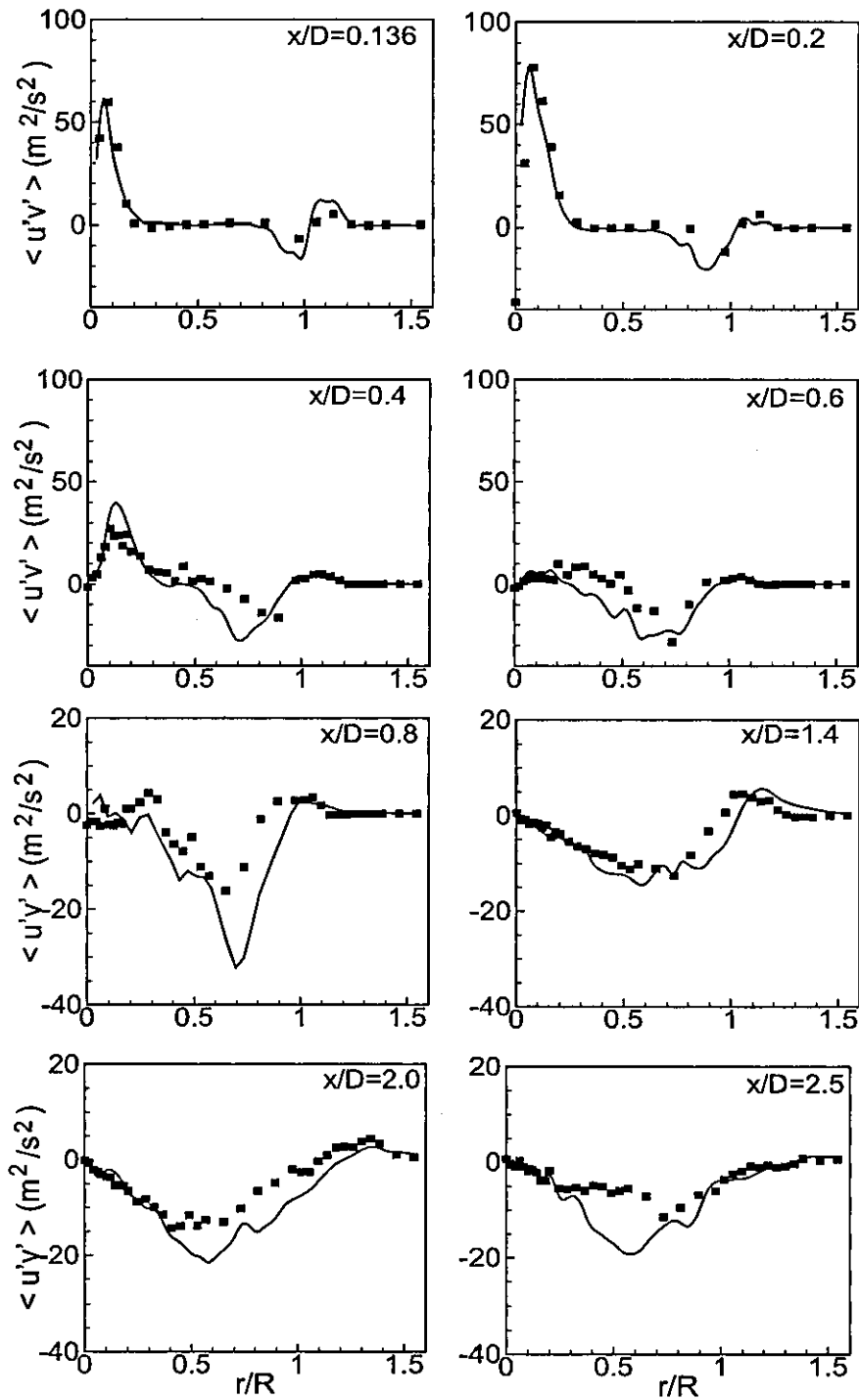


Figure 7.16: Radial profiles of Reynolds shear stress in the N29S054, lines represent LES results and symbols represent experimental measurements.

### 7.7 Flow structures of the medium-swirl case

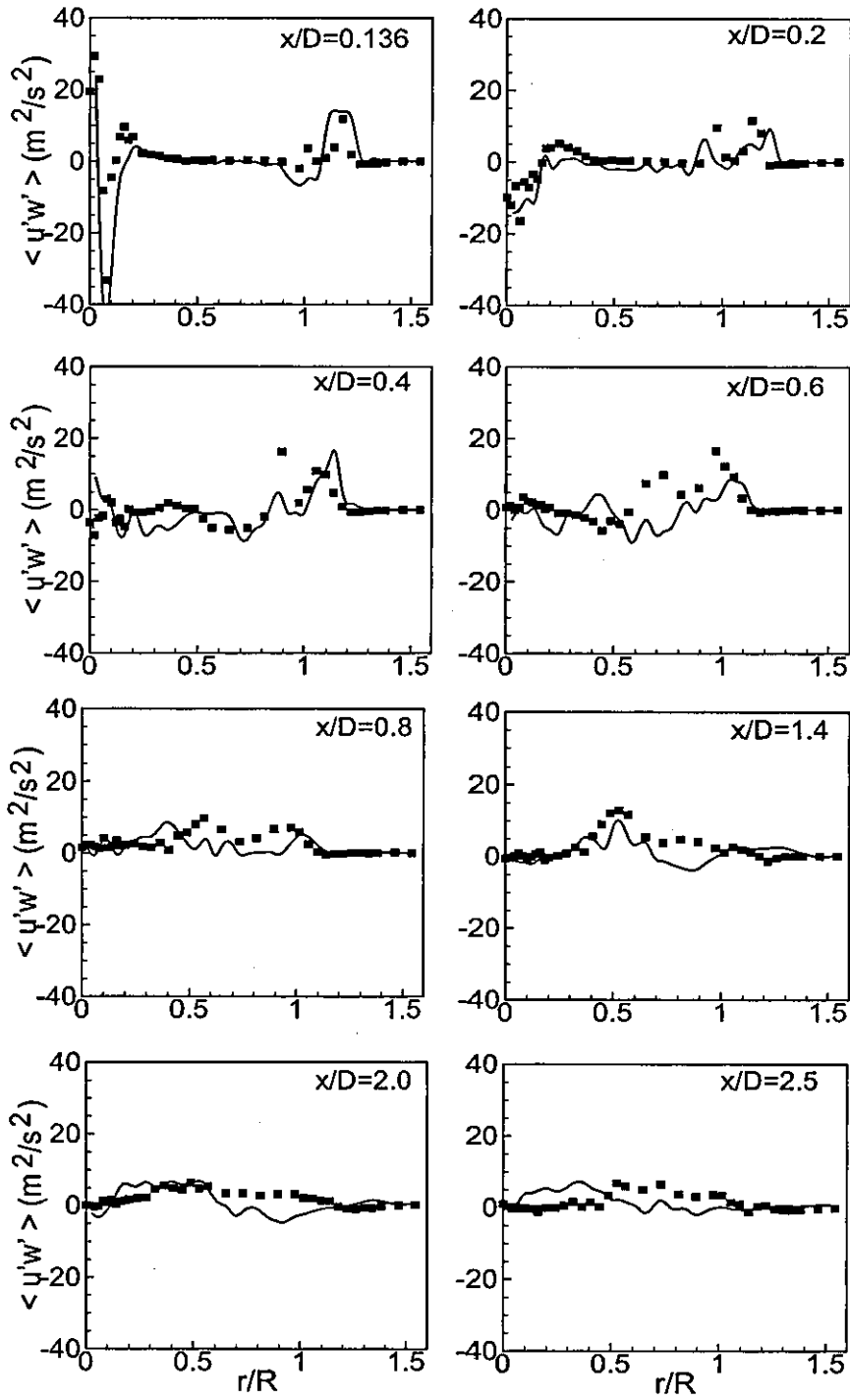


Figure 7.17: Radial profiles of Reynolds shear stress in the N29S054, lines represent LES results and symbols represent experimental measurements.

## 7.8 Flow structures of the high-swirl case

The highest swirl number case  $S = 1.59$  of set of experiments is perceived to be the most difficult case to predict. The tangential velocity components at inlet are high in this case, and as a result turbulence anisotropy is considerably high.

The streamlines corresponding to mean velocity field taken from LES predictions are shown in Figure 7.18. In comparison to Figure 7.3 and Figure 7.9 the recirculation patterns are now completely different. The high swirl causes the flow to spread radially creating a lengthy recirculation zone, which extends towards axially down the centreline up to  $x = 90 \text{ mm}$  from the burner exist plane. In the recirculation zone three different vortices are formed at the axial distance of  $x = 20, 30, 80 \text{ mm}$  corresponding to the radial distance of  $r = 10, 20 \text{ mm}$ .

The axial and radial spread of the upstream bluff body stabilized recirculation zone is much wider than that found in the non-swirl case. The sizes of the two vortices formed near to the bluff body are different to those found in the non-swirl and medium-swirl cases. The sizes of the two counter rotating vortices are relatively the same, and the axial and swirling velocities of the primary annulus play a major role in generating the vortices above the bluff body. However, the case N16S159 with highest swirl number (1.59) shows that using high swirl alone is insufficient for inducing downstream recirculation. The prediction shows the occurrence of small vortex in further downstream ( $x = 80 \text{ mm}$ ), which has also been observed experimentally by Al-Abdeli and Masri (2003a). The central jet of the high swirl case decays faster than other two cases (non-swirl and medium swirl) and the values of the centreline velocity are almost zero at  $x = 80 \text{ mm}$ . Unlike N29S054 case, N16S159 has no downstream recirculation or vortex breakdown despite having a large swirl number. It is worth noting here that N29S054, which has downstream recirculation, had the highest value of primary annulus axial ve-

## 7.8 Flow structures of the high-swirl case

locity compared to highest swirl number case lacking downstream recirculation. As mentioned earlier, this behaviour gives more evidence that the higher axial velocity of the primary annulus is the key factor for downstream recirculation.

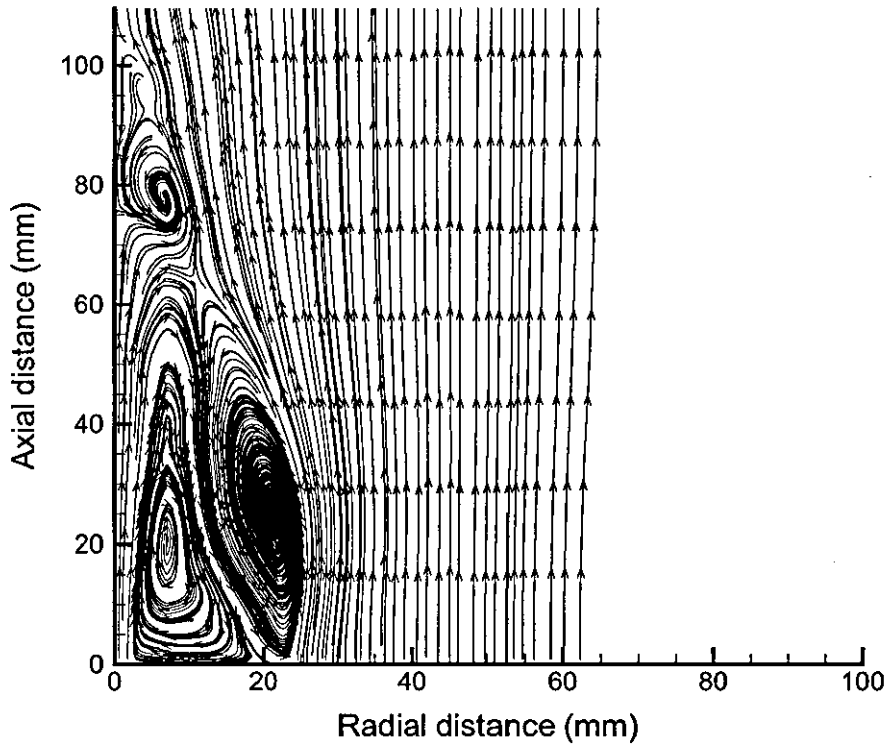


Figure 7.18: Streamlines generated from the mean velocity field of the high-swirl case obtained from LES calculation.

Figure 7.19 shows the mean axial velocity profiles at different axial locations. The comparison for the mean axial velocity is very good at all downstream axial locations. In this case, the mean axial velocity along the centreline does not reach negative values. Due to the interaction of the two incoming jets, the recirculation region moves to the centreline, where the two high swirl jets meet. As shown

in Figure 7.18, the center fluid is forced to move outward as a result of the centrifugal force generated by the swirling motion. This decreases the axial velocity in the inner part near the axis and increases in the outer part. Additionally the sudden expansion at the wall introduces another axial velocity declaration and these two affects cause to form the recirculation zone. Along the axial direction downstream, the axial and swirling velocity profiles become smoother as a result of the non-existence of downstream recirculation. At  $x/D = 1.4, 2.0, 2.5$  axial velocity component is much lower than the upstream values. This is a result of the high spreading rate of momentum in swirling flows. High spreading rate is an important property in swirling flows.

The predictions of the mean radial velocity which is small in magnitude show some notable under predictions at  $x/D = 0.6$  and  $x/D = 0.8$  (Figure 7.20). The mean swirling velocity (Figure 7.21) predictions do not capture the peak values appearing on the outer shear layer at  $x/D = 0.2, 0.4$ . The radial spread of the swirling velocity has slight variation in the region  $r/R = 0.5 - 1.0$  at the axial locations  $x/D = 0.4, 0.6, 0.8$ . In this case the flow field forms a strongly rotating, non-recirculating collar-like zone of air having peak mean swirling velocity of  $\langle W \rangle = 13 \text{ m.s}^{-1}$ . The rms of swirling velocity is also increased in this region. The maximum value of the mean swirling velocity occurs directly above the burner annulus. However the formation of the collar-like flow feature in this flow is more upstream compared to N29S054. The overall agreement is quite good for the mean swirling velocity for highest swirl number case, which is believed to be much difficult to predict in a complex flow field.

Figure 7.22 shows axial velocity fluctuations (rms). The predictions are in good agreement with experimental measurements. However, the predictions fail to capture the peak fluctuations on the outer shear layer  $x/D = 0.4, 0.8$  ( $r/R = 1.2$ ).

## 7.8 Flow structures of the high-swirl case

---

The radial velocity fluctuation is slightly overpredicted at  $x/D = 0.2$  ( $r/R = 1.2$ ) and underpredicted at  $x/D = 0.6$  ( $r/R = 0.5$ ). The overall comparison for the rms radial velocity is arguably satisfactory. In Figure 7.24, the swirling velocity fluctuation is plotted. It is noted that the LES predictions well captured the peaks of the fluctuation, which formed due to the shear layer in the flow field. However, it is worth to note that the rms swirling velocity is slightly underpredicted at last three axial locations,  $x/D = 1.4, 2.0, 2.5$ . LES calculations show highly varying nature of Reynolds stresses along the radial direction. The stresses are highest near the jet and annulus area (Figures 7.25-7.26). These stresses continue to diminish in magnitude further downstream in the flow. Near burner predictions are very good. Further down stream experimental data does not show the degree of variation seen in the predictions. The magnitude of predicted Reynolds stresses agrees with experimental values. The variations in predictions could be due to the high swirl number and the complexity of the turbulence flow field. Given that this case has a high swirl number and hence the flow features are complex, overall LES results appear to capture all important flow features reasonably well.

In all three cases considered in this study LES appears to produce good predictions. It is to be noted that LES has successfully predicted mean velocities, their fluctuations and Reynolds stresses in a range of swirling flows. With this success in predicting isothermal cases considered in this study, the next step is to model reacting cases to predict combustions flows in this burner configuration where data is available for species concentrations, temperature and other important parameters such as mixture fraction and mixture fraction variance. This forms the next chapter. Also present success with LES of isothermal flows allow carrying evaluation of performance of LES based combustion model with the confidence that turbulence is reasonably well reproduced.

## 7.8 Flow structures of the high-swirl case

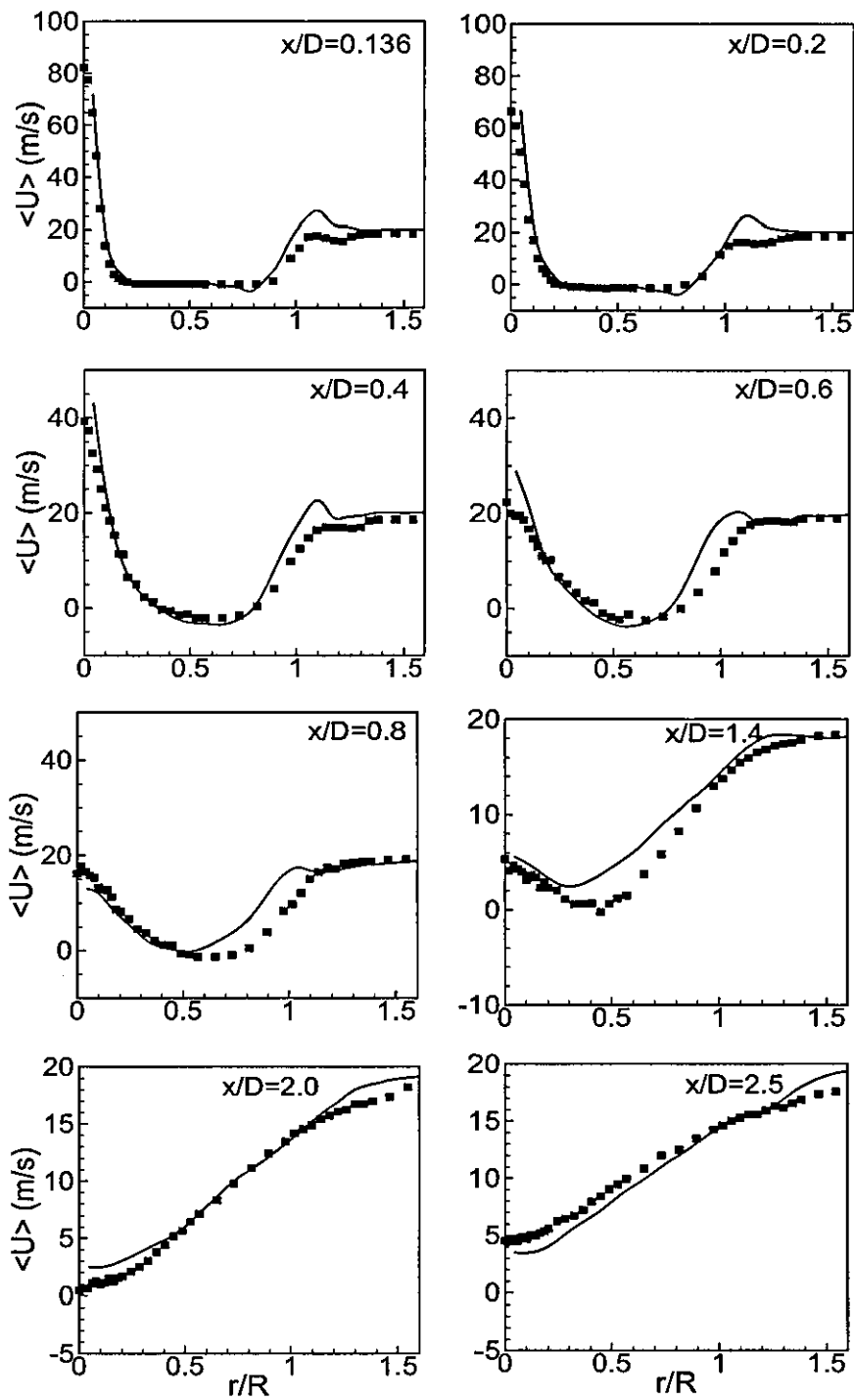


Figure 7.19: Radial profiles of mean axial velocity in the N16S159, lines represent LES results and symbols represent experimental measurements.

## 7.8 Flow structures of the high-swirl case

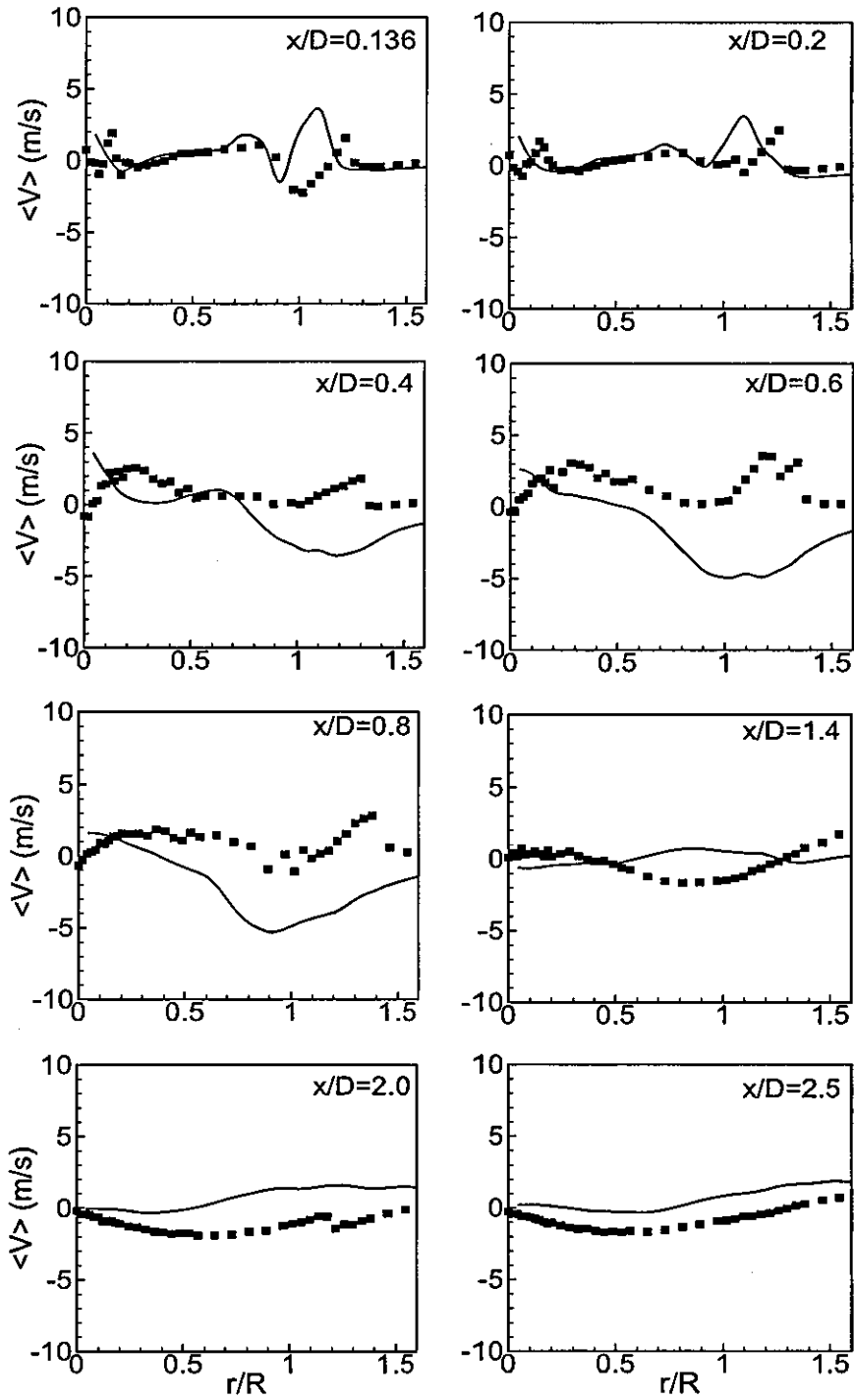


Figure 7.20: Radial profiles of mean radial velocity in the N16S159, lines represent LES results and symbols represent experimental measurements.

## 7.8 Flow structures of the high-swirl case

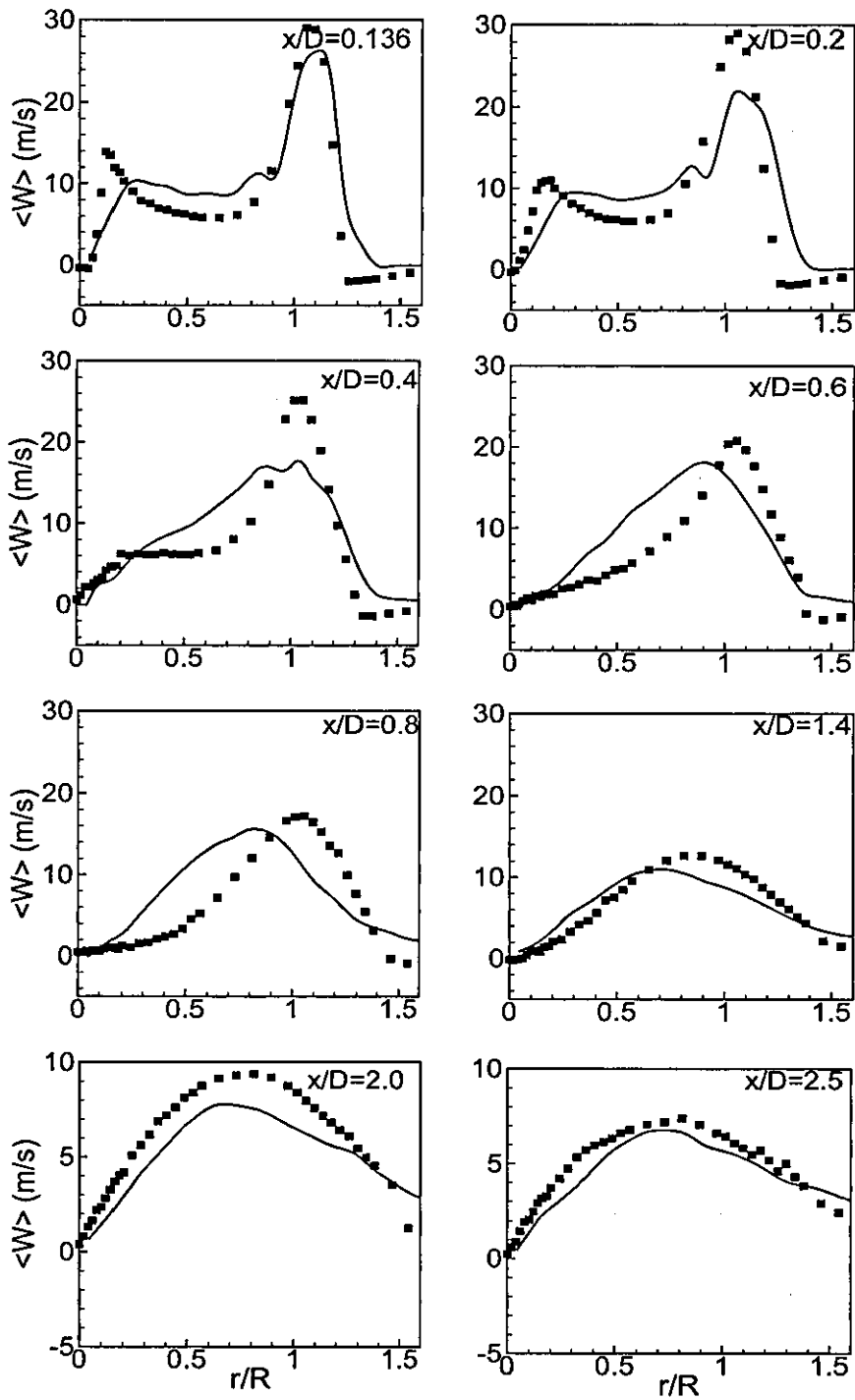


Figure 7.21: Radial profiles of mean swirling velocity in the N16S159, lines represent LES results and symbols represent experimental measurements.

## 7.8 Flow structures of the high-swirl case

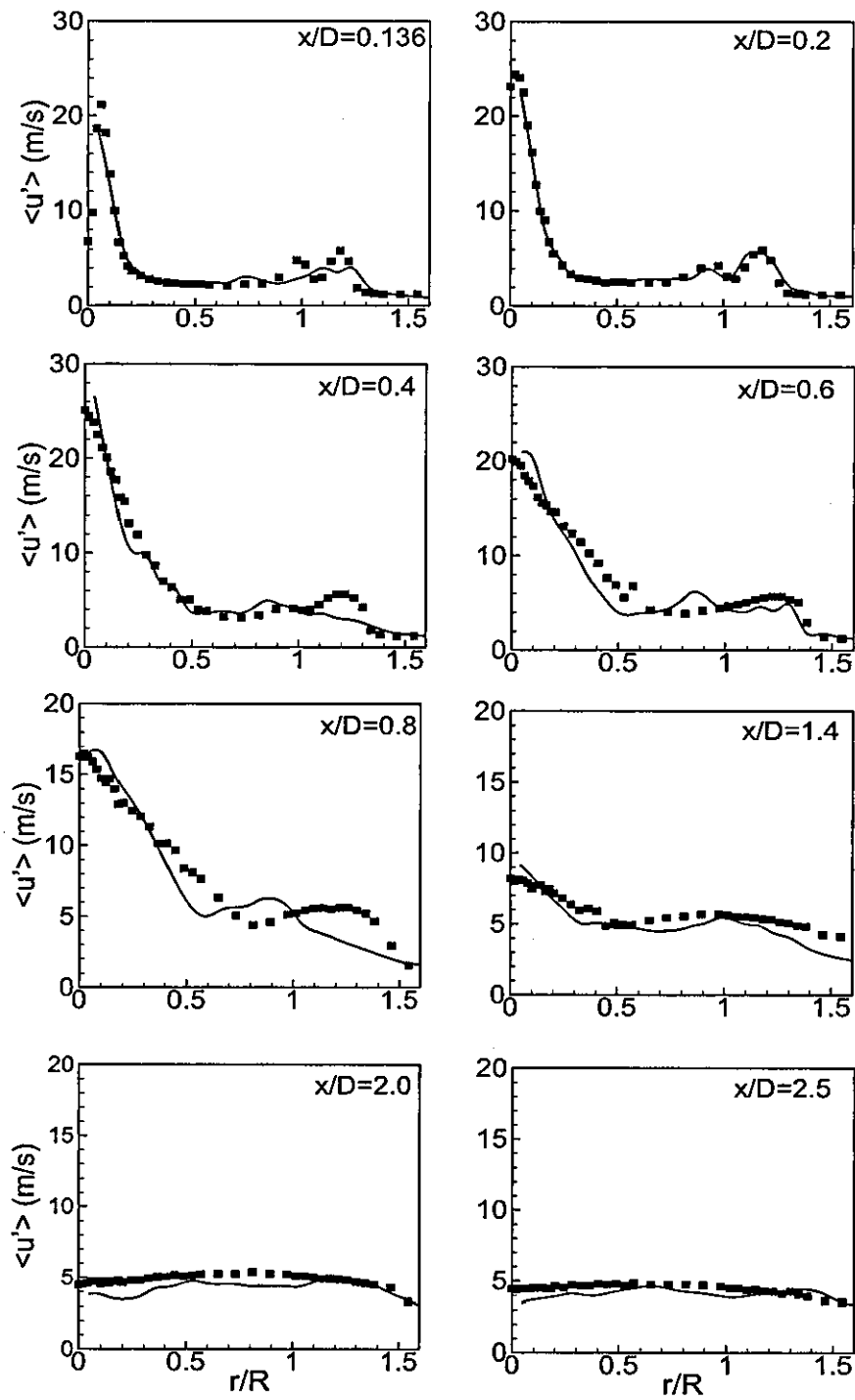


Figure 7.22: Radial profiles of RMS fluctuations of axial velocity in the N16S159, lines represent LES results and symbols represent experimental measurements.

## 7.8 Flow structures of the high-swirl case

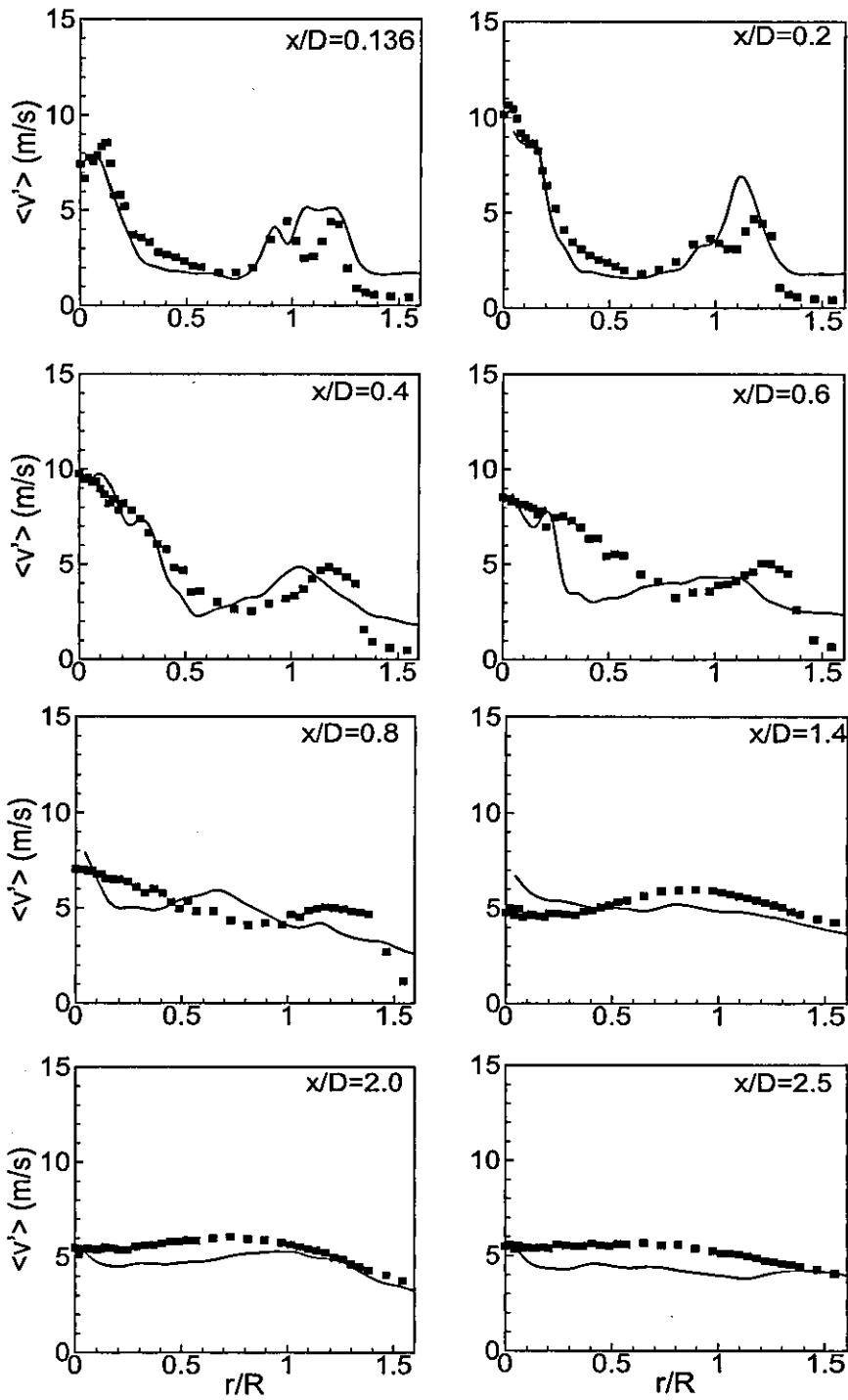


Figure 7.23: Radial profiles of RMS fluctuations of radial velocity in the N16S159, lines represent LES results and symbols represent experimental measurements.

## 7.8 Flow structures of the high-swirl case

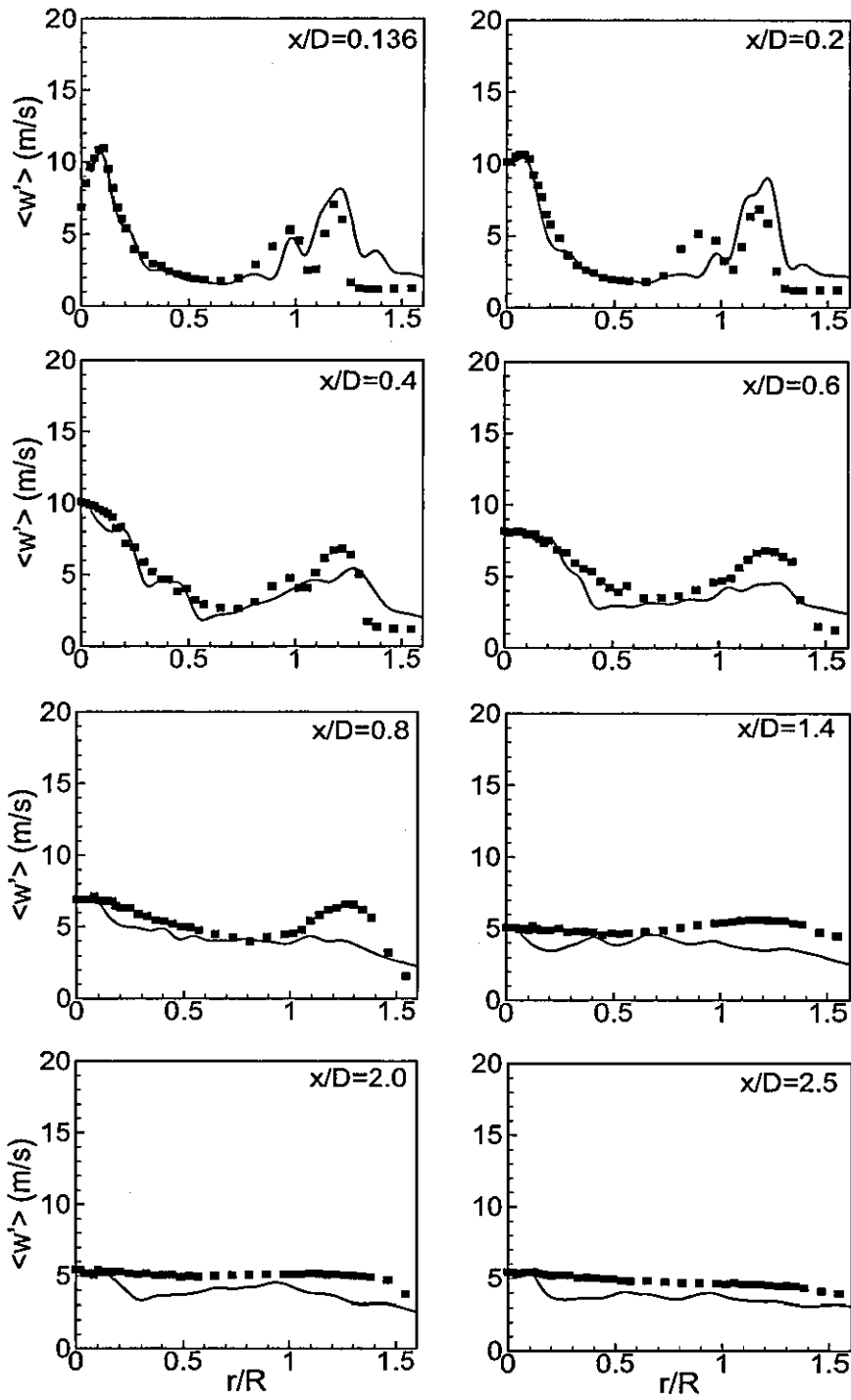


Figure 7.24: Radial profiles of RMS fluctuations of swirling velocity in the N16S159, lines represent LES results and symbols represent experimental measurements.

## 7.8 Flow structures of the high-swirl case

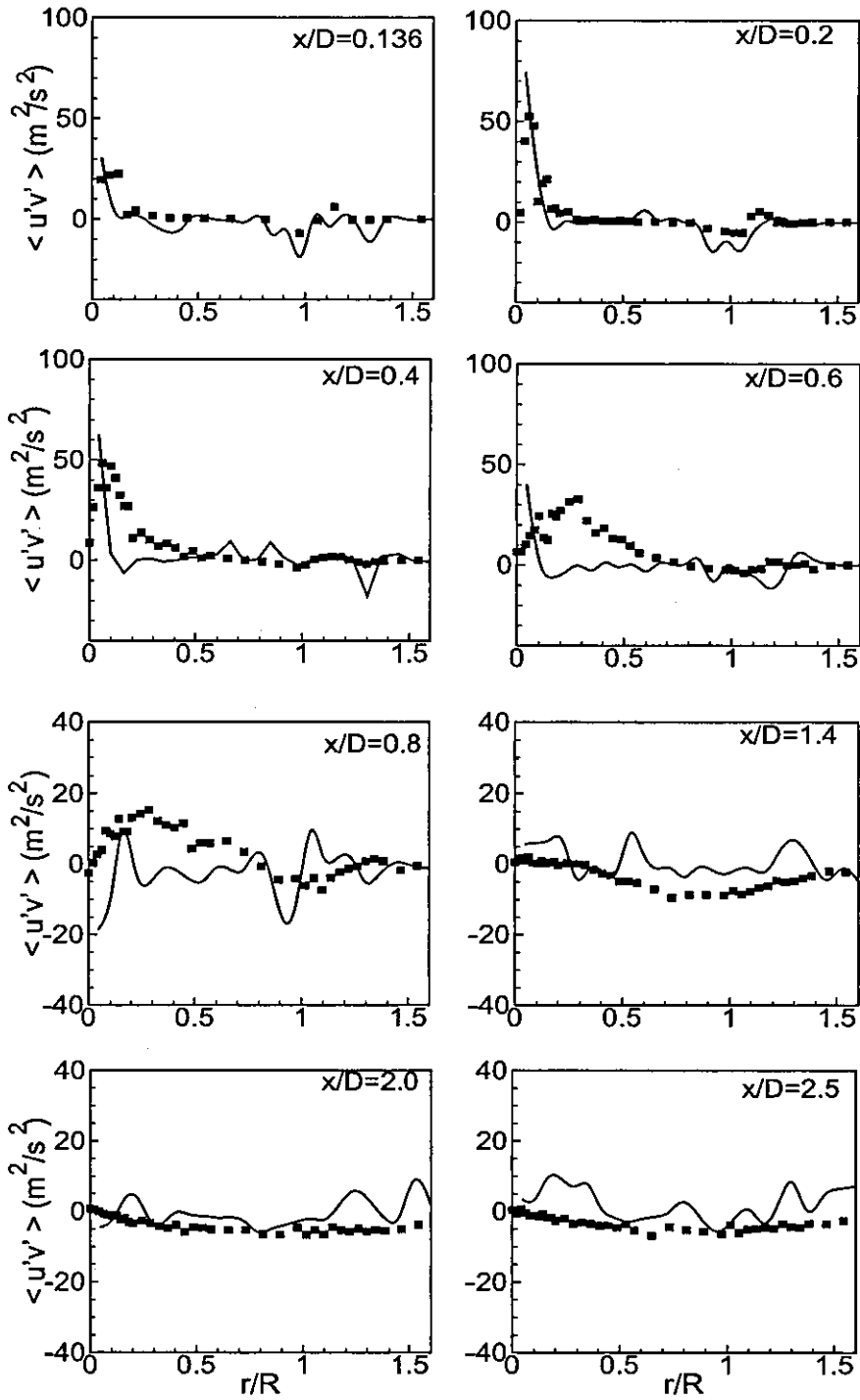


Figure 7.25: Radial profiles of Reynolds shear stress in the N16S159, lines represent LES results and symbols represent experimental measurements.

## 7.8 Flow structures of the high-swirl case

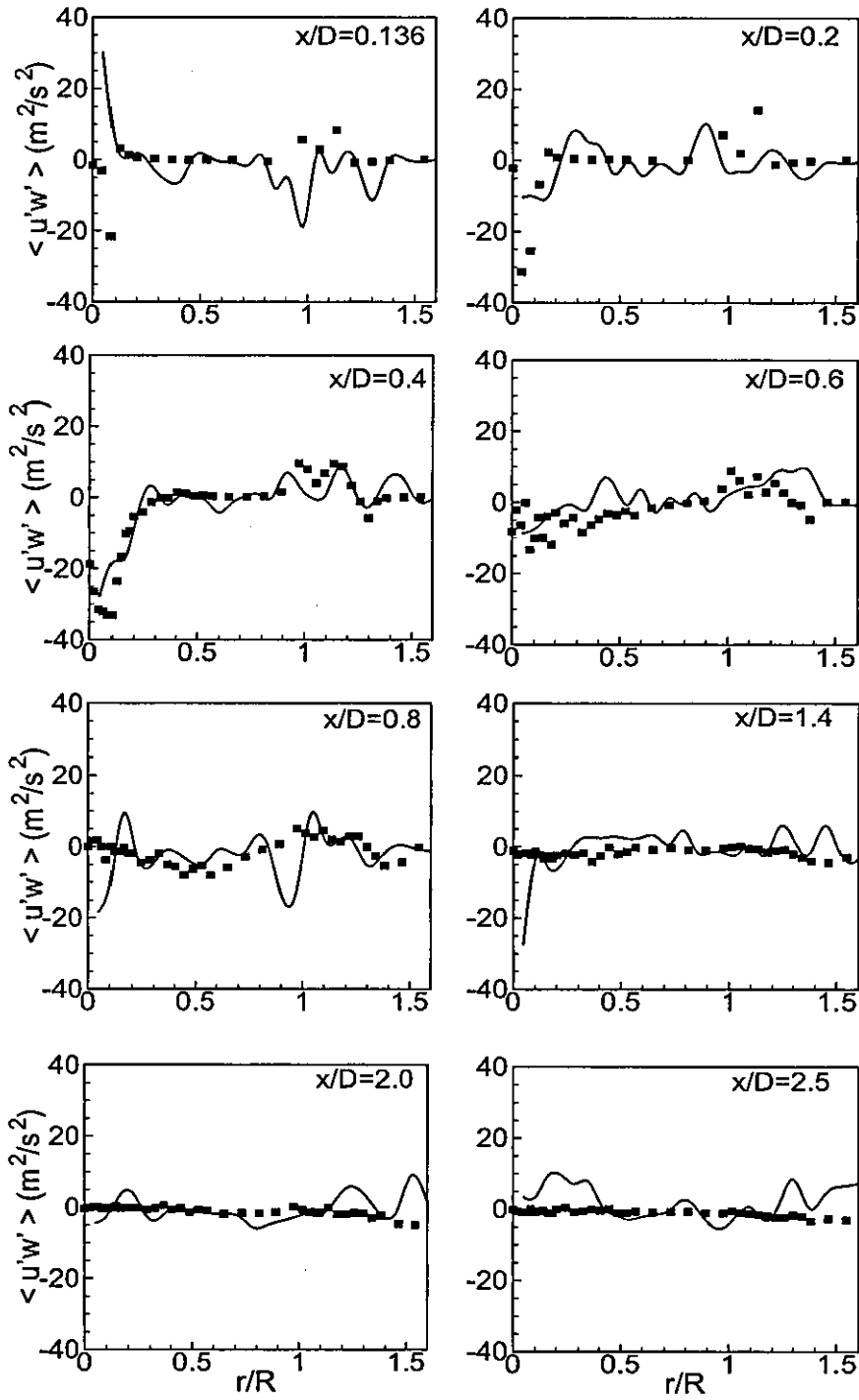


Figure 7.26: Radial profiles of Reynolds shear stress in the N16S159, lines represent LES results and symbols represent experimental measurements.

## 7.9 Vortex breakdown and recirculation

This section discusses the phenomenon of vortex breakdown (VB) in the medium swirl case (N29S054). Figures 7.27 and 7.28 show the instantaneous streamlines and velocity vector field of the cross section at 70 mm above from the burner exit plane obtained from LES calculation taken at time  $t = 30$  ms. Figures 7.27 also shows the filtered axial velocity of the cross section (colour contour), which involves the negative values as a result of the vortex breakdown.

The two plots show the formation of the low velocity region around the central axis. The low velocity region leads to forms the bubble type vortex breakdown around the central axis. Vortex breakdown has been defined as an abrupt flow transition with a free stagnation point/region on the axis followed by a reverse flow and a fully turbulent region. Especially the streamlines in the near axis core region show flow reversal generated by the recirculation zones as a result of the vortex breakdown. Even in the upstream near to the bluff body the shear layer instability evolves between the fuel jet and air annulus as well as air annulus and co-flow (Figure 7.29). These instability vortices are rapidly convected away by the mean flow. Additionally these vortices grow stronger when a vortex ring pass by from upstream, and became weak or even disappear as the vortex ring propagate further downstream. Small-scale random turbulence grow in the shear layer and flow becomes more turbulent as a result of the swirl velocity.

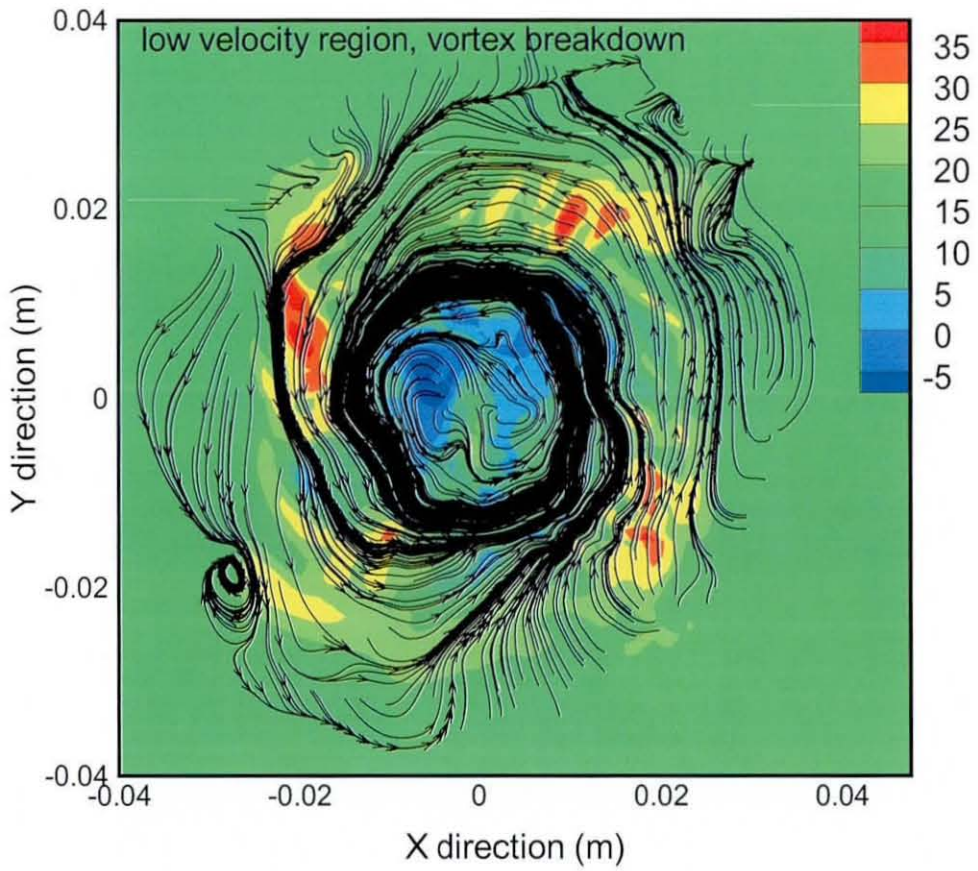


Figure 7.27: Instantaneous streamlines of the medium-swirl case on XY plane at  $z=70\text{mm}$  at  $t=30\text{ms}$ .

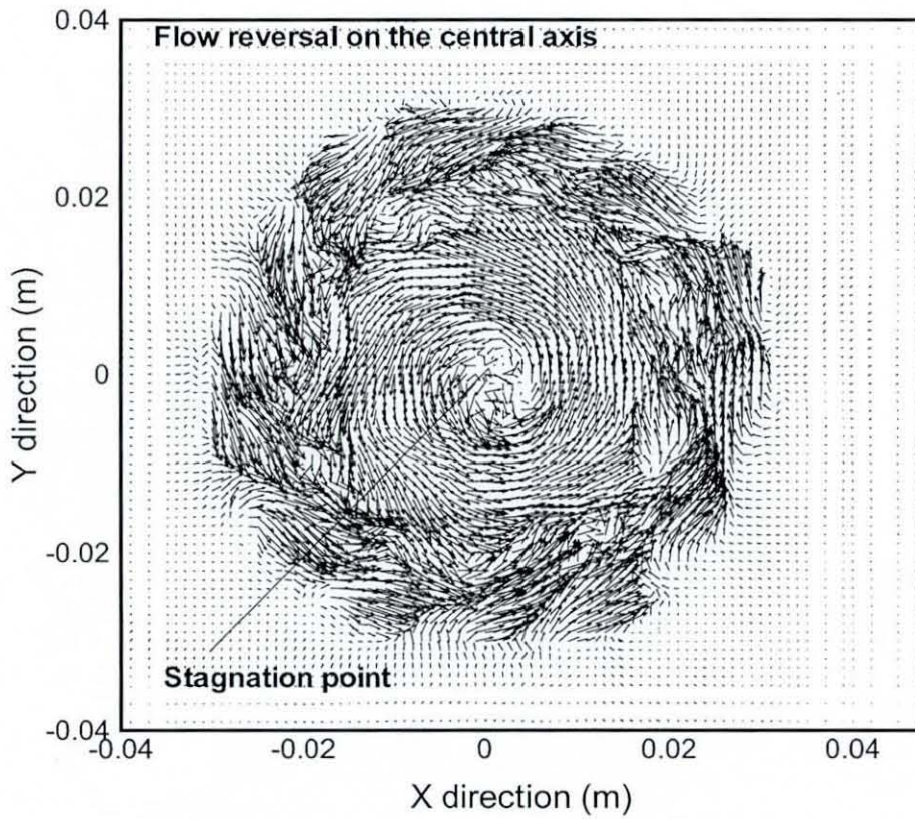


Figure 7.28: velocity vector field of the medium-swirl case on XY plane at  $z=70\text{mm}$  at  $t=30\text{ms}$ .

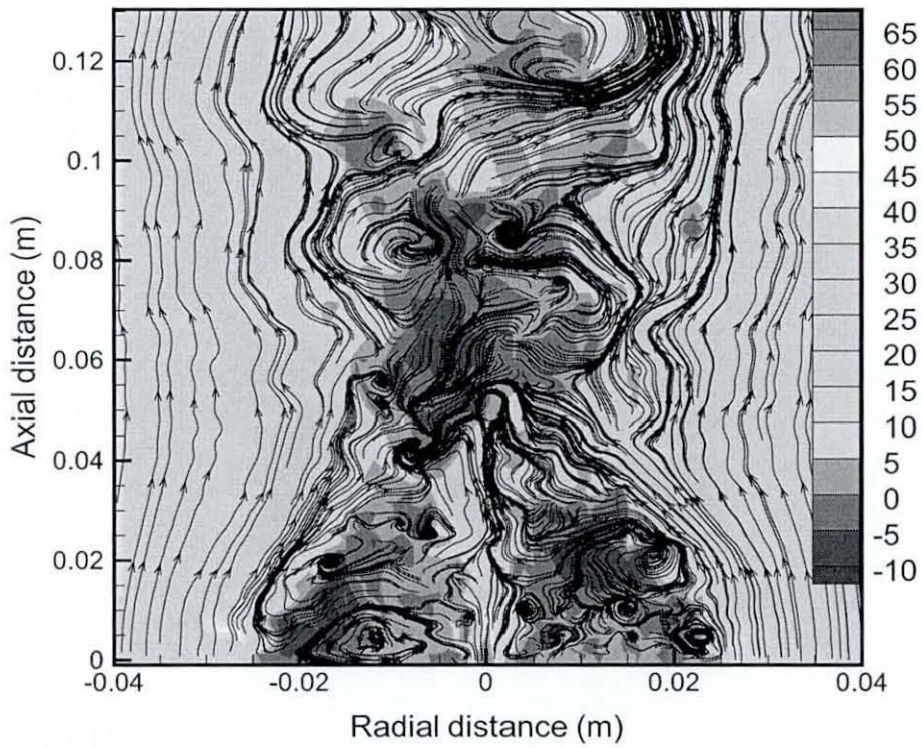


Figure 7.29: Instantaneous streamlines of the medium-swirl case on XZ plane at  $t=30\text{ms}$ .

The predicted mean flow field of the medium swirl case compared with experimental data are shown in Figure 7.30 and 7.31. The contour plots for the mean axial velocity show that a recirculation zone developed above the ceramic bluff body shrink in size and stagnates at about 25 mm from the exit plane. The primary annulus axial velocity is considerably higher ( $29.7 \text{ m.s}^{-1}$ ) and this is one of the key parameters for the occurrence of downstream vortex breakdown in this burner configuration. The bluff body stabilized recirculation zone is much thinner and compact than that formed with the non-swirl case. The existence of the second recirculation zone is attributed to the phenomenon of vortex breakdown (VB) which stagnates on the jet centreline at  $x = 50 \text{ mm}$  and  $110 \text{ mm}$ . This zone takes on the shape of a closed bubble shape vortex and has peak mean axial velocity  $\langle U \rangle = -5 \text{ m.s}^{-1}$  occurring on the centreline at  $x = 70 \text{ mm}$ . The contour plot for the mean swirling velocity (Figure 7.31) shows that the flow is less able to desire the mean swirling velocity outwards into the co-flowing secondary air stream. The radial spread of the flow field at each axial station is defined to be at the radial positions where  $\langle W \rangle = 0$ . The maximum swirl velocity appears at an axial distance of 40 mm above the burner face at  $r = 30 \text{ mm}$ .

Hence the velocity field leads to a non-recirculating collar-like flow feature in the flow just beyond the end of the first recirculation zone. As appeared in Figure 7.31 the collar-like flow feature occurs as a result of the downstream recirculation region, Al-Abdeli and Masri (2003a). Especially in this case the radial momentum across the width of the flowfield is too high as a result of the narrower flow regime. This behavior occurs since the fluid parcels are being forced to accelerate through the restricted cross-sectional area between the surrounding stagnant fluid and the edge of the recirculating vortex, Al-Abdeli and Masri (2003a).

Additionally the downstream (bubble shaped) recirculation zone and the rotating

collar-like flow structure ahead of it compresses the flow leading to higher velocity gradients and shear stresses in the region around  $x = 60 \text{ mm}$  at  $r = 13 \text{ mm}$  (comparisons of the shear stresses are already discussed in flow structures of the medium swirl case). Thus the downstream part of the flow field can expect improved mixing rates both as a consequence of the recirculation and the increased shear stresses.

The time averaged mean axial velocity along the burner centreline is shown in Figure 7.32. It can be seen in the near-field of the inlet, the centreline velocity rapidly decays with increased distance downstream. Between  $50 \text{ mm} < x < 100 \text{ mm}$ , the centreline velocity becomes negative and the flow stagnates. This flow reversal occurs due to the vortex breakdown (VB) as discussed earlier.

In a similar fashion, Figure 7.33 shows the centerline turbulent kinetic energy profile. As expected, the axial distribution of the turbulent kinetic energy is higher near to the central axis as a result of the formation of bluff body stabilized upstream recirculation zone. However, the peak value is somewhat underpredicted, but the overall agreement is acceptable. Figures 7.34 to 7.36 show more features of upstream recirculation and downstream VB bubble of the medium swirl case. The contour plots mainly show the values below zero for the mean axial velocity which indicates the formation of recirculation and vortex bubble.

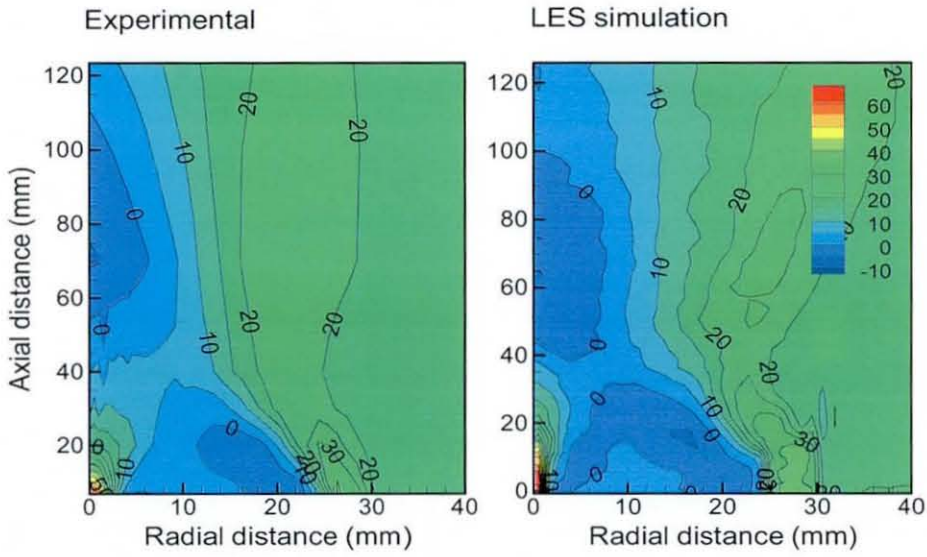


Figure 7.30: Contour plot for mean axial velocity for medium swirl-case.

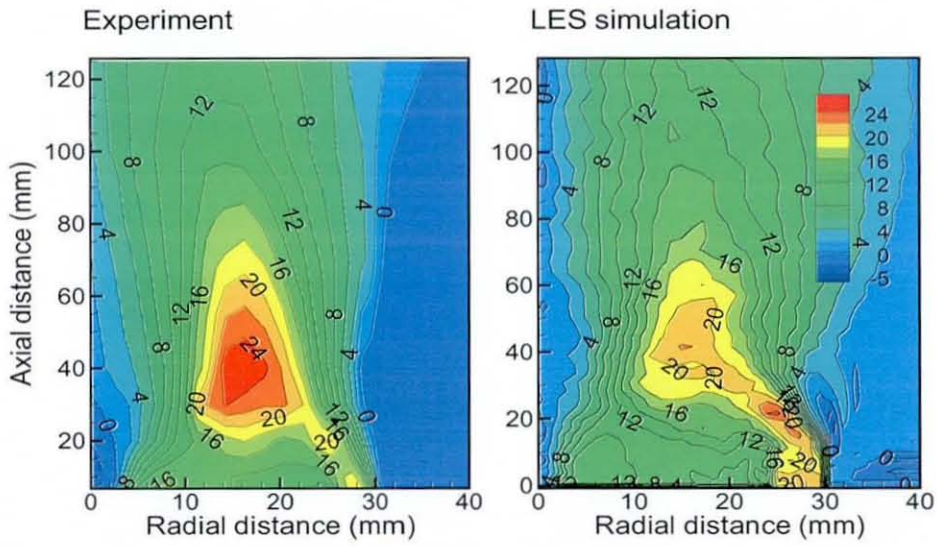


Figure 7.31: Contour plot for mean swirling velocity for medium swirl-case.

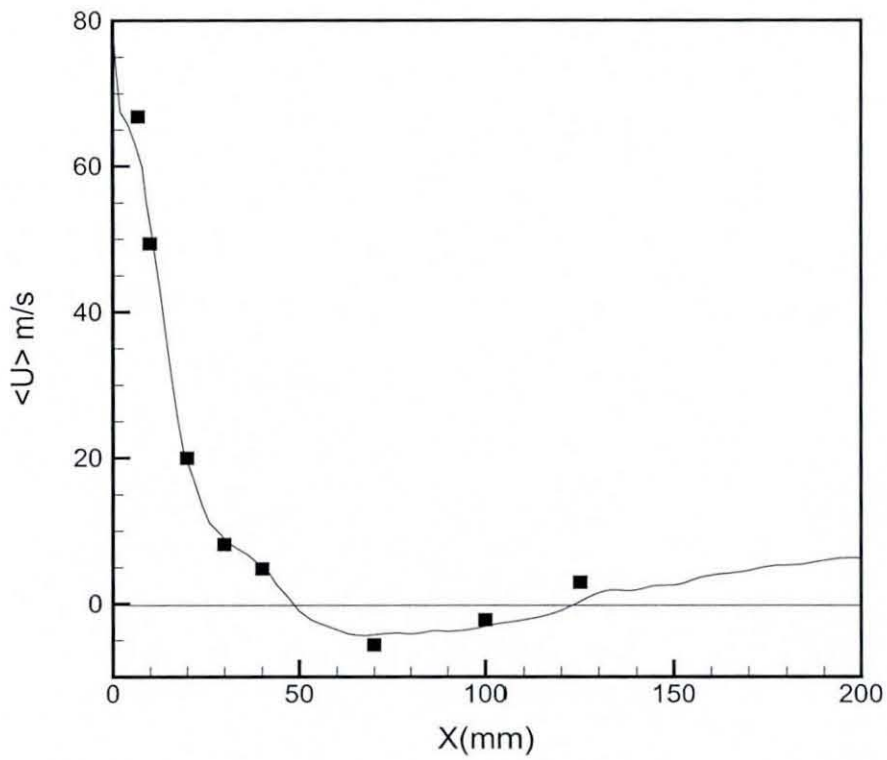


Figure 7.32: Centreline mean axial velocity for the medium-swirl case, lines represent LES results and symbols represent experimental measurements.

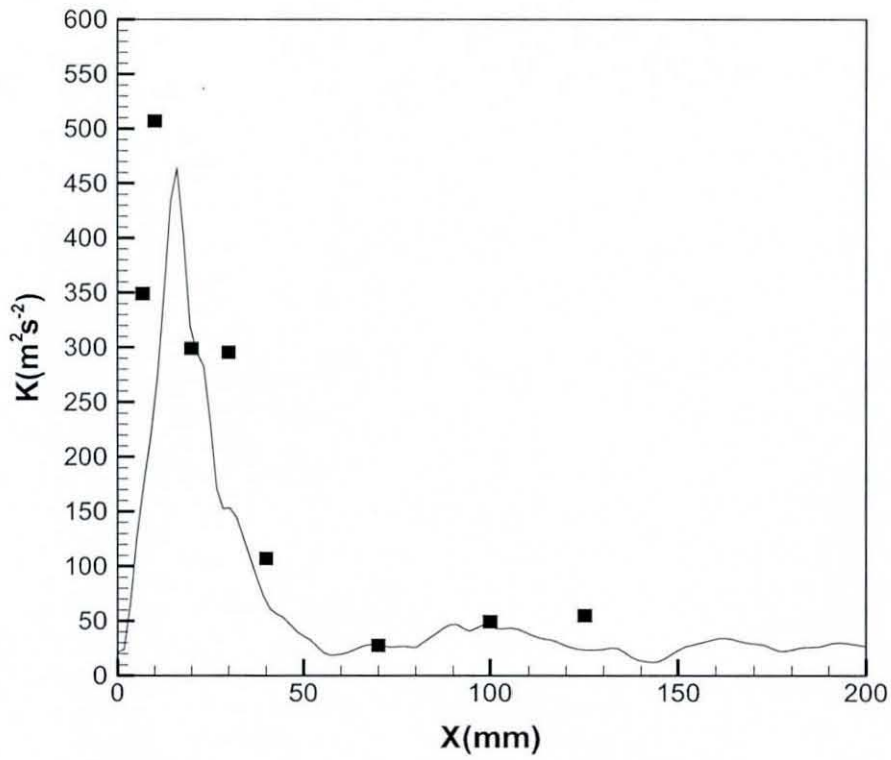


Figure 7.33: Turbulent kinetic energy for the medium-swirl case, lines represent LES results and symbols represent experimental measurements.

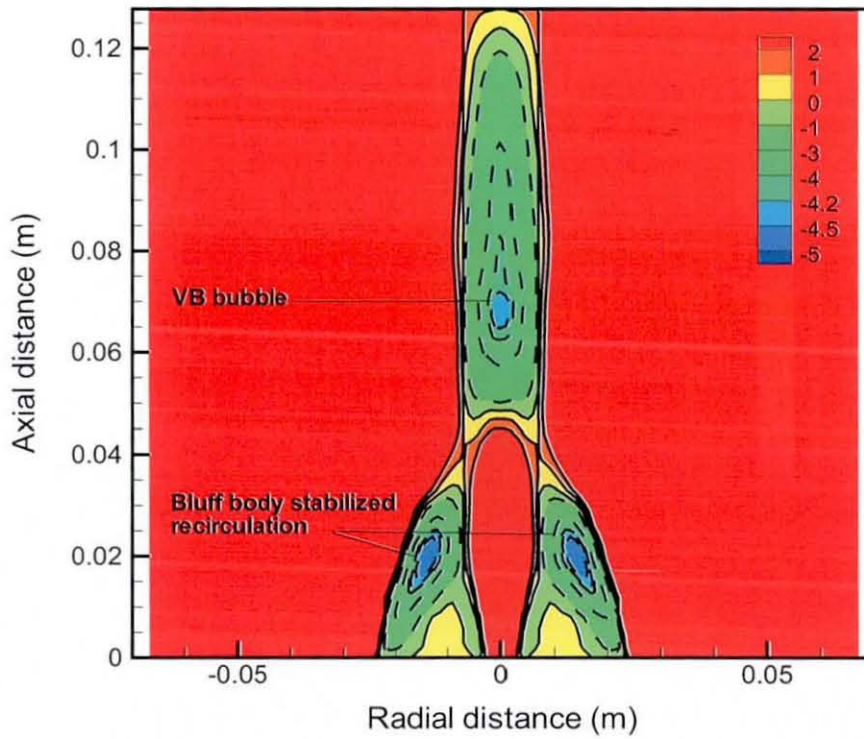


Figure 7.34: Recirculation and vortex breakdown, contour plot of the mean axial velocity for medium swirl case and dash line indicate the negative mean axial velocity.

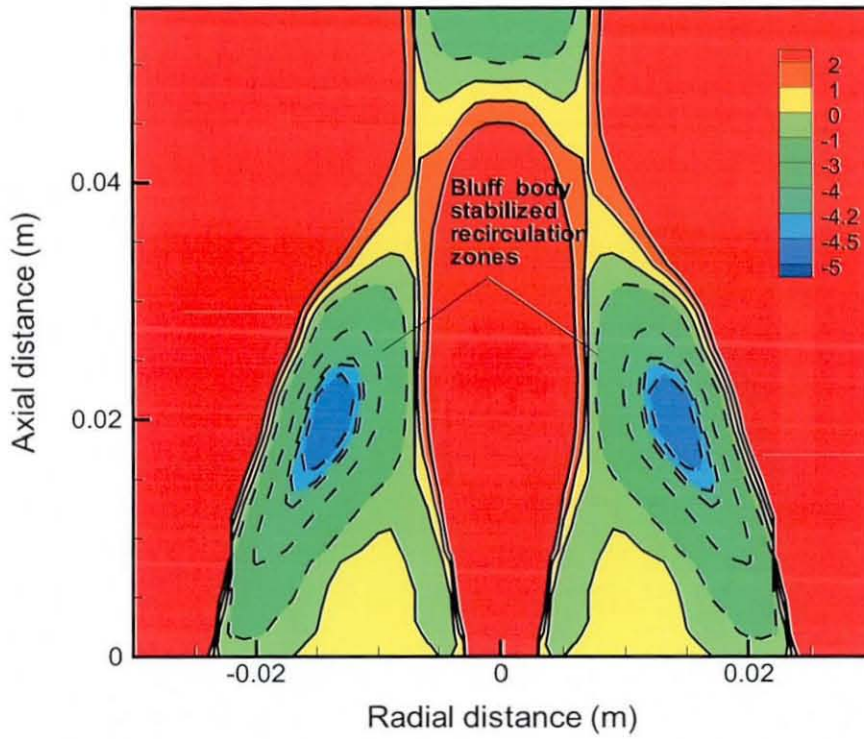


Figure 7.35: Bluff body stabilized recirculation zone, contour plot of the mean axial velocity for medium swirl case and dash line indicate the negative mean axial velocity.

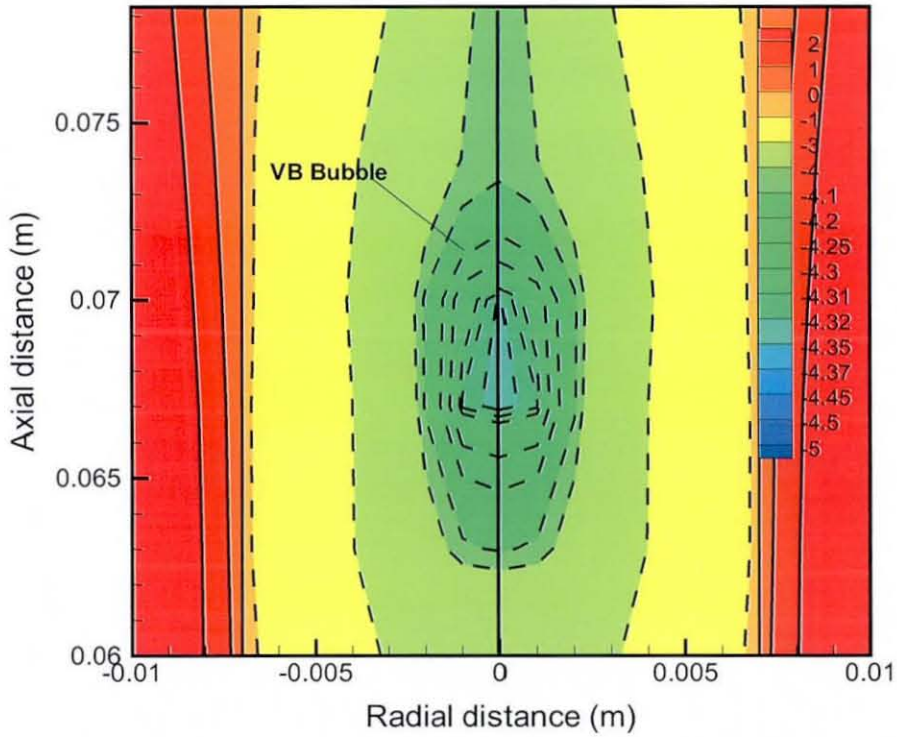


Figure 7.36: Vortex breakdown (VB) bubble, contour plot of the mean axial velocity for medium swirl case and dash line indicate the negative mean axial velocity.

## 7.10 Swirl number variation

Figure 7.37 shows the LES results of the swirl number and the mean axial velocity along the centreline for the two swirling test cases (medium and high swirl case). The decay of the swirl numbers along the centreline is identical for both cases and peaks values occur at  $x = 20 \text{ mm}$  above from the exit plane. However, near to the jet inlet the predictions underestimate the centreline velocity in the highest swirl number test case. Further downstream the axial velocity of N16S159 nearly goes to zero. However, there is no downstream recirculation or vortex breakdown despite having a larger swirl number.

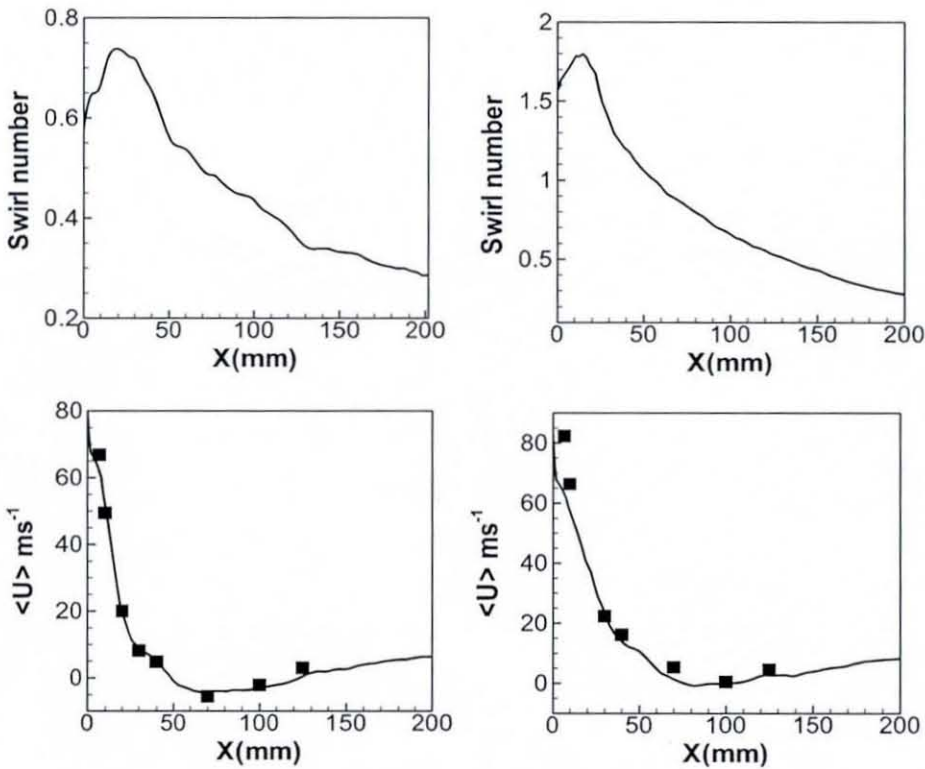


Figure 7.37: Distribution of the swirl number and mean axial velocity along the central axis (left side: N29S054, right side: N16S159).

# Chapter 8

## LES of Swirling Flames: Results and Discussion

### 8.1 Introduction

Modelling of swirl stabilized reacting flows represents the next level of computational complexity after successful simulations of the isothermal swirling flow fields. The Sydney swirl burner configuration describes the series of swirling flame structures for a range of swirl numbers and Reynolds numbers, Al-Abdeli and Masri (2003b), Masri *et al.* (2004). In previous chapter the flow structure of the non-reacting swirling flow fields were discussed and the present chapter continue the LES calculations of more complex turbulent swirling flames. The main objective is to provide a comprehensive picture of the LES calculations of different swirling flames covering a range of swirl numbers and Reynolds numbers. Two different flames SMH1 and SMH2, covering two fuel mixtures over a range of flow conditions are selected for LES calculations. The following sections describe the important flow features of selected swirling flames based on experimental observations followed by LES calculation procedure and the comparison

of predictions with experimental data.

## 8.2 Experimental observations

In this work, two swirling flames known as SMH1, SMH2 experimentally investigated by Al-Abdeli and Masri (2003b), Masri *et al.* (2004) have been selected for modelling and thus discussion of the important features of the flow field and flame structure based on experimental measurements is provided.

SMH1 used CNG-H<sub>2</sub> and operated at a fuel jet velocity of  $140.8 \text{ m.s}^{-1}$  with a swirl number of 0.32. It was a stable flame well away from the blow off limits. The velocity field measurements showed a large recirculation zone just above the bluff body extending almost entirely to the annulus at  $r = 23 \text{ mm}$ . This flame also exhibited a secondary VB recirculation zone. A strong necking region was also seen around  $x \approx 70 \text{ mm}$  where the visible flame width was reduced to about  $25 - 30 \text{ mm}$ . The upstream behavior of flow exhibited a highly rotating, downstream collar-like flow feature in region upstream of the second recirculation zone.

The flame SMH2 operated at a fuel jet velocity of  $140.8 \text{ m.s}^{-1}$ , with a higher swirl number of 0.54. This flame showed a typical bluff body stabilized upstream recirculation zone which extended up to about  $50 \text{ mm}$  along the the  $z$  direction. Unlike flame SMH1, SMH2 showed no downstream recirculation and no rotating collar-like features were observed in the measurements despite having a larger swirl number as a result of the less primary annulus axial velocity. Composition measurements showed lower peak mass fraction of  $H_2$  compared to the SMH1 flame indicating faster mixing induced by higher swirl and the SMH2 flame was broader than the SMH1 flame. Both SMH1 and SMH2 were generally asymmetric in the upstream region.

## 8.3 Numerical description

As discussed earlier, the incompressible variable density calculation procedure is used to perform LES calculations for the reacting swirling flames. Once the density is obtained from the flamelet library, the continuity equation can be imposed as a constraint on the momentum field, with the time derivative of density as a source term. This constraint is enforced by the pressure. The computational algorithm first advances the mixture fraction. The flamelet library yields the density, whose time derivative is computed. The momentum is predicted using the convective, viscous and pressure gradient at the present time step. The predicted value of the momentum is then projected such that the continuity equation is satisfied. The advection terms of the momentum equations are discretized by using SHARP Leonard (1987) scheme and other spatial derivatives in momentum equations are discretised by using standard second order central differences. Second order central differences are also used for the pressure correction equation. The transport equation for the mixture fraction uses central difference for the diffusion term and SHARP Leonard (1987) for the advection terms to ensure monotonicity of the solution. The solutions are advanced in time by using the fractional step method. The momentum equations are integrated using a third order hybrid Adam-Bashforth/Adam-Moulton scheme to give an approximate solution for the velocity field. The time discretisation of the scalar equation uses Crank-Nicolson scheme. The solution is advanced with a time stepping corresponding to Courant number in the range of  $C_0 < 0.7$ . The discretized equations are solved using a linear equation solver. Bi-Conjugate Gradient Stabilized (BiCGStab) methods with Modified Strongly Implicit (MSI) preconditioner are used to solve the system of algebraic equations resulting from the discretisation. The momentum residual error is typically of the order  $10^{-7}$  per time step and the mass conservation error is of the order of  $10^{-10}$ .

## 8.4 Grid resolutions and boundary conditions

The computational domain has dimensions  $300 \times 300 \times 250mm$ , which employed non-uniform Cartesian grid in,  $X, Y$  and  $Z$  directions respectively. Two different LES grids were employed to analyze the grid sensitivity for the SMH1 flame. Grid 1 consisted of  $100 \times 100 \times 100$  cells in  $X, Y$ , and  $Z$  directions respectively giving a total of one million grid points. A Grid 2 that was coarser than Grid 1, consisted of  $85 \times 85 \times 100$  cells in  $X, Y$  and  $Z$  directions respectively having approximately 0.72 million grid cells. The flame SMH1 with swirl number 0.32 was used as a test case for grid sensitivity analysis. LES results obtained using above two grids are compared with experimental data. The mean axial, swirl velocities and their rms fluctuations at  $x/D = 0.4$  and mean mixture fraction and its fluctuation at  $x/D = 0.5$  are compared with experimental measurements. In Figure 8.1, solid lines represent the Grid 1 results (1 million), dashed lines represent the Grid 2 results (0.72 million), and symbols represent the experimental measurements. There are slight differences between the LES results predicted from both grids. However, it has been found that the grid 1 results are much closer to the experimental measurements than grid 2, especially in outer and inner shear layers of the bluff body stabilized recirculation zone. Therefore grid 1, which includes total number of 1 million cells has been used for all LES simulations considered here and the predictions are compared with experimental measurements. For completeness, Grid 2 simulations have been carried out for the other two test cases as well and it has been established that Grid 1 provide an adequate resolution.

## 8.5 Statistics

The large computational domain was chosen to reduce the effect of the boundaries. The computations suggested that the statistics for time average calcula-

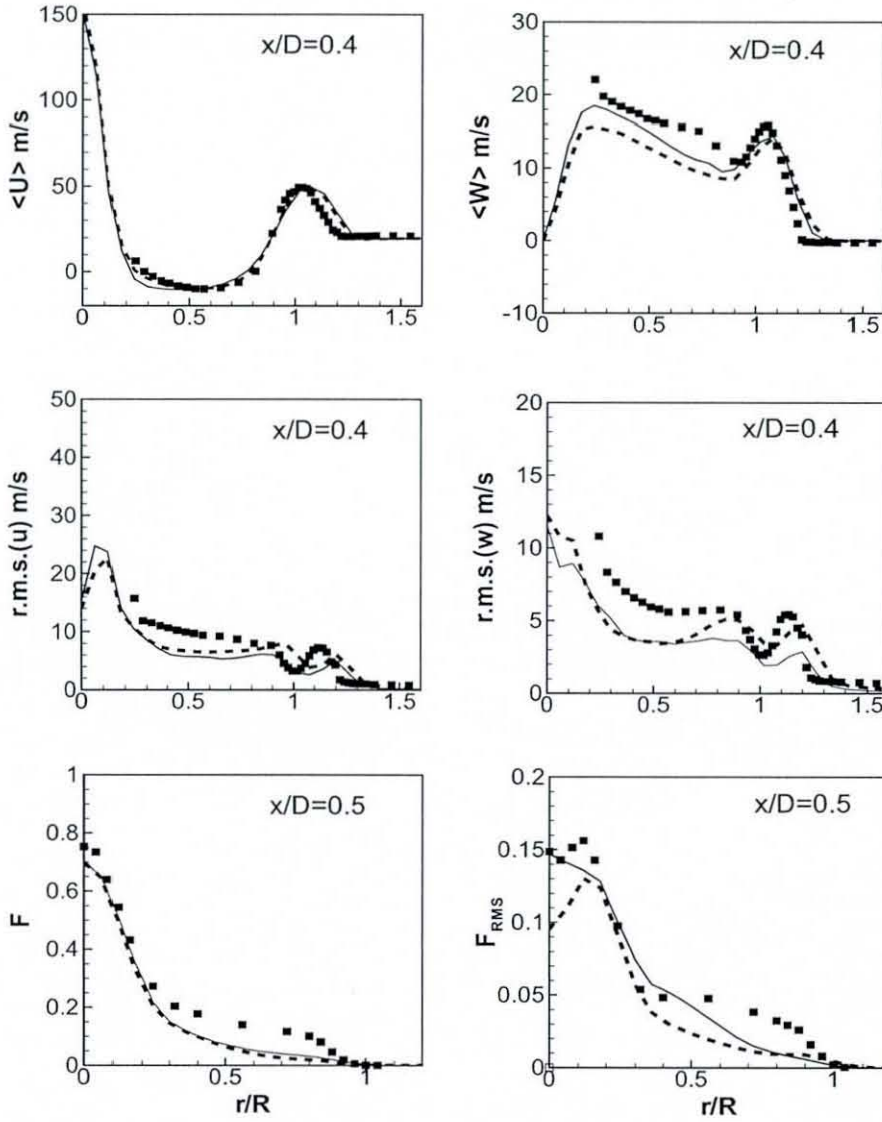


Figure 8.1: Radial profiles of mean axial velocity in the SMH1 flame, solid lines represent grid 1 results, dashed lines represent grid 2 results and symbols represent experimental measurements.

Flame	Grid Type	$N_x$	$N_y$	$N_z$	Time(s)	Cost days
SMH1	Grid 1	100	100	100	0.06	22
SMH1	Grid 2	85	85	100	0.06	17
SMH2	Grid 1	100	100	100	0.06	21
SM1	Grid 1	100	100	100	0.06	14
SM2	Grid 1	100	100	100	0.06	14

Table 8.1: Grid resolution and typical run time (s) for reacting swirling flames

tions can be started after 0.04s. Sufficient time period for the statistics is essential to achieve converged solutions for velocity components and combustion scalars. Since samples from two different intervals gives very similar results, it can be concluded that the statistics are successfully converged. To calculate the statistics of flow and combustion variables, total numbers of 1000 samples were considered within the period of 0.02s. The calculations were performed on a Pentium 4, personal computer with 4GB RAM and 3GHz processor running under Linux operating system. Table 8.1 summaries typical run times in days for each case considered.

## 8.6 SMH1 flame

SMH1 flame operates with CH<sub>4</sub>:H<sub>2</sub> (50 : 50) by volume of fuel with a central jet velocity of 140.8  $m.s^{-1}$  and 47% away from base blow-off. The operated swirl number is 0.32, Al-Abdeli and Masri (2003b).

In the flamelet approach the effect of local flame stretch, usually taken to be scalar dissipation rate, Peters (1984) provides some valuable information to identify the local extinction phenomena, Peters (1983). However in the present case SMH1 Masri *et al.* (2004), there are no experimental evidence of local extinction. Hence a single flamelet has been used to calculate the characteristic properties of

combusting flame. To find the most appropriate strain rate, the flamelet profiles are generated from two different strain rates and compared with experimental scatter plots. The rates of strain considered were  $a = 300 \text{ s}^{-1}$  and  $500 \text{ s}^{-1}$ . Figure 8.2 shows the comparison of the flamelet profiles with experimental scatter plots at  $x/D = 0.8$  for flame SMH1. It has been found that the single flamelet with the strain rate of  $a = 500 \text{ s}^{-1}$  is approximately the best flamelet for both SMH1 and SMH2 calculation. Hence a single flamelet with the strain rate of  $a = 500 \text{ s}^{-1}$  is considered for the present calculation. The flamelet calculations have been performed using the Flamemaster code Pitsch (1998). The reaction mechanism employed is the GRI 2.11 of Bowman *et al.* (1995) which includes 49 species and 279 reactions.

Figures 8.3 and 8.4 show snapshots of the filtered mixture fraction and filtered temperature respectively. The combustion products inside the recirculation zone continuously provide ignition sources, thereby stabilizing the flame. These snapshots have been taken from animations indicate the complex transient turbulent swirling flow behavior and their chemical interactions. The animation of the filtered axial velocity contour plot shows the fuel jet breaks up in the upstream recirculation zone. However the animations do not show the downstream vortex breakdown observed in experiment and the reason for LES not to capture the vortex breakdown (VB) zone in this case is unknown. One possible reason could be overprediction of the centreline axial velocity shown later in Figure 8.6.

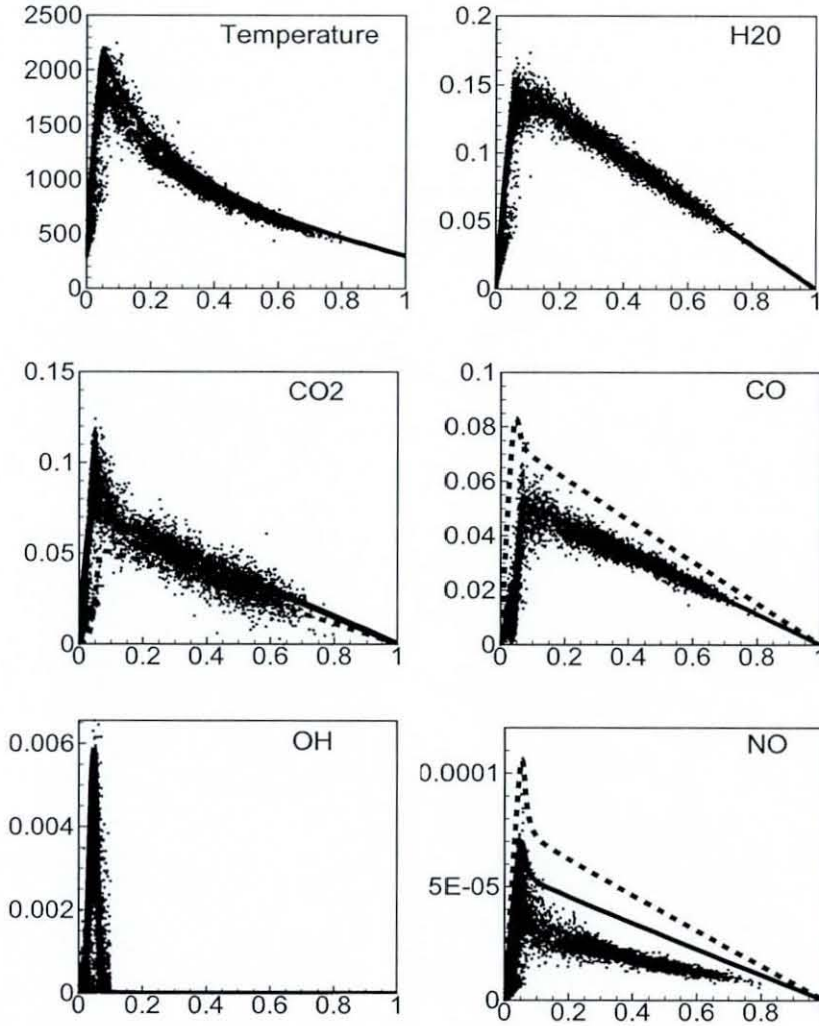


Figure 8.2: Laminar flamelet profiles, scatter plots of temperature, and mass fraction versus mixture fraction at  $x/D = 0.8$  for flame SMH1. Solid line represent strain rate of  $500\text{s}^{-1}$  and dashed line represent strain rate of  $300\text{s}^{-1}$  respectively.

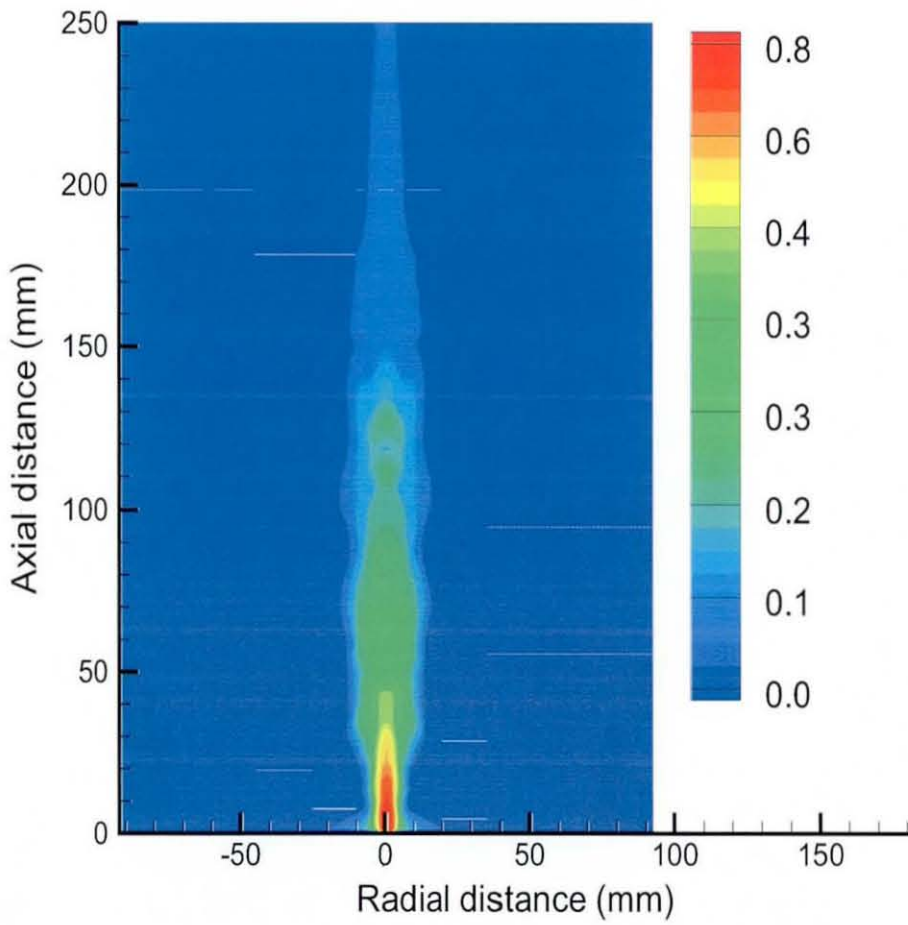


Figure 8.3: Snapshot of the filtered mixture fraction of flame SMH1.

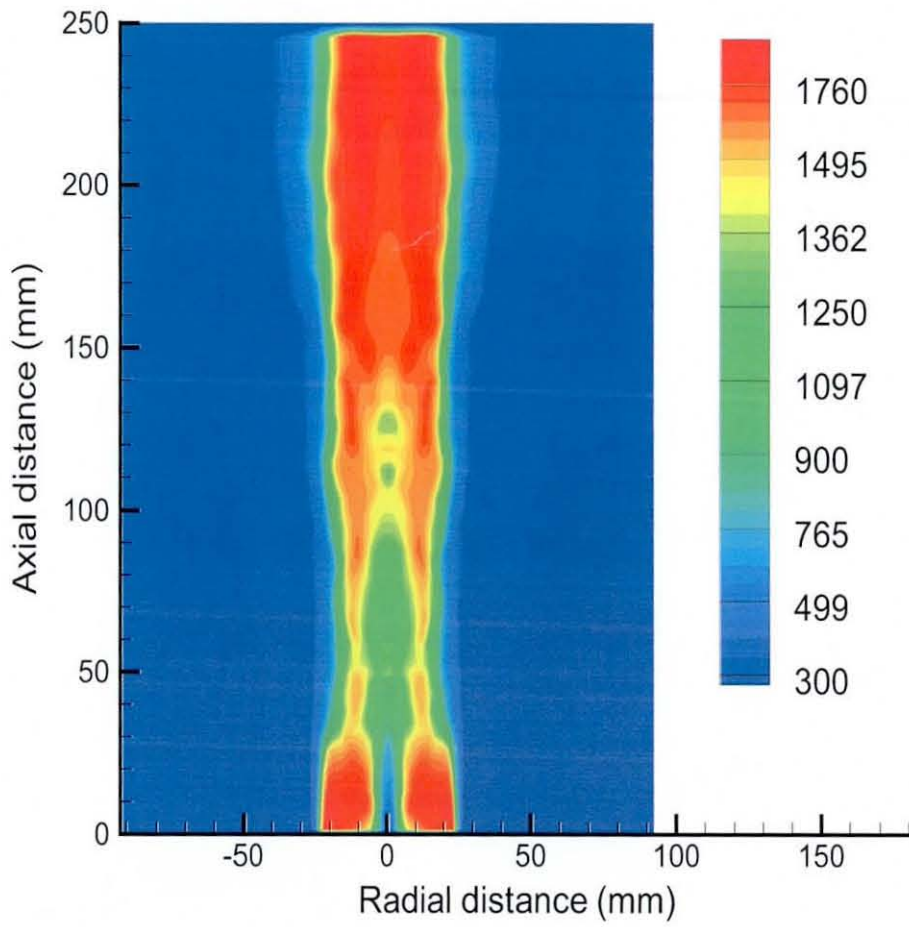


Figure 8.4: Snapshot of the filtered temperature(K) of flame SMH1.

### Velocity fields

The contour plot for the mean axial velocity and the velocity vector field generated from mean velocities are shown in Figure 8.5. The bluff body stabilized upstream recirculation zone is well captured. The comparisons of the time averaged mean axial velocity at different axial locations  $x/D \in \{0.2, 0.4, 0.8, 1.2, 1.6, 2.5, 3.5\}$  are shown in Figure 8.6. The experimental data show that the relatively short bluff body stabilized upstream recirculation zone, which extends upto 60 mm towards the axial direction from the burner exit plane, and a highly rotating downstream collar-like flow feature leads to the occurrence of vortex breakdown (VB). The predicted negative values of the mean axial velocity at  $x/D \in \{0.2, 0.4\}$  (Figure 8.6) and the contour plot (Figure 8.5) of mean velocity indicate the flow reversal, which generate the upstream bluff body stabilized recirculation zone. At  $x/D = 0.8$  the experimental and simulation data still show negative values for the mean axial velocity and hence, it can be concluded that the predictions have well captured the upstream recirculation zone that has been found experimentally. Additionally the calculations reproduced all peaks of the mean axial velocity which appears above the primary annulus. However the calculation overpredicts the centreline axial velocity at  $x/D \in \{1.2, 1.6, 2.5, 3.5\}$ .

It is also interesting to note that there are no experimental measurements on the centreline for the first few axial locations. The axial momentum of the central jet is much higher due to the higher jet velocity. It is observed that the predicted central jet breaks slower than that found experimentally. However predictions could improve with the higher resolutions along the axial direction. No radial velocities are available for comparison in this case. The comparison of the mean swirling velocity is shown in Figure 8.7. The comparisons between calculations and measurements are very good at most of the axial positions. The predictions have captured peaks appearing on the inner and outer shear layer of the

upstream recirculation zone. At  $x/D = 2.5$ , the LES swirling velocity deviates from experimental measurements. This may be attributed to non-existence of the downstream recirculation zone in the prediction ( see Figure 8.6). However, the overall agreement is quite good for the mean swirling velocity. At  $x/D = 0.2$ , the bluff body stabilized recirculation zone extends upto the swirling annulus. As mentioned earlier, the rotation rate can be used to describe the rotation of the upstream recirculation zone. At  $r/R = 0.8$ , the recirculation zone rotates at a rate of  $103 \text{ rev.s}^{-1}$ , which is derived from  $\langle W \rangle = 13.2 \text{ m.s}^{-1}$  at  $x/D = 0.2$ . For the same axial location, at  $r/R = 1.1$  (this is above the primary annulus) the mean swirling velocity of  $\langle W \rangle = 15.8 \text{ m.s}^{-1}$  leads to the rotation rate of  $92 \text{ rev.s}^{-1}$ . The difference between two rotation values at two different radial positions effectively makes the rotation of the upstream recirculation zone. The width of the upstream recirculation zone is described in the region between  $x/D = 0.4$  and  $0.8$ . However, strong negative axial velocity (approximately  $-10 \text{ m.s}^{-1}$ ) has been predicted in the core of the zone at both  $x/D = 0.4, 0.8$ , which is very close to the value observed by Al-Abdeli and Masri (2003b).

Figure 8.8 shows that comparison of the axial velocity fluctuations. RMS of axial velocity fluctuations are slightly underpredicted at first three axial locations in the region between  $r/R = 0.3 - 1.0$ . Additionally the centreline axial velocity fluctuations are slightly overpredicted at  $x/D \in \{1.2, 1.6\}$ . The overall agreement however for the rms axial velocity is good and profiles are reasonable.

Despite the small discrepancy the comparisons for the swirling velocity fluctuations agree well (see Figure 8.9). There are some discrepancies at first three axial locations same as rms axial velocity. The issue of the downstream centreline vortex breakdown remains speculative and causes may be the deviations in comparisons for mean velocities and rms fluctuations at further downstream

$x/D \in \{2.5, 3.5\}$ . The overall agreement for the mean velocities and rms fluctuations is agree well, even though vortex breakdown has not been captured.

### Scalar fields

The flame structure (mean temperature field) of the flame SMH1 calculated from LES is shown in Figure 8.10. The simulated flame show higher temperature inside the upstream recirculation zone as well as further downstream near to the centreline. Furthermore, the strong necking occurs around,  $x = 70 \text{ mm}$  (downstream from the burner exit plane), which is the link to the collar-like flow feature and as a result, the visible flame width reduced to about  $25 - 30 \text{ mm}$ . However, the flame SMH1 is relatively longer than the other fames investigated by Masri *et al.* (2004).

Figure 8.11 shows the comparison of radial profiles of the mean mixture fraction at downstream axial locations. It is evident that the mixture fraction is slightly underpredicted in between  $r/R = 0.2-0.8$  at  $x/D \in \{0.2, 0.5\}$ . Despite this slight discrepancy, the agreement between calculations and measurements are very good at all other downstream axial locations. Furthermore at any given axial position, the narrower regime of the upstream recirculation zone shifts the radial profiles toward central axis as a result of the outer shear layer. The radial profiles of the mixture fraction variance at downstream axial locations are shown in figure 8.12. The peak of the variance at  $x/D = 0.2$  is somewhat overestimated. The variance has steep gradients near to the jet centreline closer to the burner exit plane and this peak shifts towards radial direction in further downstream. The higher variance may be genuine, since higher turbulence levels are also presented on the centreline within the recirculation zone. The mixture fraction variance results are reasonably good for the other axial locations for  $x/D \leq 1.6$ . However, predictions slightly overpredict at the centreline at  $x/D \in \{2.5, 3.5\}$ . The qualitative trends

agree very well.

The comparison of the mean temperature field is shown in Figure 8.13. Despite the complexity of the flow field, the comparison of the temperature field is reasonable at most of the axial locations. However, the underestimation of the radial spread of the mixture fraction leads to a corresponding deviation of the temperature and species concentrations, which can be seen at  $x/D \in \{0.2, 0.8\}$ . In experiments, the peak temperature appeared in the outer shear layer at  $x/D = 0.8$  ( $r/R = 0.6$ ). The calculated temperature underpredicts at this location. It is also important to mention that the experimental data have some sudden increase at this location. Furthermore the steady flamelet assumption may not be perfectly valid at this point. Despite having this underestimation the comparisons are good at all other locations. The overall predictions of the mean temperature are in good agreement with experimental measurements.

The comparisons for the species concentration profiles are shown in Figures 8.14-8.16. The profiles for  $H_2O$  are consistent with those of temperature with slightly similar peaks. The radial spread of  $CO$  is underestimated at  $x/D \in \{0.2, 0.5\}$ . The  $CO_2$  is overpredicted at  $x/D \in \{1.1, 1.6, 2.5, 3.5\}$ . It has been observed that the predictions have not captured the peak values of  $CO_2$  and  $CO$  mass fractions. Further downstream the results are very good for all species concentrations. In general, given the complexity of the flame and flow field, species predictions are reasonably good.

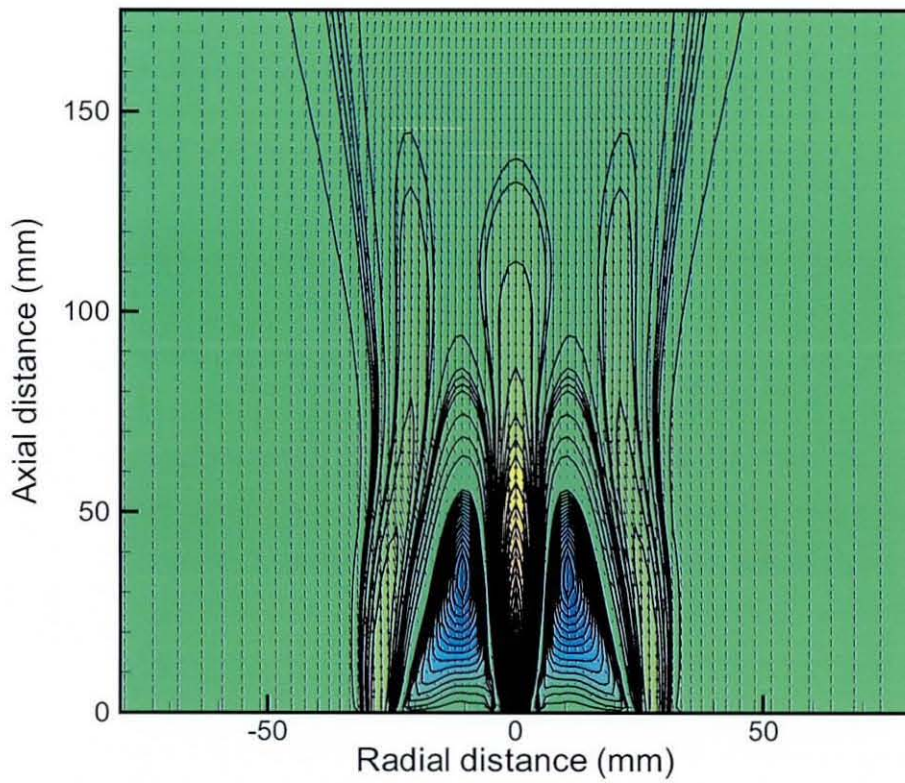


Figure 8.5: Contour plot of mean axial velocity and mean velocity vector field of flame SMH1.

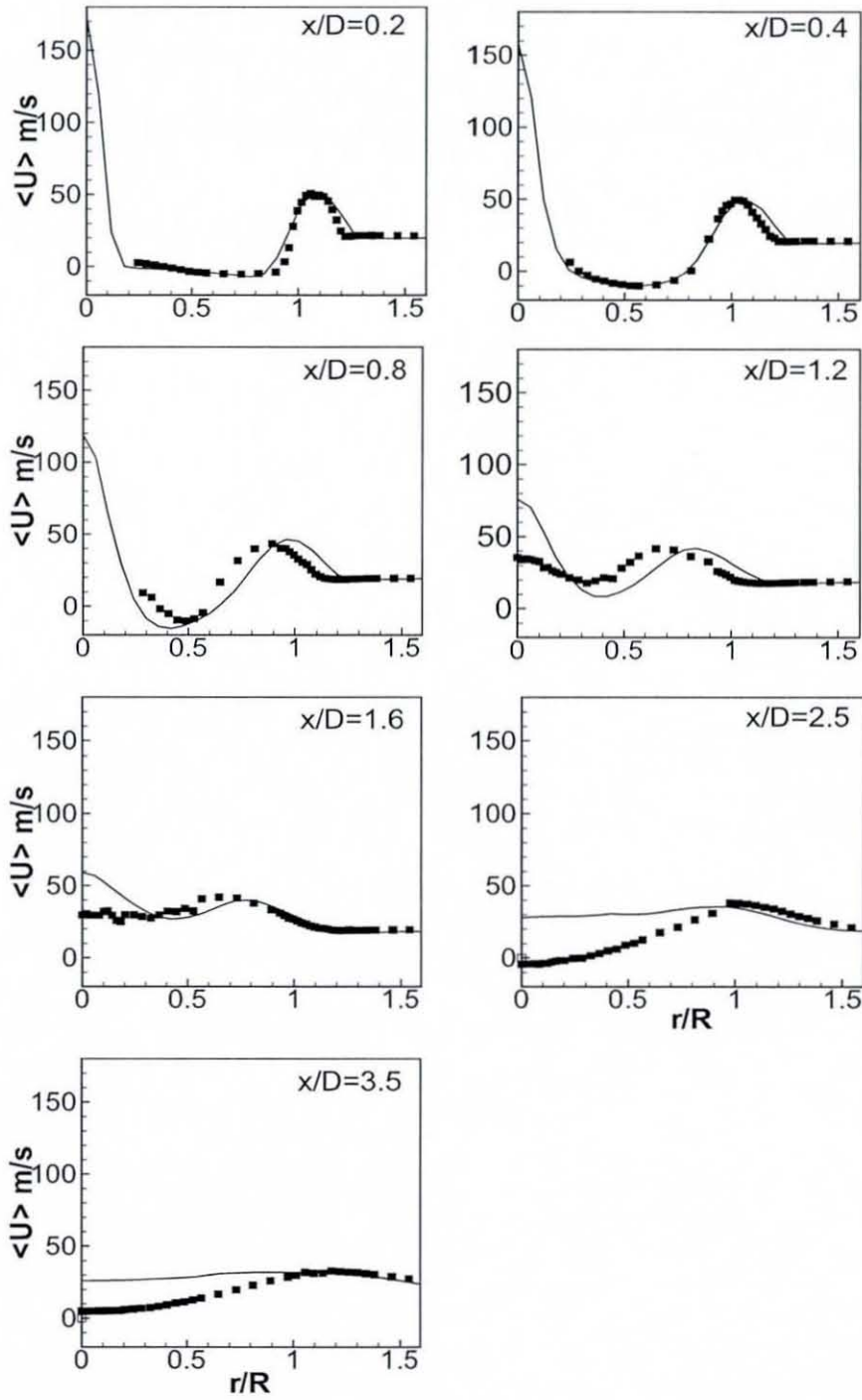


Figure 8.6: Radial profiles of mean axial velocity in the SMH1 flame, lines represent LES results and symbols represent experimental measurements.

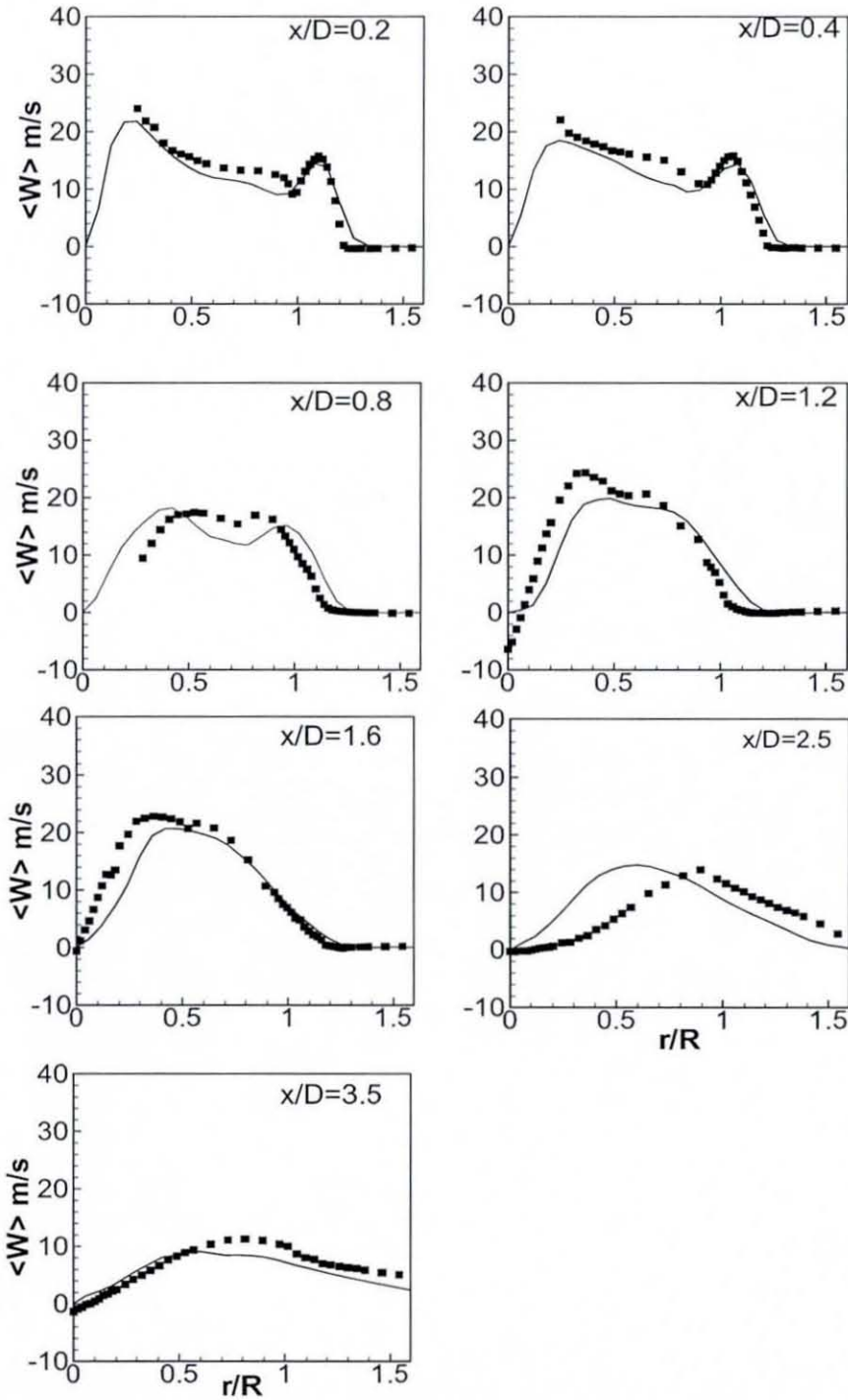


Figure 8.7: Radial profiles of mean swirling velocity in the SMH1 flame, lines represent LES results and symbols represent experimental measurements.

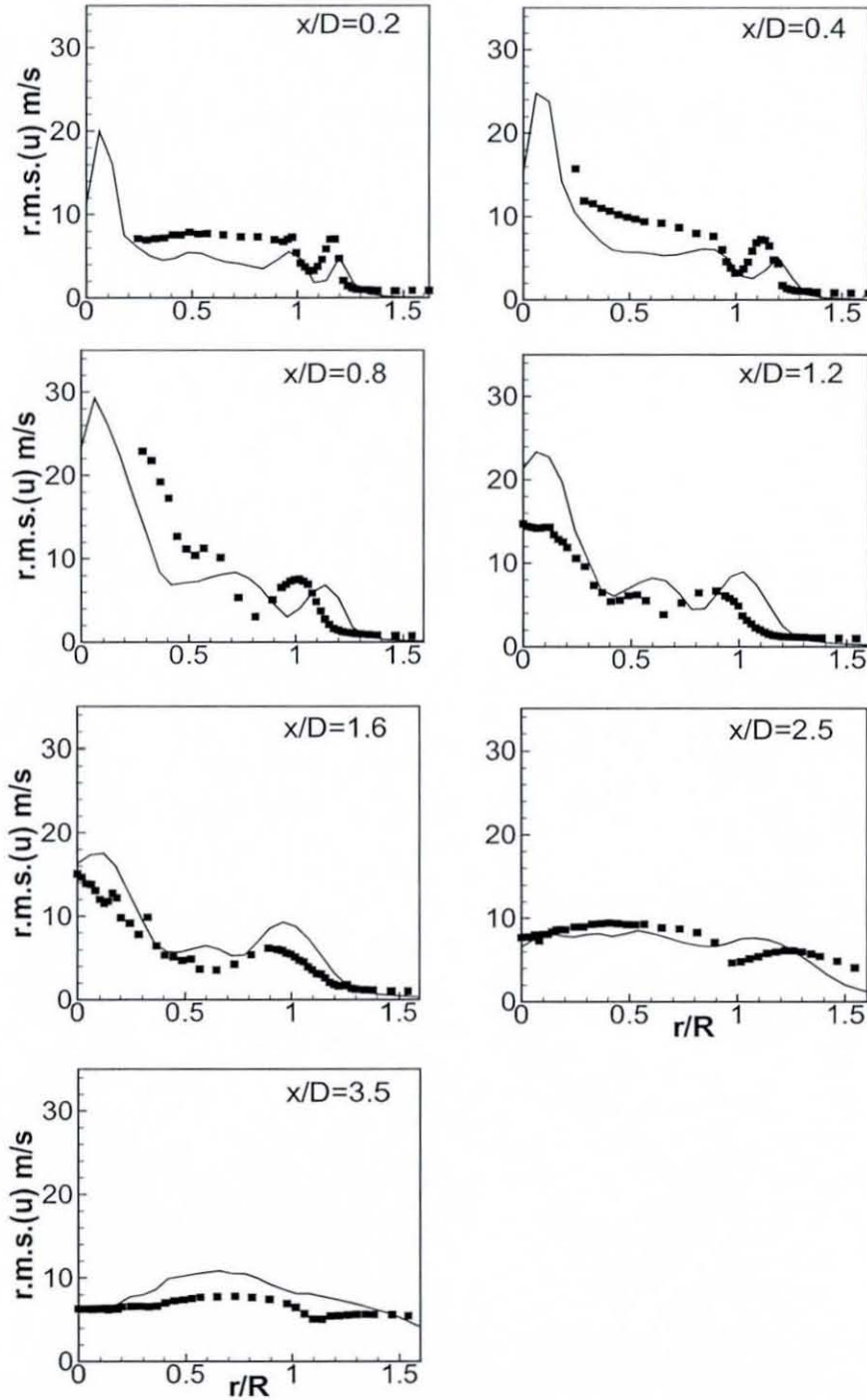


Figure 8.8: Radial profiles of RMS axial velocity in the SMH1 flame, lines represent LES results and symbols represent experimental measurements.

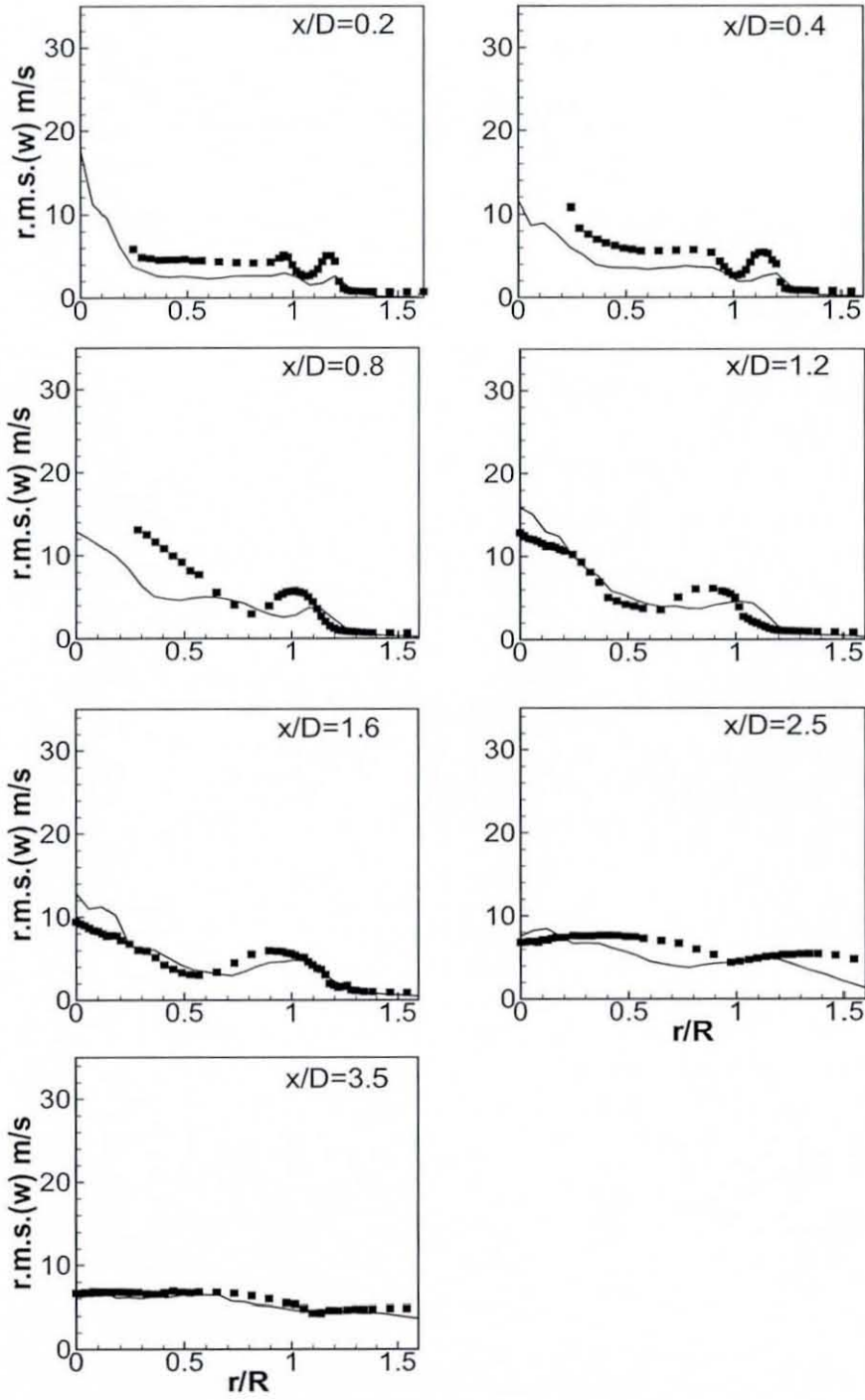


Figure 8.9: Radial profiles of RMS swirling velocity in the SMH1 flame, lines represent LES results and symbols represent experimental measurements.

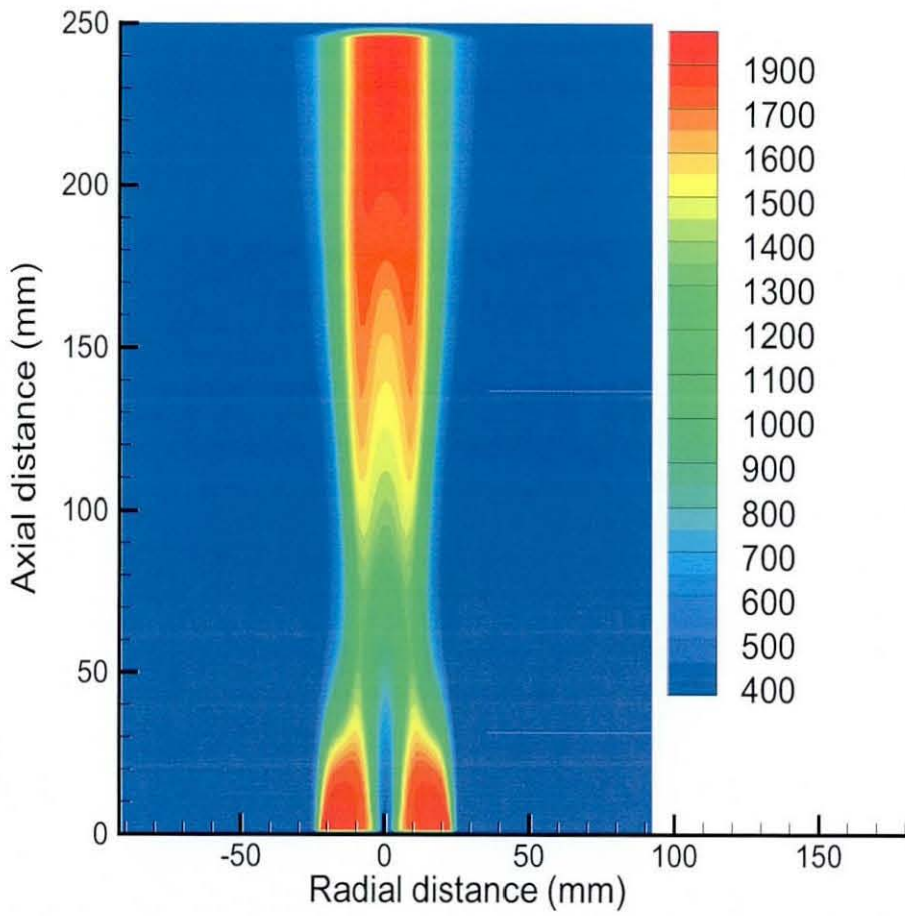


Figure 8.10: Contour plot of mean temperature,  $T(K)$  of flame SMH1.

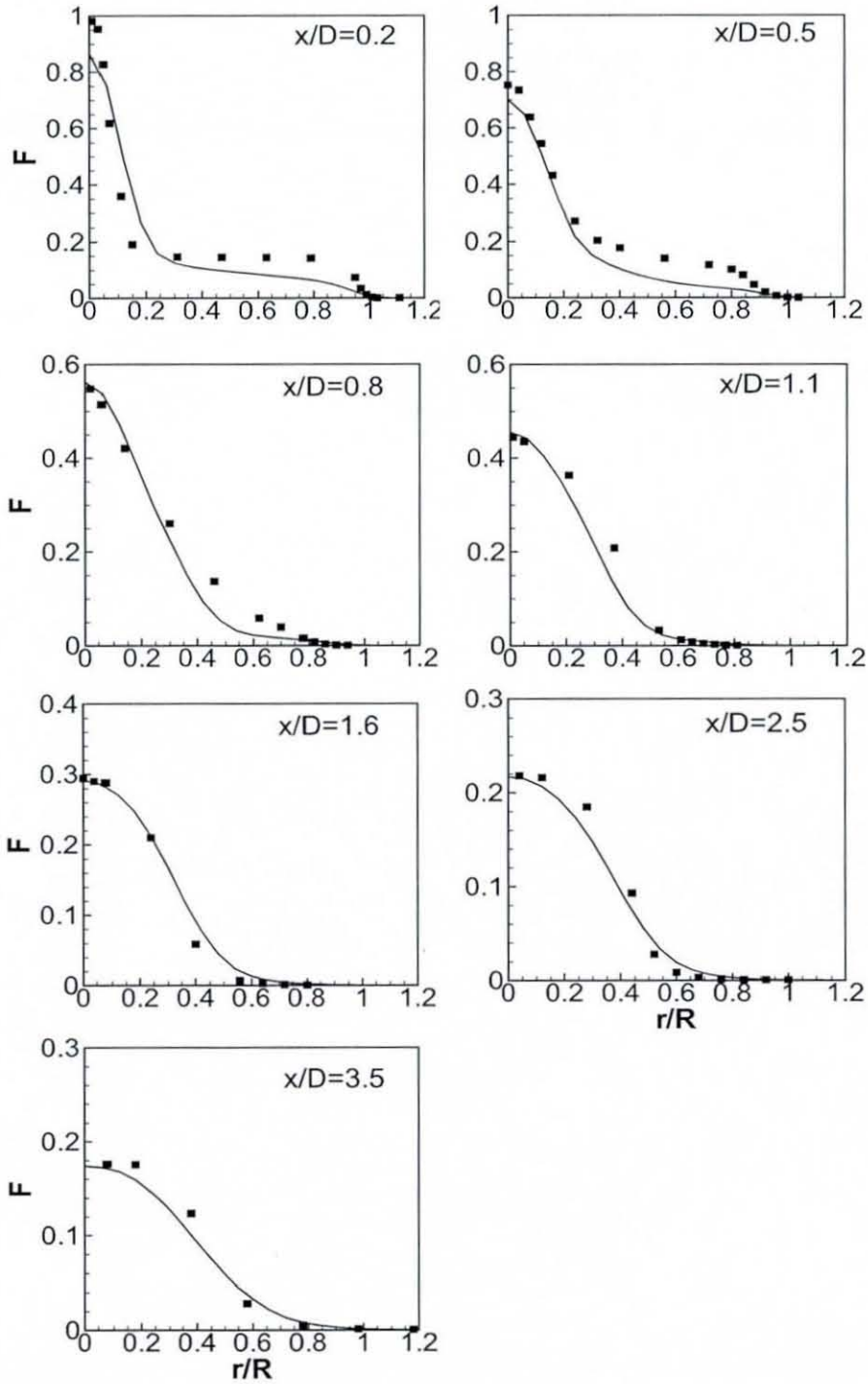


Figure 8.11: Radial profiles of mean mixture fraction in the SMH1 flame, lines represent LES results and symbols represent experimental measurements.

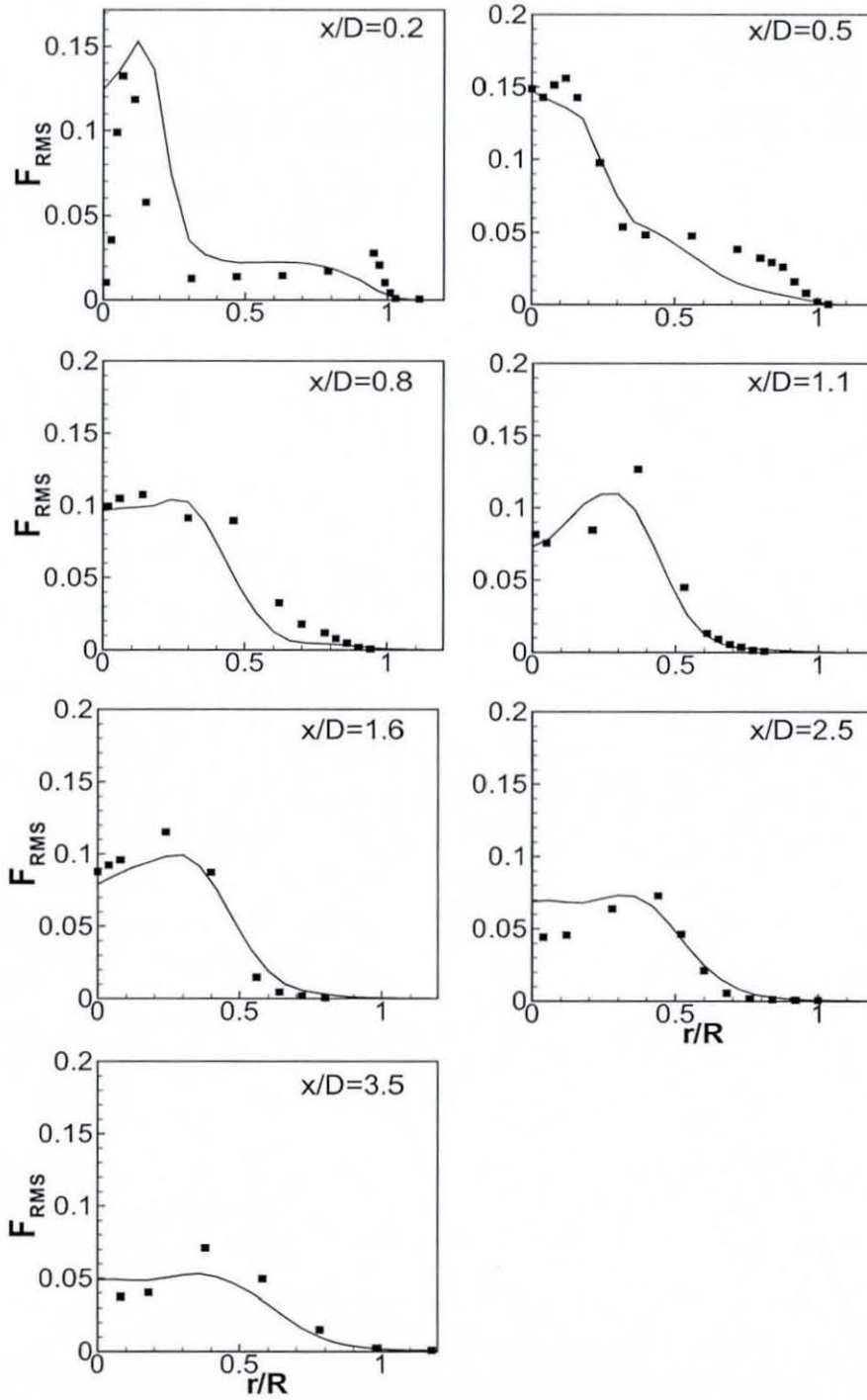


Figure 8.12: Radial profiles of mixture fraction variance in the SMH1 flame, lines represent LES results and symbols represent experimental measurements.

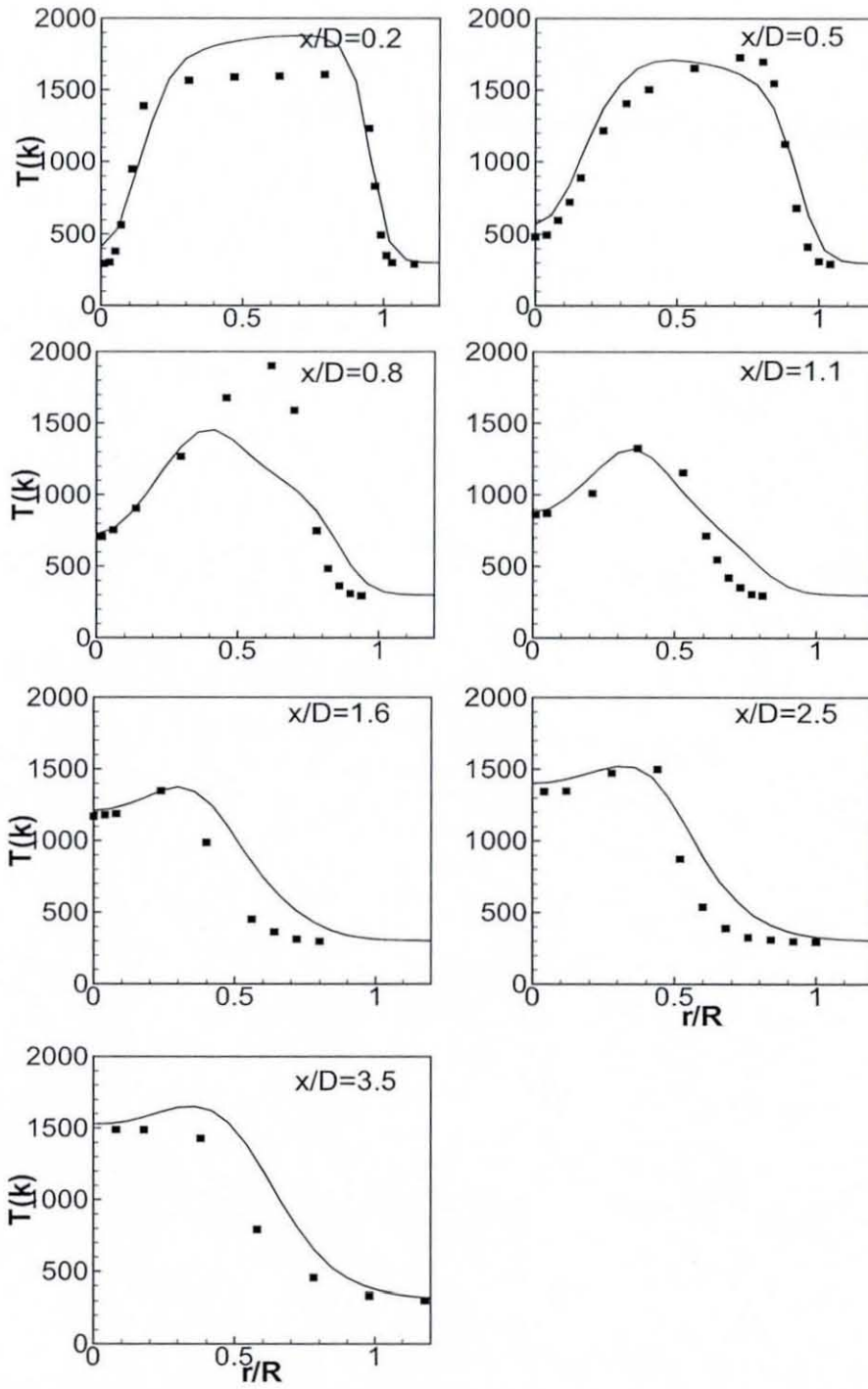


Figure 8.13: Radial profiles of mean temperature in the SMH1 flame, lines represent LES results and symbols represent experimental measurements.

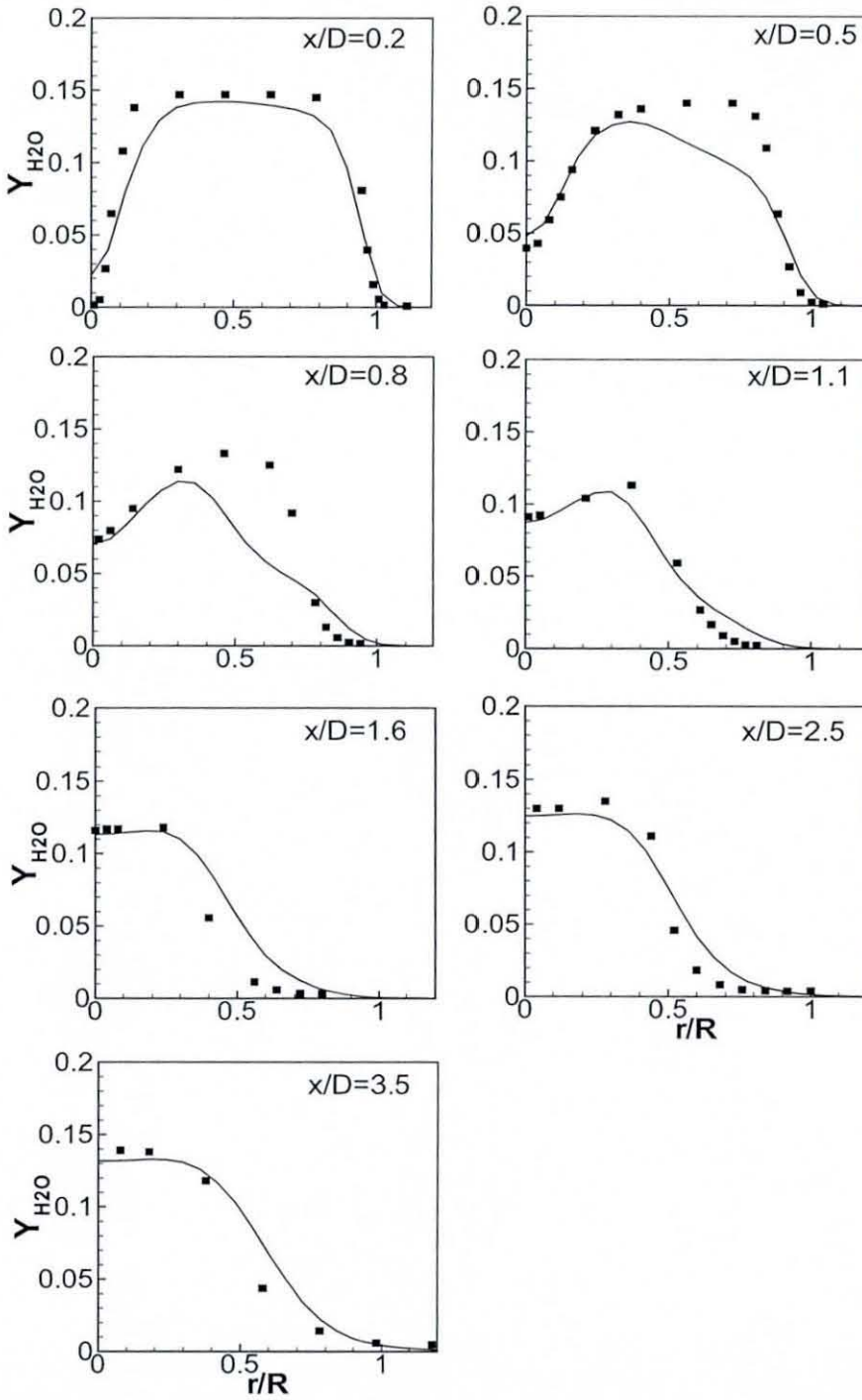


Figure 8.14: Radial profiles of mass fraction of  $H_2O$  in the SMH1 flame, lines represent LES results and symbols represent experimental measurements.

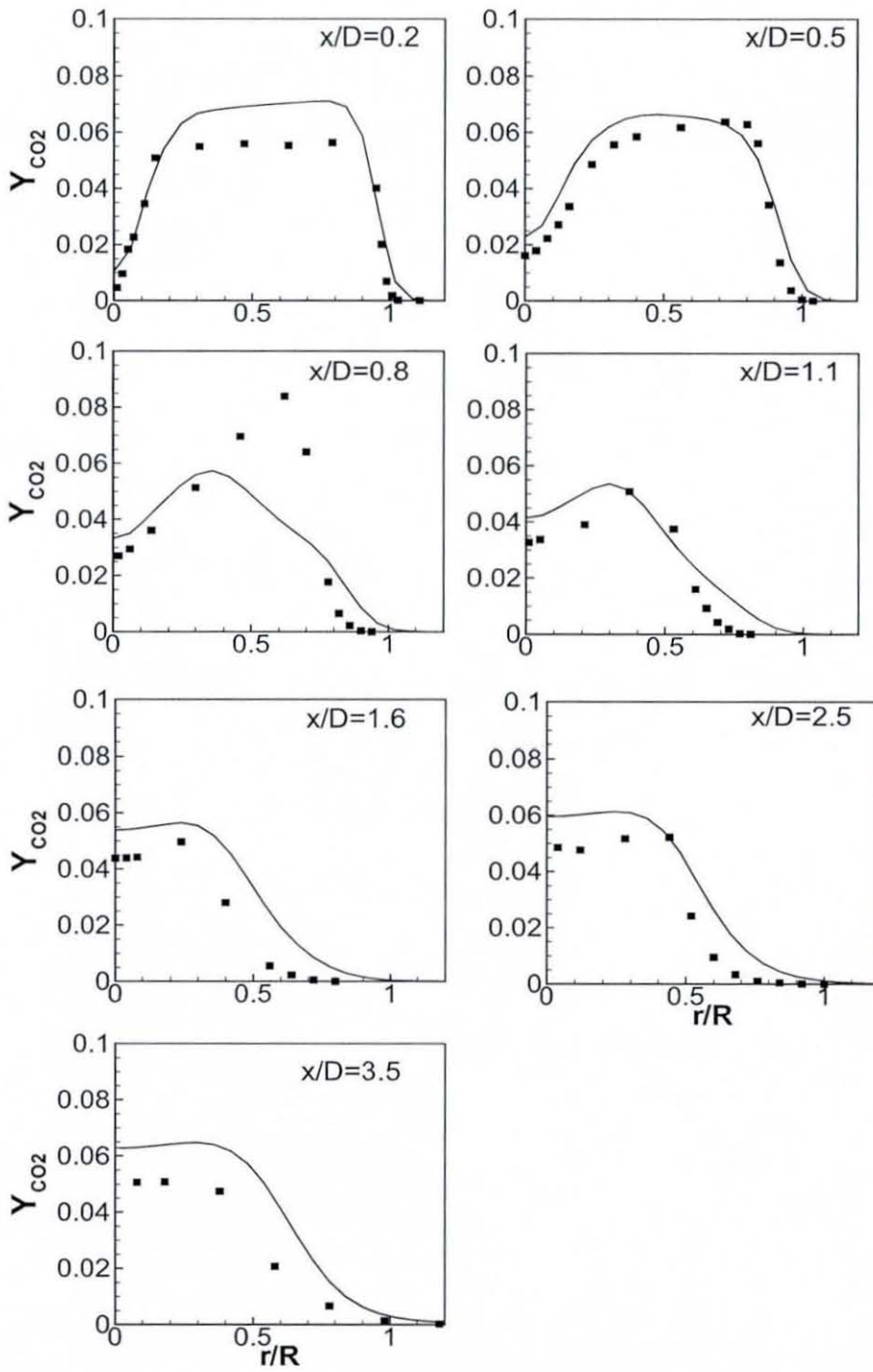


Figure 8.15: Radial profiles of mass fraction of CO<sub>2</sub> in the SMH1 flame, lines represent LES results and symbols represent experimental measurements.

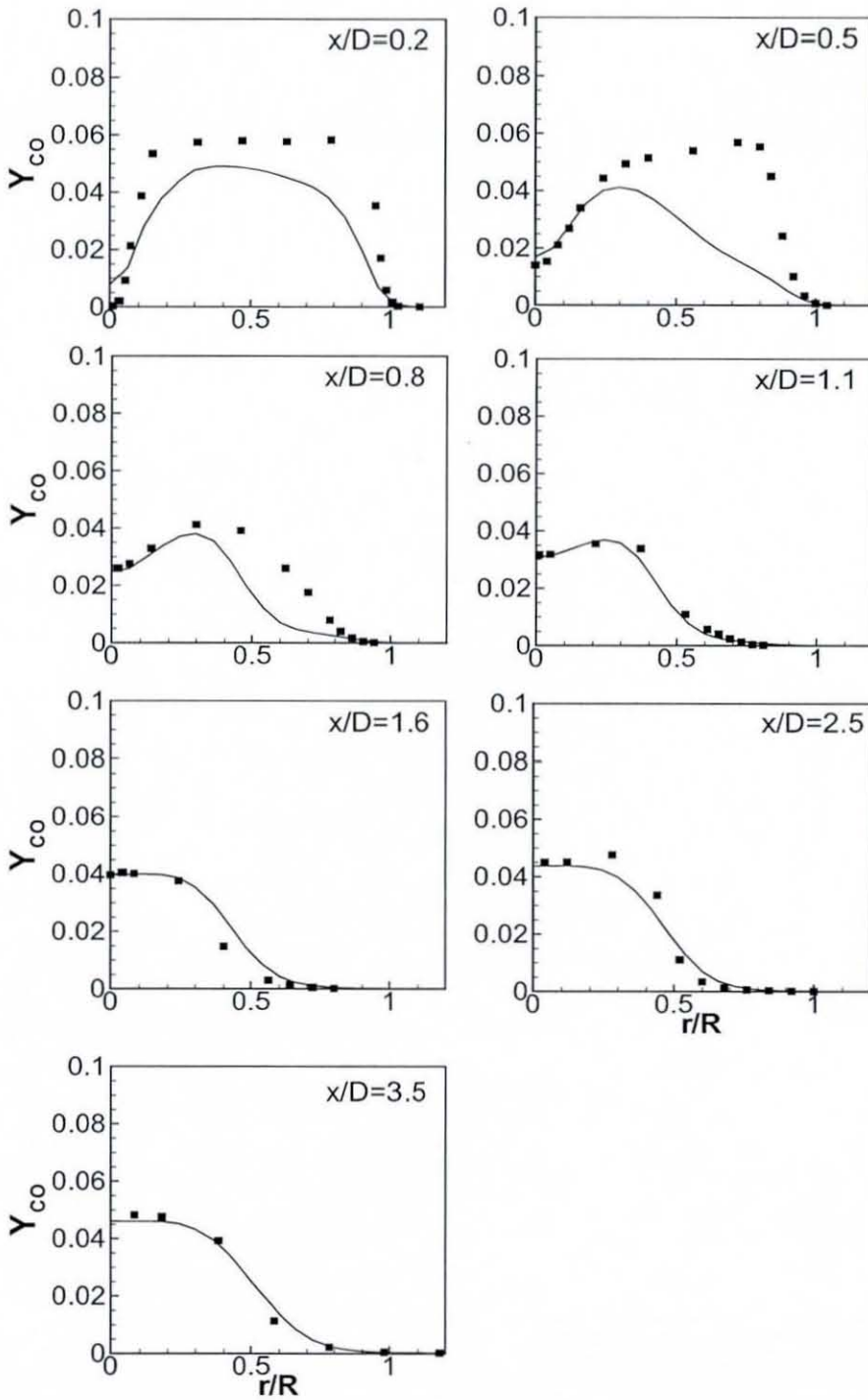


Figure 8.16: Radial profiles of mass fraction of CO in the SMH1 flame, lines represent LES results and symbols represent experimental measurements.

## 8.7 SMH2 flame

The flame SMH2 operated with CH<sub>4</sub>:H<sub>2</sub> (50 : 50) by volume, central jet velocity of  $140.8 \text{ m.s}^{-1}$ , and a moderate swirl number of 0.54, Masri *et al.* (2004), Al-Abdeli and Masri (2003b).

### Velocity fields

The experimental measurements observed an upstream recirculation zone, which extends upto  $x = 50 \text{ mm}$  along the axial direction. It is interesting to demonstrate that, SMH2 has no downstream recirculation and no centreline vortex breakdown despite having a larger swirl number (0.54). The reason behind this remains unknown and the only possibility is the lower value of the axial velocity at swirling annulus compared to SMH1. The contour plot of mean axial velocity and the velocity vector field generated from mean velocities is shown in Figure 8.17, which shows the predicted upstream recirculation zone. The time average mean axial velocity profiles at different axial locations are shown in Figure 8.18. It can be seen that the agreement is generally very good. At  $x/D = 0.8$ , the predictions well capture the negative mean axial velocity along the radial direction and the flow reversal. Hence the predicted recirculation zone is well estimated. The predicted negative values of the mean axial velocity at  $x/D \in \{0.136, 0.2, 0.4, 0.8\}$  indicate the flow reversal, which generates the upstream bluff body stabilized recirculation zone. The recirculation zone extends upto  $x/D = 1.0$ , which is in agreement with experimental observation. However, the centreline mean axial velocity is slightly overpredicted at downstream locations  $x/D \in \{1.7, 2.5, 3.5\}$ .

The comparisons of the mean radial velocities are shown in Figure 8.19. The predictions of the mean radial velocity, which is usually much more difficult to predict in swirling flow fields show reasonably good agreement. The comparison of the mean swirling velocity is shown in Figure 8.20. The peaks are well pre-

dicted in the inner shear layer at  $x/D \in \{0.136, 0.2\}$ . However, the predictions have not captured the peaks in the outer shear layer at  $x/D \in \{0.4, 0.8\}$ . Overall the mean swirling velocity predictions agree well with experimental data.

The agreement for the axial velocity fluctuations are good at all downstream axial locations (Figure 8.21). The fluctuations are very high near to the centreline at first four axial locations due to the sudden expansion of the bluff body. Figure 8.22 shows the comparison of the radial velocity fluctuations. The radial fluctuations are somewhat underpredicted at  $x/D \in \{0.136, 0.4, 0.8\}$  in between  $r/R = 0.3 - 1.0$ . Although the centreline value at  $x/D \in \{1.2, 1.7, 2.5, 3.5\}$  is overpredicted. The agreement is satisfactory at almost all downstream axial locations. The swirling velocity fluctuations shown in Figure 8.23 are very good at all downstream axial locations. The simulation successfully predicted all peak values of swirling velocity fluctuations around centreline inside the bluff body stabilized recirculation zone and around swirling annulus. The overall agreement for mean velocities and fluctuations are reasonably good for almost all axial positions.

### Scalar fields

Figure 8.24 shows the flame structure (mean temperature) of flame SMH2 predicted from LES. Figure 8.25 shows the radial profiles of the mean mixture fraction at downstream axial locations. It can be seen that the radial spread of the mixture fraction is slightly under-predicted at first four axial locations. Especially it has some large deviation in between  $r/R = 0.2 - 1.0$  at  $x/D \in \{0.2, 0.5\}$  (similar underprediction was seen in SMH1 calculation). However it is interesting to note that both flames have same deviation at this particular radial distance. The experimental data may have some errors at these two locations. The downstream predictions compare well with experimental measurements. The comparison for the mixture fraction variance is shown in figure 8.26. The results

although reasonable, fail to predict the peaks of the mixture fraction variance at some axial locations,  $x/D \in \{0.8, 1, 1\}$ . The downstream mixture fraction fluctuations, however agree well with measurements. Figure 8.27 shows the comparison of the temperature field. Compared to experimental measurements, at first three axial locations,  $x/D \in \{0.2, 0.5, 0.8\}$ , predicted temperature is well above the experimental measurements. This is mainly due to deviation in mixture fraction and its fluctuations at those axial locations. Further downstream the LES predictions of radial spread of the flame temperature agree well with experimental measurements. Figures 8.28-8.30 show the agreement between predictions and experimental measurements for all major species concentrations. The  $H_2O$  predictions are excellent at almost all axial locations. The flamelet model provides a good prediction of  $H_2O$  mass fraction inside the recirculation zone as shown in Figure 8.28. However,  $CO_2$  is overpredicted, especially in the region between  $r/R = 0.0 - 0.5$  at some axial locations. This overprediction occurs inside the recirculation region (see Figure 8.29). Radial mass fraction profiles of  $CO$  is shown in Figure 8.30. The  $CO$  predictions are slightly underestimated at  $x/D \in \{0.2, 0.5\}$ . Despite this discrepancy, the downstream predictions are very good at all considerable axial locations. The flamelet model successfully reproduces the radial spread and trends of  $CO$  mass fraction.

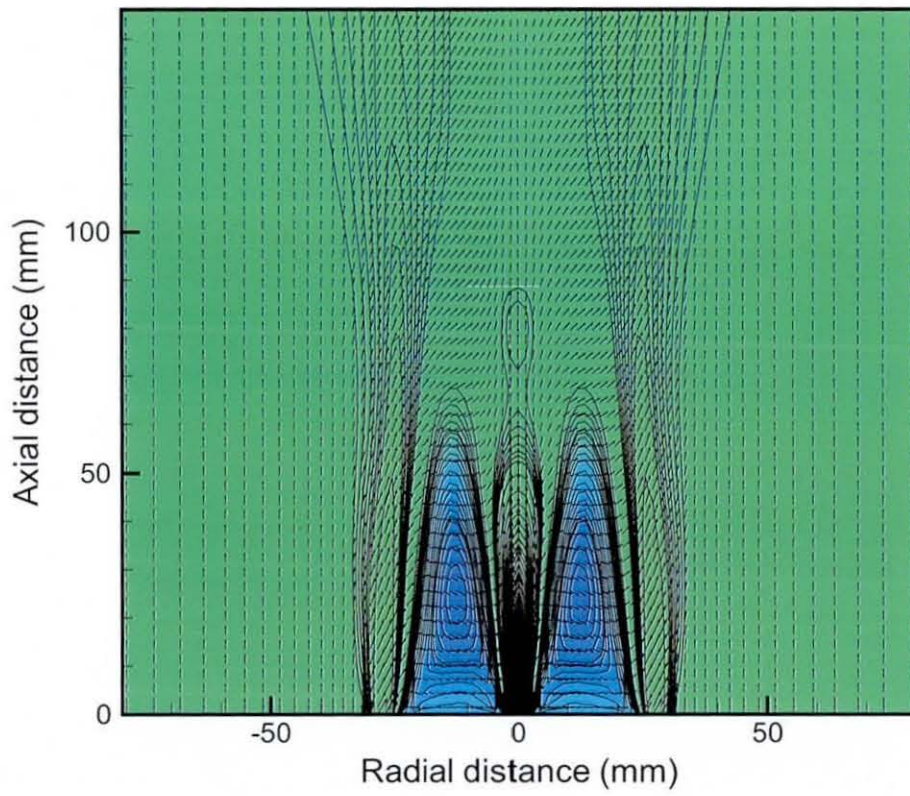


Figure 8.17: Contour plot of mean axial velocity and mean velocity vector field of flame SMH2.

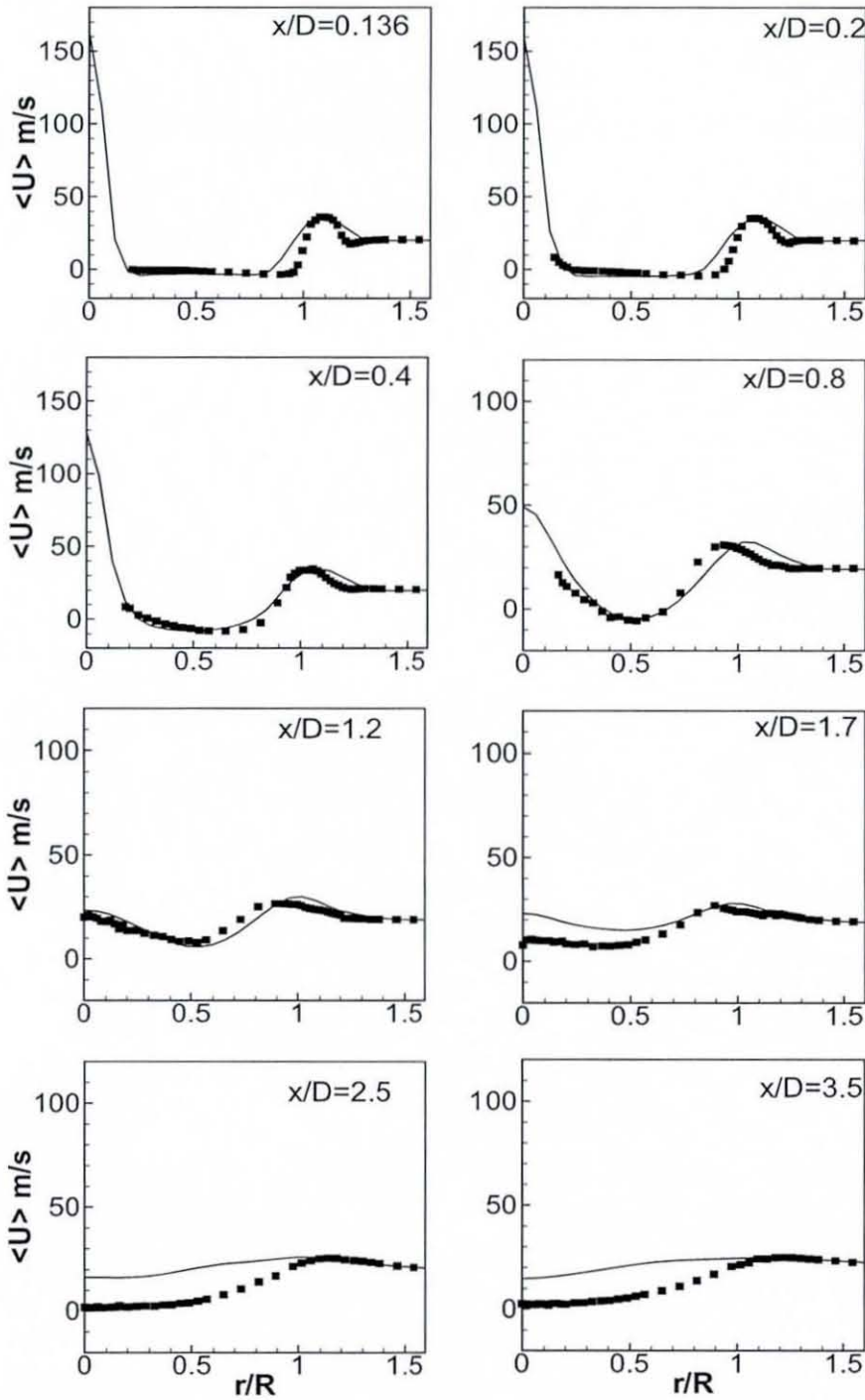


Figure 8.18: Radial profiles of mean axial velocity in the SMH1 flame, lines represent LES results and symbols represent experimental measurements.

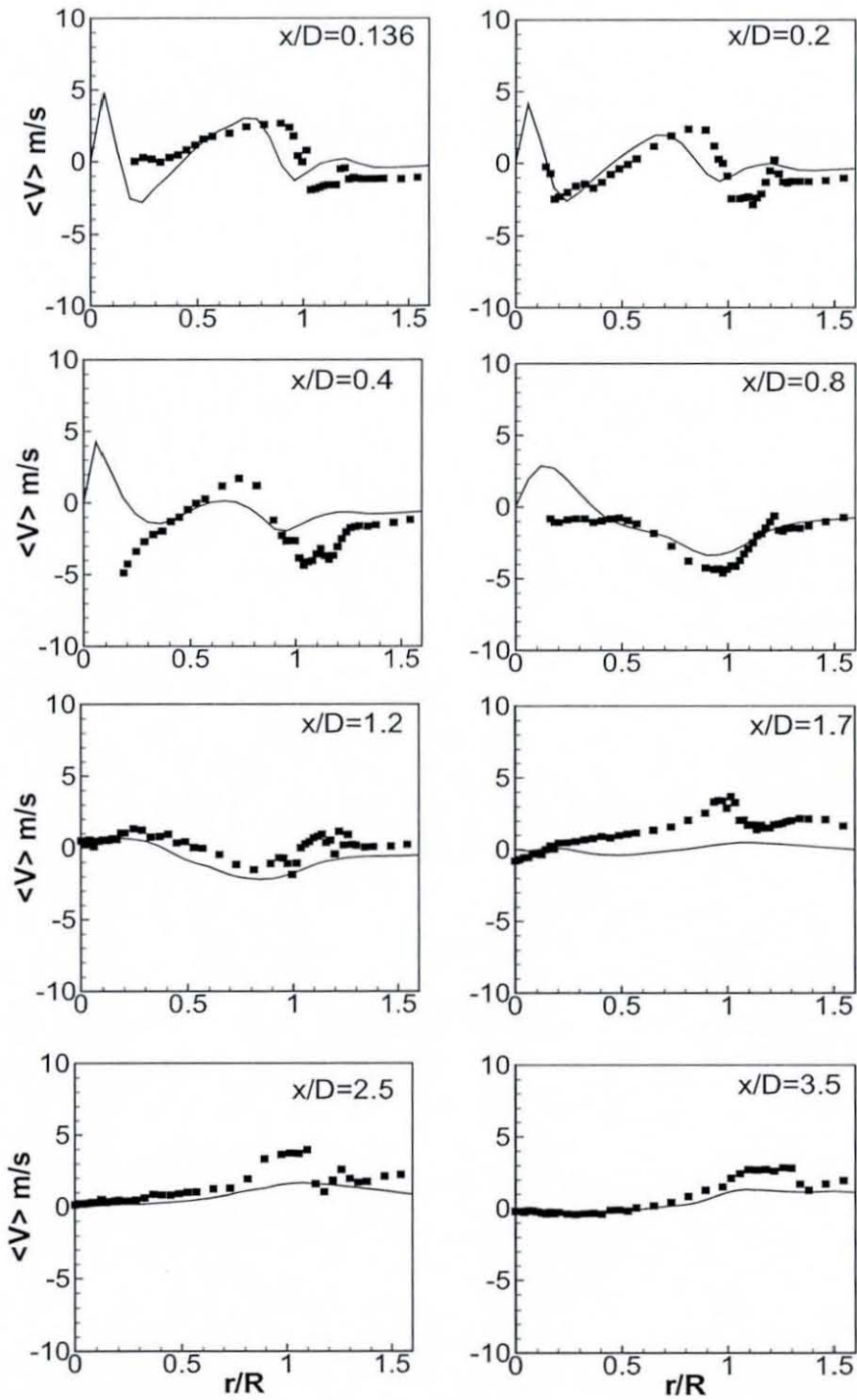


Figure 8.19: Radial profiles of mean radial velocity in the SMH2 flame, lines represent LES results and symbols represent experimental measurements.

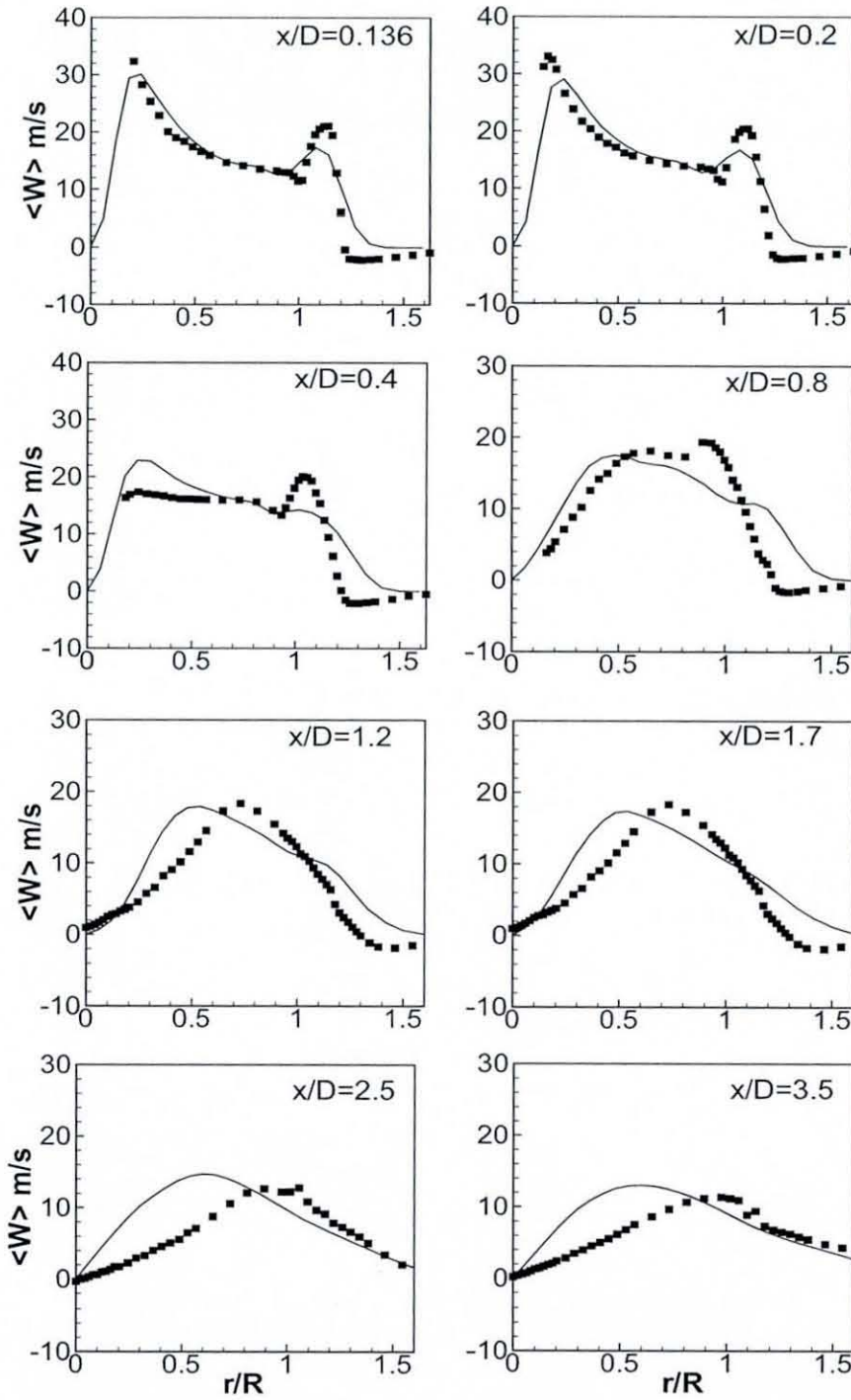


Figure 8.20: Radial profiles of mean swirling velocity in the SMH2 flame, lines represent LES results and symbols represent experimental measurements.

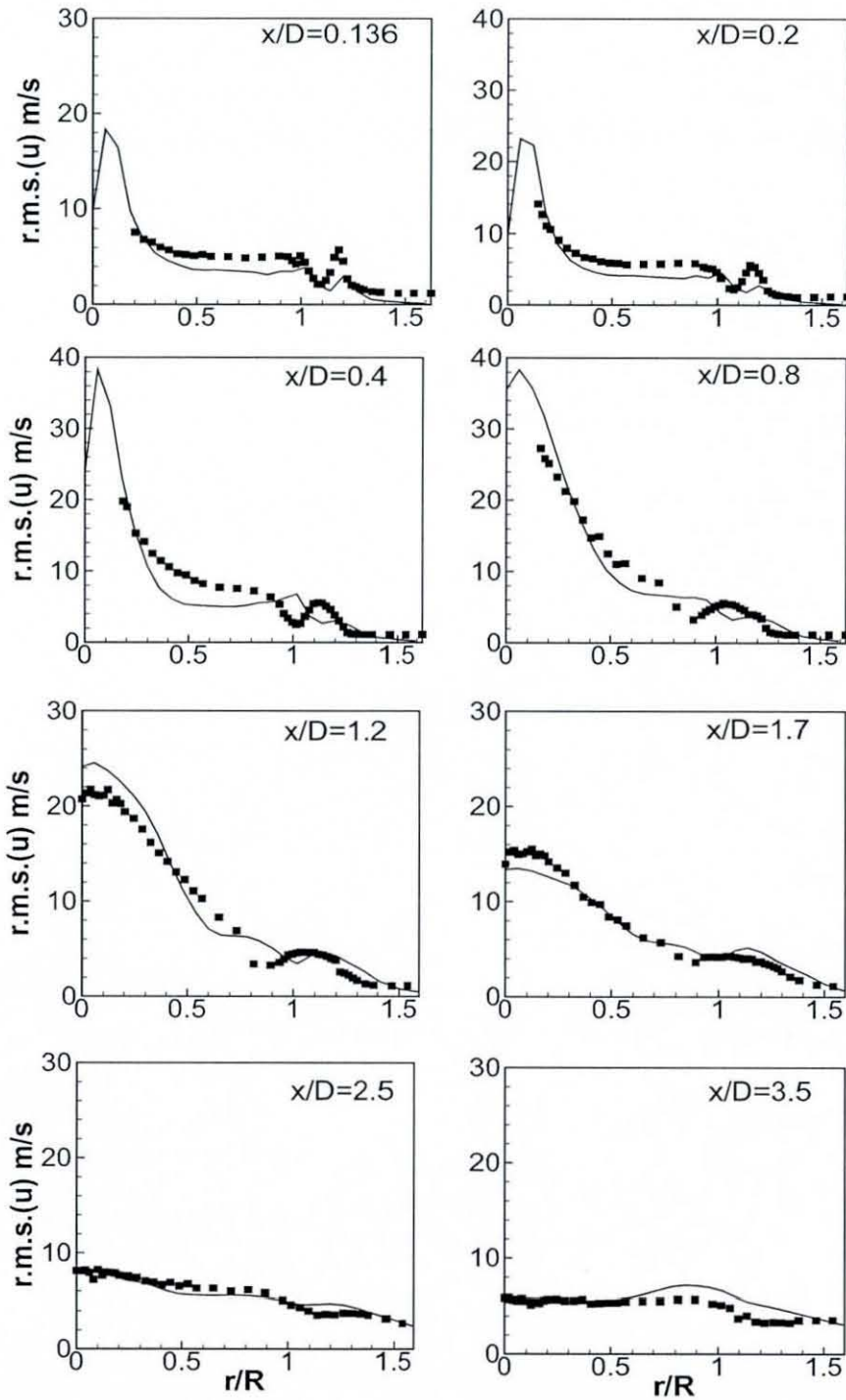


Figure 8.21: Radial profiles of RMS axial velocity in the SMH2 flame, lines represent LES results and symbols represent experimental measurements.

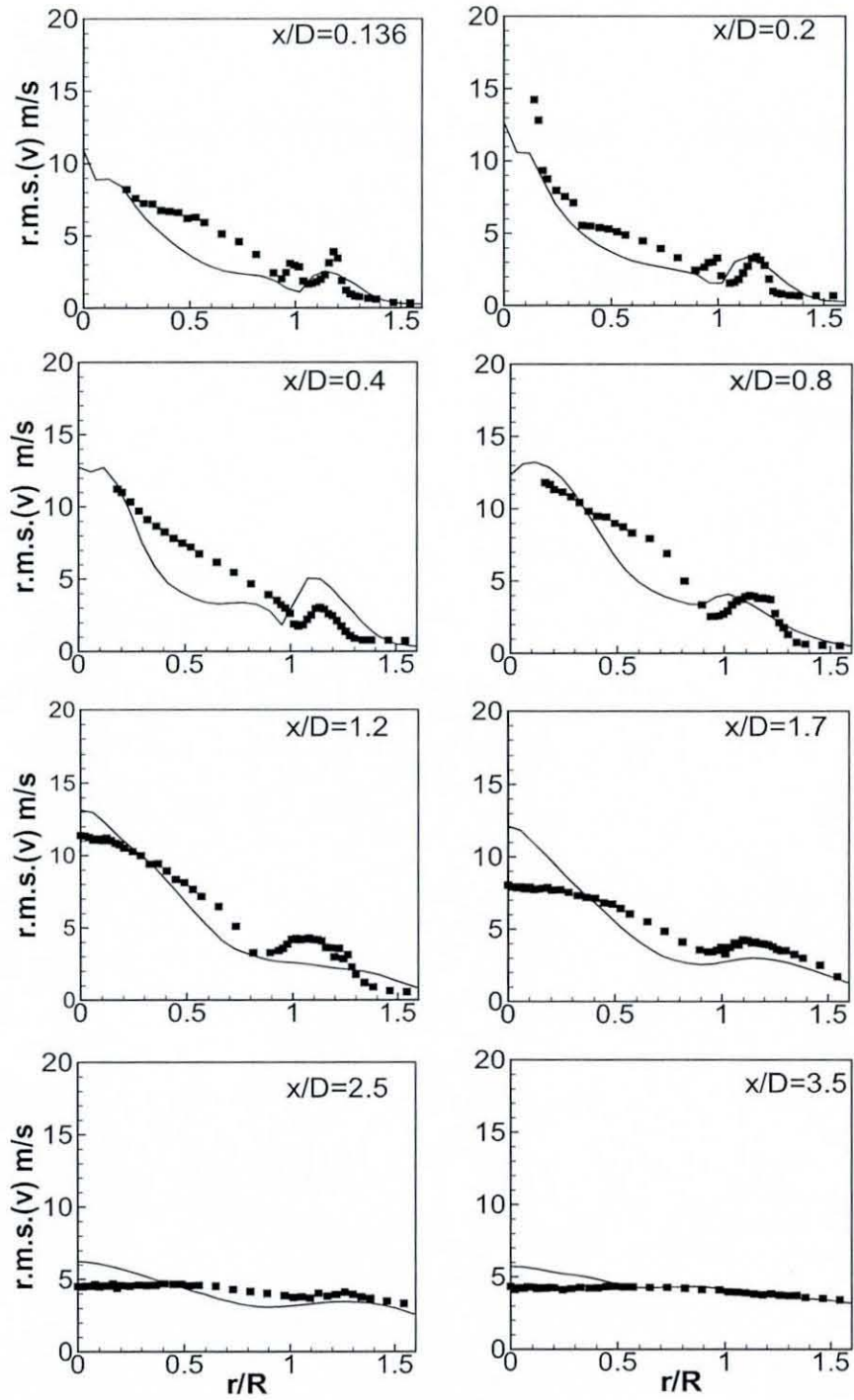


Figure 8.22: Radial profiles of RMS radial velocity in the SMH2 flame, lines represent LES results and symbols represent experimental measurements.

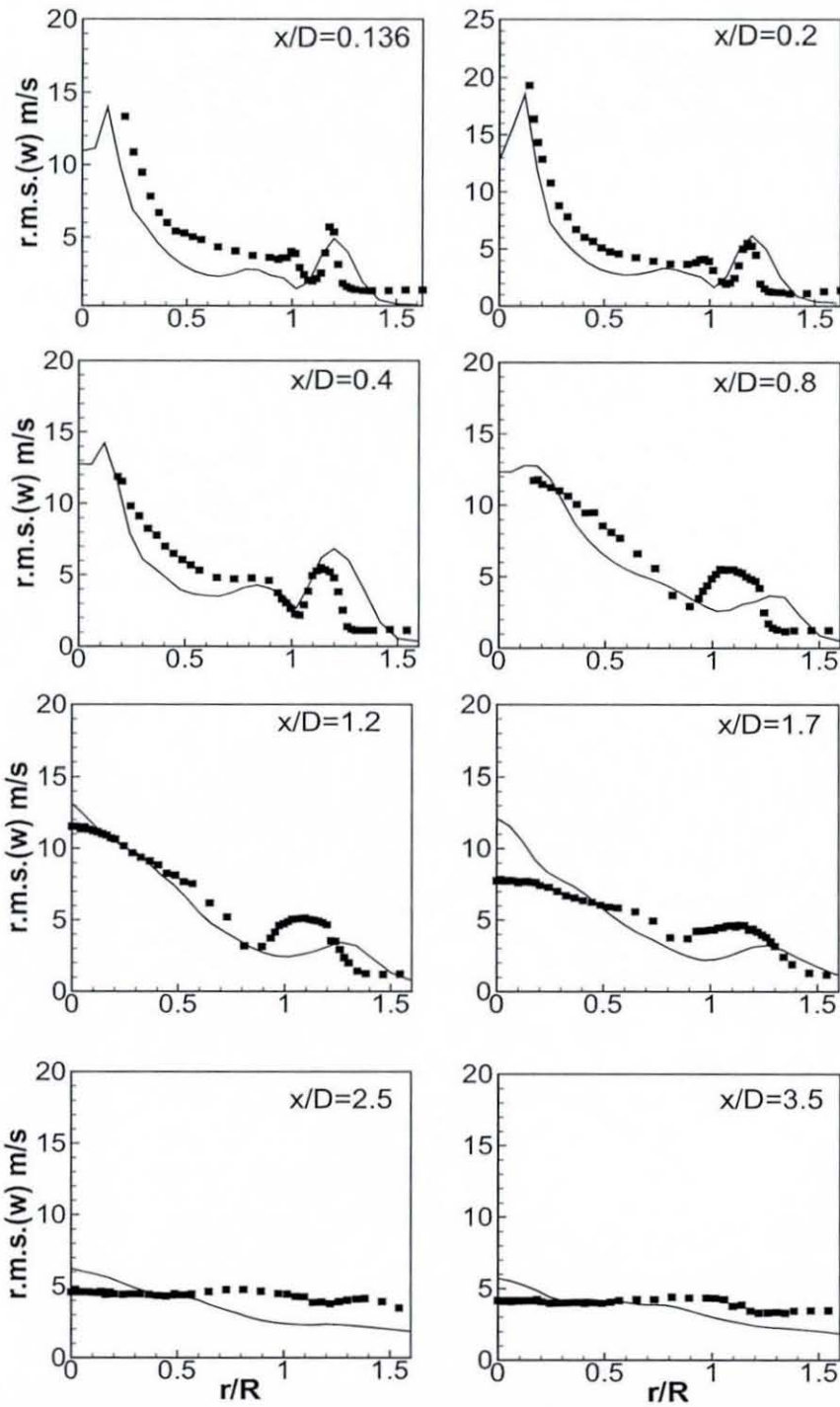


Figure 8.23: Radial profiles of RMS swirling velocity in the SMH2 flame, lines represent LES results and symbols represent experimental measurements.

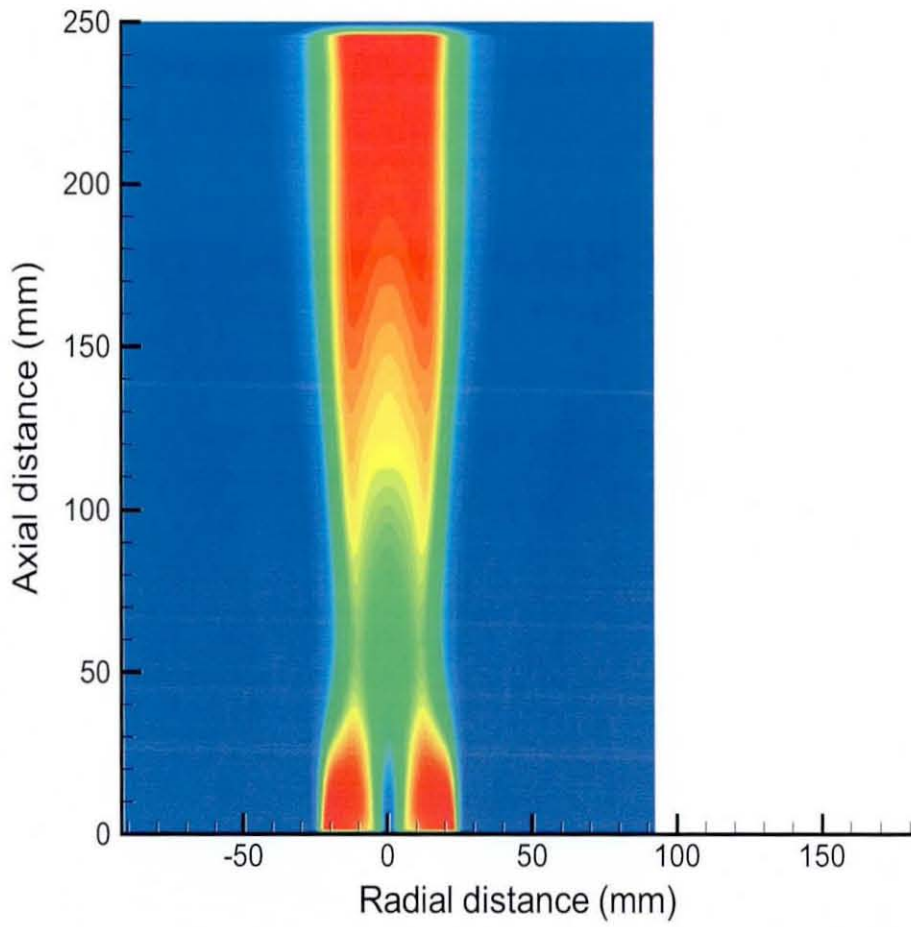


Figure 8.24: Contour plot of mean temperature of flame SMH2.

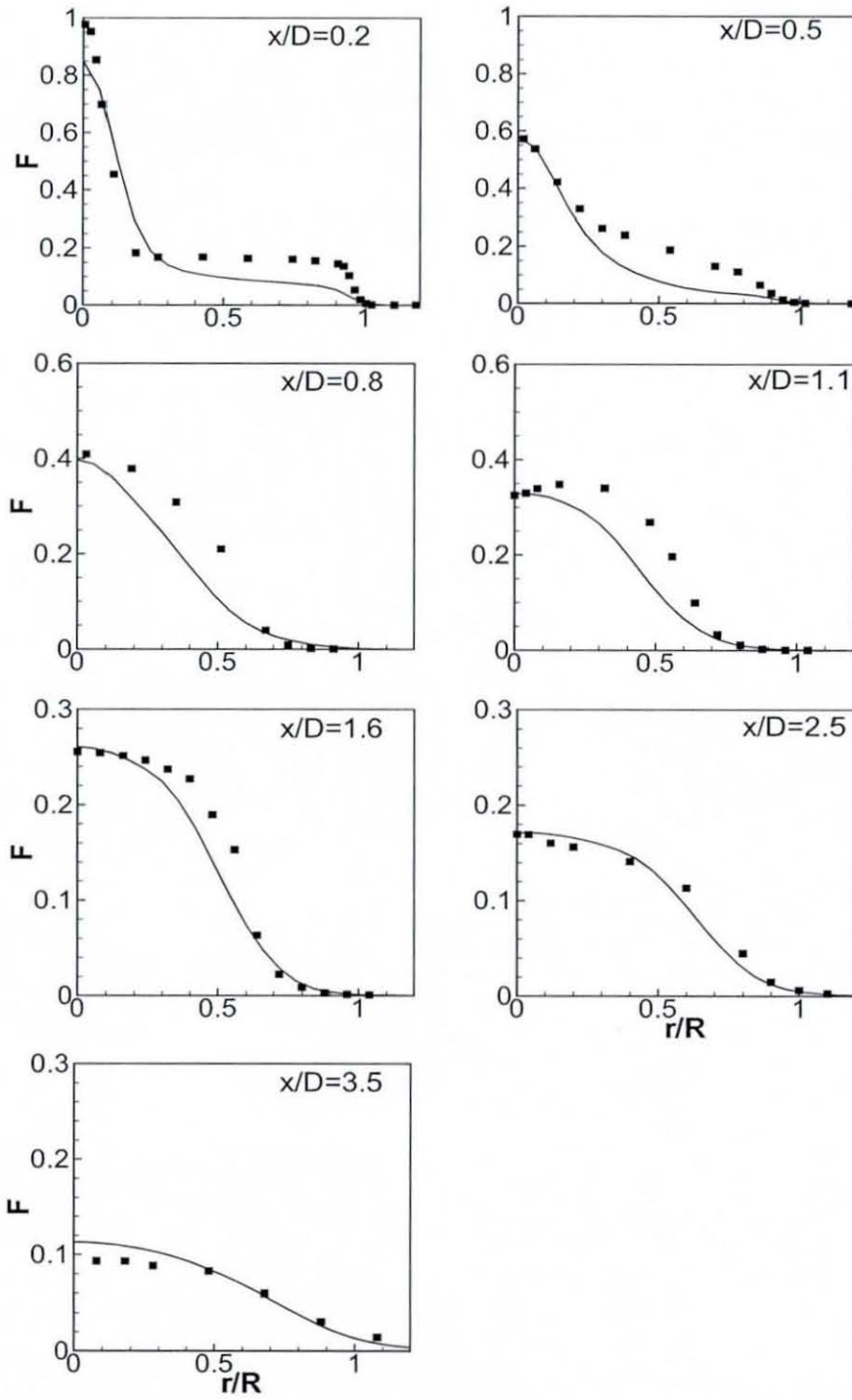


Figure 8.25: Radial profiles of mean mixture fraction in the SMH2 flame, lines represent LES results and symbols represent experimental measurements.

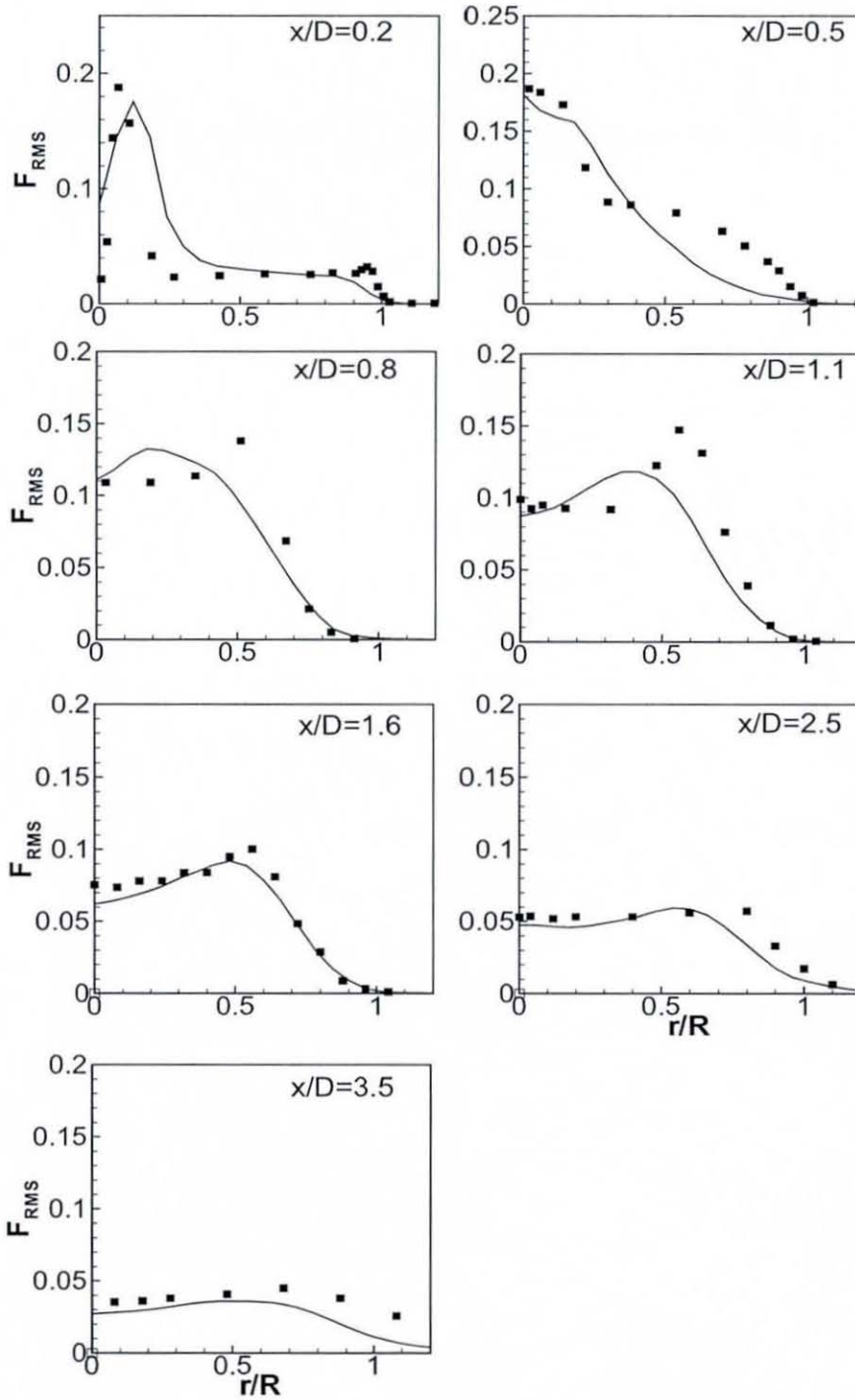


Figure 8.26: Radial profiles of mixture fraction variance in the SMH2 flame, lines represent LES results and symbols represent experimental measurements.

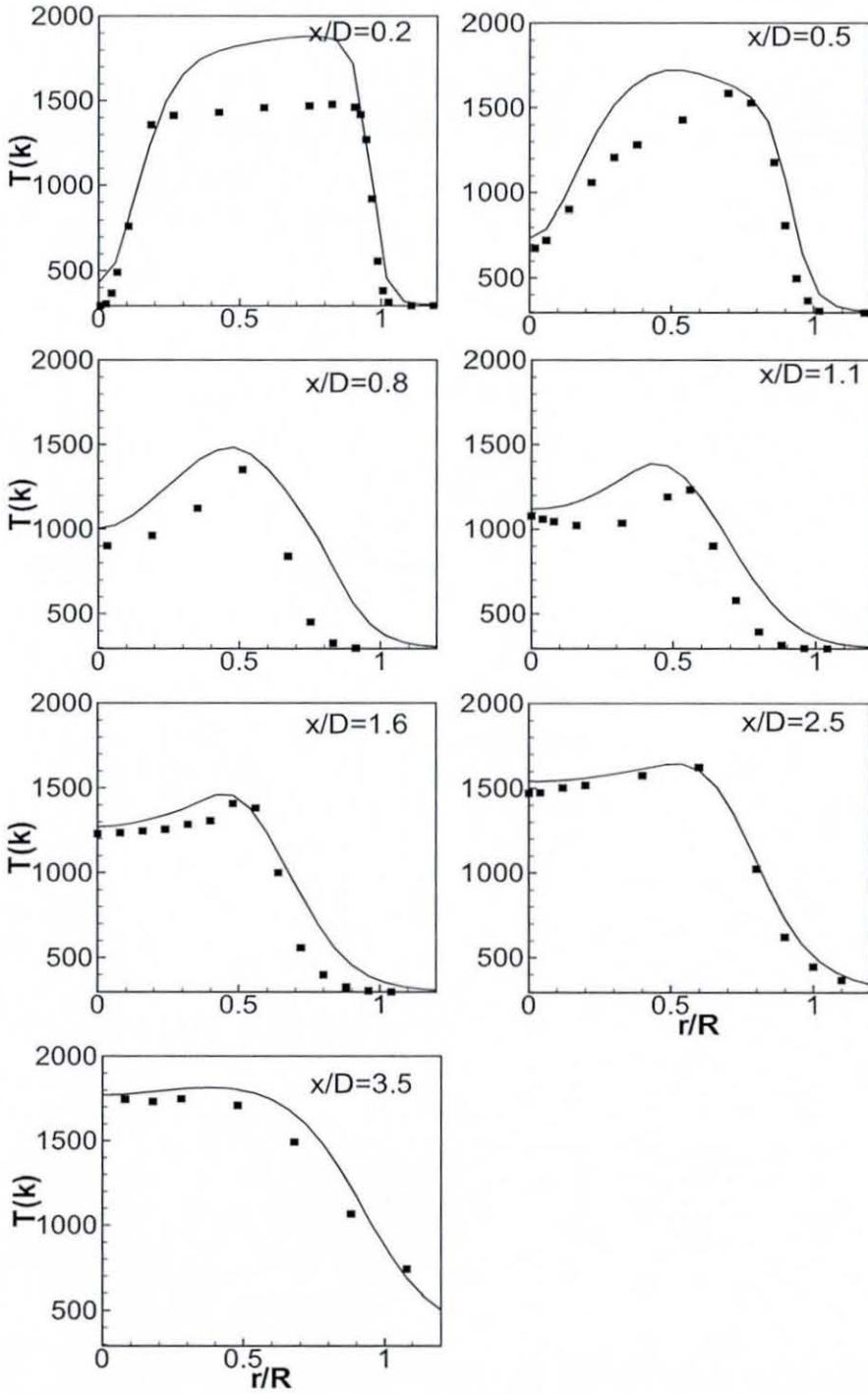


Figure 8.27: Radial profiles of mean temperature in the SMH2 flame, lines represent LES results and symbols represent experimental measurements.

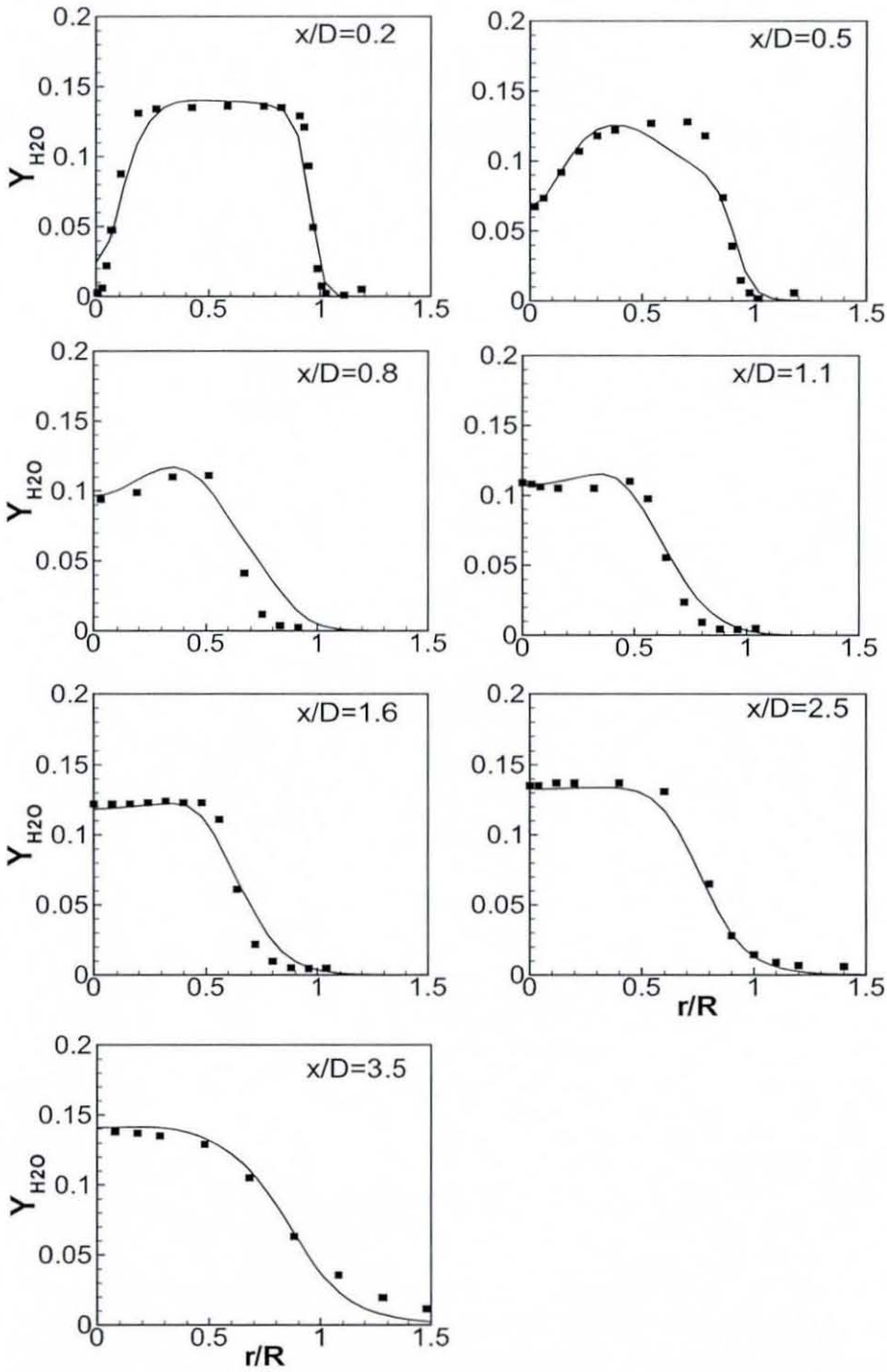


Figure 8.28: Radial profiles of mass fraction of H<sub>2</sub>O in the SMH<sub>2</sub> flame, lines represent LES results and symbols represent experimental measurements.

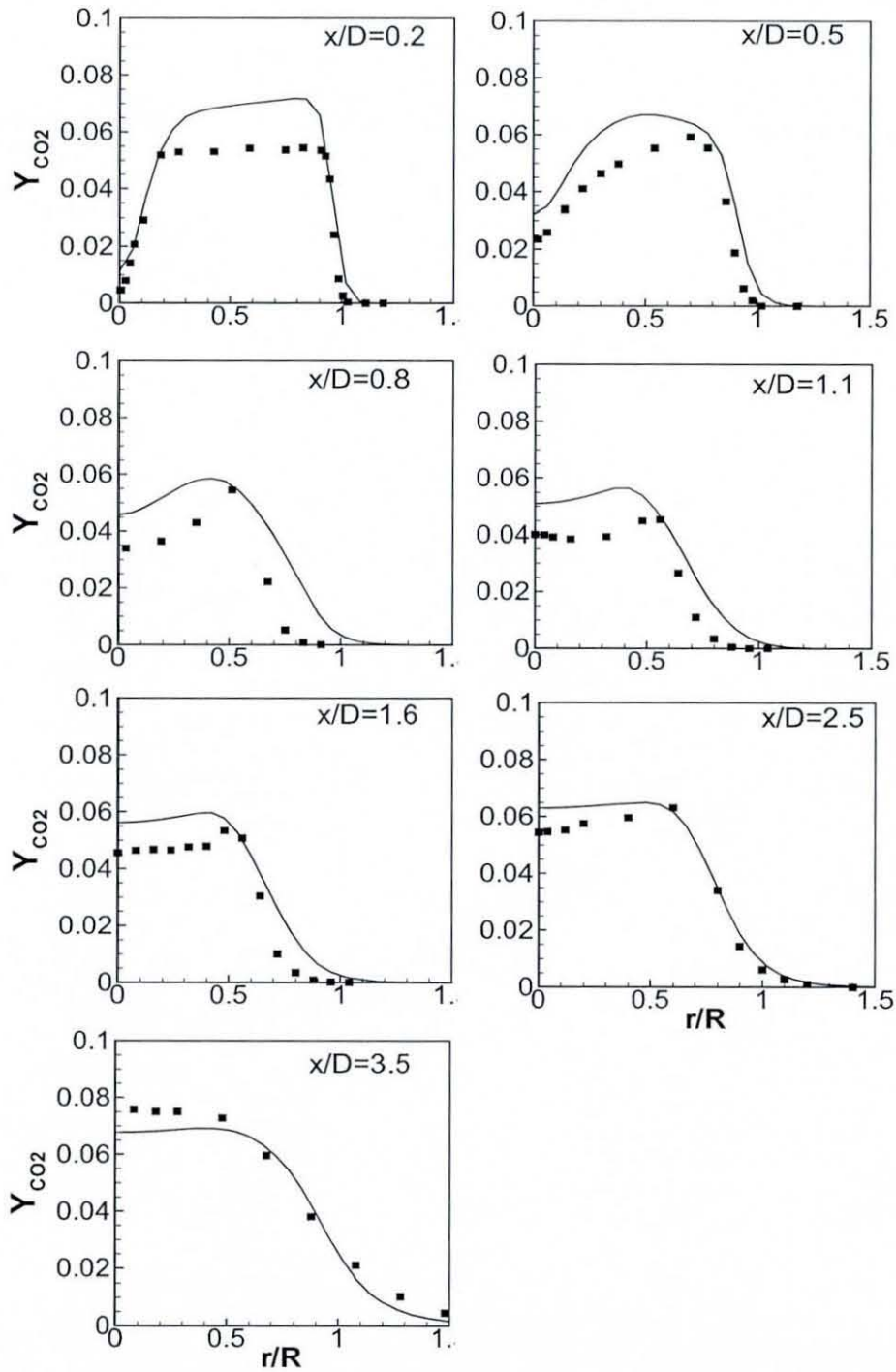


Figure 8.29: Radial profiles of mass fraction of CO<sub>2</sub> in the SMH2 flame, lines represent LES results and symbols represent experimental measurements.

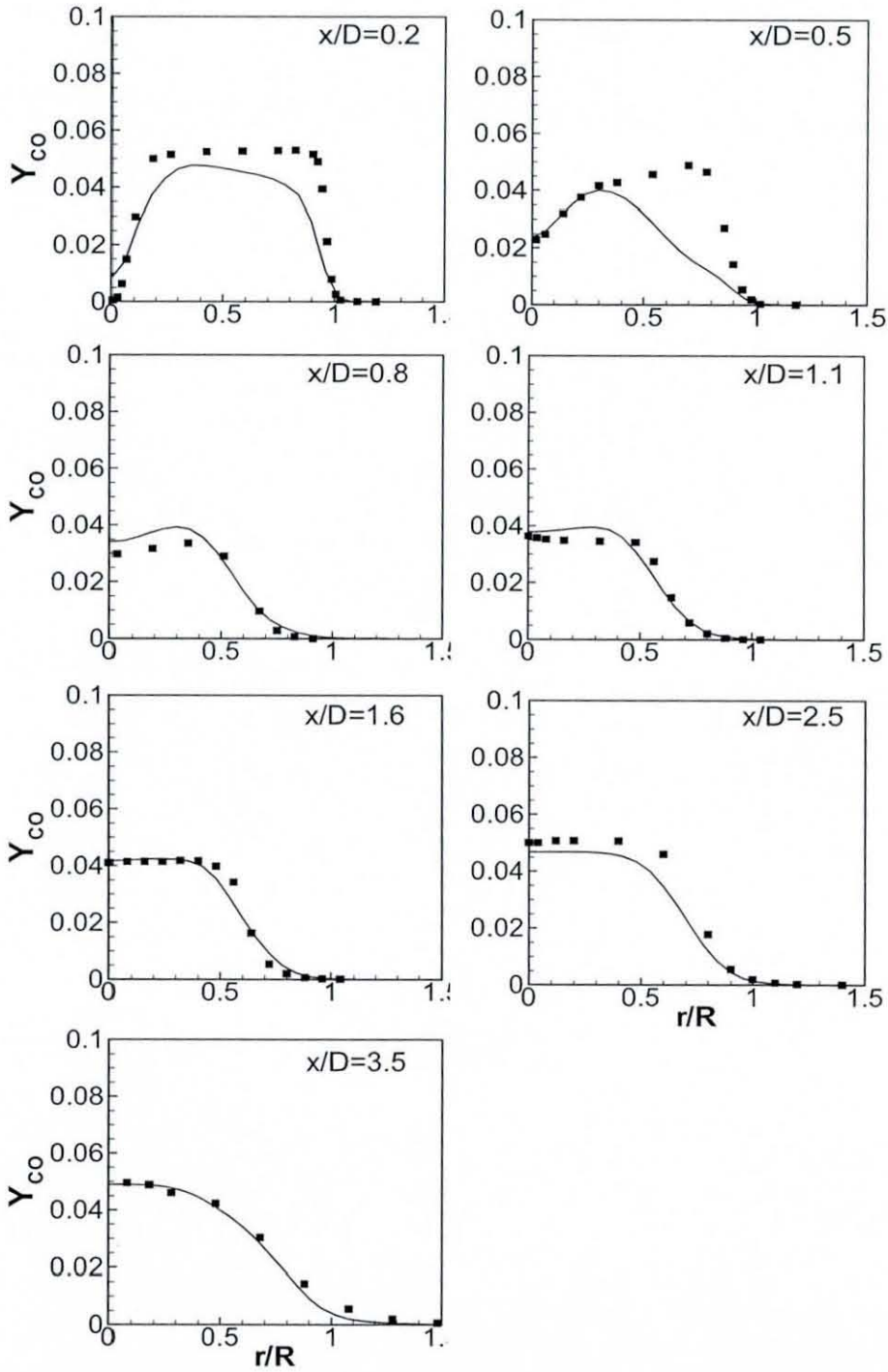


Figure 8.30: Radial profiles of mass fraction of CO in the SMH2 flame, lines represent LES results and symbols represent experimental measurements.

# Chapter 9

## Conclusions and Future Directions

### 9.1 Conclusions

The primary focus of this work has been to examine the ability of Large-Eddy Simulation (LES) methodology for modelling of flow field and flame structure in more realistic laboratory scale combustion devices. The device modelled here was the swirl-stabilized non-premixed burner known as the Sydney swirl burner, which has been a target model problem for the TNF workshop series. In this study a LES code was developed with the laminar flamelet model of combustion to model the Sydney swirl burner. The developed LES calculations were first validated the isothermal swirling jets data obtained using simple well defined boundary conditions. The calculations have been carried out for three different isothermal test cases based on their swirl and Reynolds number. The sensitivity analysis has been carried out to assess the effects of grid resolution, inlet profiles, swirl number and Reynolds number. The simulations show that with appropriate inflow, outflow boundary conditions and sufficient grid resolution LES successfully simulated the experimentally observed structure and topology of the swirling flow fields and results agree well with measured mean velocity, rms fluctuations

and the Reynolds shear stresses.

In the non-swirling case turbulence is mostly generated in the shear layer near sudden expansion at the bluff body wall. In the swirling flows turbulence is not only generated in the shear layer near the sudden expansion, but also in the vortex breakdown (VB) bubble. It is found that the centre-line axial flow recirculates or break down (bubble type vortex breakdown) is achieved in the flow with a moderate swirl number (N29S054), rather than the high swirl number (N16S159). However, it is evident from the results that the axial momentum (or Reynolds number) of the swirling annulus plays a major role in determining the onset of vortex breakdown. The combination of low swirl number and higher primary axial velocity seen to cause the vortex breakdown. Experimentally observed features of vortex breakdown and flow structures at different operating conditions were successfully reproduced by the present large eddy simulations indicating that LES is capable of predicting VB phenomena which occurs only at certain conditions. The simulations have been able to capture the fast decay of turbulence in swirling flows due to the fast transport of turbulent kinetic energy toward radial direction as a result of the high centrifugal force induced by swirling motion and this helps to reproduce the important recirculation zones seen in experimental results.

While, a considerable amount of work has been carried out here (dynamics of isothermal swirling flow field), some efforts are still required to improve the accuracy, applicability and efficiency of the LES technique to the field of turbulent combustion. As a final step, most difficult test cases of Sydney swirling flames were simulated. They feature non-premixed flames stabilized by an upstream recirculation zone caused by the bluff-body and a secondary downstream stagnation region induced by swirl, which pre-heat(s) the fuel-air mixture by recirculating reaction products. Their flow is more complex and relevant to flows in practical

combustors. Thereby facilitating a more realistic estimation prediction capability of LES.

In the present work, an algorithm was developed for large eddy simulation of variable density reacting flows in simple well-defined configurations. Particular attention was given to both the primary conservation (mass, momentum, scalar) and secondary conservation (kinetic energy, scalar energy) properties of the method. The algorithm uses the primitive variables, which are staggered in both space and time. A steady laminar flamelet model, which includes the detailed chemical kinetics and multicomponent mass diffusion has been implemented in the LES code. An artificial method was implemented to generate instantaneous turbulent velocity fields that are imposed on the inflow boundary of the Cartesian grid. To improve the applicability of the code, various approaches were developed to improve stability and efficiency. This resulted in a computer program that yields satisfactory results for the swirling flames presented in this work.

The computed program was validated for two different swirling flames from SMH group. In SMH group, the LES predictions captured the bluff body stabilized upstream recirculation zone. Although good results were achieved for the isothermal flow, the investigation of flames revealed some challenging properties and difficulties of the LES technique. In particular the occurrence of vortex breakdown, which is very sensitive to swirl, the wake-effect of the bluff-body, and interactions between the central jet and the swirling coflow was hard to predict. It is interesting to note that independent of the present work, an LES investigation by another group Stein and Kempf (2006) resulted in very similar results and the same overall flow behavior for flame SMH1. The modelled swirling flames contain highly rotating zones of gas around the geometric centreline of the flow. These zones form collar-like flow features downstream of the bluff body stabi-

lized recirculation zone near the necking region of the flame. Despite capturing the upstream recirculation zone, the simulation fails to capture the downstream vortex breakdown for the SMH1 flame, which is observed in the experimental measurements. Good agreement was obtained between computations and the experimental measurements for both mean and fluctuating velocity profiles, mean and rms of mixture fraction profiles, mean temperature and product concentration. The steady laminar flamelet model appears to be an adequate model for capturing basic flame behavior. However, the steady laminar flamelet model may not be valid in some regions of swirling flames and further improvements to the combustion model are expected to improve the peak temperature predictions. Additionally it has been found that small errors in the computed flow field, particularly the slight deviation of the mixture fraction leads magnification of errors in temperature field and major species concentrations, as shown in comparisons.

The results of this study show that LES seems to be more suitable for such complex flows. To fully appreciate the present effort, the results presented here have been compared with those presented at the Turbulent Non-Premixed Flames (TNF8) workshop (2006) and the results presented in this thesis were seen to be very good compared with results obtained by other international groups working in this series of flames. However, the present combustion simulations do not include combustion process such as pollutant formation and thermal radiation, and thus future improvements will be necessary. While, investigation on various aspects of LES of swirling flames has been investigated in this work, further effort is required to improve the robustness and accuracy of LES based swirl combustion. The effort required to accomplish these simulations was reasonably moderate, confirming that LES has a great potential in engineering applications. With further advancement of computer hardware and software technologies LES

could be more useful for general engineering flows in the future.

## 9.2 Present contribution

The major contribution of this work can be summarized as follows:

- Development of a LES code known as PUFFIN Kirkpatrick (2002) on a structured Cartesian grid to simulate combustng swirl flows. The code is written in FORTRAN 90 modular format.
- Development of accurate swirling inflow boundary conditions: the instantaneous inflow boundary conditions have been generated by using mean velocity profiles with random fluctuations. The fluctuations are generated from a Gaussian distribution such that the inflow has correct level of turbulent kinetic energy obtained from experimental measurements.
- Development of an iterative time advancement scheme for the variable density calculations: for incompressible variable density flows both the velocity and density field must be corrected to ensure conservation of mass. Since density depend on mixture fraction (in flamelet calculation) an iterative method is required.
- Implementation the flamelet based subfilter scale combustion model: the steady laminar flamelet model is used as a combustion model. The turbulence and chemistry interaction is modelled through the beta pdf approach.
- Comprehensive validation of LES predictions for turbulent isothermal swirling flow fields: the cases considered have swirl numbers ranging from 0 to 1.59 and Reynolds numbers from 32400 to 59000. With suitable inflow, outflow boundary conditions and sufficient grid resolutions the LES calculations

found to be in good agreement with experimental data. It has been observed that the onset of downstream recirculation and vortex breakdown does not depend on the attainment of high swirl number alone. It appears that the bubble type vortex breakdown is achieved in the flow with a lower rather than higher swirl number. The axial momentum of the swirling annulus plays an important role in the onset of vortex breakdown. The combination of lower swirl number and higher axial velocity of the primary annulus leads to establish the downstream central recirculation zone (VB). These features have been successfully reproduced by LES calculations. For all the cases considered here LES calculations were successful in predicting observed recirculation zones and generally showed reasonably good agreement with experimentally measured mean velocities, their rms fluctuations and Reynolds shear stresses.

- Comprehensive validation of LES predictions for turbulent swirling flames: the predicted flames are known as SMH1 and SMH2 has fuel of CH<sub>4</sub>:H<sub>2</sub> (50:50 by volume). The swirl number of SMH1 is 0.32 and SMH2 is 0.54. With appropriate inflow, outflow boundary conditions and relatively fine grid resolutions, LES well predicted the time averaged mean velocities and rms fluctuations for all considered axial positions. The LES predictions have captured the bluff body stabilized upstream recirculation zone for both flames. The swirling flames modelled contain highly rotating zones of gas around the geometric centreline of the flow. These zones leads to form the collar-like flow features downstream of the bluff body stabilized recirculation zone near the necking region of the flame. The laminar flamelet model is well capable of predicting flame temperature and concentrations of major species without local extinction.

- LES predictions of swirl induced recirculation and vortex breakdown (VB).

### 9.3 Future directions

The present LES study for isothermal and reacting swirling flows has raised some issues that need further investigation. Further improvement of grid resolution, sensitivity of the boundary conditions and the numerical schemes for variable density flows including the compressibility effects due to high velocities could be considered to improve agreement between predictions and measurements. Particularly further investigations will require analyzing the occurrence of vortex breakdown, which is directly sensitive to swirl and Reynolds number, jet precession and upstream bluff body stabilized recirculation zone. The digital filter turbulent inflow generation method introduced by Klein *et al.* (2003) could be possible to implement in the existing LES code.

It is also quite limited to handle the complex geometries in Cartesian coordinate system. With this said, there are several possible recommendations that could greatly advance the computational algorithm's edibility and efficiency. In order to model advanced combustion systems, the numerical model must be able to handle arbitrarily complex geometries. Unstructured grid algorithms may be able to treat complex flow fields better and hence converting the existing Cartesian grid into non-orthogonal curvilinear grid should leads to model the complex geometries.

Other possible area to investigate is the validation of flamelet assumption, which may not be valid in some regions of swirling flames. In terms of computational efficiency for the combustion modelling, a lookup table concept (pre-integrated tables for density, temperature and species concentrations) could be considered.

In lookup table approach the state relation and other nonlinear functions are often known prior to conducting a simulation, in which case the PDF integrals can be calculated and stored into look up table before the simulation begins.

The current combustion model is sufficient for the prediction of vortex/flame interactions and other kinematic fluid/flame processes (e.g., Vortex-Breakdown). However, it is unable to predict flame extinction or quenching induced by aerodynamic (stretch and strain) or chemical effects. Possible method for such calculation is to develop the progress-variable approach presented by Pierce (2001). It add much capability to the steady flamelet model, it is by no means a complete combustion model, but rather a first step toward a more general approach. The combination of flamelet progress variable approach and unsteady flamelet modelling should be an ideal way to predict the flame extinction in turbulent non-premixed combustion.

To model the formation of pollutants such as oxides of nitrogen  $NO_x$  an additional equations having significantly slower time scales should be considered. In terms of computational cost, this can also use the pre-integrated chemistry table with further development of the procedure for efficient calculation.

## References

- AL-ABDELI, Y.M. AND MASRI, A.R. (2003a). Recirculation and flowfield regimes of unconfined non-reacting swirling flows. *Exp. Thermal Fluid Sci.*, **27**, 655–665.
- AL-ABDELI, Y.M. AND MASRI, A.R. (2003b). Stability characteristics and flowfields of turbulent non-premixed swirling flames. *Combust. Theory Model.*, **7**, 731–766.
- AL-ABDELI, Y.M. AND MASRI, A.R. (2004). Precession and recirculation in turbulent swirling isothermal jets. *Combust. Sci. Tech.*, **176**, 645–665.
- ANACLETO, P., HEITOR, M.V. AND MOREIRA, A. (1996). The mean and turbulent flow field in a model rql gas turbine combustor. *Exp. Fluids*, **22**, 153–166.
- BARDINA, J., FERZIGER, J.H. AND ROGALLO, R.S. (1985). Effects of rotation on isotropic turbulence: computation and modeling. *J. Fluid Mech.*, **154**, 321–336.
- BARLOW, R.S. AND FRANK, J.H. (1998). Effect of turbulent on species mass fractions in methane/air jet flames. *Proc. Combust. Inst.*, **27**, 1087–1095.

- BELL, J.B. AND COLELLA, P. (1989). A second order projection method for the incompressible navier-stokes equations. *J. Comput. Phys.*, **85**, 257–283.
- BENJAMIN, T.B. (1962). Theory of the vortex breakdown phenomenon. *J. Fluid Mech.*, **14**, 593–605.
- BILANIN, A.J. AND WIDNALL, S.E. (1973). Aircraft wake dissipation by snuoidal instability and vortex breakdown. *AIAA*, **107**, 11–17.
- BILGER, R.W. (1976). The structure of diffusion flames. *Combust. Sci. Tech.*, **13**, 155–178.
- BILGER, R.W. (1988). The structure of turbulent non-premixed flames. *Proc. Combustion Inst.*, 475–488.
- BILGER, R.W. (1993). Conditional moment closure for turbulent reacting flow. *Phys. Fluids*, **A5**, 436–444.
- BILGER, R.W., POPE, S.B., BRAY, K.N.C. AND DRISCOLL, J.F. (2005). Paradigms in turbulent combustion research. *Proc. Combust. Inst.*, **30**, 21–42.
- BILLANT, P. AND CHOMAZ, J.M. (1998). Experimental study of vortex breakdown in swirling jet. *J. Fluid Mech.*, **376**, 183–198.
- BOWMAN, C.T., HANSON, R.K., DAVIDSON, D.F. AND WILLIAMS, J. (1995). Gri 2.11. <http://www.gri.org>.
- BRANLEY, N. (1999). *Large eddy simulation of non-premixed turbulent flames*. Ph.D. thesis, Imperial college, UK.

- BRANLEY, N. AND JONES, W.P. (2001). Large eddy simulation of a turbulent non-premixed flame. *Combust. Flame*, **127**, 1914–1934.
- BRAY, K.N.C. AND PETERS, N. (1994). *Laminar flamelets in turbulent flames*. In a P. A. Libby and F. A. Williams editors, Turbulent reacting flows, Academic press.
- BREUER, M. AND HANEL, D. (1993). A dual time stepping method for 3d, viscus incompressible vortex flows. *Comput. Fluids*, **22**, 467–484.
- BUCKLEY, P.L., CRAIG, R., DAVIS, D. AND SCHWARTZKOPF, K. (1983). The design and combustion performance of practical swirlers for integral rocket/ramjets. *AIAA J.*, **21**(5), 733–740.
- BUSHE, W.K. AND STEINER, H. (1999). Conditional moment closure for large eddy simulation of non-premixed turbulent reacting flows. *Phys. Fluids*, **11**, 1896–1906.
- CASTRO, I.P. AND JONES, J.M. (1987). Studies in numerical computations of recirculating flows. *Int. J. Numer. Meth. Flui.*, **7**, 793–823.
- CHANAUD, R.C. (1965). Observations of osillatory motion in certain swirling flows. *J. Fluid Mech.*, **21**, 1–27.
- CHEN, C.S., CHANG, K.C. AND CHEN, J.Y. (1996). Application of a robust beta pdf treatment to analysis of thermal no formation in nonpremixed hydrogen air flame. *Combust. Flame*, **98**, 375–390.
- CHEN, R.H. (1995). Some caharacteristics of nox emission of turbulent non-premixed htdrogen air flames stabilized by swirl generated recirculation. *Combust. Sci. Tech.*, **110**, 443–460.

- CHIGIER, N.A. AND BEER, J.M. (1964). Velocity and static pressure distribution in swirling jets issuing from annular and divergent nozzles. *ASME J.*, **86**, 788-796.
- CHOLLET, J.P. AND LESIUR, M. (1981). Paramtrization of small scales of three dimensional isotropic turbulence utilizing spectral closures. *J. Atmos. Sci.*, **38**, 2747-2757.
- COOK, A.W. AND RILEY, J.J. (1994). A subgrid model for equilibrium chemistry in turbulent flows. *Phys. Fluids*, **6**, 2868-2870.
- COOK, A.W. AND RILEY, J.J. (1998). Subgrid scale modeling for turbulent reacting flows. *Combust. Flame*, **112**, 593-606.
- DALLY, B.B., MASRI, A.R., BARLOW, R.S. AND FITCHER, G.J. (1998). Instantaneous and mean compositional structure of bluff body stabilized non-premixed flames. *Combust. Flame*, **114**, 119-148.
- DEARDORFF, J.W. (1970). A numerical study of three dimensional turbulent channel flow at large reynolds numbers. *J. Fluid Mech.*, **41**, 453-480.
- DEBRUYN, S.M., RILEY, J.J., KOSALY, G. AND COOK, A.W. (1998). Investigation of modeling for non-premixed turbulent combustion. *Flow Turbul. Combust.*, **60**, 105-122.
- DIMARE, F., JONES, W. AND MENZIES, K. (2004). Large eddy simulation of a model gas turbine combustor. *Combust. Flame*, **137**, 278-294.
- EFFELSBERG, E. AND PETERS, N. (1988). Scalar disipation rates in turbulent jets and jet diffusion flames. *Proc. Combustion Inst.*, 693-700.
- ESCUDIER, M. (1987). Confined vortex in flow machinery. *Ann. Rev. Fluid Mech.*, **19**,

- ESCUDIER, M. (1988). Vortex breakdown: Observations and explanations. *Prog. Aerosp. Sci.*, **25**, 189-229.
- FALER, J.H. AND LEIBOVICH, S. (1977). Disrupted states of vortex flow and vortex breakdown. *Phys. Fluids*, **20**, 1385-1400.
- FAROKHI, S., TAGHAVI, R. AND RICE, E.J. (1988). Effect of initial swirl distribution on the evaluation of a turbulent jet. *AIAA J.*, **27**(6), 700-706.
- FAROKHI, S., TAGHAVI, A. AND WHITELAW, J.H. (1989). Effect of initial swirl distribution on the evaluation of a turbulent jet. *AIAA J.*, **27**, 700-706.
- FAVRE, A. (1969). *statistical equations of turbulent cases in problems of hydrodynamics and continuum mechanics*. Society of Industrial and applied mathematics, Philadelphia.
- GERMANO, M., PIOMELLI, U., MOIN, P. AND CABOT, W.H. (1991). A dynamic subgrid scale eddy viscosity model. *Phys. Fluids*, **3**(7), 1760-1765.
- GRABOWSKI, W.J. AND BERGER, S.A. (1976). Solutions of the navier-stokes equations for vortex breakdown. *J. Fluid. Mech.*, **75**, 525-544.
- GUPTA, A.K., LILLY, D.G. AND SYRED, N. (1984). *Swirl Flows*. Abacus, England.
- HAFEZ, M., AHMED, J., KURUVILA, J. AND SALAS, M.D. (1987). Vortex breakdown simulation. *AIAA*, **87**, 1343-1349.
- HALL, M.G. (1972). Vortex breakdown. *Ann. Rev. Fluid Mech.*, **4**, 195.

- HARVEY, J.K. (1962). Some observation of the vortex breakdown phenomenon. *J. Fluid Mech.*, **14**, 585–592.
- HORIUTI, K. (1997). A new dynamic two parameter mixed model for large eddy simulation. *Phys. Fluids*, **9**, 3443–3464.
- HORIUTI, K. AND YOSHIZAWA, A. (1985). *LES of turbulent channel flow by one equation model*. In E. H. Hirschel editor, Finite approximations in fluid mechanics, Vieweg.
- JONES, J.P. (1964). On the explanation of vortex breakdown. *IUTAM Conf. on VB.*, **21**, 4984–5000.
- JONES, W.P. (1994). *Turbulence modeling and numerical solution methods for variable density and combusting flows*. In P. A. Libby and F. A. Williams editors, Turbulent reacting flows, Academic press.
- KEMPF, A.M. (2003). *Large eddy simulation of non-premixed turbulent flames*. Ph.D. thesis, TU-Darmstadt, Germany.
- KEMPF, A.M., KLEIN, M. AND JANICKA, J. (2005). Efficient generation of initial and inflow conditions for transient turbulent flow in arbitrary geometries. *Flow Turb. Combust.*, **74**, 67–84.
- KEMPF, A.M., JANICKA, J. AND LINDSTEDT, R.P. (2006). Large eddy simulation of a bluff body stabilized non-premixed flame. *Combust. Flame*, **144**, 170–189.
- KIM, S.H. AND HUH, K.Y. (2002). Use of conditional moment closure to predict soot formulation in a turbulence methane-hydrogen flame over bluff body. *Combust. Flame*, **130**, 94–111.

- KIM, S.H. AND PITSCH, H. (2005). Conditional filtering method for large eddy simulation of turbulent non-premixed combustion. *Phy. Fluids*, In press.
- KIM, W., MENON, S. AND MONGIA, H. (1999). Large eddy simulation of a gas turbine combustor flow. *Combust. Sci. Tech.*, **143**, 1–25.
- KIRKPATRICK, M.P. (2002). *A large eddy simulation code for industrial and environmental flows*. Ph.D. thesis, University of Sydney, Australia.
- KIRKPATRICK, M.P., ARMFIELD, S.W. AND KENT, J.H. (2003). A representation of curved boundaries for the solution of the navier-stokes equations on a staggered three dimensional cartesian grid. *J. Comput. Phys.*, **184**, 1–36.
- KLEIN, M., SADIKI, A. AND JANIKAJAN (2003). A digital filter based generation of inflow data for spatially developing direct numerical or large eddy simulation. *J. Comput. Phys.*, **186**, 652–665.
- KLIMENKO, A.Y. (1990). Multicomponent diffusion of various scalars in turbulent flow. *Fluid Dyn.*, **25**, 327–334.
- KOPECKY, R.M. AND TORRANCE, K.E. (1973). Initiation and structure of axisymmetric eddies in a rotating stream. *Comput. Fluids.*, **1**, 289–300.
- KRAICHNAN, R.H. (1976). Eddy viscosity in two and three dimensions. *J. Atmos. Sci.*, **33**, 1521–1536.
- KRAUSE, E. (1990). The solution to the problem of vortex breakdown. *Lecture notes in physics*, **371**, 35–50.
- KRIBUS, A. AND LEIBOVICH, S. (1994). Instability of strong non-linear waves in vortex flows. *J. Fluid Mech.*, **269**, 247–265.

- LAMBOURNE, N.C. AND BRYER, D.W. (1961). The bursting of leading edge vortices—some observations and discussion of the phenomenon. *Aeronaut. Res. Council.*, **36**, 3862–3870.
- LEIBOVICH, S. (1978). The structure of vortex breakdown. *Ann. Rev. Fluid Mech.*, **10**, 221.
- LEIBOVICH, S. AND MA, H.Y. (1983). Soliton propagation on vortex cores and the hasimoto soliton. *Phys. Fluids*, **26**, 3173–3190.
- LENTINI, D. (1994). Assesment of stretched laminar flamelet approach for non-premixed turbulent combustion. *Combust. Sci. Tech.*, **100**, 95–122.
- LEONARD, A. (1974). Energy cascade in large eddy simulation of turbulent fluid flows. *Advances in geophysics*, **18(A)**, 235–248.
- LEONARD, B.P. (1979). A stable and accurate convective modeling procedure based on quadratic upstream interpolation. *Comput. Meth. Appl. Mech. Engr.*, **19**, 59–98.
- LEONARD, B.P. (1987). Sharp simulation of discontinuities in highly convective steady flow. Tech. Rep. 100240, NASA Tech. Mem.
- LESSEN, M., SINGH, P.J. AND PAILLET, F. (1974). The stability of trailing line vortex. *J. Fluid Mech.*, **63**, 753–763.
- LILLY, D. (1992). A proposed modification of the germano sub-grid closure method. *Phys. Fluids*, **4(3)**, 633–635.
- LILLY, D.K. (1967). The representation of small scale turbulence in numerical simulation experiments. *In proceedings of the IBM scientific computing symposium on enviromental sciences*, **320-1951**, 195–210.

- LUCCA-NEGRO, O. AND O'DOHERTY, T. (2001). Vortex breakdown: a review. *Prog. Energy Combust. Sci.*, **27**, 431-481.
- LUDWEIG, H. (1964). *Flugwiss*, **12**, 304-312.
- MAHESH, K., CONSTANTINESCU, G., S. APTE, G.I., HAM, F. AND MOIN, P. (2005). Large eddy simulation of reacting turbulent flows in complex geometries. *ASME J. Appl. Mech.*, **In press**.
- MASRI, A.R., POPE, S.B. AND DALLY, B.B. (2000). Probability density function computation of a strongly swirling nonpremixed flame stabilized on a new burner. *Proc. Combust. Inst.*, **28**, 123-131.
- MASRI, A.R., KALT, P.A.M. AND BARLOW, R.S. (2004). The compositional structure of swirl stabilised turbulent non-premixed flames. *Combust. Flame*, **137**, 1-37.
- MENON, S., YEUNG, P. AND KIM, W. (1996). Effects of subgrid models on the computed interscale energy transfer in isotropic turbulence. *Comput. Fluids*, **25**, 165-180.
- NAUGHTON, J.W., CATTAFESTA, L.N. AND SETTLES, G.S. (1997). An experimental study of compressible turbulent mixing enhancement in swirling jets. *J. Fluid Mech.*, **330**, 271-305.
- NEJAD, A.S. (1989). Application of a laser velocimetry for characterization of confined swirling flow. *J. Eng. for gas turbines and power*, **111**, 36-45.
- PANDA, J. AND MCLAUGHLIN, D.K. (1994). Experiments on the instabilities of a swirling jets. *Phys. Fluid.*, **6**, 263.
- PECKHAM, D.H. AND ATKINSON, S.A. (1957). Preliminary results of low speed wind tunnel test on a gothic wing of aspect ratio. *ARC CP.*, **1.0**, 508-513.

- PETERS, N. (1983). Local quenching due to flame stretch and non-premixed turbulent combustion. *Combust. Sci. Tech.*, **30**, 1–17.
- PETERS, N. (1984). Laminar diffusion flamelet models in non-premixed turbulent combustion. *Prog. Energy Combust. Sci.*, **10**, 319–339.
- PETERS, N. (2000). Turbulent combustion. In *Turbulent combustion*, Cam. Uni. Press.
- PIERCE, C.D. (2001). *Progress variable approach for large eddy simulation of turbulent combustion*. Ph.D. thesis, Stanford University, California, USA.
- PIERCE, C.D. AND MOIN, P. (1998). A dynamic model for subgrid scale variance and dissipation rate of a conserved scalar. *Phys. Fluids*, **10**, 3041–3044.
- PIERCE, C.D. AND MOIN, P. (2004). Progress-variable approach for large eddy simulation of non-premixed turbulent combustion. *J. Fluid Mech.*, **504**, 73–97.
- PIOMELLI, U. (1999). Large eddy simulation: achievements and challenges. *Phys. Aeros. Sci.*, **35**, 335–362.
- PIOMELLI, U. AND CHASNOV, J.R. (1996). *Large eddy simulations: theory and applications*. Kluwer, United Kingdom.
- PIOMELLI, U. AND LIU, J. (1995). Large eddy simulation of rotating channel flows using a localized dynamic model. *Phys. Fluids*, **7**, 839–848.
- PITSCH, H. (1998). A c++ computer program for 0-d and 1-d laminar flame calculations. Tech. rep., RWTH Aachen.

- PITSCH, H. (2002). Improved pollutant predictions in large eddy simulations of turbulent non-premixed combustion by considering scalar dissipation rate fluctuations. *Proc. Combust. Inst.*, **29**, 1971–1978.
- PITSCH, H. (2006). Large eddy simulation of turbulent combustion. *Annu. Rev. Fluid. Mech.*, **38**, 453–482.
- PITSCH, H. AND PETERS, N. (1998). A consistent flamelet formulation for non-premixed combustion considering differential diffusion effects. *Combust. Flame*, **114**, 26–40.
- PITSCH, H. AND STEINER, H. (2000). Large eddy simulation of a turbulent piloted methane-air diffusion flame (sandia flame d). *Phys. Fluids*, **12**(10), 2541–2554.
- POINSOT, T. AND VEYNANTE, D. (2001). Theoretical and numerical combustion. In *Theoretical and numerical combustion*, R. T. Edwards.
- POPE, S.B. (1990). Computations of turbulent combustion: progress and challenges. *Proc. Combust. Inst.*, **23**, 591–612.
- POPE, S.B. (2000). *Turbulent Flows*. Cambridge University press, United Kingdom.
- PRESS, W.H., FLANNERY, B.P., TEUKOSKY, S.A. AND VETTERLING, W.T. (1996). *Numerical Recipes in Fortran 90*. Cambridge University press, United Kingdom.
- RAMAN, V. AND PITSCH, H. (2005). Large eddy simulation of bluff body stabilized non-premixed flame using a recursive-refinement procedure. *Combust. Flame*, **142**, 329–347.

- RANDALL, J.D. AND LEIBOVICH, S. (1973). The critical state: a trapped wave model of vortex breakdown. *J. Fluid Mech.*, **53**, 495–508.
- RAYLEIGH, L. (1916). *Proc. R. Soc.*, **93**, 148–154.
- REPP, S., SADIKI, A., SCHNEIDER, C. AND JANICKA, J. (2002). Prediction of swirling confined diffusion flame with a monte carlo and a presumed pdf model. *Int. J. Heat and Mass Transfer*, **45**, 1271–1285.
- SAGUAT, P. (2002). *Large eddy simulation for incompressible flows*. Springer-Verlag, Berlin Heidelberg.
- SANKARAN, V. AND MENON, S. (2002). Les of spray combustion in swirling flows. *J. Turbulence*, **3**, 11–23.
- SARPKAYA, T. (1971). Vortex breakdown in swirling conical flow. *AIAA*, **9**, 1792–1799.
- SCHUMANN, U. (1975). Subgrid scale model for finite difference simulation of turbulent flows in plane channels and annuli. *J. Comput. Phys.*, **18**, 376–404.
- SHEEN, H.J. AND CHEN, W.J. (1996). Correlation of swirl number for a radical type swirl generator. *Exp. Therm. Fluid Sci.*, **12**, 444–451.
- SHI, X. (1985). Numerical simulation of vortex breakdown. *Proc. Collo. on VB*, **25**, 69–80.
- SHTERN, V. AND HUSSAIN, F. (1999). Collapse, symmetry breaking, and hysteresis in swirling flows. *Annu. Rev. Fluid Mech.*, **31**, 537–566.
- SLOAN, D.G., SMITH, P.J. AND SMOOT, L.D. (1986). Modeling of swirl in turbulent flow systems. *Prog. Energy Combust. Sci.*, **12**, 163–250.

- SMAGORINSKY, J. (1963). General circulation experiments with the primitive equations, the basic experiment. *Mon. Weath. Rev.*, **91**, 99–164.
- SMITH, L.M. AND YAKHOT, V. (1993). Short and long time behavior of eddy viscosity models. *Theo. Comput. Fluid Dyn.*, **4**, 197–207.
- SPALL, R.E. AND GATSKI, T.B. (1987). A numerical simulation of vortex breakdown. *ASME F. on Uns. Flow. Sep.*, **52**, 25–33.
- SQUIRE, H.B. (1962). Analysis of the vortex breakdown phenomenon. *Academic Verlag*, 306.
- STEIN, O. AND KEMPF, A. (2006). Les of the sydney swirl flame series: a study of vortex breakdown in isothermal and reacting flows. *Proc. Combust. Inst.*, **31**, 1975–1982.
- SYRED, N. AND BEER, J.M. (1972). The damping of precessing vortex cores by combustion in swirl generators. *Ast. Acta*, **17**, 783–801.
- SYRED, N. AND BEER, J.M. (1974). Combustion in swirling flows: a review. *Combust. Flame*, **23**, 143–201.
- TANGIRALA, V. AND DRISCOLL, J.F. (1988). Temperature within non-premixed flames: effects of rapid mixing due to swirl. *Combust. Sci. Tech.*, **60**, 143–162.
- TENNEKES, H. AND LUMLEY, J.L. (1972). *A first course in Turbulence*. MIT press, USA.
- TNF (2006). International workshop on measurements and computation of turbulent non-premixed flames. <http://www.ca.sandia.gov/TNF/abstract.html>.

- VANKAN, J. (1986). A second order accurate pressure correction scheme for viscous incompressible flow. *J. Sci. Stat. Comput.*, **7**, 870–891.
- WALL, C.T. AND MOIN, P. (2005). Numerical methods for less of acoustic combustion instabilities. *Tec. Rep.*, **91**, 22–45.
- WANG, P. AND BAI, X.S. (2005). Large eddy simulation of turbulent swirling flows in a dump combustor: a sensitivity study. *Int. J. Num. Meth. Flu.*, **47**, 99–120.
- WANG, S. AND RUSAK, Z. (1997). The dynamics of a swirling flow in a pipe and transition to axisymmetric vortex breakdown. *J. Fluid Mech.*, **340**, 177–198.
- WARNATZ, J., MASS, U. AND DIBBLE, R.W. (1996). *Combustion: physical and chemical fundamentals, modeling and simulation, experiments, pollutant formation*. Springer-Verlag, Berlin.
- WEBER, R. (1986). Vortex breakdown: Observations and explanations. *21st Int. Symp. on Combust.*, 1435–1443.
- WEBER, R., VISSER, B.M. AND BOYSAN, F. (1990). Assessment of turbulent modelling for engineering prediction of swirling vortices in the near zone. *Int. J. Heat and Fluid Flow*, **11**, 225–240.
- WERNER, H. AND WENGLE, H. (1991). Large eddy simulation of turbulent flow over an around a cube in a plate channel. *In 8th Sym. Turb. She. Flow.*, 102–110.
- WILLIAMS, F.A. (1985). *Combustion Theory*. Addison-Wesley, California.

- XIA, J.L., LIU, Y.S. AND SMITH, B.L. (1998). Numerical and experimental study of swirling in a model combustor. *Int. J. Heat and Mass Tran.*, 41, 1485-1498.



